Università degli Studi di Ferrara

INTERNATIONAL DOCTORAL COURSE IN
EARTH AND MARINE SCIENCES (EMAS)
CYCLE XXXV

COORDINATOR Prof. CIAVOLA PAOLO

IMPACT OF THE CARNIAN PLUVIAL EPISODE ON DEPOSITIONAL SYSTEMS AND WEATHERING

Scientific/Disciplinary Sector GEO/02

Candidate
Dott. PECORARI MATTEO

_____
(signature)

Supervisor
Prof. GIANOLLA PIERO

_____
(signature)

Co-Supervisors

Dr. CAGGIATI MARCELLO _____

Prof. CRUCIANI GIUSEPPE _____

Dr. TATEO FABIO _____

Years 2019/2022

ACKNOWLEDGEMENT

First, I would like to thank Prof. Daoliang Chu for the final preparation of the samples and performing the geochemical analyses in XRF and ICP-MS, and Dr. Jacopo Dal Corso for being a connection with the Wuhan University laboratories and especially for cooperation in writing the paper that resulted from this project and for the helpful and stimulating discussions.

I would also like to thank: Dr. Umberto Tessari for his help in calcimetry analysis; Dr. Guido Roghi, Prof. Andrea Marzoli, Prof. Matteo Ardit and Dr. Alberto Riva for their useful discussions on many occasions during these three years; Greta Alverà for her help in the sampling activity.

Also, my gratitude goes to the reviewers, Prof. Marco Franceschi and Prof. Massimo Setti, for their helpful suggestions and comments which improved the scientific quality of the manuscript.

The last acknowledgement, but not in order of importance, is for my supervisors: Prof. Piero Gianolla, Dr. Marcello Caggiati, Prof. Giuseppe Cruciani, and Dr. Fabio Tateo, who accompanied and guided me along this path.

ABSTRACT

This PhD project aims to review the effects of the Carnian Pluvial Episode (CPE) on global sedimentation and its impact on weathering of Carnian successions in the Dolomites which, due to the extraordinary preservation of depositional geometries and the high-resolution stratigraphic framework, represent a key area for the Triassic and for understanding the CPE. To obtain a more complete and comprehensive picture, not only the syn-event stratigraphic interval, represented in the Dolomites by the Heiligkreuz Fm, was studied, but also the pre- and post-CPE conditions were considered, covering a stratigraphic interval between the underlying San Cassiano Fm and the overlying Travenanzes Fm. The CPE is a climatic perturbation that had important consequences on biota and sedimentation, and its global character is now widely recognized by the scientific community. By analyzing the successions deposited during the Carnian in different areas and depositional settings worldwide, it became particularly evident that occurring changes in sedimentation were more or less synchronous with the CPE. Comparison between different areas also revealed the great heterogeneity in the robustness of the stratigraphic constraints. Many areas have already been the subject of paleoclimatic studies that have related changes recorded by the sedimentary successions to the CPE. This project particularly highlighted areas where it would be necessary to improve the stratigraphic resolution instead and to further investigate the possible link between interesting changes recorded in sedimentation and climate. On the other hand, it has been observed that in some areas, during the CPE, despite recorded changes in sedimentation, the climate was humid even before the event and does not show climatic changes referable to it; or remains under typically arid conditions of the Upper Triassic.

The CPE is marked by perturbations in the Carbon cycle that resulted in increased temperature and intensification of the global hydrologic cycle, enhanced runoff and weathering. The characterization and quantification of these latter holds great interest from a paleoclimate reconstruction perspective. Therefore, in this project, geochemical analyses aimed at calculating weathering indices and constructing diagrams discriminating sediment provenance, were applied for the first time to well-known stratigraphic successions of the Dolomites, together with qualitative and quantitative mineralogical analyses, with particular focus on clay minerals, which are weathering products. Hence, the sampling work targeted intervals rich in fine sediments and resulted in the building of a composite section. The analyses showed that in the Dolomites, an increase in chemical weathering (indicative of climate humidification) compared to the pre-CPE conditions (San Cassiano Fm), is recorded synchronously with the onset of the CPE (Alpe di Specie Mb - Heilgkreuz Fm) and with geochemical-mineralogical variations recorded by other studies carried out in other areas of the world and in different depositional environments. After the onset of the CPE, a strong eustatic sea level fall occurred (Borca Mb). This caused a rejuvenation of the river systems, resulting in a large increase in erosion, which carried older, recycled sediments into the basins. Source diagrams showed that samples from the different units can be grouped into two different clusters, respectively before and after sea level fall, indicating two different sources. The source change partially obliterates the paleoclimatic signal derivable from the weathering; in fact, a decoupling in the trend of weathering indices was observed since the sea level fall. However, the interpretation of a wet climate within this interval remains confirmed by other sedimentological or palynological proxies. Post-CPE (Travenanzes Formation), geochemistry and mineralogy confirm a return to arid climatic conditions under high physical weathering.

TABLE OF CONTENTS

1 GENERAL INTRODUCTION

1.1 THE CARNIAN PLUVIAL EPISODE

The Carnian Pluvial Episode (CPE) is a climatic perturbation occurred between 232 and 234 Ma, during the Carnian (Late Triassic). It is biostratigraphically constrained to the time interval spanning from the boundary between Julian 1 and 2 substages (*Trachyceras aonoides* Subzone – *Austrotrachyceras austriacum* Zone) and the Tuvalian 2 substage (*Tropites subbullatus* Zone; Dal Corso et al. 2018 a and b). The CPE was recognized and proposed for the first time by Simms and Ruffell (1989). They found evidence of a shift to more humid climate and of widespread extinctions, studying the sedimentology and crinoid fauna of the North Curry Sandstone and Dunscombe Formation in UK, and of the Stuttgart Fm in Germany. They suggested that the environmental change was global and named it as "Carnian Pluvial Episode". Since this pioneer study, several papers have been published dealing with other successions worldwide (Simms and Ruffell, 2018; Dal Corso et al. 2020 and references therein) which substantiated the hypothesis of Simms and Ruffell (1989). In literature the CPE was alternatively called: "Reingraben Event" (e.g. Hornung et al., 2007b), "Carnian Pluvial Event" (e.g., Roghi, 2004; Furin et al 2006; Rigo et al., 2007; Roghi et al. 2010),: "Mid Carnian Wet Intermezzo" (MCWI; Kozur and Bachmann, 2010; Ogg, 2015), "Carnian Pluvial Phase" (CPP; Mueller et al., 2016a; Shi et al., 2017), "Carnian Pluvial Episode" (CPE – e.g., Dal Corso et al. 2015, 2018; Jin et al., 2020), "Carnian Humid Episode" (CHE; e.g., Sun et al., 2016; Chatalov 2017; López-Gómez et al., 2017; Jin et al., 2018; Reolid et al., 2018) and "Carnian crisis" (e.g., Hornung et al., 2007a).

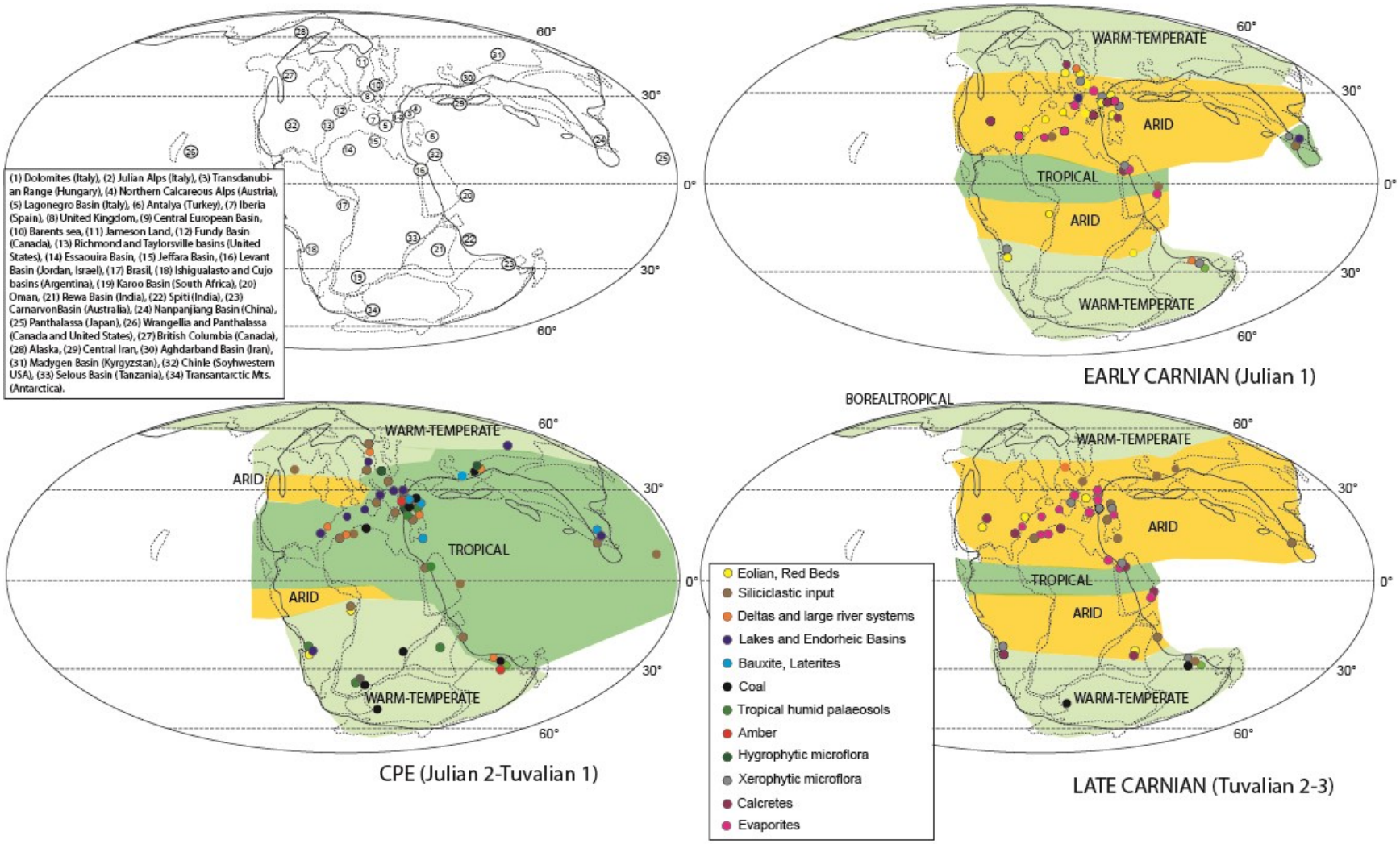

Figure 1.1 World paleogeographic map at Carnian age with different climatic zones and paleoclimatic proxies. From Mazaheri-Johari (2021).

However, the global character of the CPE has not been unanimously accepted by the scientific community, especially by those scientists working on the Central European Basin (CEB). Visscher et al. (1994) first rejected the CPE, analysing palynological assemblages collected in southern Germany, from the Estherenschichten, Schilfsandstein and Lehrbergschichten. They argued that the humid climatic shift noted by Simms and Ruffell (1989) was only a local expression of the setting of the large fluvial system (Schilfsandstein) in the CEB. This early rejection suffered from the lack of available data from other localities at that time. More recently, the non-global nature of the CPE was also suggested in other studies from the CEB (Franz et al., 2014 and 2019). These diverging interpretations are mostly related to the fact that the CPE did not have the same expression everywhere. Anyway, very recent works corroborated and demonstrated the original thesis, which finally reached an almost global acceptance (Fig. 1.1 and Simms and Ruffell, 2018; Dal Corso et al., 2019 and 2020). The CPE is generally characterized by a humid climate phase which interrupts the Late Triassic arid conditions (Preto et al., 2010; Stefani et al., 2010; Miller and Baranyi, 2019). In fact, the whole Triassic is considered a broadly arid period, punctuated by some humid intervals during the Anisian, Ladinian and Carnian (Preto et al., 2010; Stefani et al., 2010). The latter interval is the CPE (Fig. 1.1) and is considered the most important one because of its relevant impact on sedimentation and biota (Dal Corso et al., 2020 – Fig. 1.2, 1.3).

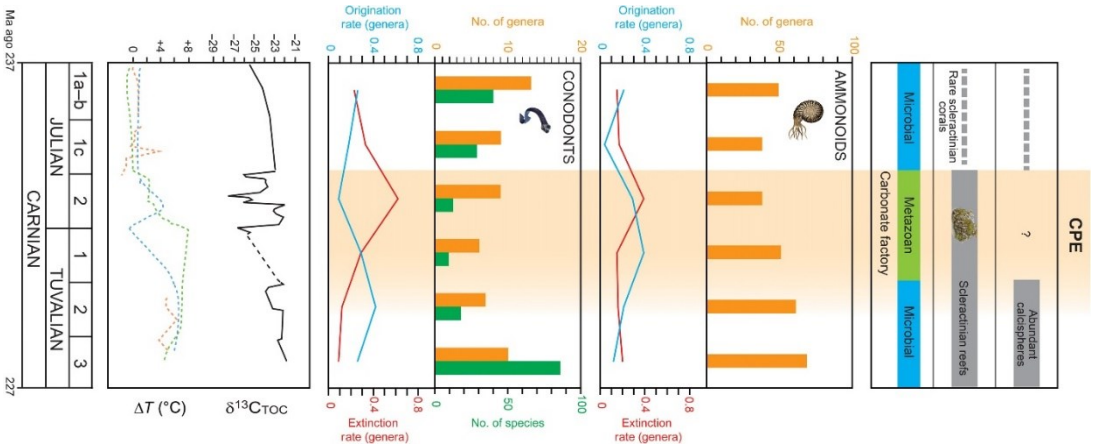

Figure 1.2: Major changes in marine biota occurred during the CPE. From Dal Corso et al. (2020).

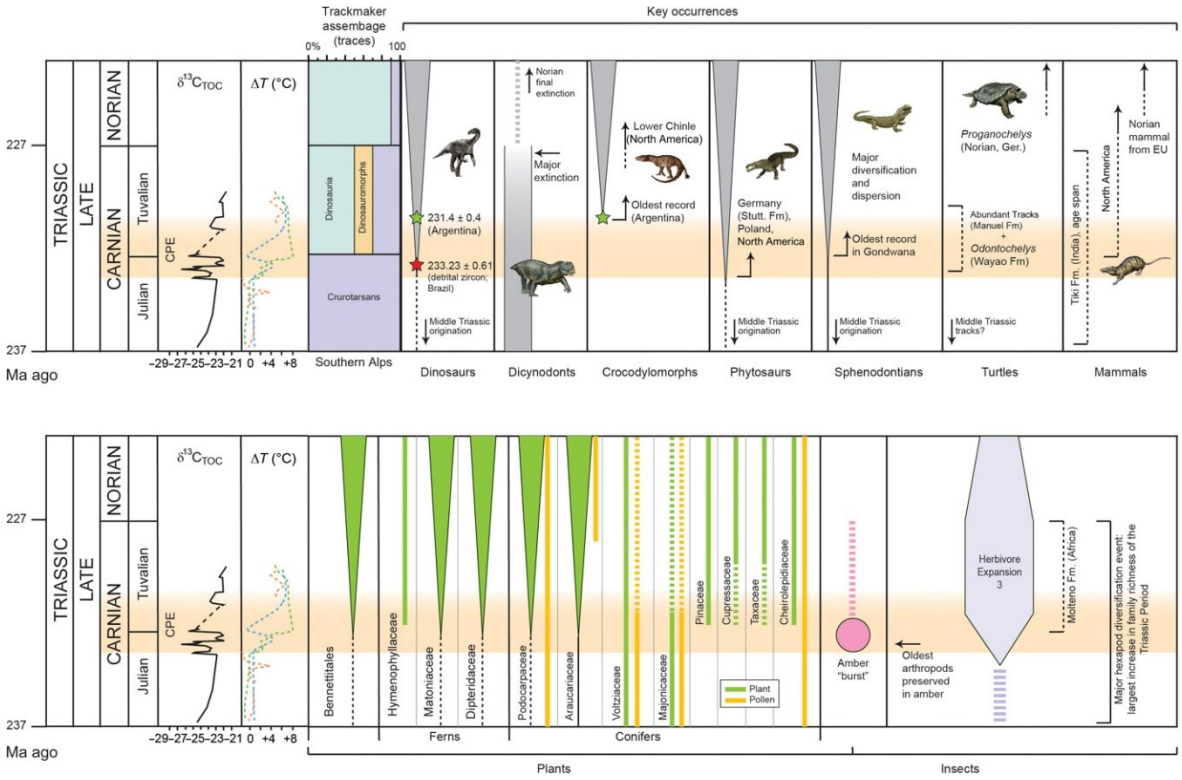

Figure 1.3: Major changes in terrestrial biota occurred during the CPE. From Dal Corso et al. (2020).

It has been demonstrated that the CPE is a multipulse event, marked by perturbations of the global carbon cycle: at least four negative carbon-isotope excursions (NCIEs) have been recognized from different areas so far (Dal Corso et al., 2012, 2015, 2018; Sun et al., 2016 and 2019; Miller et al., 2017- Fig. 1.3, 1.6). The most accepted hypothesis relates these NCIEs to massive volcanic eruptions, in particular the magmatic activity of the Wrangellia Large Igneous Province (LIP – Furin et al., 2006; Dal Corso et al., 2012), which injected a large amount of CO_2 into the atmosphere-ocean system. This hypothesis is suggested my many works and authors (Furin et al., 2006; Dal Corso et al., 2012 and 2015; Xu et al., 2014; Nozaki et al., 2019). Some uncertainties about this hypothesis are because a precise temporal relationship between the emplacement of the Wrangellia LIP and the climatic perturbation has not been established yet. On the other hand, Sun et al. (2019) purposed other volcanic centres, which erupted during the Carnian and whose contribute could be ascribed as a cause of the CPE: for instance, Huglu-Pindos and Kara Dere (Turkey), Mammonia (Cyprus) or South Taimyr (Russia). Sun et al. (2019) also invoked another theory proposed during the last years (Hornung et al., 2007a), suggesting that the CPE could be related to disruption of athmospheric circulation induced by the Cimmerian Ororgeny, connected to the closure of the Paleotethys Ocean. This hypothesis has been confuted by Mazaheri-Johari et al. (2022). Other Authors suggest that the climatic changes triggered by the CPE were due to astronomical forcing (Miller et al., 2017; Ikeda et al., 2020).

The input of CO_2 determined a rise in global temperatures and an enhancement of the hydrological cycle (Trotter et al., 2015; Sun et al., 2016). The consequent increased rainfall triggered increased continental runoff, which led to erosion and transport to the basins of a great quantity of siliciclastic material. The onset of the CPE is followed by turnover of carbonate factories from microbial- to skeletal-dominated and the demise of microbial high relief carbonate platforms (Jin et al., 2020). Then a eustatic sea level fall occurred (Jin et al., 2022; Mazaheri-Johari et al. 2022). Some areas (from both marine and continental setting) record this eustatic sea level fall in strongly stratigraphic constrained succesions, allowing to date the sea level fall just after the onset of the CPE (Gattolin et al., 2015; Jin et al., 2022

– Figure 1.4). In the Dolomites, the seal level fall is marked by the boundary between the Cassian Dolomite/San Cassiano Fm and the Heiligkreuz Fm. The same is for the Julian Alps, where the sea-level fall is marked by the boundary between "Schlern" and Conzen fms (Jin et al., 2022). In addition, synchronous subaerial unconformities have been reported also from Northern Calcareous Alps, Central European Basin, Barents Sea, Aghdarband Basin and Iberia (Jin et al., 2022 and references therein). In the Sichuan Basin, a subaerial unconformity is likewise recorded on top of the Tianjingshan Fm: the very strong erosion reached the lowermost Julian sediments (dated by conodonts and ammonoids) and elided both the NCIE-1 and 2 (Jin et al., 2022).

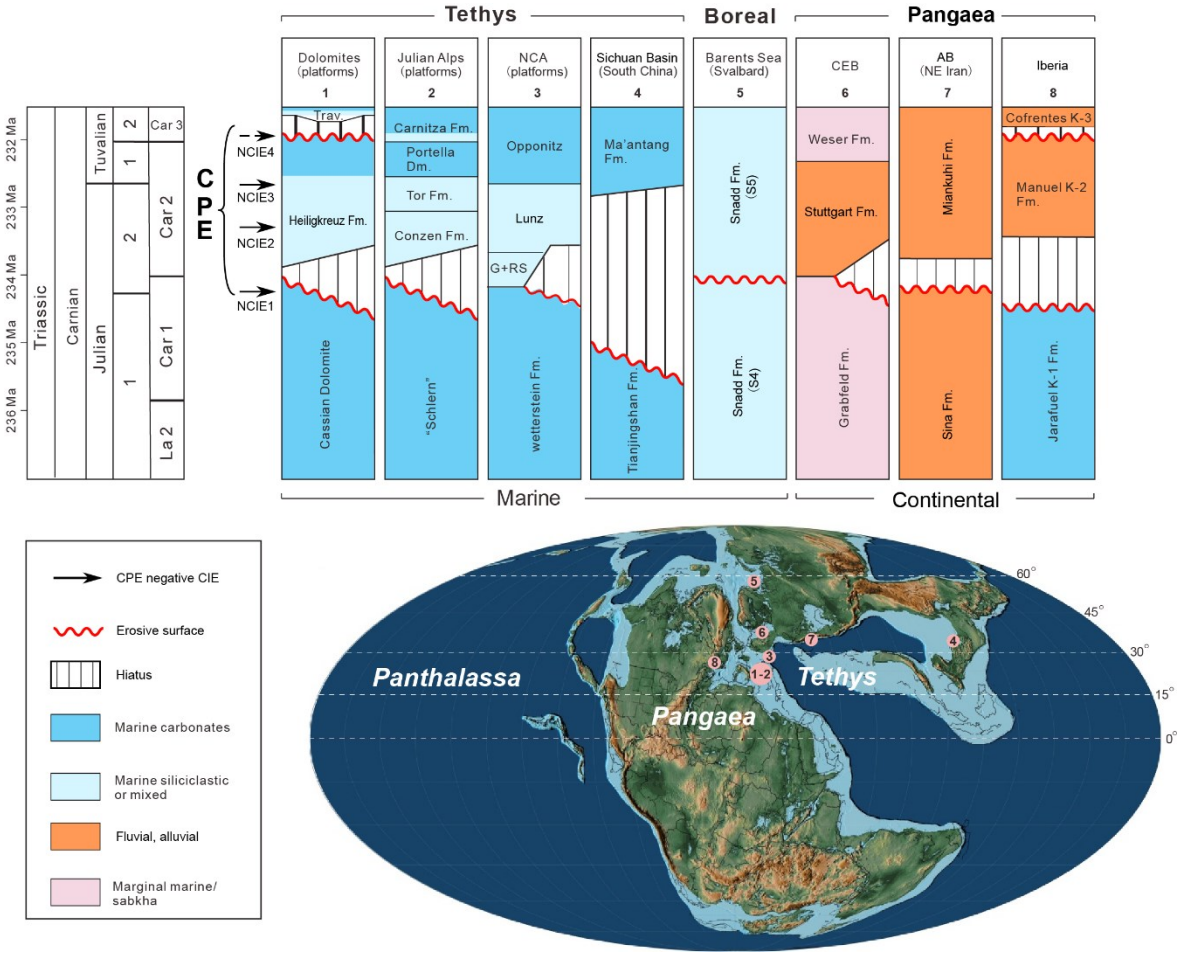

Figure 1.4: Record of the Carnian eustatic sea-level fall and NCIEs related to the CPE in marine (Tethyan and Boreal) and continental well-constrained areas (Pangaea). Modified from Jin et al. (2022). Abbreviations: G+RS = Göstling Mb. and Reingraben Shales; AB = Aghdarband Basin.

Other feature commonly related to the CPE in continental settings is the development of fluvio-deltaic systems or lacustrine environments rich in coal deposits. For a detailed analysis of the global evolution of the sedimentation during the Carnian and the relationship with the CPE refer to Chapter 2. Climatic changes strongly impacted on ecosystems: both marine and terrestrial biota have been affected by the CPE, with numerous important turnovers and changes. For instance, the production of amber, which is a stress indicator for plants, increased (Gianolla et al., 1998a; Roghi et al., 2006, 2022; Seyfullah et al., 2018a, b) and floristic associations became dominated by hygrophytic taxa at the expense of the xerophytic ones (e.g.,: Roghi, 2004; Roghi et al., 2010; Fijałkowska-Mader, 2015; Mueller et al., 2016a; Baranyi et al., 2019a; Fijałkowska-Mader et al., 2020; Lu et al., 2021; Peng et al., 2021; Li et al., 2022; Mazaheri-Johari et al., 2022), even if there is some local exception for this latter point (Franz et al., 2019; Baranyi et al., 2019b). Moreover, many important families of ammonoids, conodonts, crinoids, bryozoans and vertebrates experienced a crisis

during the CPE (Dal Corso et al., 2018a, 2020). After extinctions, new groups radiated (e.g., Reolid et al., 2018; Buffa et al., 2019) and occupied the ecological niches left free (Dal Corso et al., 2020): the most notable case being undoubtedly the dinosaurs. In fact, their diversification started during the Carnian (e.g., Brusatte et al., 2010; Benton et al., 2014; Baron et al., 2017) but recently this event has been strongly linked to the CPE (Bernardi et al., 2018; Garcia et al., 2019; Mancuso et al., 2020). Furthermore, calcareous nannofossils, scleractinian corals, and modern families of conifers became abundant after this episode (Preto et al., 2013; Dal Corso et al., 2020, 2021). Also, new availability of ecological niches and nutrient supply related to the CPE favored the diversification of dinoflagellate cysts (Mantle et al., 2020).

To avoid misunderstandings and to separate the "episode" itself (global) from its effects on sedimentary environments (local) and biosphere (global/local), the CPE is here defined as a climatic perturbation whose onset is marked in the stratigraphic record by the NCIE-1 and whose end occurs briefly after the NCIE-4. This definition reflects the global character of the perturbation, since the $\delta^{13}C$ shifts, documenting the beginning of C-cycle perturbation that led to biological and geological consequences reshaping the Carnian world, are recorded globally and in extremely narrow intervals.

1.1 AIM OF THIS PROJECT

The complexity displayed by the CPE have required the application of several different methods to characterize and better understand the phenomenon at global scale: palynology (e.g., Roghi, 2004; Mueller et al., 2016a and b; Paterson et al., 2016a; Baranyi et al., 2019a and b), bio- and isotope stratigraphy (e.g., Dal Corso et al., 2012, 2015 and 2018; Muller et al., 2016a and b; Miller et al., 2017; Shi et al., 2019), sedimentology (e.g., Andrews et al., 2014; Arche and López-Gómez, 2014; Franz et al., 2014; Mueller et al., 2014; López-Gómez et al., 2017; Barrenechea et al., 2018; Horn et al., 2018; Jewuła et al., 2019; Jiang et al., 2019), clay mineralogy (Rostási et al., 2011; Decou et al., 2017; Barrenechea et al., 2018; Baranyi et al., 2019a; Mancuso et al., 2020; Zhang et al., 2021).

These works considered together show that the sedimentological expression of the CPE is not the same everywhere. For this reason, the first aim of this PhD project is to examine published data about sedimentology of successions deposited during the Carnian worldwide. Hence, a review of the sedimentological features of the CPE has been carried out and, coupled with data from areas where no paleoclimatic study have been conducted yet to obtain a complete picture of sedimentation during the Carnian (see Chapter 2). This is the first goal of this project: this is not a simple work of revision of previously published literature about the CPE and allowed to: highlight interesting peculiarities where the CPE was already recognized, witnessing that the CPE is not uniform everywhere; detect changes in sedimentation and environment in areas that are poorly studied but which deserve future investigations on paleoclimatic evolution; point out the disproportion in stratigraphic resolution among different areas.

Secondly, the focus of this project is the CPE across the Dolomites. The Dolomites are unanimously considered an open-air laboratory for Triassic geology, owing to the noteworthy preservation of the depositional geometries (Fig. 1.5). Moreover, most of stratigraphic sections through the Dolomites carry abundant and biostratigraphically-relevant fossils, making the succession strongly constrained by biostratigraphy (e.g., De Zanche et al., 1993, 2000; Gianolla et al., 1998b, 2003, 2018; Neri et al., 2007; Breda et al., 2009; Roghi et al., 2010; Dal Corso et al., 2015, 2018), isotope stratigraphy (dal Corso et al.,2012, 2015, 2018), magnetostratigraphy (Maron et al., 2017 and 2019), and physical

stratigraphy (e.g., Pisa et al., 1980; De Zanche et al., 1993; Gianolla et al., 1998a; Keim et al., 2001, 2006; Neri et al., 2007; Stefani et al., 2010; Gattolin et al., 2013, 2015).

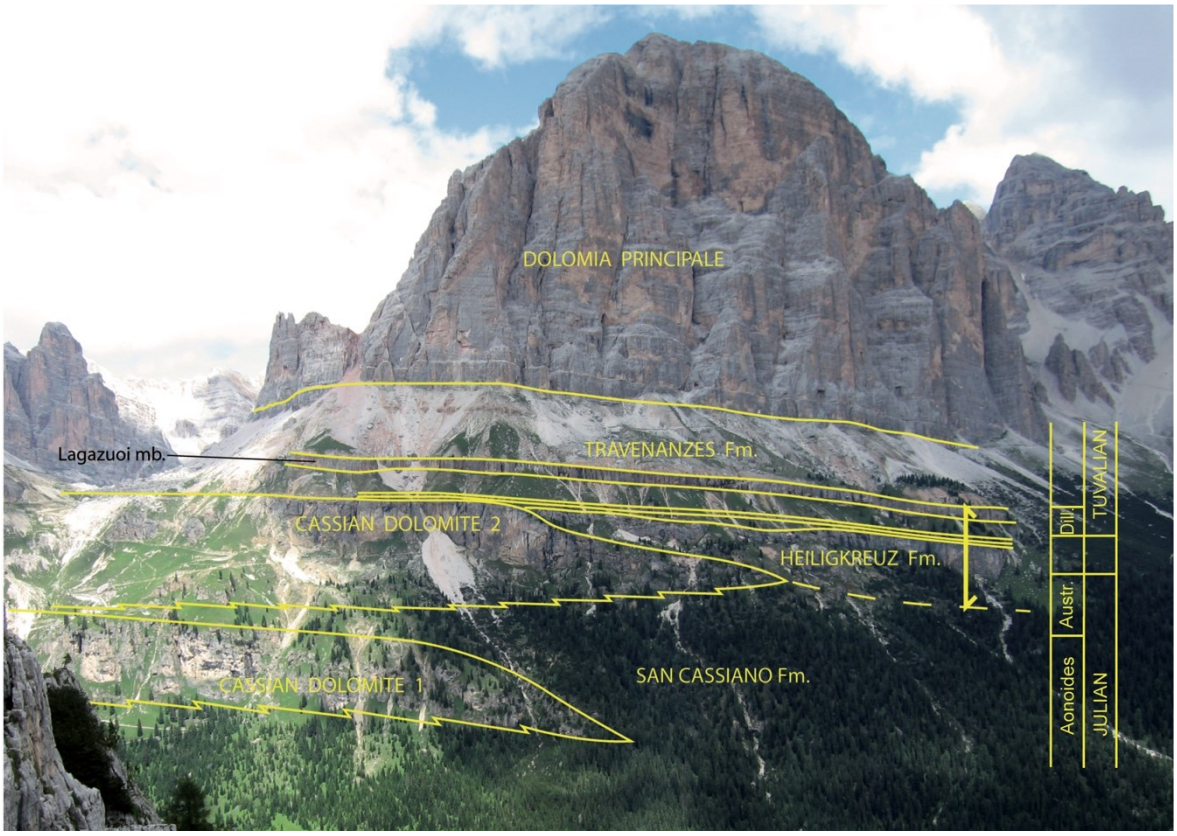

Figure 1.5: Outcrop of the Upper Triassic succession near the Tofana di Rozes (Dolomites), an area where the depositional geometries are well preserved and easily recognizable. From Gianolla et al. (2010).

The CPE in the Dolomites is represented by the Heiligkreuz Formation (cf. Neri et al., 2007 and Chapter 2), deposited from late Julian to early Tuvalian and displaying remarkable changes in sedimentation and biota. Therefore, the unit has been object of many studies about sedimentology and stratigraphy; paleobotany and palynology; geochemistry (e.g., stable isotope and Hg-geochemistry) during last decades (Gianolla et al., 1998a; Preto and Hinnov, 2003; Roghi et al., 2006, 2010, 2022; Breda et al., 2009; Bernardi et al., 2018; Dal Corso et al., 2018; Preto et al., 2019; Mazaheri-Johari et al., 2021 and ref. therein).

With respect to other as well-studied and constrained areas (e.g., Transdanubian Range or China – Rostasi et al., 2011; Shi et al., 2017 and 2019; Baranyi et al., 2019; Zhang et al., 2021) the Dolomites are lacking geochemical and mineralogical studies on fine-grained sediments, especially clay minerals. The latters could be helpful to quantify weathering processes and therefore act as paleoclimate proxies, due to the close relationship between chemical weathering and climate (e.g., Dinis et al., 2020). Indeed, chemical weathering usually increases under humid climate, while physical weathering dominates when climate is more arid. Therefore, is possible to use weathering indices in paleoclimatic studies (e.g., Garzanti et al., 2014; Baranyi et al., 2019b; Dinis et al., 2020; Zhang et al., 2021). Weathering indices are equations that consider different chemical elements and result in a numerical value indicative of the degree of chemical weathering undergone by a sample (e.g., Dinis et al., 2020). These indices are indeed based on the fact that as the chemical weathering proceeds, it leads to depletion of a sample in its mobile elements (e.g., Ca, Mg, Na, K), while immobile elements (being Al the main one) are unaffected by the process (e.g., Dinis et al., 2020). Several different weathering indices have been proposed over the years. The differences between the various indices lie basically on the distinct pool of elements used to represent the mobile and "immobile" components of the soil (e.g., Dinis et al., 2020

and references therein). The choice of these representative elements mainly depends on the chemical context derived from the areas of origin at the time of soil formation, and on the subsequent geological history of the succession. In fact, not all indices can be freely used on all types of samples. Since the posting of older formulated indices, such as CIA and WIP that consider a wider range of mobile elements (Parker, 1970; Nesbitt and Young, 1982), researchers have observed over the years that these indices were sometimes subject to bias due, for example, to diagenetic processes. Therefore, they suggested new weathering indices that exclude elements affected by bias (e.g., Cullers, 2000; Garzanti et al., 2014). For an extensive discussion of factors that may impact the results of weathering indices, see Chapters 4 and 5.

INDEX	EQUATION	RESPONSE TO WEATHERING INCREASING	REFERENCES
WIP (Weathering Index of Parker)	$(CaO^*/0.7 + 2Na_2O/0.35 + 2K_2O/0.25 + MgO/0.9) \times 100$	Decreases	Parker (1970)
CIA (Chemical Index of Alteration)	$Al_2O_3/(Al_2O_3 + K_2O + CaO^* + Na_2O) \times 100$	Increases	Nesbitt and Young (1982)
CIW (Chemical Index of Weathering)	$Al_2O_3/(Al_2O_3 + CaO + Na_2O) \times 100$	Increases	Harnois (1988)
PIA (Plagioclase Index of Alteration)	$(Al_2O_3-K_2O)/(Al_2O_3 + K_2O + Na_2O) \times 100$	Increases	Fedo et al. (1995)
CPA (Chemical Proxy of Alteration)	$Al_2O_3/(Al_2O_3 + Na_2O) \times 100$	Increases	Cullers (2000); Buggle et al. (2011)
CIX (modified CIA)	$Al_2O_3/(Al_2O_3 + K_2O + Na_2O) \times 100$	Increases	Garzanti et al. (2014)
WI	$(Na+K_2O)/Ti$	Decreases	Summa et al. (2018)
Rb/K_2O	Rb/K_2O	Increases	Nesbitt et al. (1980); McLennan et al. (1990); Plank and Langmuir (1998); Dinelli and Lucchini (1999)

Table 1: Weathering indices calculated for this work, with relative equations, trends with respect to increasing weathering conditions, and references.

Starting from these considerations and in order to provide new data that improve the knowledge about the CPE, pelitic beds and interbeds have been sampled in different localities of the Dolomites, building a composite section (Fig. 1.6) encompassing the San Cassiano Fm (i.e., pre-event conditions) to the Travenanzes Fm (i.e., post-event conditions). Geochemical and mineralogical analyses have been carried out on the samples to obtain a quantitative parameter useful to study the weathering conditions across the CPE (see Chapter 4). Indeed, another goal of this project is to consider not only the syn-CPE interval, but also the pre-and post-event intervals. This allows to get a more complete picture, which also considers the conditions prior to the CPE and in its aftermath, and to achieve more complete paleoclimatic reconstruction (see Chapter 5 for details). Table 1 shows the formulas of the weathering indices considered in this work (with references) and their response to increased chemical weathering. Any index has been excluded a priori: comparing the results of some

different indices afterwards allows to better highlight which indices display meaningful results and which do not, and to identify bias.

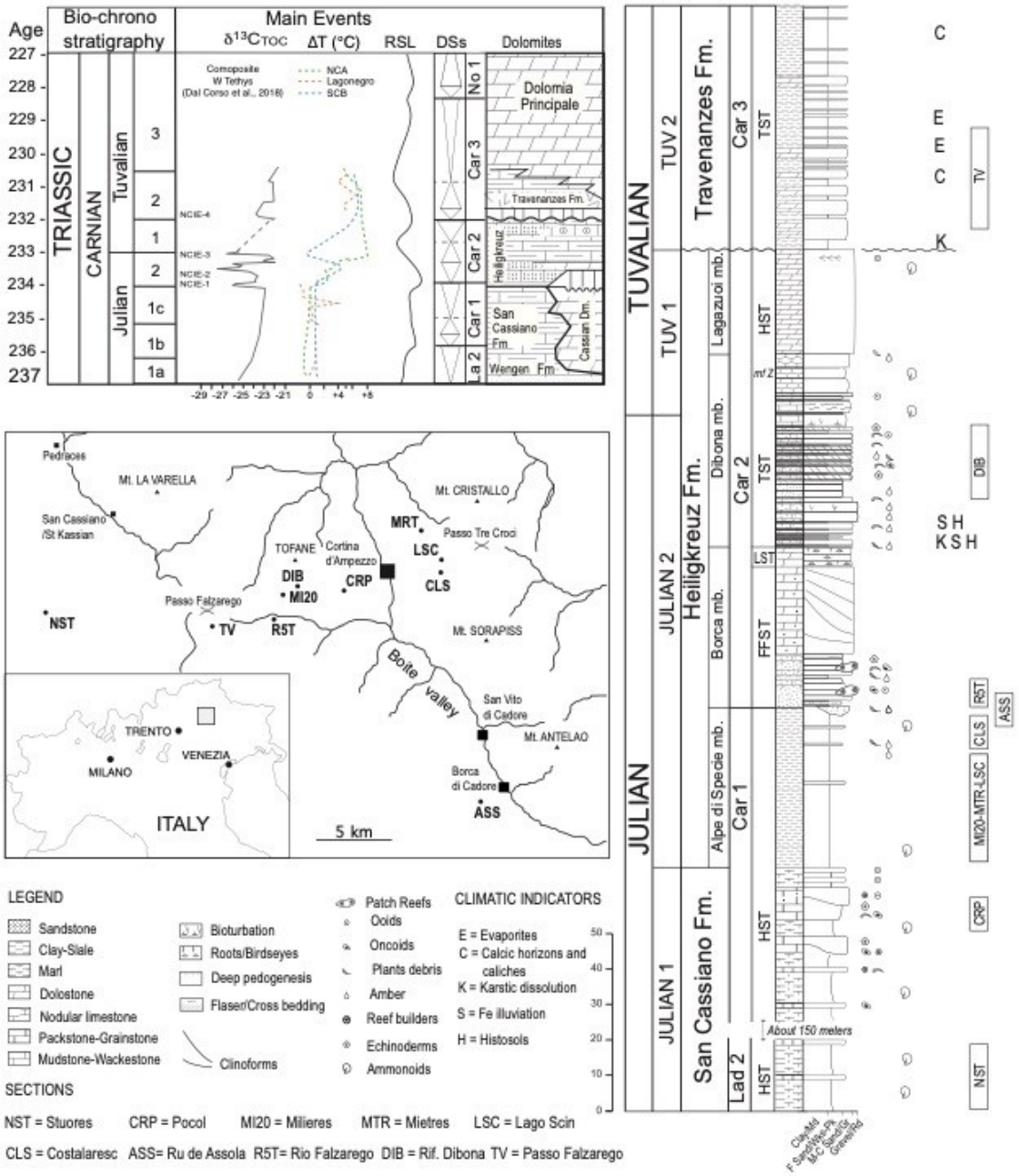

Figure 1.6: Studied area and composite section (see Chapter 5 for further details).

2 REVIEW OF GLOBAL CARNIAN STRATIGRAPHY AND RESPONSE OF SEDIMENTARY ENVIRONMENTS TO THE CPE

2.1 INTRODUCTION

Modelling suggests that increases in temperature driven by injections of volcanic CO_2 into the exogenic C-cycle could enhance, in pulses, the hydrological cycle, increasing continental runoff (Dal Corso et al., 2022) and resulting in higher transport into the basins of siliciclastic material. One of the most spectacular characteristics of the CPE, which makes it somehow different from other more famous events, is indeed this sharp change in sedimentation observed in many areas in both continental and marine settings. In some places these sedimentological changes are so large-scale and pervasive that can be easily detected simply looking at the outcrops from distance, and define today landscapes (Fig. 2.1).

Figure 2.1: Impact of the CPE in on the nowadays landscape: the evident ledge separating carbonate platforms is due to the demise of the microbial carbonate factory during the CPE time (Nuvolao, Lastoi de Formin and Croda da Lago, Dolomites).

However, the sedimentological expression of the CPE was not the same everywhere. Sedimentological changes also occurred in other areas which have not been studied for paleoclimatic reconstructions yet. Moreover, other areas did not record any change in sedimentation during the Carnian. The aim of this first part of the PhD project is to analyze globally sedimentary successions deposited during the Carnian, from marginal-marine to deep-water to continental settings, in order to highlight differences also for the robustness of the stratigraphic constrains. The here discussed successions are divided in eleven macro areas (Western Tethys, Northern and Central Europe, Central Atlantic Domain, Southern Gondwana, Northern Gondwana, Southern Tethys, Northern Tethys and Eastern Laurasia, Eastern Tethys, Cimmerian Blocks, Panthalassa, Wrangellia). The investigated areas were grouped according to their paleogeographical-structural setting. Carnian time is unfortunately affected by the lack of detailed published paleogeographic reconstructions: in fact, they are usually focused on Anisian or Norian time and the most accurate

paleogeographies reconstruct since 180 Ma, due to more exhaustive and complete dataset compared to previous periods. Also, the notorious global reconstructions proposed by the research group led by Scotese are affected by a variable detail gap from area to area, as in the case of the Western and Eastern Tethys. During last tens of years several paleogeographic reconstructions have been published for the Late Triassic (e.g., Dercourt et al., 2000; Stampfli, 2001; Golonka, 2007a, b; Schettino and Turco, 2011; Haas et al., 2015; Stampfli et al. 2013; Scotese, 2014; Barriere et al., 2018; Golonka et al., 2018; van Hinsberger et al., 2019), but they display many significant differences and disagreements, mainly because they are based on contrasting structural interpretations or developed on single proxy (e.g., petrography, stratigraphy, paleomagnetic poles, ecc.) without taking in consideration in conjunction each other. This implies that one fully accepted interpretation for Carnian world paleogeography does not exist yet.

To takle these issues, all the more recent local and global paleogeographies (see specific references in the text) have been critically reviewed and combined in a single geodatabase built by ArcGIS, to obtain a solid background for the global revision of Carnian sedimentation and paleoenvironments.

Each macro-area is subdivided in regions, of which the different depositional settings (continental, shallow and deep water) are finally discussed. The areas where the CPE has been already recognized are reviewed, focusing on the sedimentary response to the CPE C-cycle perturbations in each basin.

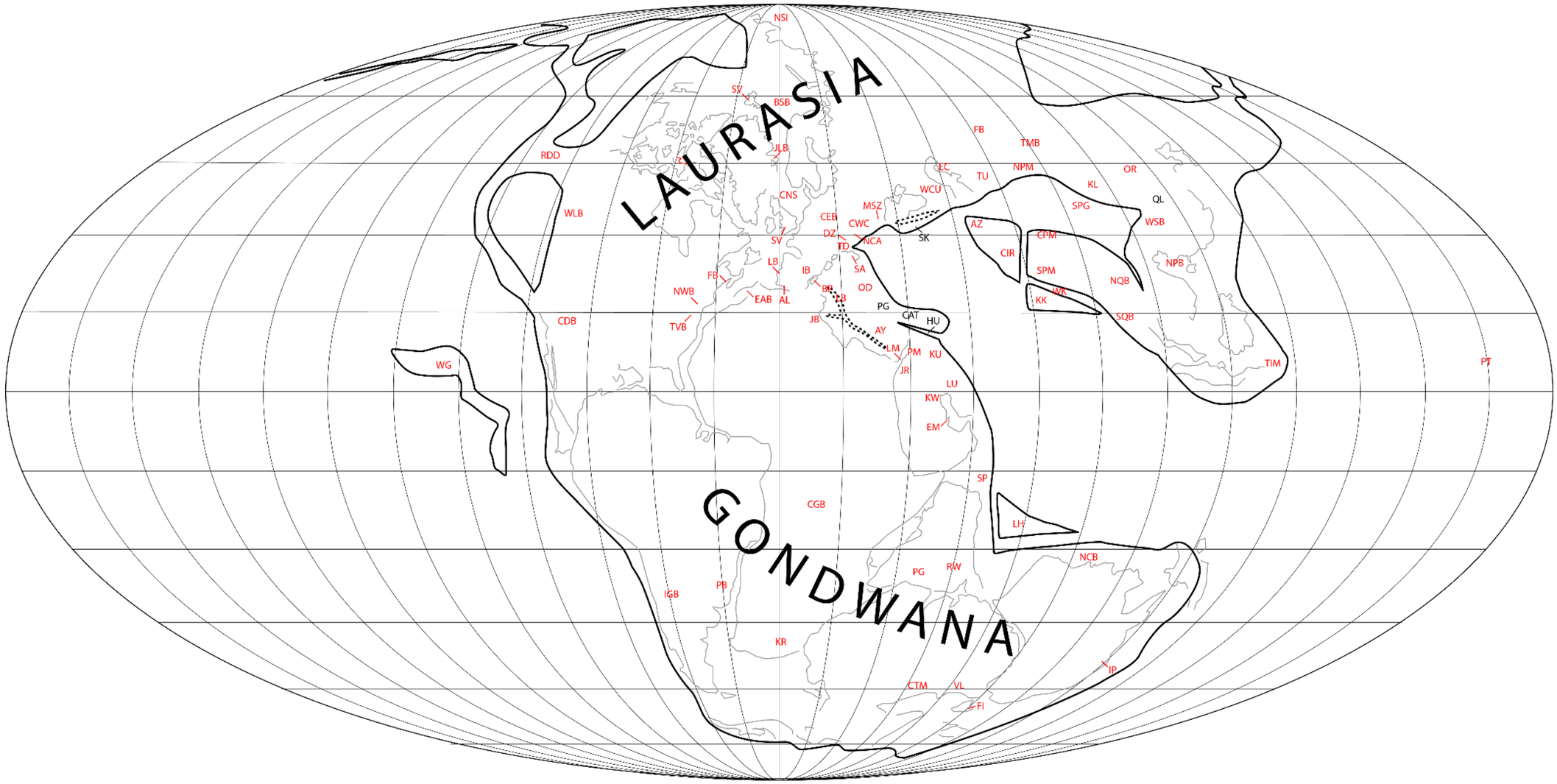

NCB - North Carnarvon Basin (Australia)
FI - Fingal Valley (Tasmania)
IP - Ipswich Basin (Australia)
VL - Victoria Land (Antarctica)
CTM - Central Transantarctic Mountains (Antarctica)
PG - Pranhita-Godawari Basin (India)
RW - Rewa Basin (India)
KR - Karoo Basin (Africa)
CGB - Congo Basin
IGB - Ischigualasto- Villa Union Basin (Argentina)
PB - Paranà Basin (Brasil)
FB - Fundy Basin (New Brunswick)
NWB - Newark Basin (New Jersey)
TVB - Taylorsville Basin (Virginia)
WLB - Williston Lake Basin (British Columbia)
RDD - Red Dog District (Alaska)
CDB - Chinle-Dockum Basin (western USA)
EAB - Essaouira and Argana basins (Morocco)
IB - Iberian Basin (Spain)
BP - Balearic Plateaux (Spain)

LB - Lusitanian Basin (Portugal)
AL - Algarve Basin (Portugal)
MSZ - Moesia-Strandja Zone
CEB - Central European Basin
CNS - Central North Sea
BSB - Barent Sea Basin
SV - Svaalbard Islands
JLB - Jameson Land Basin (Greenland)
SA - Southern Alps (Dolomites and Julian Alps, Italy)
OD - Outer Dinarides
LB - Lagonegro Basin (Italy)
DZ - Drauzug and Northern Karawanken (Austria)
NCA - Northern Calcareous Alps (Austria)
WC - Central and Western Carpatians
AY - Antalya (Turkey)
SV - Severn Basin (UK)
JB - Jeffara Basin (Tunisia)
LM - Levant Margin (Israel)
KU - Kurdistan
LU - Lurestan (Iran)

PM - Palmyrides (Syria)
JR - Jordan
KW - Kuwait
EM - Emirates
SP - Spiti Basin (Himalaya)
LH - Lhasa Block (Tibet)
WCU - Western Caucasus
EC - Eastern Caspian Region
FB - Fergana Basin (Kyrgizistan)
TMB - Tarim Basin (China)
NPM - Northern Pamir
SPG - Songpan Ganzi (China)
NSI - Northern Siberia
OR - Ordos Basin (China)
WSB - Western Sichuan Basin (China)
NPG - Nanpanjiang Basin (China)
WG - Wrangellia Terrane
CPM - Central Pamir
SPM - Southern Pamir
WK - Wakhan Basin

KK - Karakoram
NQB - Northern Qiangtang Block
SQB - Southern Qiangtang Block
PT - Panthalassa
TIM - Timor-Leste
KL - Kunlun belt
AZ - Alborz (Iran)
CIR - Central Iran Block
QL - Qinling orogenic belt
SK - Sakaria Zone (Turkey)
CAT - Central Anatolian Zone
HU - Huglu Zone (Turkey)
PG - Pelagonian Zone (Kosovo to Greece)

Figure 2.2: Map of Carnian world (modified from Scotese). Labels in red represent areas considered for this revision.

2.1.1 WESTERN TETHYS

The Western Tethys realm displays a great number of outcrops and stratigraphically well-constrained sections (Fig. 2.3) which encompass all kinds of depositional settings, from continental to marine deep water basins. For this revision, we decided to take into consideration the many successions that are today located in Italy, Slovenia, Austria, Hungary and Turkey. High-resolution studies on magnetostratigraphy (Maron et al., 2017, 2019), sequence stratigraphy (Gianolla and Jacquin, 1998; Gianolla et al., 1998b), conodont, ammonoid and palynomorphs biostratigraphy (e.g. Rigo et al., 2018; Mietto et al., 2012; Lukeneder and Lukeneder 2014; Roghi 2004; Roghi et al., 2010; Mueller et al., 2016b; Dal Corso et al., 2020 and references therein) and geochronology (Furin et al., 2006; Aubrecht et al., 2017; Dunkl et al., 2019) are helpful to date and correlate distant geological units and events recorded therein.

In general, the shallow water sedimentation was predominantly carbonate throughout the whole Western Tethys, from the latest Ladinian until the Julian 1 (earliest Carnian), except for the Antalya region in which it lasted up to the Julian 2 (late Early Carnian; Lukeneder et al., 2012). The widespread occurrence of high-relief microbial carbonate platforms, as the ones represented by the Cassian Dolomite or Wetterstein Fm or Budaörs Dolomite (e.g., Dal Corso et al., 2015), favoured a mainly carbonate sedimentation also in the neighbouring basins (San Cassiano, Predil Limestone, Füred Limestone, Calcari con Selce and Reifling Fms). At the end of the Julian 1, the carbonate factory shifted from microbial to metazoan, the carbonate production suddenly decreased, and the sedimentation became predominantly siliciclastic: fluvio-deltaic, marginal-marine or shallow water mixed carbonate–siliciclastic facies developed (Stefani et al., 2010; Haas et al., 2012; Dal Corso et al., 2015; Gattolin et al., 2015; Jin et al., 2020). These conditions continued until Tuvalian 2, when the high-relief microbial carbonate platforms (e.g., Dolomia Principale/Hauptdolomit) recovered (Gianolla et al., 2003; Hornung et al., 2007; Stefani et al., 2010; Haas et al., 2012; Caggiati et al., 2018; Dal Corso et al., 2018b; Gale et al., 2018).

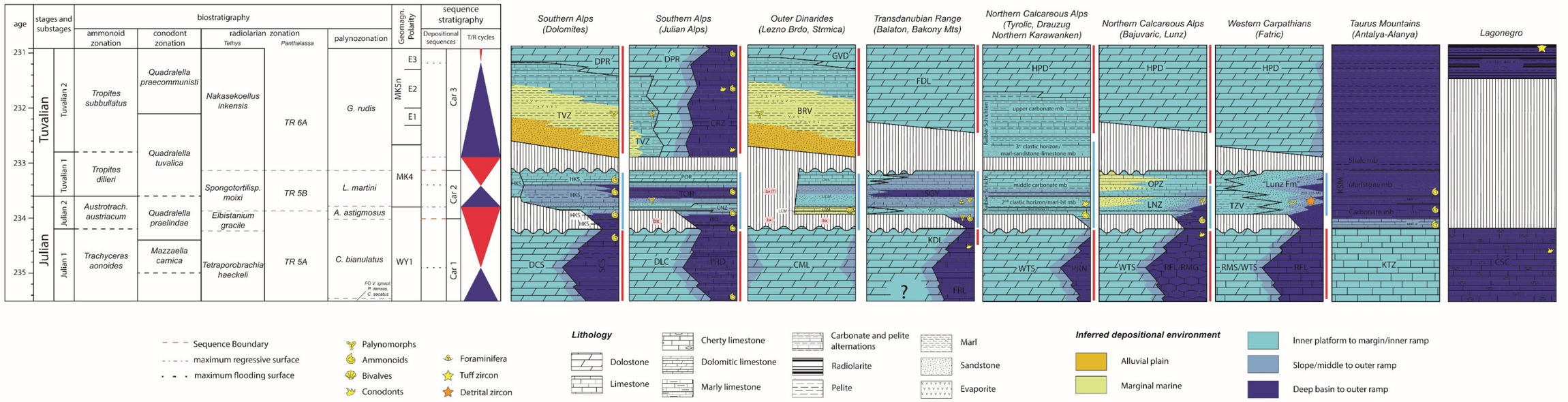

Figure 2.3: Chronostratigraphic framework of selected areas belonging to the Western Tethys: Dolomites, Julian Alps, Outer Dinarides, Transdanubian Range, Northern Calcareous Alps, Western Carpathians, Taurus Mountains, Lagonegro. Vertical strips represent certain or inferred hiatus. Lateral bars indicate the occurrence of arid (red) or humid (blue) paleoclimate proxies. Chronostratigraphy from GTS v2022/10. Biostratigraphy after Mietto and Manfrin 1995 and Krystyn et al. 2007 (ammonoids), Orchard, 2010 (conodonts), Sugyama 1997, Kozur 2003 (radiolarians), Roghi et al., 2010 (palynomorphs). Magnetostratigraphy after Maron et al., 2019, Ogg et a., 2020. Sequence stratigraphy after Gianolla et al., 1998, Gianolla et al., 2021.

Abbreviations: DCS – Cassian Dolomite; SCS – San Cassiano Fm; HKS – Heiligkreuz Fm- 4 Alpe di Specie Mb, 1 Borca Mb, 2 Dibona Mb, 3 Lagazuoi Mb, 5 Durrenstein Mb; TVZ: Travenanzes Fm; DPR: Dolomia Principale; DLC: Ladinian-Carnian Dolomite ('Schelrn'); PRD-Predil Limestone; RDL: Rio del Lago Fm; CNZ: Conzen Fm; TOR: Tor Fm; POR: Portella dolomite; CRZ: Carnitza Fm; CML: Cordevolian Massive Limestone; LCM: Lower Clastic member; CBM: Carbonate member; UCM: Upper Clastic member; OLS: Oncholithic limestone; BRV: Borovnica Beds; GVD: Glavni Dolomit; FRL: Fured Limestone; KDL: Kadarta Dolomite; VSZ: Veszprém Marls; SGY: Sandorhegy Fm; GMY/SDG: Ghemegy Fm and Sedvolgy Dolomite; FDL: Fodolomit; WTS: Wetterstein Fm; PRN: Partnach Fm; HPD: Hauptdolomit; RFL/RMG: Reifling and Raming fms; GST: Gostling Mb; RGB: Reingraben Shales; LNZ: Lunz Sandstones; OPZ: Opponitz Fm; RMS: Ramsau Fm; TZV: Trzinovo Fm. KTZ: Kartoz Fm; KSM: Kasimlar Fm; CSC: Calcari con Selce Fm; Bx: bauxite deposits.

2.1.1.1 DOLOMITES (SOUTHERN ALPS, ITALY)

The Southern Alps (northern Italy) are a fold-and-thrust belt of the Alpine Chain, bounded to the north by the Periadriatic Lineament and to the south by a south-verging thrust system (Castellarin and Cantelli, 2000; Castellarin et al. 2006). The Dolomites are a circa 35 km large pop-up structure of the Southern Alps (Castellarin and Doglioni 1985; Castellarin and Cantelli, 2000), and are UNESCO World Heritage site for their landscapes and scientific importance for geology, geomorphology and palaeontology (Gianolla et al., 2009; Panizza, 2018). During the Triassic the Dolomites occupied the passive margin of the western Tethys (Bosellini et al., 2003; van Hinsbergen et al. 2020).

The typical Carnian succession of the Dolomites region encompasses the time span between Julian 1 (Dolomia Cassiana/San Cassiano Fm.) and Tuvalian 3 (Dolomia Principale) (Dal Corso et al., 2018b and references therein). Above the clino-bedded slope facies of the high-relief, microbial Cassian platform, small, mainly microbial, carbonate mounds occur in lateral heteropy with a more terrigenous interval constituted by dark, sometimes marly pelites and argillites (locally black-shales), with local, rare arenaceous or micritic intercalations (Alpe di Specie mb, Heiligkreuz Fm; corresponding to the member A in Russo et al., 1991; Keim et al., 2006; Tosti et al., 2014; Fedares mb in Brandner et al., 2007; lithozone L-2 in Gattolin et al., 2015). The latter prevails in basinal settings (*Austrotrachyceras austriacum* Zone; Breda et al. 2009), above the last facies of the San Cassiano Fm and it is characterized locally (restricted basins) by a slightly brackish water (Keim et al. 2006). The transition from San Cassiano Fm to the Heiligkreuz Fm documents an increased siliciclastic input during the late Julian, as well as a turnover of the carbonate factory, with the demise of M-factory (sensu Schlager 2003) and the predominance of loose, skeletal grain sediment (Dal Corso et al. 2015; Gattolin et al. 2015; Jin et al., 2020). This affected the last, high-relief carbonate platforms (Keim and Schlager 1999; Keim and Brandner 2001), eventually leading to a change in depositional geometries towards ramp settings (Keim et al. 2006; Breda et al. 2009; Gattolin et al., 2015).

The progressive basins infilling is marked by a huge terrigenous input during the Julian 2, as documented by massive arenites and coarse siliciclastics found together with hybrid arenites and, to a lesser extent, dolostones, and clays and marls (Borca mb – Neri et al., 2007; Breda et al. 2009; Gattolin et al. 2015). Above, well-bedded dolomites often arranged in peritidal cycles capped by stromatolites and paleosols (Preto and Hinnov 2003; Breda et al. 2009; Gattolin et al., 2015), mark the final emplacement of inner ramp settings. The overlaying Dibona mb is characterised by conglomerates, sandstones and pelites coupled with oolitic/bioclastic packstones-grainstones, organized in a transgressive stacking pattern. Coal layers are present, and plants and vertebrate remains (both marine and terrestrial) have been observed (Preto and Hinnov 2003; Breda et al., 2009). Above, the unit is characterized by nodular limestones and marly limestones, and sharply changing upward (*Tropites dilleri* Zone; Gianolla et al., 1998b; De Zanche et al., 2000; Breda et al. 2009) to massive dolomitized oolithic/bioclastic grainstones (Lagazuoi mb), related to a high-energy carbonate ramp setting. Locally, hybrid arenites and siliciclastics with herringbone cross bedding replace pure carbonates (Falzarego Sandstones; Bosellini et al. 1978; Neri et al., 2007; Breda et al., 2009). The top of the Heiligkreuz Fm is marked by an emersion surface, above which the Travenanzes Formation deposited, documenting the emplacement of marginal marine dryland coastal system in the Tuvalian 1 – Tuvalian 2 and the seaward shoreline shift for tens of kilometres (Breda and Preto, 2011). Finally, the transition to well bedded peritidal cycles of the Dolomia Principale marks the return of inner platform settings, related to a high-relief, epi-continental (microbial) carbonate platform occupying most of the Western Tethys passive margin (Caggiati et al., 2018; Haas et al., 2015).

Palaeosols in the uppermost Borca Mb are characterized by spodic and histic horizons that are typical of today tropical humid climates and are markedly different from palaeosols found stratigraphically below and above, which instead developed in a more arid environment (Preto and Hinnov 2003; Breda et al., 2009). In the "humid" palaeosols and in the sandstones of the Borca and Dibona members, a considerable amount of amber is found (Gianolla et al., 1998b; Ragazzi et al., 2003; Roghi et al., 2006, 2022; Seyfullah et al., 2018b). Carnian fossil resin is thought to be of Cheirolepidiacean (an extinct conifer family) affinity (Breda et al., 2009; Schmidt et al., 2012; Seyfullah et al., 2018b; Stilwell et al., 2020), likely indicating that plants were under high environmental stress during the CPE (Seyfullah et al., 2018a). Microflora associations show a shift from assemblages dominated by xerophytic sporomorphs (representing an arid environment), to others dominated by hygrophytic ones (e.g.,: *Cycadopites* sp*., Aulisporites astigmosus, Lagenella martini*), the latter indicators of more humid environmental conditions (Kustatscher et al., 2010; Roghi et al., 2010, 2022). This is recorded through the Borca and Dibona members, whilst in the Lagazuoi Mb studies report a return to more arid conditions (Breda et al., 2009; Dal Corso et al., 2018b). An important faunal change is recorded among tetrapods within the Heiligkreuz – Travenanzes Formations. Footprints found in the Dolomites indicate a shift from a Crurotarsans-dominated assemblage of the early Julian to a Dinosaur-dominated assemblage at the Julian – Tuvalian boundary (Bernardi et al., 2018).

Carbon isotope curves from Carnian succession of the Dolomites show a positive $\delta^{13}C$ trend in the Julian 1, a global feature of the carbon isotope record (Korte et al., 2005; Dal Corso et al., 2012, 2015), suddenly interrupted by a major negative δ13C shift at the Julian 1–2 boundary, i.e. at the onset of the CPE, recorded by higher plant n-alkanes, isoprenoid lipids, wood and total organic carbon (TOC) (Dal Corso et al., 2012, 2015, 2018). The initial negative carbon isotope excursion (NCIE-1) is followed by other negative $\delta^{13}C$ shifts in the topmost Borca mb, within the Julian 2 (*A. austriacum* ammonoid Zone); in the upper part of the Dibona member (close to the Julian–Tuvalian boundary) and at the base of the Travenanzes Fm. (base of the Tuvalian 2; Dal Corso et al., 2018b).

2.1.1.2 WESTERN JULIAN ALPS (SOUTHERN ALPS, ITALY – SLOVENIA)

The Julian Alps stretch from north-eastern Italy to western Slovenia and are part of the Southern Alps belt. A SW-NE oriented fault system (Val Coritenza Line; Gale et al. 2015) separates the region in two tectonic nappes, namely the Western and Eastern Julian Alps. Here we consider the Cave del Predil Area, which is representative of the western domain and where a fairly continuous succession crops out. At Cave del Predil many stratigraphic sections of Carnian age have been measured and studied over the years (e.g., Rio dei Combattenti, Rio Conzen, Portella sections in Assereto et al., 1968; De Zanche et al., 2000; Dal Corso et al., 2018b). Basinal Carnian successions start with the carbonate deposits of the Predil Limestone (*T. aonoides* Zone; Dal Corso et al., 2018b), a succession of dark, platy bituminous limestones with rare marly interbeds, interfingered at the base with coarse to fine grained dolostones (Assereto et al., 1968). The transition to the overlying Rio del Lago Fm marks the beginning of the basins infilling at the end of the Julian 1 (Dal Corso et al. 2018b), similarly to the Dolomites (see paragraph 2.2). The unit is characterized at the base by a short marly interval lacking fossils, followed by shale, marl and marly limestone alternations organized into a shallowing upward trend (Barren Beds *Auctorum*). The Rio del Lago Fm evolves to a middle ramp succession in the Julian 2, where calcareous intercalations with bivalves, ostracods and fecal pellets become more common (De Zanche et al., 2000). The overlying Conzen Fm is deposited on a shallow ramp setting, and is constituted by a succession of dolostones, dolomitic limestones and subordinate marls arranged in asymmetric peritidal cycles (De Zanche et al., 2000; Roghi, 2004). A mixed terrigenous–

carbonate interval occupies the upper portion of the unit: it consists of nodular marly limestones, black siltstones and marls (Roghi, 2004; Dal Corso et al., 2018b). The subsequent Tor Formation is similar at the base, but is upward characterized by alternating marls, siltstones and marly limestones commonly bioturbated and rich of bioclasts. The unit evolves to middle-outer ramp facies associations dated to Tuvalian 1 (Roghi, 2004; Dal Corso et al., 2018b). The overlying Portella dolomite (De Zanche et al., 2000) is characterized by a massive dolostone horizon that is laterally continuous and can be recognized for dozens of kilometres, related again to a shallow carbonate ramp environment. The Carnian succession continues with the Carnitza Fm, dated to Tuvalian 2 – 3 (Liebermann, 1978; Gianolla et al., 2003): it is composed of pelagic bioclastic limestones and calciturbidites with pelites, marls and siltstones interbeds (De Zanche et al., 2000; Gale et al., 2015), rarely with chert nodules. A thickening/coarsening upward trend has been recognized in the upper part and related to the progradation of the heteropic Dolomia Principale carbonate platform (Gianolla et al., 2003; Caggiati et al., 2012, 2018). Its slope facies are composed of clinobedded dolostones, rarely showing a breccia to mega-breccia texture, laterally passing to massive facies of upper slope-to-margin environment, dominated by encrusting organisms (e.g., microproblematica) and microbialites. Similarly, to the Dolomites, the recovery of high-relief microbial flat topped carbonate platforms in the late Tuvalian is documented (Gianolla et al., 2003; Caggiati et al., 2018).

Quantitative palynological and palynostratigraphic analysis of the Cave del Predil area revealed several abundance/dominance variations within the palynological associations along the succession (Roghi, 2004). In particular, the palynological assemblage from the uppermost part of the Conzen Formation to Tor Formation, suggest humid conditions (Roghi, 2004), while palynology indicates a return to arid conditions in the Tuvalian 2 (Roghi, 2004; Roghi et al., 2010). Furthermore, the Tor Fm in two areas of Julian Alps (Cave del Predil and Dogna Valley) records the presence of amber traces within some palynological samples (Roghi et al., 2006), and inside the Tor Fm macroscopic amber samples were found associated to conifer plant remains (Roghi et al., 2006, 2022; Seyfullah et al., 2018b).

The C-isotope record from the Carnian succession in the Julian Alps (Dal Corso et al., 2015, 2018b) shows two sharp negative $\delta^{13}C_{TOC}$ shifts, which correspond to the NCIE-1 and 2 *sensu* Dal Corso et al. (2018b), and can be correlated to the NCIEs found in the Dolomites. Moreover, a negative δ^{13}CTOC shift at the boundary between the Tuvalian 1 and 2, is correlatable to the NCIE-4 found in the Dolomites (Dal Corso et al., 2018b; see paragraph 2.1). The NCIE-3 is missing due to a sampling hiatus within the studied interval (Mazaheri-Johari et al., 2021).

2.1.1.3 LAGONEGRO BASIN (SOUTHERN ITALY)

Remnants of the Lagonegro Basin (Scandone, 1967; Gaetani, 2010) occur in several, N-S elongated, tectonic slices of the Southern Apennines fold-and-thrust belt (southern Italy), originated by thrusting onto the Apulian plate during the Neogene stage of the Alpine orogenesis. The Lagonegro Basin developed since the Middle Triassic on the southwestern passive margin of the Western Tethys. The Calcari con Selce Formation encompasses large part of the Upper Triassic of the area. It was deposited in a deep water setting and consists of hemipelagic cherty and nodular limestones with radiolarians, *Halobia* and rare ammonoids, alternating with thin clayey horizons (Rigo et al., 2012). The carbonate component is mainly represented by mudstone and wackestone, and in suborder packstone, grainstone, grainstone-rudstone and calcareous breccia (Rigo et al., 2012). The deposition of the cherty limestone is suddenly interrupted in the entire area and replaced by ca. 6 m thick green radiolaritic clays, with 0% carbonate content (Furin et al., 2006; Rigo et al., 2007, 2012; Maron et al., 2017). Upward, the recovery of pelagic carbonate sedimentation is

witnessed by the reappearance of cherty limestones. Limestones below the radiolaritic horizon contain a typical Julian conodont fauna (*P. polygnathiformis* zone), while the overlaying beds contain Tuvalian forms (e.g., *Carnepigondolella*; Maron et al., 2017). Similarly, two different palynomorph assemblages typical of the Julian 1 – Tuvalian 1 and of the Tuvalian 2 – 3 have been found respectively below and above the radiolaritic horizon (Furin et al., 2006; Maron et al., 2015, 2017). Zircons from an ash bed in the uppermost part of the green clay rediolaritic horizon gave a U/Pb age of 230.91±0.33 (Furin et al., 2006). A temporal hiatus is thought to be at the base of the green clay radiolaritic horizon, as indicated by biostratigraphy and magnetostratigraphy (Rigo et al., 2007; Zhang et al., 2020).

The halt in carbonate sedimentation coupled with a drastic turnover in conodont fauna, has been interpreted as evidence of a shallowing of the CCD (Rigo et al., 2007). Remarkably, the carbonates of the Calcari con Selce above the green clay radiolaritic horizon contain a substantial amount of calcisphere, which are thought to belong to the *Orthopythonella* group (Preto et al., 2012) in agreement with observation from other areas of Western Tethys where the radiation of calcispheres is synchronous with the onset of the CPE (Dal Corso et al., 2021).

2.1.1.4 NORTHERN KARAVANKE AND DRAUZUG (SLOVENIA - AUSTRIA)

The northern Karavanke are part of the Australpine nappes, representing remnants of the Adria micro-plate, strongly deformed during the Alpine orogeny (Handy et al., 2010). Particularly, they belong to the upper Australpine nappe and are closely related to the Drauzug area succession (Tollmann, 1977; Mandl, 1999; Schmid et al., 2004). Carnian stratigraphy is characterized in both aforementioned areas by discrete siliciclastic pulses that interrupt the shallow water carbonate sedimentation, referred as “Raibl Beds” in the Northern Karavanke or “Raibl Group” in the Drauzug (Bechstädt and Schweizer, 1991; Roghi et al., 2010).

The succession has been outlined by Kolar-Jurkovšek and Jurkovšek (2009, 2010) close to the Mežica mine (northern Slovenia): limestone to dolomite cyclic beds often capped by stromatolitic levels pass upward to a coated grain-rich level, sharply overlapped by a decametric clastic horizon mainly consisting of shale and marlstone beds. Upward, a carbonate interval like the underlying one occurs for more than 100 m, covered by few oncoidal/oolitic beds and suddenly passing upward to a second marly to shaly horizon. Above, carbonate- siliciclastic, shallow ramp facies alternations grade upward to a pure carbonate interval consisting of massive dolomites and, after few meters of oncoidal limestones, a third clastic horizon interrupting the succession is represented by marly limestones. Upward, the siliciclastic succession is again limited to fine intercalations within peritidal limestone beds, eventually grading to Main Dolomite peritidal cycles.

Based on ammonite, palynomorph and conodont associations both the first (bearing *Carnites floridus*) and second (bearing *Nicoraella ? budaensis*) siliciclastic horizons in the Mežica area are dated to the Julian 2 (Kolar-Jurkovšek and Jurkovšek, 2010 and ref. therein), while the third one is likely attributable to the Tuvalian (Roghi et al., 2010). The first clastic horizon is dominated by pteridophyte spores (reflecting a humid, fluvio–deltaic environment), the second horizon is characterized by spores of mangrove-like trees (*Aratrisporites*), and in the third horizon xerophytic groups (Jelen and Kusej, 1982) prevail, testifying to a return to more arid conditions (Kolar-Jurkovšek and Jurkovšek, 2009, 2010; Roghi et al., 2010).

In Rubland (Drauzug) the stratigraphic succession is quite similar: the Wetterstein Fm is Julian 1 in age (Hornung et al., 2007a) and its beds consist in shallow water peritidal cycles,

with megalodontids and capped by stromatolite layers (Bechstadt and Schweizer, 1991) and a widespread emersion surface (Mandl, 2000; Lein et al., 2012). In the Julian 2, it starts the deposition of the informal unit called "Raibler Schicten", which is characterized by three clastic horizons interrupting the carbonate succession: the first one mainly consists of shales with few sandstone intercalations and is overlain by cyclic peritidal limestones capped by stromatolites. The carbonate sedimentation is interrupted again after more than 50 m by a decametric shaly horizon with thin sandstone and ooidal limestone intercalations. Upward, carbonate sedimentation resumes, characterized by cyclic dolostones similar to the previous ones, and are capped by an oncoidal limestone layer, preceding a third clastic horizon. The latter mainly consists of shales with sandstone and oncoidal limestone intercalations. Finally, the succession turns to shallow water limestones rich in coated grains, and then to peritidal cycles of Hauptdolomite (Bechstadt and Schweizer, 1991).

The first and the second shale of the Raibler Schichten contain dominant hygrophytic sporomorphs, which, in the upper part of the third shale, decrease (Roghi et al., 2010). Moreover, the lower portion of the third shales shows an acme of acritarch *Balthisphaeridium*, evidence of marine environment, whilst in the other portion *Aratrisporites* becomes dominant, reflecting the establishment of mangrove-like ecosystem (Roghi et al., 2010). The Raibler Schichten are partly coeval to the *A. austriacum* Zone (Hornung et al., 2007a; Roghi et al., 2010).

2.1.1.5 TRANSDANUBIAN RANGE (HUNGARY)

The Transdanubian Range (TR) represents a tectonic slice that was extruded during the Alpine orogeny in the Oligocene (Kovac et al., 2018) and is in a more eastern position with respect to the original one: the TR was indeed likely located between the Southern Alps and the Australpine, on the western margin of the Tethys. The Carnian succession of the TR in Hungary can be described mainly from core material since outcrops are limited to small areas (Rostási et al., 2011; Haas et al., 2012; Dal Corso et al., 2015, 2018b; Baranyi et al., 2019b). From a stratigraphic point of view, two different areas can be defined, in which the studied cores were drilled: the Balaton Highland-Bakony Mts. and the Zsámbék Basin.

Carnian stratigraphy in the Balaton Highland-Bakony Mts. area starts with the pelagic basin carbonates of the Füred Limestone (Julian 1), followed by fine siliciclastic basinal facies representing the Veszprém Fm (Julian 2). This latter unit is further subdivided into four members, named from lower to upper: Mencshely Marl, Nosztor Limestone, Buhimvölgy Breccia and Csicsó Marl (Baranyi et al., 2019b). The Mencshely Marl consist of dark clayey pelagic marls with silty to sandy intercalations and grades upward to the cherty Nosztor Limestone, related to low-energy, relatively deep and open marine environment (Rostasi et al., 2011). Upward, the siliciclastic content again increases leading to the final transition to the Csicsó member, composed of clayey to calcareous marls dated to the *A. Austriacum* ammonoid zone. Laterally, both the Nosztor Limestone and the lower part of the Csicsó member pass to toe-of-the-slopes deposits of the Buhimvölgy Breccia, mainly consisting of intraclastic brecciated beds and conglomerates (Budai et al., 1999). The Veszprém Fm is overlapped by the Sándorhegy Formation (Tuvalian 1), mainly composed of shallow marine dolomite and limestone with marl intercalations (Budai et al. 1999). The unit represents the final intraplatform basin infill before the late Carnian deposition of the Main Dolomite/Fodolomit (Haas et al., 2015). On the other hand, in the Zsámbék Basin the Füred Lst. is substituted by etheropic platform facies of the Budaörs Formation. The overlying Veszprém Marls Fm is limited to the Mencshely Marl member, and is followed upward by cherty dolomites of the Csákberény Formation (Julian – Tuvalian). This latter unit can be correlated to the Sándorhegy Fm and represents the intraplatform basin infill (Baranyi et al.,

2019b). A peculiar common characteristic of the two units is the presence of amber droplets inside (Csillag. and Földvári 2007; Baranyi et al., 2019b).

$\delta^{13}C_{TOC}$ records come from boreholes. At the transition from the Füred Limestone to the Mencshely Marl Mb, i.e., at the boundary between Julian 1 and 2, a first NCIE is recorded (Dal Corso et al., 2018b). A second NCIE is recorded within the Mencshely Mb., and a third NCIE has been found between the Julian and Tuvalian in the Csákberény Fm. (Dal Corso et al., 2018b). These NCIEs can be correlated to those found in the Dolomites and Julian Alps (Dal Corso et al., 2018b).

Rostási et al. (2011) studied the clay minerals composition of the TR succession in the same boreholes, while Baranyi et al. (2019b) used weathering proxies (see Paragraph 4.2 for details) coupled with palynomorph associations as paleoclimatic indicators. Quantitative palynological analysis indicates a shift towards hygrophytic elements in the Julian 2 (Csicsó Marl). The increase in the hygrophytic forms is also partially coincident with an increase of weathering indeces, indicating strong continental runoff and more humid environmental conditions in the lower part of the Veszprém Formation (Baranyi et al., 2019b), and also in agreement with the enhanced kaolinite content recorded along the Veszprém Fm by Rostási et al. (2011). On a higher detail, the wetter conditions in the Julian 2 appear to have been periodically interrupted by shorter periods of drier climate marked by the deposition of carbonates and breccias, which interfinger the marly units (Baranyi et al., 2019b). Another humid episode is highlighted in the late Julian 2 by a second peak of hygrophytes species, but a contemporaneous decrease in kaolinite content (Rostási et al., 2011) and the weathering indices might suggest an interval of stronger seasonality. Finally, xerophytic associations return in the Tuvalian (Baranyi et al., 2019b).

2.1.1.6 NORTHERN CALCAREOUS ALPS (AUSTRIA) AND CENTRAL WESTERN CARPATHIANS (SLOVAKIA)

In the western portion of the Northern Calcareous Alps (NCA; e.g., Heiterwand, Radonatobel; Bechstadt and Schweizer, 1991) the outcropping succession is very similar to that described in the Drauzug area: three clastic horizons have been recognized, interrupting the carbonate sedimentation. The latter is represented at the base of the Carnian succession by peritidal cycles of the Wetterstein Fm, and by commonly brecciated shallow ramp dolostone beds capped by stromatolites in the second carbonate interval. Sandstone intercalations in the shaly horizons are more frequent and thicker than in the Drauzug area. The final transition to the Hauptdolomit is characterized by recrystalized and brecciated vuggy dolostones (Bechstadt and Schweizer, 1991). In the eastern portion of the NCA (e.g., at Lunz am See), Carnian stratigraphy starts with basinal marly deposits of the Partnach Fm, overlain by limestones with subordinate shales of the Raming Fm. These units are etheropic to the Reifling Fm, which represents calcareous slope facies (Mueller et al., 2016b). The Partnach, Raming and Reifling Fm are Julian 1 in age (*Trachyceras aonoides* Subzone – Roghi et al., 2010; Mueller et al., 2016b). The uppermost part of the Reifling Fm is represented by laminated bituminous limestones, named Göstling Member (Roghi et al., 2010), and is biostratigraphycally constrained to the *Austrotrachycheras austriacum* Zone (Julian 2; Mueller et al., 2016b). The Julian 2 succession continues with the Reingraben Shales and the Lunz Formation. The first unit basically consists of marine shales. The Lunz Fm, formerly known also as Lunzer Schichten or Lunzer Sandstein (Tollmann, 1976; Krystyn et al., 1991; Köppen, 1997), is mainly made of sandstones and siltstones deposited in a deltaic environment (Roghi et al., 2010; Dal Corso et al., 2015; Mueller et al., 2016b). In the Tuvalian 1 (*T. dilleri* Zone) a shift to marine conditions occurs with the deposition of the shallow water carbonates of the Opponitz Fm (Roghi et al., 2010). Finally, during the

Tuvalian 3, Main Dolomite/Hauptdolomit started to deposit (Hornung et al., 2007b), a regional feature of the whole Western Tethys. Microflora of both the Reingraben Shales and Lunz Fm is dominated by hygrophytic forms; whilst xerophytic groups are rare, with the exception of Bisaccates (Roghi et al., 2010; Mueller et al., 2016b). *Aulisporites astigmosus* reaches an acme in the upper part of the Lunz Formation (Roghi et al., 2010; Mueller et al., 2016b). From the medium member of the Lunz Fm (Hauptsandstein Mb.) the abundance of hygrophytic forms gradually decreases up to the lower–middle part of the Opponitz Formation, in which xerophytic taxa dominate (Roghi et al., 2010; Mueller et al., 2016b). Thus, the Opponitz Fm marks the end of a humid phase in the area (Roghi et al., 2010; Mueller et al., 2016b). Amber has been reported both from Lunz Fm and Raibler Schicten (Seyfullah et al., 2018b).

Lunz am See area has been also object of high-resolution carbon isotope analyses (Dal Corso et al., 2015; Mueller et al., 2016b). $\delta^{13}C_{TOC}$ values show a negative spike at the base of the Julian 2 (Göstling Fm) that is correlatable to the NCIEs recorded in other areas at the same stratigraphic level, and is synchronous with the shift in palynomorphs associations toward hygrophytic forms (Dal Corso et al., 2015; Mueller et al., 2016b). $\delta^{18}O$ analyses on conodont apatite suggest a rise of temperature at the boundary between Julian 1 and 2, during the CPE (Hornung et al., 2007b).

The Western Carpathians are a portion of the Carpathian chain, which belongs to the ALCAPA (Alps-Carpathians-Pannonia) Mega-unit. The Slovakia territory is crossed by the Central Western Carpathians, which represent a further subdivision of the former chain (the other are defined as Inner/Internal and Outer/External), connected westward to the Eastern Alps and to the east to the Outer/External Carpathians, which was formed by the complex stacking of several nappes and units occurred during Mesozoic and Cenozoic, due to Alpine orogenesis (Plašienka, 2019; Szaniawski et al., 2020). The Upper Triassic of Central Western Carpathians in Slovakia records a temporary interruption of carbonate sedimentation and an enhanced siliciclastic deposition during the Carnian (Sýkora et al. 2011; Aubrecht et al., 2017). In the Krížna Unit of the Fatric Basin (Malá Fatra Mountains, north-west of Central Slovakia) in particular, in the early Carnian, the deposition of the Ramsau Dolomite Formation ends. This unit is constituted mainly by fine-grained lagoonal dolostones with rare bivalves, echinoids, peloids and algae. Locally, bedded lenses of bioclastic limestones with crinoids fragments are found (Sýkora et al. 2011). The Ramsau Fm. is overlain by two different isochronous clastic units (Sýkora et al. 2011). The first is the Lunz Formation; it outcrops throughout the Central Western Carpathians and it is characterized by turbiditic facies composed of alternating black shales and sandstones (Aubrecht et al., 2017). The second unit is the Tržinovo Formation (Sýkora et al., 2011), which instead is typical of the Malá Fatra Mountains. It consists of two members: the Tržinovo Claystone and the Tržinovo Dolomite (Sýkora et al., 2011). The former is composed of shales and claystones with some specimen of foraminifers, lingulids and conchostracans, while the latter member consists of dolomites and rare dolomicritic limestones, with sporadic traces of peloids and intraclasts conchostracans. The biostratigraphic attribution of the formation between Julian and Tuvalian is mainly based on conchostracans (Sýkora et al. 2011). The terrigenous facies of the Lunz and Tržinovo Formations started to be replaced in the Late Carnian by the carbonates of the Hauptdolomit (latest Carnian-Norian), consisting of grey dolomitic facies typical of a sabkha environment (Sýkora et al. 2011; Aubrecht et al., 2017).

2.1.1.7 OUTER DINARIDES

The Outer Dinarides represent one of the less deformed regions of the Dinaric part of the Alpine orogenetic chain. During the Triassic, they were part of the Adria plate, on the western passive margin of the Tethys, roughly located adjacent to the Southern Alps. At Lesno Brdo (central Slovenia), the Carnian succession of the Hrusica nappe (Placer, 2008) crops out, consisting at the base of a mainly clastic interval, resting on bauxites or paleokarsts developed at the top of Ladinian to early Carnian massive reefal limestones (Gale et al., 2018). The clastic interval is made of conglomerate breccia layers, marlstones and sandstones, with coal lenses and interbeds occurring in the upper part. It grades upward to bioclastic limestones with common lumachellae alternating to centimeter-thick coal beds, the latter decreasing in frequency upward. Based on bivalves and foraminiferal association these limestones are dated to the late Julian (Gale et al., 2018 and ref. therein). A second decimetric clastic interval occurs at the top, mainly consisting of conglomerate beds, sandstones and marly limestones to a lesser extent. It passes again to an overlying carbonate interval, consisting of platy, often laminated, limestones and thick-bedded massive limestones. According to Gale et al. (2018), the reddish pelites and sandstones with conglomerate interbeds occurring at the top of this interval are correlated to the Travenanzes Fm. of the Dolomites and Julian Alps, based on close stratigraphic analogies, thus a Tuvalian age is inferred. A coal horizon has been reported also in southern Croatia at Strmica, lying in dark grey shales interposed within Upper Triassic bioclastic dolomites and limestones (Schubert, 1906). The occurrence of *Myophoria kefersteini* documents the Carnian age of the coal seam (Schubert, 1906, 1909).

A succession partly similar to that of Lezno Brdo has been described by Dozet (2009) in the Bostetje area (southern Slovenia): here, Julian dark platy and bedded bituminous limestones rest on late Ladinian/early Julian platform limestones, and are overlain by bedded, coarse-grained tuffites. The latter are unconformably overlapped by reddish siliciclastics. Elsewhere in the Outer Dinarides (e.g., Medvedica, Muljava, Gorski Kotar, Velebit, Svilaja Mt.; Dozet and Godec 2009; Gale and Skaberne, 2014; Buckovic and Stampar, 2016) the Carnian succession starts directly with the reddish siliciclastics underlying the late Carnian-Rhaetian Main Dolomite peritidal cycles, often overlapping well developed bauxites, the latter likely developed during a long-lasting emersion in relatively wet conditions (Celarc et al., 2008).

2.1.1.8 ANTALYA (TURKEY)

The Anatolian Plate has undergone a complex geological history, which has resulted in a mosaic of terranes and nappes (cf. Moix et al., 2008). A well-preserved Carnian succession crops out in the Taurus Mountains, located in SW Turkey between Antalya and Isparta cities (Lukeneder et al., 2012) and belonging to the Adria-derived Antalya-Alanya nappes according to Schmid et al. (2020). During the Carnian the region constituted part of the southwestern margin of the Tethys. The succession starts with the Kartoz Formation, consisting of shallow water platform carbonates (coral bafflestone within a grainstone matrix) with megalodonts and corals and capped by a dissolution surface which marks the transition to the disconformably overlying Kasımlar Formation (Lukeneder et al., 2012). This latter consists of three members: deep-water limestones, marlstones, and shales. In detail, the first, carbonate member is made of bioclastic wackestones, with megalodontids, halobiids, gastropods, benthic foraminifera, radiolaria and authigenic pyrite, passing upward to mass flow deposits with carbonate olistoliths and to bioclastic micrites with foraminifera, green algae and sponge fragments, alternating to mudstones with authigenic pyrite again (Lukeneder et al., 2012). Pyrite framboids are also common in the following marlstone member, characterized in the upper part by shales with calcareous intercalations containing

bivalves. The member ends with a centimetric sandstone layer with bryozoan and echinoid fragments. The last member of the Kasımlar Formation is composed of shales with sporadic thin limestone intercalations (Lukeneder et al., 2012). The first two members of the Kasımlar Formation also contain ammonoids, which have helped to biostratigraphically date the unit: the Carbonate member of the Kasımlar Formation results to have an age restricted to the *Austrotrachyceras austriacum* Zone (Julian 2) and the following Marlstone member to the *Tropites dilleri* Zone (Tuvalian 1). Therefore, the underlying Kartoz Fm has been dated as Julian 1 (Lukeneder and Lukeneder, 2015 also for detailed description of the ammonoid fauna).

2.1.2 NORTHERN AND CENTRAL EUROPE

In this section we will consider the Carnian successions located in today Northern Europe (Greenland, Barents Sea, Svalbard and UK), and in the Central European Basin (CEB; i.e., in today Germany, France, Poland, and Slovakia) (Fig. 2.4).

2.1.2.1 GREENLAND

During Late Triassic Greenland constituted a cratonic high connected to the Laurentia to the west and eastward separated from the Mid-Norwegian Shelf by several continental to shallow marine basins generated by continental rifting due to Pangea break-up (Leleu and Hartley, 2010; Golonka et al., 2018). Most of Greenland was therefore subject to subaerial erosion, while the Triassic succession is preserved mostly in basins. The Jameson Land Basin (Central East Greenland) was one of them. There, Carnian stratigraphy starts with the upper portion of the Pingo Dal Formation. It is subdivided into two members in lateral contact: the Klitdal Member and the Paradigmabjerg Member (Andrews et al., 2014; Decou et al., 2017). Lithologically, the formation is mainly constituted by coarse conglomerates, indicating an alluvial setting, but there are also several finer intervals interpreted as ephemeral lakes/playas due to the presence of gypsum, desiccation cracks, vertisols and calcretes (Decou et al., 2017). On this basis, the whole unit is thought to have been deposited under arid conditions (Decou et al., 2017). The overlying Gipsdalen Formation comprises the Kolledalen, Solfaldsdal and Kap Seaforth members. The age of the Gipsdalen Fm to the Carnian is constrained mainly by palynomorphs, but to a lesser extent also by bivalves and green algae (Andrews et al., 2014). The Kolledalen Mb marks the contact to the underlying Pingo Dal Fm and consists of cross-bedded sandstones, testifying for an aeolian deposition. The Solfaldsdal Member contains red mudstones and siltstones, commonly with red sandstones intercalations; at the base of the member, the Gråklint Beds are instead made of black fine-laminated calcareous mudstones (Decou et al., 2017). Thin laminations and organic matter content suggest a deep lake depositional setting for the Gråklint Beds; similarly, even for the main body of the Solfaldsdal Member a low-energy depositional environment is proposed (fine grain-size and laminated structure; Decou et al., 2017). Finally, the overlaying Kap Seaforth Member is characterized by an alternation of red and grey mudstones, siltstones and by the presence of evaporites (playa settings, arid indicators; Decou et al., 2017). Information derived from the macrofauna association suggests that the Gråklint Beds was likely deposited in a lacustrine setting with intermittent marine influence.

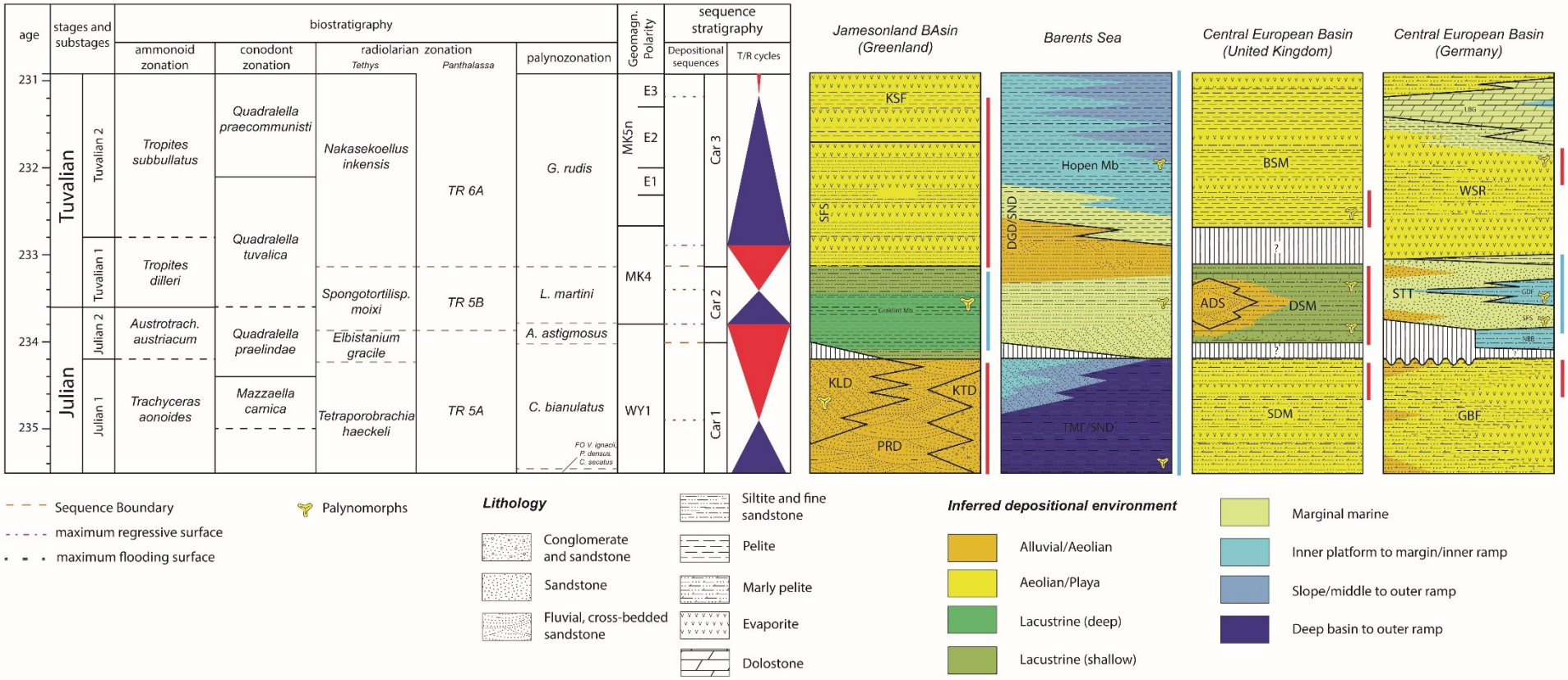

Figure 2.4: Chronostratigraphic framework of selected areas belonging to Northern and Central Europe cratonic area: Barents Sea and Central European Basin (United Kingdom and Germany). Vertical strips represent certain or inferred hiatus. Lateral bars indicate the occurrence of arid (red) or humid (blue) paleoclimate proxies. References for left panels as in Fig. 2.3.

Abbreviations: PRD: Paradigmabjerg Fm; KTD: Klitdal Fm ; KLD: Kolledalen; SFS: Solfaldsdal ; KSF: Kap Seaforth Fm; TMF/SND: Tschermakfjellet and Snadd fms; DGD/SND: De Geerdalen and Snadd fms; SDM: Sidmouth Fm; DSM: Dunscombe Mudstone Fm; ADS: Arden Sandstones Fm; BSM: Branscombe Mudstone Fm; GBF: Grabfeld Fm; STT: Stuttgart Fm; NBB: Neubrandeburg Mb; SFS: Schilfsandstein Mb; GDF: Gaildorf Mb; WSR: Weser Fm; LBG: Lehrberg mb.

2.1.2.2 BARENTS SEA

During the Triassic, the Barents Sea area was part of the continental shelf of north-western Eurasia located at a latitude of approximately 60°N (Paterson et al., 2019), occupied by an epicontinental sea. The basin was surrounded by emerged areas to the south (Baltic continent) and to the west (North American continent), and by an open seaway to the northwest (Glørstad-Clark et al., 2010 and references therein). The Late Triassic succession is documented both in outcrops on the Svalbard archipelago and in cores from the Barents Sea.

Strata deposited during the Upper Triassic are grouped into the Kapp Toscana Group. The Early Carnian Tschermakfjellet Fm is composed mainly of grey shales with intercalations of siltstones and siderite nodules in the upper portion. A thin conglomerate present at the base of the unit has been interpreted as the result of offshore marine deposition evolving upward into a prodelta setting (Mueller et al., 2014). This interpretation is corroborated by bivalve and ammonite fauna (Mueller et al., 2014) and palynoflora content, which also constrain the unit to the earliest Carnian (Paterson and Mangerud, 2019). The overlying De Geerdalen Fm has a predominant fluvial character: mudstones, siltstones and sandstones are the main lithological components with colours varying from dark greenish for the former to light brown for the latter (Mueller et al., 2014). More specifically, the lower part represents an interdistributary bay evolving to delta front, whereas the upper portion has been interpreted as a delta plain to coastal plain setting, using benthic foraminiferal assemblages (Mueller et al., 2014). Palynological content has helped to constrain the age of the De Geerdalen Fm between the early to the latest Carnian (Paterson and Mangerud, 2019). The lowermost part of De Geerdalen Fm, considering the high amorphous organic material (AOM) content, seems to record dysoxic – anoxic conditions, while the environment became more oxic going upward through the unit (Paterson et al., 2019). The De Geerdalen Fm shows some lithological peculiarities in Hopen Island, where the upper portion of the unit (Hopen Member) is dominated by dark claystones with subordinate fine- grained sandstones (Paterson et al., 2016a). Its uppermost part is characterized by brown bivalve-bearing marls, ironstones and black shales, interpreted as evidence of full marine conditions (Paterson et al., 2016a), constrained to the Tuvalian 3 by palynology and magnetostratigraphy (Lord et al., 2014; Paterson et al, 2016a).

In southern Barents Sea, the Snadd Formation is characterized by a succession of shales to claystones, siltstones and sandstones (Paterson et al., 2016b; Paterson and Mangerud, 2017). The lower part of the formation is interpreted as a prodeltaic environment due to a mixed composition of palynomorph assemblages (Paterson and Mangerud, 2017). Conversely, the upper portion is rich in phytoclasts and algae, which are typical of fresh-brackish water, testifying for a nearshore to coastal setting (Paterson and Mangerud, 2017).

At Binnedalen (Hopen Island) Paterson et al. (2016a) reported a negative $\delta^{13}C_{TOC}$ shift in the lower part of the De Geerdalen Fm, followed by a shift towards more positive values in the Hopen Mb. This positive shift is comparable to that obtained by Mueller et al. (2014 and 2016b) at Juvdalskampen on Spitsbergen. The De Geerdalen Fm also documents another negative shift in the Julian 2, which is correlated to the Tethyan NCIE-2, and a third in the Tuvalian (Mueller et al., 2016a).

Palynological data show a climate which is relatively wetter during Longobardian (upper Ladinian, Botneheia Fm) and becomes drier during the deposition of the Tschermakfjellet Formation (Julian-1). The De Geerdalen Formation marks a sharp humidification until the

top of the unit (Mueller et al., 2016a). Moreover, the microflora at Hopen Island shows a peak of a hygrophytic spores (*Leschikisporis aduncus*) indicative of swamp habitats within an association that is, as a whole, lacking xerophytic elements (Paterson et al., 2016a). A similar situation is also recorded at Spitzbergen and southern Barents Sea (Snadd Fm), where persistent humid climatic conditions are recorded in this stratigraphic interval throughout the region (Paterson et al., 2016a).

2.1.2.3 NORTH SEA

The Central North Sea (CNS) is situated among UK, Norway and Denmark. There, the Skagerrak Formation encompasses the Middle and the Upper Triassic and it represents a fluvial environment composed of six alternating sandstone (namely, the Judy, Joanne and Josephine) and mudstone (namely, Julius, Jonathan and Joshua) members. The Joanne Mb spans from the lower/middle Ladinian to the basal Norian, but age constraints for this unit are poor (Burgess et al., 2020).

2.1.2.4 UK

During the Late Triassic, the part of the craton now occupied by the UK was fragmented in several emerged areas surrounded by shallow marine and continental basins (Leleu and Hartley, 2010). From Ladinian to earliest Rhaetian the stratigraphy of the area is represented by the Mercia Mudstone Group, (Milroy et al., 2019; Gallois, 2019 and references therein). The Carnian succession starts with the deposition of the upper part of the Sidmouth Mudstone Formation, referred to a mudflat and constituted by red-brown mudstones and siltstones (Milroy et al., 2019). The overlying Dunscombe Mudstone Formation consists of laminated mudstones, interbedded in the lower part with thin calcareous siltstone– sandstone beds, and containing paleosols and trace fossils (Milroy et al., 2019). Their facies represent a fluvio-lacustrine setting and palynological associations indicate a Julian to earliest Tuvalian age (Baranyi et al., 2019a). In the Midlands (Devon) a distal correlative of the middle part of the Dunscombe Mudstone Formation crops out, the Arden Sandstone Formation, which represents a fluvial environment (Baranyi et al., 2019a; Gallois, 2019). The Carnian succession ends with the Branscombe Mudstone Formation, which encompasses the upper Carnian (Tuvalian) until the upper Norian. This formation is dominated by mudstones and siltstones, representing a saline mudlflat setting (Milroy et al, 2019).

Clay minerals analysis of the Mercia Mudstone Group shows a proportional increase in kaolinite/illite ratio in the Arden Sandstone Fm, which indicates more humid conditions than in the units below and above (Simms and Ruffell, 1989). Similarly, detailed facies analysis of the Sidmouth Sandstone Formation and the Branscombe Mudstone Formation by Milroy et al. (2019) pointed out that these units, containing features documenting an arid phase like vertisols and evaporites, are separated by fluvial and fluvio-lacustrine facies (Arden Sandstones and Dunscombe Mudstone Formation) that suggest a temporary increase in humidity and rainfall, coeval to the CPE. Carbon isotope analysis of bulk organic carbon and compound specific of plant leaf wax n-alkanes (weighted mean of C_{27}-C_{35} n-alkanes) of the Sidmouth and Dunscombe Formations, shows five NCIEs within the Dunscombe Formation that can be correlated to NCIEs recorded in the Southern Alps (Miller et al., 2017; Dal Corso et al., 2018; Baranyi et al., 2019a).

2.1.2.5 CENTRAL EUROPEAN BASIN

The Central European Basin (CEB) represents a large region spanning on the European craton in a E-W direction from Poland to France. The “Germanic Basin” is located in its central portion and is a classic study area for the CPE. The Keuper Group includes all the

Upper Triassic stratigraphic units (see references in Franz et al., 2019). The basal Grabfeld Fm (upper Ladinian-lower Carnian) consists of evaporitic claystones deposited in a playa or sabkha environment, containing palynomorphs and conchostracans (Zhang et al., 2020). Above, the arid sedimentation is interrupted by deposition of clayley sandstones of the Stuttgart Fm. This unit is subdivided into four members: Neubrandenburg, Lower Schilfsandstein, Gaildorf and Upper Schilfsandstein; the second and the fourth ones are fluvio-deltaic while the others contain more marine-brackish facies (Zhang et al., 2020). According to sequence stratigraphic observations, the Stuttgart Fm. spans from the upper Julian to lower Tuvalian, encompassing all the *A. austriacum* Zone and part of the *T. dilleri* (Franz et al., 2014). The Carnian ends with the deposition of the Weser Formation: reddish shales rich in gypsum representing again a playa/sabkha setting. The basal part (Beaumont Member) is attributed to the Tuvalian based on palynomorphs and by the presence of the lamellibranch *Costatoria vestita* (Zhang et al., 2020). The Weser Fm also contains thin dolomitic layers in its middle portion, named Lehrberg-Horizon

In the western part of the CEB, the Late Triassic succession is well preserved in the nowadays France mainly East to the Massif Central. It was deposited in basins controlled by sin-sedimentary tectonics (Burquin and Durand, 2006), from the neighbourhoods of Paris to the Lorraine, and from here toward Belgium (Arche and López-Gómez, 2014). Above the basal unconformity developed on the *Marnes Irisées Inferiour*, the Carnian succession is characterized by the *Gres a Roseaux* Formation and by lateral equivalents (e.g., *Sainte Colombe Voulzie* sandstones, Attert Fm; Burquin and Durand, 2006; Arche and López-Gómez, 2014), consisting of fluvial sandstones and conglomerates, with facies associations related to alluvial deposits with anastomosed and meandering channels. The unit grade upwards to the clayey coastal sabkha to playa deposits of the *Argiles bariolées intermediaires* (Burquin and Durand, 2006).

In the northern part of the CEB (Danish basin), Carnian units are the Falsterbo (the uppermost portion), Vellinge, Fuglie and Stavsten formations. The Falsterbo Fm consists of grey sandstones, while the overlying Vellinge Fm is composed of red sandstones and conglomerates with traces of manganese minerals, interpreted as indices of a shift from humid to arid conditions. Aridity is also witnessed by the playa depositional setting of the Fuglie Fm, characterized by calcareous, dolomitic mudstones, argillaceous sandstones and mudclast conglomerates. Carbonate cements decrease whilst silica content increases within the following Stavsten Fm, which is lithologically very similar to the underlying unit (Lindström et al., 2017 and references therein). Therefore, only a small part of the succession can be related to a humid climate, even if the typical palynological assemblages that are considered to be indices of the CPE in the Germanic Basin (and not only therein) are missing in the cores sited in the Höllviken Half-graben in the northeastern margin of the Danish Basin (Lindström et al., 2017). On the whole, no assemblages from “middle” Carnian to Norian have been discovered, suggesting the existence of a hiatus.

Poland represents the easternmost portion of the CEB. Most of the Polish Keuper stratigraphic nomenclature has been influenced by the Germanic Basin’s one, despite many informal regional denominations are still used (Fijałkowska-Mader et al., 2020). The Grabfeld Formation is characterized mainly by grey, greenish and red claystones with subordinate mudstones and locally sulphate accumulations, testifying hypersaline arid conditions, typical of a playa setting (Fijałkowska-Mader et al., 2020). The following Stuttgart Formation represents delta and channel-floodplain environments and it is constituted by mainly grey (brown-red in the upper portion) laminated claystones and siltstones locally interbedded with sandy mudstones. Findings of sporadic ostracods, and

remains of animals, fish and plants, spores and chitinozoa are reported (Fijałkowska-Mader et al., 2020).

2.1.2.6 BULGARIA

the Glavatsi Member and the overlying Komshtitsa Formation (or Chelyustnitsa Fm) outcrop in northwestern Bulgaria and belong to the Moesian Group. Age constrains for the Group are missing, but they are inferred as Carnian–Norian based on stratigraphic relationships: the immediately underlying Rusinovdel Fm has been biostratigraphically dated to the early Carnian through its bivalves and brachiopods content (Chatalov, 2017). The Glavatsi Mb represents the lower part of the Chelyustnitsa Fm and it is characterized by quartzose/quartz-feldspatic sandstones, while the Chelyustnitsa Fm (s.s.) is composed of red-pink sandstones and conglomerates in suborder (Chatalov, 2017). The Komshtitsa Fm is lithologically almost identical to the Chelyustnitsa Fm and they are often interfingered (Zagorchev and Budurov, 2007). Chatalov (2017) found quartz arenites and laterites, typical of an alluvial environment and a gravel-dominated river, respectively, and a decrease in compositional maturity of the sandstones forming the Glavatsi Member (from quartzarenites to litharenites) and the disappearance of the lateritic crusts in the lower part of the Komshtitsa Fm. This latter unit and also the Chelyustnitsa Fm show typical facies of a playa and fluvial environments. These features suggest a progressive transition from humid to subhumid climate, and then to persistent semi-arid conditions. The formation of quartzarenites and lateritic crusts could have been connected to several humid pulses (Chatalov, 2017): A supporting evidence is the alternation of ironstone crusts with siliciclastic deposits unaffected by laterization.

2.1.3 CENTRAL ATLANTIC DOMAIN

The successions that are nowadays located between the eastern coast of USA and Canada (Newark Supergroup), and their lateral equivalents in Morocco (Argana) and Iberia are considered in this section; the denomination of “Central Atlantic Domain” has been chosen following Leleu et al. (2016) (Fig. 2.5). These successions represent the infilling of rift basins developed during the Permian – Triassic breakup of Pangea (Leleu et al., 2016 and references therein). Carnian sediments are deposited in continental settings in all the examined areas. These are on the whole poorly biostratigraphically constrained (Arche and López-Gómez, 2014; Leleu et al., 2016; Weems et al., 2016; Mader et al., 2017 and references therein), but the Newark Supergroup has been well studied for magnetostratigraphy and astrochronology (e.g., Kent et al., 2017).

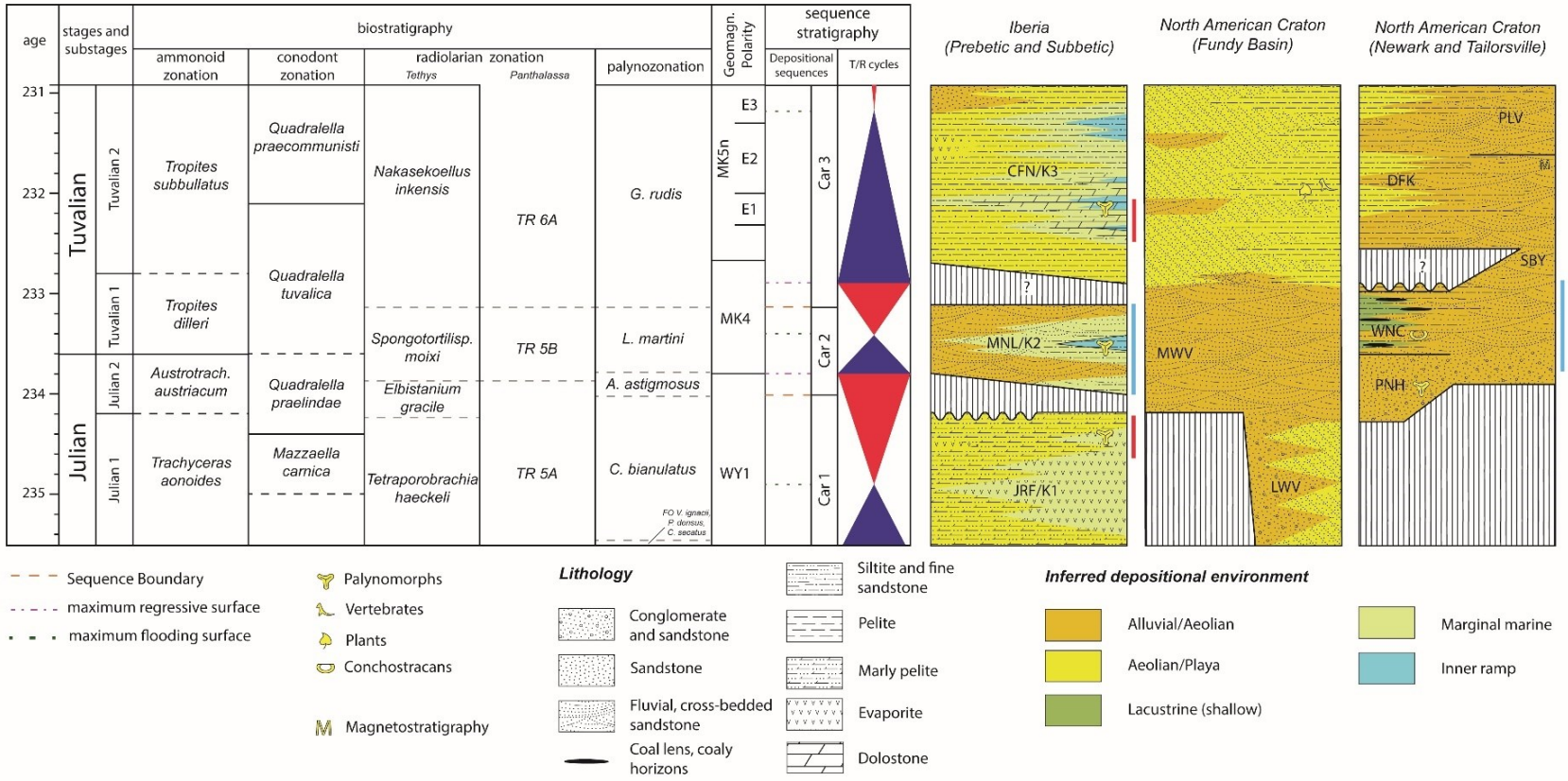

Figure 2.5: Chronostratigraphic framework of selected areas belonging to Central Atlantic Domain: Iberia and North American Craton. Vertical strips represent certain or inferred hiatus. Lateral bars indicate the occurrence of arid (red) or humid (blue) paleoclimate proxies. References for left panels as in Fig. 2.3.

Abbreviations: JRF/K1 Jarafuel Fm/Keuper 1; MNL/K2: Manuel Fm/Keuper 2; CFN/K3: Cofrentes Fm/Keuper 3; LWF: Lower Wolfville Fm; MWF: Middle Wolfville Fm; PNH; Pinehall Mb; WNC: Walnut Cove Mb; SBY: Solebury Mb; DFK: Dry Fork Mb; PLV: Prallsville Mb.

2.1.3.1 NORTH AMERICAN CRATON

The Newark Supergroup occurs in the Newark, Taylorsville and Fundy sedimentary basins. The Doswell Formation and Stockton Formation recognized in Newark and Taylorsville basins are Carnian in age, as indicated by integrated biostratigraphy, magenetostratigraphy and astrochronology (Weems et al, 2016; Kent et al., 2017). The Doswell Formation (Julian) is characterized by deep lake and swamp deposits with coal horizons, particularly evident in Taylorsville basin (Leleu et al., 2016). The unit is capped by an unconformity and the sedimentation resumed in the latemost Julian, with the fluvio-aeolian facies of the Stockton Fm (Leleu et al., 2016). Its basal part is constituted mainly by conglomerates, interfingered by sandstones and shales; subsequently sandstones became dominant and in the upper part they are cyclically interbedded with mudstones, showing a fining upward succession (Weems et al., 2016).

The Carnian succession of the Fundy Basin (Nova Scotia, eastern Canada) is represented by the Wolfville Formation, which age is based on mollusk, reptile, and amphibian remains (Leleu et al., 2010). It is informally subdivided in a lower, middle and an upper part and it is constituted by aeolian deposits, fluvial sandstones and alluvial fan sediments. In particular, the lower part consists of mainly fluvial facies while the middle part contains mudstone-dominated ephemeral-lake facies. Overall, the sedimentological features suggest variable climatic conditions from semiarid to sub-humid (Leleu et al., 2010).

On the western side of North America, the Carnian Baldonnel Formation (British Columbia) was deposited in the mid–proximal sector of a mixed carbonate-siliciclastic ramp system (proximal offshore to shoreface and foreshore setting; Zonneveld et al., 2007; Schultz et al., 2016). It is composed of skeletal, fine to coarse-grained carbonates, organic-rich siltstones and fine- to very fine-grained sandstones (Zonneveld et al., 2007). Beds of Baldonnel Fm contain a rich and diversified palaeontological content, often concentrated in patch reefs: conodonts, brachiopods, crinoids, echinoids, asteroids, molluscs, scleractinian corals, spongiomorphids, hydrozoans, fish remnants, microbialites and trace fossils (Zonneveld et al., 2007; Martindale et al., 2010; Schultz et al., 2016). The reefs, developed into three separated intervals, have been dated by conodonts as Tuvalian, belonging to the *Carnepigondolella samueli* Zone (Zonneveld et al., 2007; Rigo et al., 2018; Orchard, 2019), representing therefore the first and oldest occurrence of scleractinian-microbial reef in the Upper Triassic of the North American craton (Zonneveld et al., 2007; Martindale et al., 2010).

On the north western part of the Craton, the Otuk Formation (Alaska) was deposited into an outer shelf to basin, oxic/dysoxic setting during the Middle to Late Triassic (Dumoulin et al., 2011). The unit is made of three members, of which we consider only the middle one because it spans from middle Anisian (within *Hozmadia ozawai* Radiolarian Zone) to the end of the Carnian (the upper part is biostratigraphically less costrained - Dumoulin et al., 2011). It has been informally named “chert member” since it is mainly composed of cherts, interfingered in the lower portion with silty shales. This part also contains radiolarians and spicules of sponges, rare phosphatic bioclasts and quartz, barite and pyrite crystals (Dumoulin et al., 2011). The upper part of the “chert mb.” consists of calcareous/dolomitic to siliceous mudstones, shales and a black shales interval, named “Dark marker horizon”. Radiolarians and phosphatic bioclasts are still present, together with foraminifers and bivalve shell fragments (Dumoulin et al., 2011). $\delta^{13}C_{TOC}$ analyses have been provided on several core sections and interestingly two negative excursions are recorded during the Carnian: the first, sharper, just below the “Dark marker horizon” and the second within this interval (Dumoulin et al., 2011).

In most of the central-western to southern part of USA (Texas, New Mexico, Arizona, Colorado, Utah, Nevada, and also in Wyoming and Idaho), a significant portion of the Upper Triassic is represented by the Chinle Formation (Ramezani et al., 2014). The age of the unit has been object of a debate. Based on conchostracan, tetrapod and palynomorph biostratigraphy, Lucas and Tanner (2018) suggest that the lower part of the Chinle Fm (Shinarump, Bluewater Creek and Blue Mesa members) is Carnian in age. Particularly, the Shinarump Mb should has been deposited from Julian to Tuvalian time. On the other hand, U-Pb dating on detrital zircons and magnetochronology rejected the hypothesis of a Carnian age, since results provided a Norian maximum depositional age (from 224.25 Ma to ca. 208.9 Ma; Kent et al., 2019; Rasmussen et al., 2020).

2.1.3.2 MOROCCO

The Atlantic rifting related to the Pangea breakup generated several horst and graben or strike-slip basins in Morocco (Mader et al., 2017). Two examples are the Argana Valley and the Essaouria basin, which are located between the Moroccan Meseta and the High Atlas chain. Here, the Timezgadiouine (Olenekian-Carnian) and Bigoudine Fms. (Carnian-Norian) consist of alternating alluvial conglomerates, sandstones and mudstones, representing fluvial and cyclical playa deposits (Mader et al., 2017). The uppermost member of the Timezgadiouine Fm (Irohalene Mb) is Carnian in age (attribution based on archosaur ichnofauna – Zouheir et al., 2018) and mainly consists of alluvial plain mudstones intercalated to vertisols and sandstones (Zouheir et al., 2018). The overlying first two members of the Bigoudine Fm deposited from the Julian to the Tuvalian (Mader et al., 2017): the oldest one (Tadart Ouadou Member) is composed of fluvial conglomerates and aeolian sandstones, and is overlain by fine-grained, partially evaporitic playa red bed deposits of the Sidi Mansour Mb (Zouheir et al., 2018).

2.1.3.3 IBERIA

Occurrences of Carnian beds in the Iberian Peninsula are widespread in the stable Iberia but are also present in the Balearic plateau and in the Betic Cordillera. In Spain, the Valencia Group includes the Jarafuel (Unit K-1), Manuel (K-2) and Cofrentes (K-3) Formations (Arche and López-Gómez, 2014). The Manuel Fm is subdivided into three subunits, namely K2.1, K2.2 and K2.3. The K2.1 and K2.2 subunits are dominated by fluvial facies, with floodplains and paleosols (plant remains occur in K2.2). The subunit K2.3 shows a shift from fluvial to coastal environment (sabkha; e.g., Barrenechea et al., 2018). A tentative correlation of the Manuel Fm. with the Silves Group in Algarve and Lusitanian Basin, Portugal, has been proposed by Arche and López-Gómez (2014). The Silves Group consists of red continental siliciclastic sediments passing to red and grey mudstones containing dolomites and evaporites, corresponding to a transition from fluvial–coastal siliciclastic sediments to shallow marine carbonates (Arche and López-Gómez 2014).

The lateral marine equivalents of the Manuel Fm. are represented by the Arenal d'en Castell and Fontanelles Formations, occurring in Minorca. The Arenal d'en Castell Fm is dated mainly with ammonoids to a timespan going from the end of Fassanian (late Ladinian) to the early Julian, and its depositional setting is interpreted as a mixed, outer to middle ramp. The overlying Fontanelles Fm is dated to the Julian and its facies witness a shallowing-upward marine environment, evolving from an inner ramp to a tidal flat. It is mainly carbonate and precedes the more siliciclastic Keuper-type facies (López-Gómez et al. 2017).

2.1.4 SOUTHERN GONDWANA

2.1.4.1 SOUTH AMERICA

The most representative Late Triassic successions in the south American craton occur in the southern Paraná Basin in Brazil and the Ischigualasto-Villa Unión Basin in central-western Argentina. Both of these areas yield many detrital zircon horizons that provide chronostratigraphic constrains (Martinez et al., 2011; Marsicano et al., 2016; Ezcurra et al., 2017; Langer et al., 2018; Philipp et al., 2018; Desojo et al., 2020; Mancuso et al., 2020).

The Carnian succession in the Paraná Basin occurs in the Santa Maria Formation (Schultz et al., 2020). The unit is subdivided, from bottom to top, into the Passo das Tropas Member and the Alemoa Member. The lower member consists of fluvial conglomerates and fine to coarse-grained sandstones rich in mud clasts and locally plant debris, interpreted as the result of sedimentation in a floodplain environment. The transition to red, massive to poorly stratified mudstones rich in vertebrate fossils, aeolian deposits and paleosols with rhyzocretion features, typical of the Alemoa Member, marks the evolution towards an ephemeral lacustrine-fluvio-deltaic depositional system (Horn et al., 2018; Garcia et al., 2019; Rodriguez et al., 2019; Schultz et al., 2020).

Biostratigraphically, the upper Carnian part of the Santa Maria Formation (Candelária Sequence) encompasses the *Hyperodapedon Assemblage Zone (AZ)* (i.e., rhynchosaurs) and the basal portion of the *Riograndia AZ* (cynodonts – Horn et al., 2018; Garcia et al., 2019; Schultz et al., 2020). Noteworthy, the *Hyperodapeon AZ* records the highest degree of diversity among all the AZs of the Brazilian Triassic (Schultz et al., 2020). These numerous findings of dinosauromorphs fossils in the Brazilian Carnian strata (Schultz et al., 2020) show that there the diversification of dinosaurs and other relative groups (lagerpetids) occurred during a humid interval, which has provided optimal environmental conditions for their development (Garcia et al., 2019), in agreement with the hypothesis of Bernardi et al (2018) formulated in the Dolomites (see paragraph 2.1).

Carnian stratigraphy of the Ischigualasto-Villa Unión Basin in Argentina (Fig. 2.6) starts with the Chañares Formation, which is characterized by tuffaceous sandstones, siltstones and mudstones with a significant vertebrate fossils content, deposited in a fluvio-lacustrine environment (Colombi et al., 2017; Mancuso et al., 2020; Ordoñez et al., 2020). Its time span is bracketed between the late Ladinian and early Carnian (Julian; Ezcurra et al., 2017); the vertebrate fossils content is also remarkable (e.g: *Tarjadia, Dinodontosaurus* – Ezcurra et al., 2017; Ordoñez et al., 2020 and references therein). Above, the Los Rastros Formation, composed of cycles of black shales, mudstones and sandstones rich in plant remains, insects, fish, crustaceans and tetrapods tracks (Mancuso and Marsicano, 2008; Lutz et al., 2011; Mancuso and Caselli, 2012; Colombi et al., 2017; Mancuso et al., 2020; Pedernera et al., 2020; Lara et al., 2021 and references therein) points to a shallow lacustrine-deltaic depositional setting, deposited between the latemost Julian and the earliest Tuvalian (Ezcurra et al., 2017; Mancuso et al., 2020). The overlying Ischigualasto Formation, consisting of sandstones, conglomerates and mudstones, with stacking patterns reflecting different ratios of subsidence (Colombi et al., 2017), spans from the Tuvalian to the lower Norian (~230-221 Ma – Colombi et al., 2017; Ezcurra et al., 2017; Desojo et al., 2020): its lower part corresponds to an interfingering of fluvial and lacustrine deposits (contact with the Los Rastros Fm), while the middle and upper portions are markedly fluvial (Colombi et al., 2017). The unit is also rich in plant fragments and microflora (Colombi and Parish, 2008; Césari and Colombi, 2013 and 2016), and vertebrate fossils (Martinez et al., 2013).

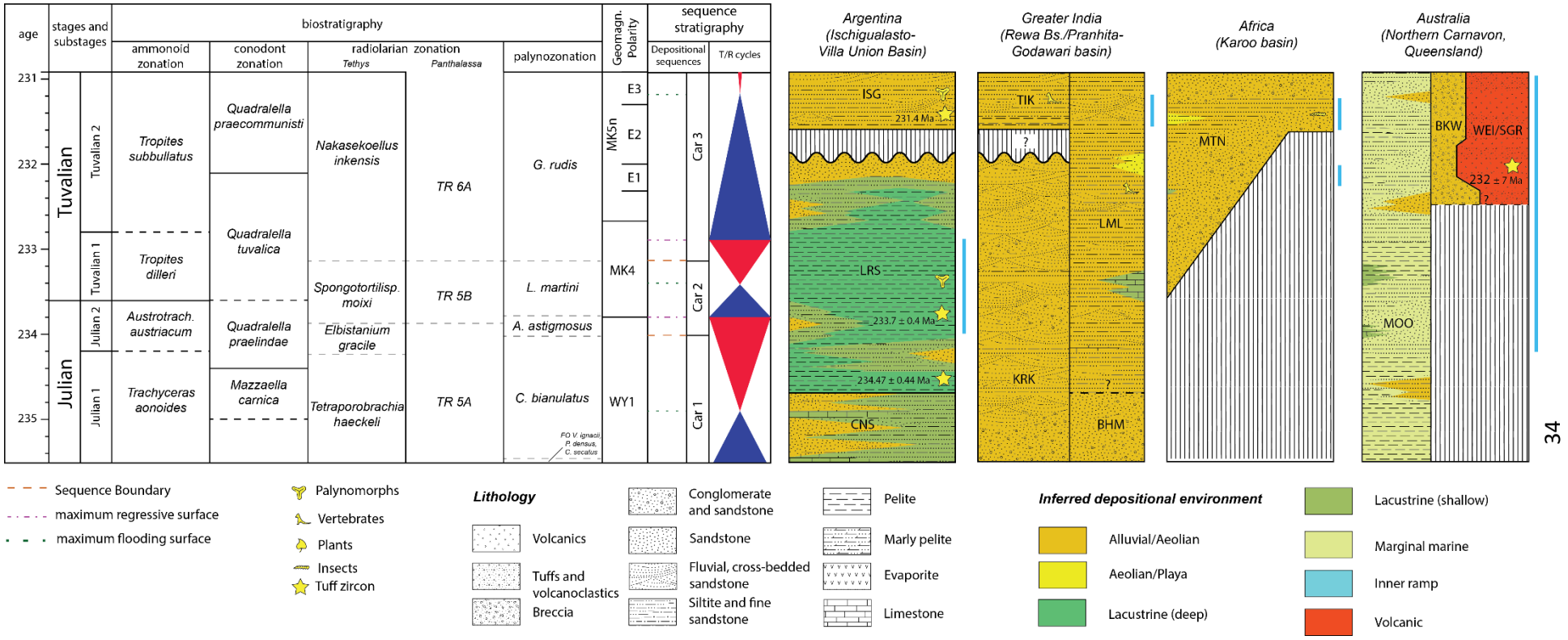

Figure 2.6: Chronostratigraphic framework of selected areas belonging to southern Gondwana: Argentina, Greater India, Africa, Australia. Vertical strips represent certain or inferred hiatus. Lateral blue bars indicate the occurrence of humid paleoclimate proxies. References for left panels as in Fig. 2.3.

Abbreviations: CNS: Chanares Fm; LRS: Los Rastros Fm; ISG: Ischigualasto Fm; KRK: Karki Fm; TIK: Tiki Fm; BHM: Bhimaram Fm; LML: Lower Maleri Fm; MTN: Molteno Fm; MOO: Mangaroo Fm; BKW: Blackwall Breccia; WEI/SGR: Weir and Sugar basalts.

2.1.4.2 AFRICA

The Carnian succession in eastern Gondwana is well preserved in several sedimentary basins formed as a consequence of the Permian break up of Gondwana (Catuneanu et al., 2005; Labandeira et al., 2018), nowadays scattered throughout the southern and eastern part of Africa, with the largest ones located in South Africa, Namibia, Zambia and Zimbabwe (Karoo supergroup; Sciscio et al., 2020; Zeiger et al., 2020). In the Karoo basin (Fig. 2.6), after a long hiatus covering the late Anisian – early Carnian timespan, the Stomberg Group was deposited (Catuneanu et al., 2005; Labandeira et al., 2018). The oldest unit of the group is the Molteno Formation, dated to the Carnian age, overlayed by the Norian – Sinemurian Elliot Fm (Bordy et al., 2020).

The lowermost portion of the Molteno Fm is mainly composed of conglomerates and sandstones, with the latter progressively prevailing upward (Labandeira et al., 2018). Sandstones form alternations with (subordinated) siltstones or mudstones, which sometimes are carbonaceous. Coal deposits are rare (Labandeira et al., 2018). The basal part of the Formation is interpreted as a floodplain environment punctuated by ephemeral streams which rapidly transitioned to a more developed fluvial braided system (Cairncross et al., 1995; Labandeira et al., 2018), whilst the final depositional phase has been characterised by a shift towards a meandering river system (Anderson et al., 1998; Labandeira et al., 2018). Crevasse splays, sheet flood deposits and local laminated shales, the latter representing lacustrine and swamp environments, have been also reported (Cairncross et al., 1995; Anderson et al., 1998; Labandeira et al., 2018). The Carnian Karoo basin' succession can be confidently correlated with other basins, such as the Mid-Zambezi basin and the Cabora Bassa basin (Scicio et al., 2020). In other sedimentary basins of central Africa, the biostratigraphic or geochronologic resolution is poor, but fluvial successions similar to those of the Karoo basin can be tentatively correlated, as in the case of the Congo basin, where red-brown coarse-grained sandstones and siltstones intercalations overlie a subaerial unconformity in the upper part of the Haute Lueki Group (Linol et al., 2014).

The Molteno Fm contains also many faunal (some conchostracans but especially insects) and floral elements, and several ichnofossils (Cairncross et al., 1995; Anderson et al., 1998; Labandeira et al., 2018 and references therein). In particular, the Molteno flora consists of bryophytes, hepatophytes, lycopods, horsetails; but ferns and seed plants (cycads, conifers, peltasperms, ginkgophytes, corystosperms, bennettitaleans) dominate the vegetation (Labandeira et al., 2018).

2.1.4.3 GREATER INDIA

During the Middle and Late Triassic, intra-cratonic sedimentary basins of central-eastern India were progressively filled by sediments of continental origin: in the Rewa Basin (Fig. 2.6), the Karki Formation spans from Anisian to Carnian (Julian – Datta et al., 2019) and is mainly composed of sandstones and coarse grained lithologies (Mukherjee and Ray, 2012). It is overlain by the Tiki Fm, which is mainly mud-dominated, with well-developed paleosol profiles, and subordinate sandstones (Mukherjee and Ray, 2012). Well-preserved fossils, like fish and vertebrates such as reptilians, amphibians and mammals, and related trace fossils like coprolites, are abundant (e.g., Ray, 2015; Rakshit et al., 2018; Bandyopadhyay and Ray, 2020 and references therein). The unit has been interpreted as the result of channel infilling in an anastomosing river system, set in an alluvial plain environment (Mukherjee and Ray, 2012). In the Pranhita-Godawari basin, the Carnian succession (Lower Maleri Fm; Datta et al., 2019) mainly consists of alternations of massive and laminated, fine-grained

siliciclastics (sandy siltstones and pelites), recording sedimentation in a floodplain setting. Additionally, thin marl and carbonate grainstone intercalations, represent freshwater carbonate precipitation in swamp-like environments (Sarkar, 1988: Dasgupta et al., 2017).

The age of the Tiki Fm is constrained by sporomorphs. The assemblage is similar to the *Samaropollenites speciosus* Zone (Mukherjee and Ray, 2012), which is Carnian in age (Cirilli, 2010). Furthermore, vertebrate fossils suggest a correlation between the Tiki Fm., the upper part of the Santa Maria Formation in Brazil (Upper *Hyperodapeon* AZ), and the lower Ischigualasto Formation in Argentina (Ray, 2015). The age of the Tiki Formation, considering the age of the Upper *Hyperodapeon* AZ and the *Scaphonyx-Exaeretodon-Herrerasaurus* biozone (lower Ischigualasto Formation), is likely Tuvalian in age(Martinez et al., 2011; Langer et al., 2018; Garcia et al., 2019; Datta et al., 2019).

The transition from intra-cratonic to open marine sedimentation on the northern margin of the Indian plate is documented in different places of the northern Pakistan and India. For instance, the Upper Triassic of the Mar-Koh succession mainly consists of barren limestones with quartzite intercalations, yielding megalodonts and Carnian to Norian conodonts (Montenat, 2009). To the nowadays east, beds become progressively more terrigenous and include continental deposits (Ibrahim Shah, 1977).

2.1.4.4 AUSTRALIA

The Mungaroo Fm was deposited in the North Carnarvon Basin (North-western Australia) (Fig. 2.6) between the Anisian and the Norian (Yllirian – Sevatian; Zeng et al., 2019). It is composed of multiple fining upward fluvio-marine aggradational cycles, characterized by distributary channel sandstones interbedded with inter-distributary bay mudstones and coal horizons (Zeng et al., 2019), clearly pointing to a delta plain environment. Palynological analysis shows a peak in abundance of hygrophytic species during the Carnian (Zeng et al., 2019). Together with other successions occurring in Australia and New Zealand, the unit witnesses the onset of the coal recovery after a long gap lasting since the Permo-Triassic boundary: reappearance of coal deposition is dated to the Anisian, but thick coal measures are reported only since the Carnian (Retallack et al., 1996).

Coal deposits within Upper Triassic continental fluvial successions are also common in eastern and southern Tasmania (e.g., Tiers Fm.; Bacon, 1991). The upper part of the Upper Parmeener Supergroup is mainly characterized by volcanic-lithic sandstones and mudstone intervals alternations, organized in fining upward cycles reflecting sedimentation in a meandering stream fluvial system. Recently, amber hase been found in the terrestrial deposits of the Fingal Valley (Stilwell et al., 2020). In Queensland (North-eastern Australia) (Fig. 2.6), within the Ipswich Coal Measures, the Carnian to Norian succession consists of alternations of shales and sandy beds, sometimes conglomeratic (Tivoli Formation; Pattemore and Rigby, 2005), which are related to a floodplain where a fluvial system developed. Upward, alluvial facies related to a meandering river system (Blackstone Formation; Thulborn, 1998), rich in coaly beds, become dominant. The age could be Norian, based on unpublished radioisotope ages (Raven et al., 2015). Within this unit, findings of footprints of a small tetrapod have been reported (Thulborn, 1998; Bernardi et al., 2018).

2.1.4.5 ANTARCTICA

Relicts of Upper Triassic from Antarctica crop out in the central-eastern part of the continent. In the Central Transantarctic Mountains the Late Triassic is represented by the Falla Fm., unconformably overlying Middle Triassic deposits and consisting of sandstone (often bearing coalified plant stems) to carbonaceous shale, fining-upward cycles (Elliott, 1996). These deposits have been related to base level changes in a low sinuosity braided river

system, characterized by common lacustrine and swamp areas (Barrett et al., 1986). Based on palynological data, the lower part of the Falla Fm. can be considered Carnian in age (Escapa et al., 2011 and ref. therein).

In northern Victoria Land, Late Triassic deposits unconformably overlie the Paleozoic succession or directly rest on the crystalline basement (Escapa et al., 2011 and ref. therein). They are grouped in the Section Peak Formation (Schoner et al., 2011), mainly consisting of medium to coarse-grained sandstones with common cross bedding and siltstone to mudstone intercalations, rich in coal and plant remains. Sometimes a conglomeratic horizon characterizes the base of the succession (Schoner et al., 2011). The alternations of fluvial coarse sediments and overbank fines can be related to a low sinuosity river system here too. In southern Victoria Land the Upper Triassic is represented by members C and D of the Lashly Formation: they are composed of alternations of fluvial sandstones and fine overbank deposits, with the ratio of the two main lithologies varying in cycles and in members. Noteworthy, member C is characterized by a higher proportion of fine-grained sediments and coal, probably deposited by meandering streams (Escapa et al., 2011). Member C also contains a siliciclastic tuff layer with proxies of a proximate source of volcanism (Kumar et al., 2011).

2.1.5 **NORTHERN GONDWANA**

2.1.5.1 CENTRAL AND SOUTHERN TUNISIA

South to the Kabylydes orogenetic chain, the sedimentary succession of Tunisia is relatively poorly deformed. The area was involved since the early Permian in the break-up of Pangea, influencing its palaeotopography and sedimentary evolution by developing half-graben systems and relatively fast-subsiding zones (Guiraud, 1998; Soua, 2014). During the Carnian, the central and southern Tunisia were located on northern Gondwana near to the western margin of the Tethys (Tun3 in Fig. 2.2).

In Southern Tunisia (Jeffara basin), the Carnian succession is characterized by the Azizia Fm: at the base, bioturbated dolostones of the Mekraneb Mb. occur, grading upward to laminated and bioclastic dolostone beds, often with short-lasting exposure traces on top (Soussi et al., 2017). They are overlapped by shales related to marine shelf deposition, marked at the top by a significant unconformity. Above, the Touareg mb consists of a basal conglomerate grading upward to massive sandstones and then to cross and planar bedded sandstones (Soussi et al., 2017). The unit presents in the upper part lenticular bedding related to a tidal environment (Carpentiel et al., 2016) and is sharply overlain by the late Carnian Rehach Formation, consisting at the base of shallowing upward cycles with shales grading to fossiliferous limestones (Soussi et al., 2017). The succession of the Jeffara basin continues with the evaporitic Norian Mhira Formation.

In central Tunisia, the Carnian succession is characterized at the base by a 20 to 50 m- thick interval, consisting of intermediate to shallow water black dolostones and limestones alternating to dark pelites and marls (Rhéouis Formation). The organic content in these deposits varies locally from low to high values, depending on the existing paleotopography (Soua, 2014). Upward, the shallow water dolostones grade to an evaporitic succession with common gypsum layers (Middle Gypsum mb). According to Soua (2014), the interval with black shales testifies for a ca. 2 Myrs long interval of anoxic conditions in the basin, spanning from the *Aonoides* to the *Austriacum* ammonoids zones. They contain the whole *Aulisporites astigmosus* and *Lagenella martini* assemblages of Roghi et al. (2010): bennettitales, cycadales, lycopodiophyta, and equisetophyta have indeed an hygrophytic affinity, testifying humid climates.

2.1.5.2 LEVANT MARGIN

The Levant region belongs to the norteastern part of the African plate, more precisely to the Israel-Sinai subplate (Bialik et al., 2012), separated from the Arabian Plate by the Dead Sea transform fault. Since the Triassic this region was affected by rifting related to the opening of the Neo-Tethys (Fig. 2.2). In Israel, small basins developed on the epicontinental shelf, separated from open marine settings developed from rifting stages (Bialik et al., 2012; Korngreen and Benjamini, 2013).

Carnian stratigraphy of Israel begins with the upper portion of the Saharonim Formation (uppermost S3 and S4 members), which is Julian 1 in age based on ammonite content (*T. aon* Zone -Bialik et al. 2013). In the Julian 2 - Norian, the Mohilla Formation deposited (Korngreen and Benjamini, 2011). The lowermost member of the Mohilla Fm is labelled as M1. Bialik et al. (2013) consider that M1 encompasses the *A. austriacum* and the *T. dilleri* Zones, thus it should be deposited between the Julian 2 and the Tuvalian 1.

Considering the lithologies, the upper part of the Saharonim Fm is characterised by some gypsum occurrence (only S3 Mb) and on the whole by an alternation of open and marginal

marine limestones (dominant) and shales, locally microbialitic, and sporadic sandy carbonates (S4 Mb – Korngreen and Benjamini, 2011; Bialik et al., 2013; Meilijson et al., 2015). Turning to the overlying Mohilla Fm, the M1 Mb mainly consists of dolomites, locally interbedded with gypsum, interrupted by some shaly or clayey horizon (Bialik et al., 2013). Within the M2 Mb evaporites are dominant (with subordinate dolostones and shales), while the M3 Mb is constituted by stromatolites, limestones and dolostones again (Bialik et al., 2013; Meilijson et al., 2015).

The deposition of M1 Member has recorded six sedimentary cycles. Three of them have witnessed humid climatic conditions (Bialik et al., 2013), characterised by a siliciclastic input (shales – Bialik et al., 2013): the interruption of dolomite-gypsum deposition occurred between Julian and Tuvalian has been interpreted as short-lived humid climatic shift, related to the CPE (Korngreen and Benjamini, 2011; Bialik et al., 2013). In addition, the CPE interval was characterised by the absence of microbialites (Meilijson et al., 2015). The re-establishing of arid conditions after the humid cycles is represented by the return to evaporites deposition, while the M2 Member marks a definitive arid climatic regime (Bialik et al., 2013).

2.1.6 **SOUTHERN THETYS**

2.1.6.1 ARABIAN PLATE

In the Arabian plate (Fig. 2.7) the Carnian succession has been investigated in the subsurface through several well-logs (e.g., Lunn et al., 2020). In Kurdistan, the Kurra Chine Formation mainly consists of three main carbonate-evaporite cycles corresponding to as many relative sea-level fluctuations (Lunn et al., 2020). Carbonates are mainly dolostones, with limestones largely present in the lower part of the unit and limited to intercalations in the rest of the formation. Evaporites are essentially anhydrites (Lunn et al., 2020; Davies and Simmons, 2019). A shaly siliciclastic interval at the base of the upper cycle of the formation interrupts the carbonate-evaporitic sedimentation: it is also clearly present in other parts of the Arabian plate like in Lurestan (Northwest Iran) and in the Palmyrides (Adayah formation; Lucic et al., 2010), as well as in Kuwait, Emirates and Saudi Arabia subsurface logs where it is however difficult to recognize, occurring in the upper part of the Jilh Formation and middle/upper Gulailah Formation (Lun et al., 2020 and references therein). Close to the Upper Carnian/Lower Norian boundary, another significant siliciclastic interval (Baluti Formation) again breaks the shallow water to evaporitic sedimentation.

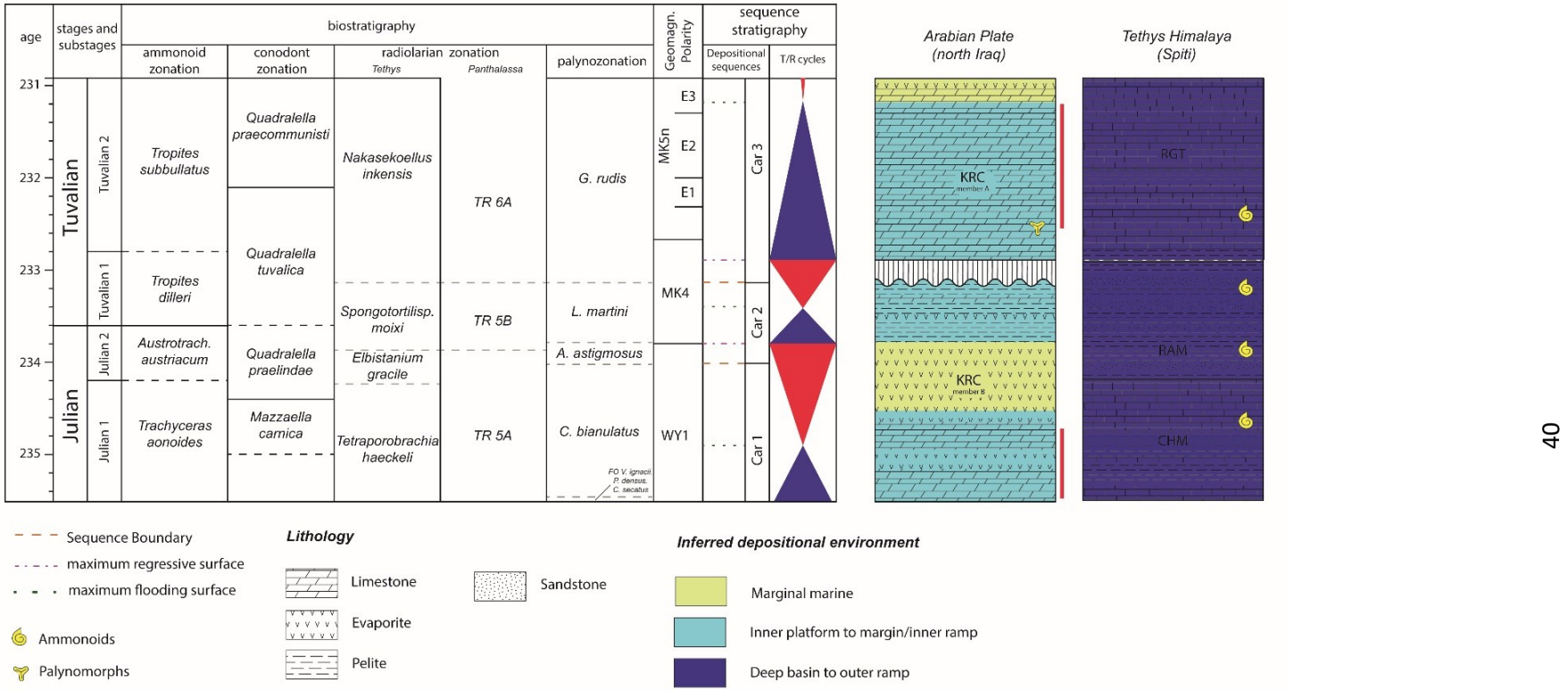

Figure 2.7: Chronostratigraphic framework of selected areas belonging to the southern Tethys area: Arabian Plate and Tethys Himalaya. Vertical strips represent certain or inferred hiatus. Lateral bars indicate the occurrence of arid (red) or humid (blue) paleoclimate proxies. References for left panels as in Fig. 2.3.

Abbreviations: KRC: Kurra Chine Fm; CHM: Chomule Fm; RAM: Rama Fm; RGT: Rongtong Fm.

The middle-upper part of the Carnian succession of the Arabian plate crops out in Jordan, where it is represented by the Abu Ruweis Formation (Abu Hamad et al., 2014 and references therein). The succession is lithologically similar to that described from well-logs: massive gypsum beds and intercalated coaly layers (cf. Arabian Keuper Facies), alternations of marly limestones, siltstones and shales intercalations (Abu Hamad et al., 2014). Facies associations point to playas, salinas, mud flats and some sporadical ephemeral lakes (Dill et al., 2012), set in a general marginal marine mixed siliciclastic-carbonate setting. Upward, the succession shows facies associations recording a marine transgression followed by delta progradation (Dill et al., 2012). Clastic facies likely correspond to the siliciclastic interval present in the upper member of the Kurra Chine Fm. in Kurdistan (Lunn et al., 2020). The carbonate-terrigenous alternations characterizing the upper part of the Abu Ruweis Formation are capped by a pisolitic paleosoil interval, unconformably overlapped by Jurassic deposits (Abu Hamad et al., 2014). Carnian basin to periplatform slope facies associations are exposed at Wadi Mayhah: shales, alternated to calci-turbidites and micritic limestones compose the upper part of the Al Jil Formation, while radiolarian cherts and cherty limestones with shales and calci-turbidites characterize the lower portion of the Matbat Formation, dated to the late Carnian to early Norian.

2.1.6.2 HIMALAYA

Remnants of the southern Tethys passive margin are widespread along the Himalayan chain (Tethys Himalaya in Garzanti et al., 1995 and Hornung et al., 2007b). The Spiti Basin (Fig. 2.7) displays a sudden change from basinal carbonates to argillaceous and silty marls during the Carnian (Hornung et al., 2007b). The succession starts with the Chomule Formation, dominated by dark carbonates, intercalated with marls and shales (Hornung et al., 2007b). Despite the recrystallization, halobiids, algal relics, benthic foraminifera and crinoids have been recognized in micrites sedimented along a distal deep shelf (Hornung et al., 2007b). The overlying Rama Formation marks a sharp shift to siliciclastics (prevailing shales) in the early Carnian (uppermost *T. aonoides* Ammonoid Subzone), while carbonates constitute a minor component upward in the formation. Among them, thin shelled coral bioclasts and oolites are present (Bhargava et al., 2004). The basal part of the Rama Fm. locally displays dark laminated shales suggesting anoxic conditions (Hornung et al., 2007b). Nodular limestones interbedded to shales mark the transition from Rama to Rongtong Formation. Even though carbonates dominate the unit, siliciclastics (sandstones and marls) are remarkably common in the middle member of the formation (Bhargava et al., 2004), dated as Tuvalian 2 (Hornung et al., 2007b).

2.1.6.3 LHASA BLOCK

The Mesozoic evolution of the Lhasa block is still highly debated: according to some authors (e.g., Zhu et al., 2011), the Lhasa terrane separated from the southern Tethyan margin drifting northward in the Late Triassic. Other researchers detected instead traces of accretion and collision related to the closure of Paleotethys in the same time span (e.g., Chen et al., 2020). The Middle and Upper Triassic are represented both by sediments related to terrestrial magmatic arc settings and to isolated carbonate platform to intra-platform basinal settings (Wu et al. 2021). In shallow water areas, platform carbonates, sometimes containing conglomerate lenses, have been assigned to the Ladinian and Carnian (Wu et al., 2021). The Carnian succession in basinal depressions is documented by an almost homogeneous sequence of cherty limestones (Zhulong Fm), containing conodont assemblages useful for biostratigraphic correlations (Wu et al., 2021).

2.1.7 NORTHERN TETHYS AND EASTERN LAURASIA

The southern margin of the Laurasia plate was strongly involved in terrane-collisions occurring during different orogenetic phases since the Late Triassic. Remnants of the active margin occur in poorly preserved fragments scattered in the Alpine-Himalayan chain, particularly in its external (northern) part.

2.1.7.1 CAUCASUS AND CASPIAN ZONE

In Crimea and western Caucasus, the Carnian-Norian is mainly composed of flysch-like successions, consisting of shale, siltstone, and sandstone alternations, sometimes containing older olistoliths (e.g., Kurtsovsky Fm, Yutsis et al., 2014), and representing deposition of sediments eroded from the Ukrainian shield in a back-arc basin. In the central-eastern Caucasus and in the Caspian area, the Upper Triassic is mainly represented by continental terrigenous sediments (e.g., Dagestan; Adamia et al., 2011). Noteworthy, in southern Armenia, a Carnian to Norian a succession composed of shales with sandstone and coaly intercalations is reported (Brownfield et al., 2000). In the eastern Caspian (Mangyshalk) a similar Carnian-Norian stacking pattern with siliciclastic sediments (Shair Formation) conformably lies above early Carnian limestones (Akmysh Formation; Palfy and Ozsvart, 2005) (Fig. 2.8).

2.1.7.2 TIAN SHAN BLOCK

The Madygen Formation mainly crops out in southwestern Kyrgyzstan (Moisan et al., 2011 - Fig. 2.8), unconformably overlying Carboniferous limestones: it consists of shales and siltstones with intercalated sandstones and conglomerates and also coal beds, organized in lacustrine, swamps and alluvial (fans and plains) facies (Dobruskina, 1995; Moisan et al., 2011). The stack of facies associations represents the progressive infilling of a tectonically controlled basin in a continental setting (Jolivet et al., 2013). The Madygen Fm is considered to be one of the most important Triassic fossils Lagerstätte, because of its richness of well-preserved fossil taxa, such as aquatic invertebrates and vertebrates, and insects (Moisan et al., 2011 and references therein). The Madygen Fm floral content is also remarkable and it is considered Carnian in age (Dobruskina, 1995; Moisan et al., 2011; Kustatscher et al., 2018).

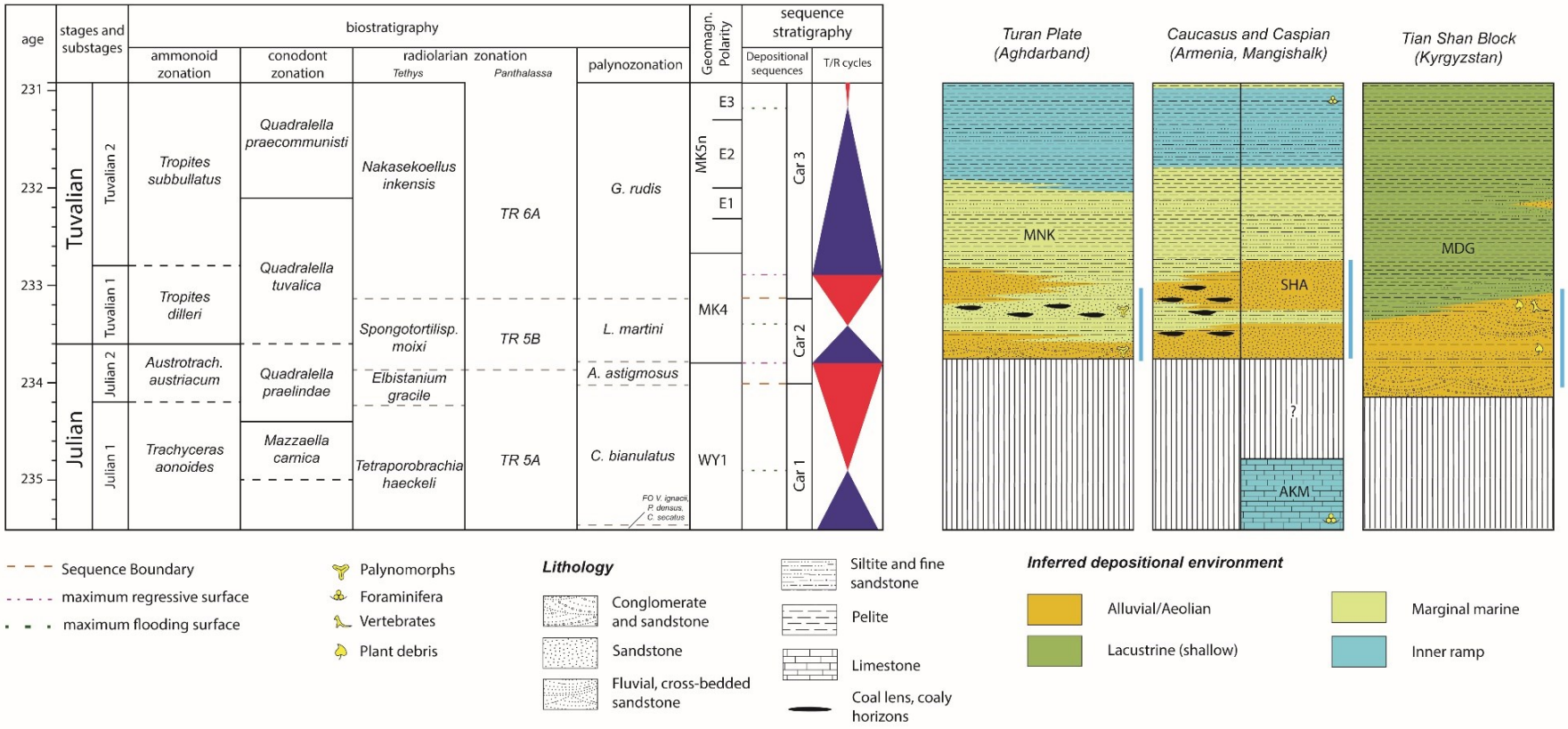

Figure 2.8: Chronostratigraphic framework of selected areas belonging to northern Tethys area and Eastern Laurasia: Turan Plate, Caucasus and Caspian zone, Tian Shan Block. Vertical strips represent certain or inferred hiatus. Lateral bars indicate the occurrence of arid (red) or humid (blue) paleoclimate proxies. References for left panels as in Fig. 2.3.

Abbreviations: MNK: Miankhui Fm; SHA: AKM: Akmysh Fm; Shair Fm; MDG: Madygen Fm.

2.1.7.3 TURAN, NORTHERN PAMIR AND SONGPAN GANZI TERRANES

Due to subduction processes of the Paleotethys under the active margin, the Middle to Late Triassic deposits are often characterized by volcano-sedimentary sequences, related to magmatic-arc and back-arc settings (e.g., Brookfield and Hashmat, 2001). In the Aghdarban area (north-eastern Iran - Fig. 2.8), the mainly volcanoclastic, early to late Ladinian Sina Formation is unconformably overlapped by the Miankhui Formation, whose lower part is dated to the late early Julian (*A. Austriacum zone*) through palinostratigraphy (Mazaheri-Joari et al., 2022). Basal conglomerates are followed upward by a succession consisting of mainly fine siliciclastics with fluvial sandstone intercalations and coal layers, referred to a deltaic environment (Mazaheri-Joari et al., 2022). The whole succession, characterized by a transgressive trend leading to the deposition of shallow water, marginal marine terrigenous sediments in the Late Carnian, was strongly deformed by transpressive and compressive movements linked to the oblique collision of the Iranian Cimmerian blocks in the Norian age (Mazaheri-Joari et al., 2022).

A similar configuration is present in northern Afghanistan (Band-e Turkestan Mts), where the Upper Triassic mainly comprises continental deposits, as red sandstones, shales and siltstones, sometimes with coaly intercalations (Montenat, 2009 and ref. therein), related to fluvial to marginal-marine depositional settings. On the other hand, in the North Hindu Kush, a magmatic-arc related succession (volcanics and clastics) is documented still in the Lower Carnian, overlapped by Late Triassic continental clastic sediments (Montenat, 2009).

The Upper Triassic of the Northern Pamir and Songpan Ganzi terranes is generally poorly preserved and mainly consists of sedimentary successions related to magmatic arc and forearc systems. Examples of the former come from Tagikistan (Karakul-Mazar zone), where volcanic and volcaniclastic sediments of Paleozoic to Triassic age have been basically metamorphosed (Imrecke et al., 2019). In the Sonpan Ganzi zone, a very thick turbiditic succession related to fore-arc settings (Xinduqiao Fm; Ding et al., 2013) collected sediments deriving both from the inner margin of Laurasia and from the northward-drifting Qiangtan Block (Jian et al. 2019; Tang and Zhang, 2012). Noteworthy, in the eastern part of the Kunlun terrane (located in an inner position), a fluvial siliciclastic succession bearing coal beds has been doubtfully attributed to the Upper Triassic (Sailiyakedaban Formation; Liu et al., 2021; Zhang et al., 2021).

2.1.7.4 SIBERIA

The back side continental eastern Laurasia has been mainly recognized in the Caspian area and in Siberia. The Carnian of the Central Siberia is represented by the Osipa Fm., the overlying Nemtsov Fm. and their lateral equivalents Ebitiem and Chaidakh Fms (Ilyna and Egorov, 2008 and ref. therein). All these units are rich in bivalves, ammonoids and variegated plant remains and traces, and are markedly siliciclastic. The Osipa Fm, is indeed constituted by shales, with siltstones in the upper part, transitioning upward to the siltstone-sandstone alternations of the Nemtsov Fm (late Carnian-early Norian). These units have been interpreted as representing a marine to continental environment (Ilyna and Egorov, 2008 and ref. therein). A similar argument can be made for the units Ebitiem and Chaidakh Fms, which are both coeval and correlatable to the upper Osipa/Nemtsov Fm and display the same lithofacies (Ilyna and Egorov, 2008 and ref. therein). Shales dominate also the Sheina and the Tikhaya Reka Formations, which record respectively the early and the late Carnian-Norian (age based on ammonoids and radiolarians) of Northern Siberia (Bragin et al., 2012 and ref therein). More specifically, these units are mainly made of brown or grey, dark

massive shales punctuated by concretions made of limestone, apatite, siderite or pyrite. These nodules are abundant within the Sheina and the upper Tikhaya Reka Fm, while its lower part contains rare intercalations of marly limestones (Bragin et al., 2012; Kosko and Korago, 2009).

2.1.8 EASTERN TETHYS

Several large plates were grouped in the Paleozoic to Mesozoic to form a peninsula connected with Laurasia, and protruding southward, bordering the eastern Tethys. While remnants of the Late Triassic active margin are often lacking or poorly studied, significant information comes from the sedimentary cover on cratons.

2.1.8.1 TARIM BASIN

The Tarim Basin represents an intracontinental basin since the Permian time, basically dominated by non-marine sedimentation in the Triassic. The Triassic successions irregularly crop out across the northern and southwestern margins of the basin, but a conspicuous information comes also from subsurface data. The lower Upper Triassic is mainly represented by a siliciclastic succession overlying the Middle Triassic beds: the Huangshanjie Formation consists of grey mudstones, siltstones and fine sandstones, often organized in regressive cycles, deposited in a lacustrine setting. The occurrence of carbonaceous mudstone intercalations and coals is frequent (Jiang et al., 2008). Sandstone and conglomerate intercalations are reported in the basal part (Peng et al., 2018).

2.1.8.2 NORTH CHINA PLATE

The North China Plate (Fig. 2.9) can be considered tectonically stable during the Early and Middle Triassic, while in the Late Triassic its southern margin was involved in the Qingling orogenesis, originated from collision between the North China Plate and the Yangtze Block (South China Plate). The Triassic cover of the North China Plate is well-documented by outcrops and subsurface data from the Ordos Basin, one of the largest intra-cratonic sedimentary basin of the Mesozoic. Since the Middle Triassic, a lacustrine environment is recorded by a thick siliciclastic succession. Facies associations change laterally, depending on the location along the general lake depositional system and local progradation of deltaic lobes: in the area close to Tongchuan, shallow lake to deltaic facies associations are reported (upper Yangchang Formation; jin et al., 2021 and ref. therein), while in the area close to Zhengzhou (Jiyuan Basin) shore-shallow lake deltaic to deep-lake related sediments prevail (Tanzuhang and Anyao formations; Lu et al., 2021). Noteworthy, in a mudstone to silty mudstone dominated interval of the Carnian succession recovered from cores from the Jiyuan Basin, four $\delta^{13}C_{org}$ shifts have been documented (Lu et al., 2021).

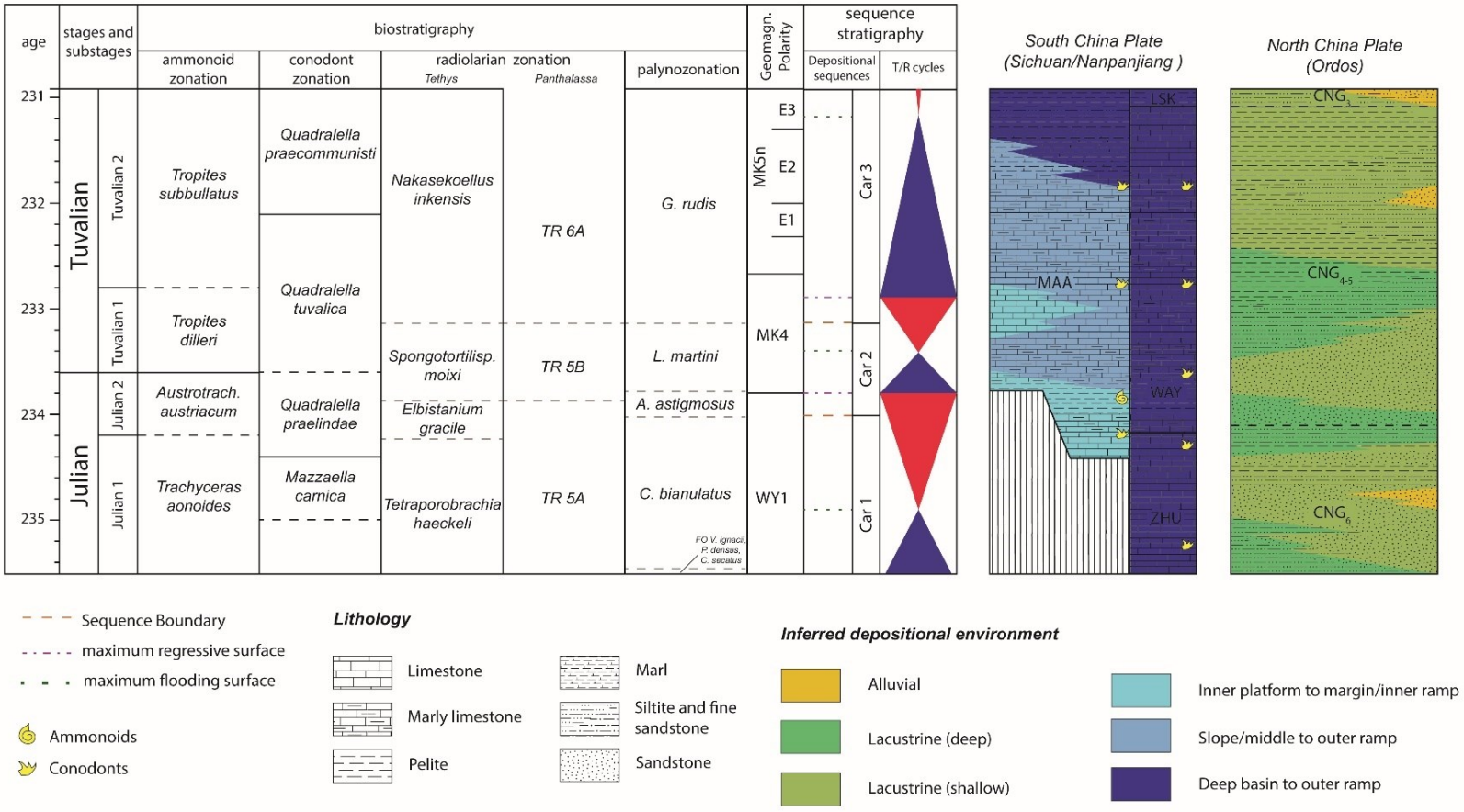

Figure 2.9: Chronostratigraphic framework of selected areas belonging to eastern Tethys: South and North China plates. Vertical strips represent certain or inferred hiatus. References for left panels as in Fig. 2.3.

Abbreviations: ZHU:Zhuganpo Fm; WAY: Wayao Fm; MAA: Ma'antang Fm; LSK: Laishike Fm; CNG: Yangchang Fm, members 3 to 6.

2.1.8.3 SOUTH CHINA PLATE

The depositional record of the north-western part of the South China Block craton (western Yangtze block), facing the Eastern Tethys, is well-preserved in the Sichuan Basin (Fig. 2.9): the Ma'antang Fm has been dated to the Carnian stage based on conodonts and ammonoids (Jiang et al., 2019; Jin et al., 2018 and 2019; Mietto et al., 2021). In Hanwang area, the unit consists of oolitic-bioclastic limestones in its lower part, followed by microbial- sponge boundstones locally forming mounds. Upward, fossil-rich mudstones, shales and siltstones occur (Jiang et al., 2019; Jin et al., 2019 and 2020). Interestingly, two phases of mound growth and demise, each one followed by a siliciclastic interval and separated by a karst surface (i.e., subaerial exposure), have been identified (Shi et al., 2017). Jiang et al. (2019) outlined that the quartz content within the thrombolytic limestone and the sponge is more abundant than in the overlying mainly siliciclastic succession. The disappearance of oolites occurred within the upper Julian (*Mazzaella carnica* range zone; Jiang et al., 2019), and the second sponge-terrigenous interval is late Tuvalian in age, or even later (Shi et al., 2017). Carbon isotopes analysis of bulk carbonates and total organic carbon (TOC) from the Ma'antang Formation at Ma'antang show negative $\delta^{13}C$ shifts in the microbial-sponge dominated unit (*Austrotrachyceras* Ammonoid Zone; Shi et al., 2019).

In the Long Chang/Yongyue area (Giuzou Province), that was situated in a transitional zone between the Yangtze Platform and the Nanpanjiang Basin (Sun et al., 2016 and 2019 - Fig. 2.9), the Carnian is characterized by basinal units, well-constrained in age by combined bivalves, conodonts and ammonoids biostratigraphy (Sun et al., 2016): the Zhuganpo Fm (Julian) consists of bioclastic wackestones, intraclastic limestones passing to two distinct manganese-rich limestone beds in the upper part. The overlying Wayao Fm (Julian 2-Tuvalian 2) is mainly composed of black shales with subordinate carbonate interbeds, and is followed by the Laishike Fm (likely Tuvalian 3 in age; Sun et al., 2016), consisting of basal black shales strata followed by turbidite sandstones, marking the start of flysch-like sedimentation (Sun et al., 2016). Carbonate and total organi matter $\delta^{13}C$ curves from the Long Chang section reveal multiple negative shifts at the transition from the Zhuganpo to the Wayao Formation (Sun et al., 2016).

Due to the Indosinian Orogenesis, the Carnian successions on the southern part of the South China Block were uplifted and mainly eroded, with the renewed sedimentation starting again only in the Norian (Rossignol et al., 2018).

2.1.9 CIMMERIAN BLOCKS

During the Late Triassic, Cimmerian Blocks rapidly drifted northward, progressively colliding with the northern Tethyan margin. The tectonic deformations and uplifts related to the Cimmerian Orogeny favoured the erosion of part of the Mesozoic cover on those plates, and the Carnian succession is recorded only scattered and is often lacking (Mazaheri-Johari et al., 2022).

2.1.9.1 IRAN PLATE

In the Alborz mountains (northern Iran) the lower Carnian is basically composed of shallow water dolomites of the upper part of Elikah Fm (BadriKolalo et al., 2014), that is upward capped by an erosional unconformity. The above lying bauxites (Kani Zarrineh; Abedini et al., 2021) have been attributed to the late early Julian (Mazaheri-Johari et al., 2022), and are separated from Norian deposits of Shemshak Group by a significant erosional unconformity. The group consists of mixed siliciclastic-carbonate alternations transitioning upward to a

thick succession of sandstones and alluvial facies associations (Ekrazar and Shahmirzad formations; Fursich et al., 2009; Seyed-Emami et al., 2009).

The Carnian succession of the Central Iran terrane is sparsely preserved in different structural units (Tabas block, Nayband, Zofreh/Soh, Kerman zones) and is essentially composed of shallow water carbonates of the Shotori Fm, capped by a subaerial unconformity (Krystyn et al., 2019). The overlapping succession consists again of dolostones and limestones related to shallow marine carbonate environments (Espahk Limestone; Krystyn et al., 2019), that has been associated to a renewed sedimentation in the latemost Carnian – early Norian (Mazaheri-Johari et al., 2022).

2.1.9.2 KARAKORAM, WAKHAN BASIN, SOUTH PAMIR AND SOUTH QIANGTANG BLOCK

The South Pamir- Karakoram terrane was part of the Cimmerian mega-terrane, that was divided in different blocks during its Triassic northward drifting (Kapp et al., 2003; Zanchi and Gaetani, 2011; Zhai et al., 2011; Zanchetta et al., 2018). The northern margin of the terrane and the transition to oceanic domain in the Middle to Late Triassic was mainly characterized by a volcano-sedimentary succession with cherty limestones, shales and sandstones intercalated to basalts and andesites, capped by volcanics of the Gumbezkol Group (Yogibekov et al., 2020), developed in a magmatic arc setting (Angiolini et al., 2013). The Upper Triassic of the South Pamir and adjacent zones mainly consists of shallow water, stromatolithic cyclic beds, laterally transitioning to external, bioturbated platform carbonates (Montenat, 2009). In the Wakhan sedimentary basin, a meta-sedimentary succession unconformably overlies Permian beds: it consists of a mixed terrigenous-carbonate succession (cherty limestones and siltstones) followed by a thick pile of sandstone, siltstone and shale (with a minor fine-carbonate component) alternations, sometimes with coal seams and plant remains, assigned to the Upper Triassic (Montenat, 2009; Zanchi and Gaetani, 2011). In the southern part of the terrane (Karakoram zone), different paleoenvironments coexisted during the Middle to Late Triassic. In the Lashkargaz nappe, stromatolithic to massive dolostones (Ailak Fm) constitute a thick succession, capped by a karst surface, cutting down the carbonates for more than 100 m and infilled by volcanic and metamorphic quartz grains in an iron-rich matrix (Zanchi and Gaetani, 2011). Jurassic units unconformably lie on top denoting a significant gap (Gaetani et al., 2013; Angiolini et al., 2013). In other nappes of Karakoram, the Upper Triassic is composed of massive to bedded limestones and dolostones with megalodontids (Aghil Fm), likely separated by weak unconformities related to sedimentary gaps (Gaetani et al., 2013). Sometimes, the upper part of the succession is characterized by radiolarian-bearing subtidal carbonates, pointing to a more basinal environment (Zanchi and Gaetani, 2011; Gaetani et al., 2013). In the Kabul Block, intra-formational breccias and volcanic tuffs are interbedded in dolomitic limestones and dolostones (Fischer, 1971).

The southern transition of the terrane to the oceanic realm is composed of Upper Triassic fine siliciclastics with intercalations of radiolarian limestones and radiolarites, often associated with mafic massifs and calcareous olistoliths, or more rarely by thick turbiditic sequences (Montenat, 2009). The Qiangtang Block constitutes one of the easternmost Cimmerian terranes. Recent research pointed out that the block is formed by two different terranes that were occupying different paleogeographic positions during the early Mesozoic, at least up to the Late Triassic (e.g., Huang et al., 2018). According to this scenario, we consider the South Qiangtang Block as a lateral equivalent of the South Pamir. The Upper Triassic is characterized by marginal marine facies associations, suggesting a depositional environment ranging from outer shelf to deltaic setting. One of the most known units is the

Carnian Tumengela Fm, that at Suobucha mainly consists of pelite and siltite alternations with common ripple marks and cross bedding (Wang et al., 2022). Elsewhere in the South Qiangtang Block, siliciclastic swamp facies with coaly horizons crop out and have been correlated to the same interval (Wang et al., 2022). The terrigenous interval is upward followed by carbonate ramp facies dated to the Norian stage.

Fragments of the southern margin of the Qiangtang Block occur sparsely in the Bangong-Nujiang Suture Zone: the Triassic succession mainly consists of deep basinal facies (radiolarites and micritic limestones; Gajia Fm), noteworthy with siliciclastics increasing upward in the Carnian (Wu et al., 2019) and the Norian mainly composed of micritic and bioclastic limestones (Wu et al., 2021).

2.1.9.3 CENTRAL PAMIR, BAND E BAYAN AND NORTH QIANG TANG BLOCK

Most of the Triassic cover in the Band-e-Bayan zone is missing due to the erosion of uplifted blocks of the Cimmerian Orogeny, unconformably covered by Jurassic sediments. In places, bauxites of doubtful age have been reported between the Hercynian basement and the Jurassic cover (Montenat, 2009).

The Permian to Jurassic succession of Central Pamir was involved in different orogenetic processes since the Late Triassic, leading to strong tectonic deformations and development of a complex nappe-structure, and metamorphism of the original sedimentary and magmatic rocks (cf. Rutte et al., 2017; Imrecke et al., 2019). The Middle to Upper Triassic cover occurs spotted, often with a very poor biostratigraphic resolution, and is characterized by different successions depending on the thrust sheet. Generally, the Upper Triassic is composed of siliciclastics: dark slates with rare carbonate intercalations, associated with meta-arenites rich in plant debris are found unconformably overlying platform carbonates of early Carnian age (Desio, 1975; Dobruskina, 1994). Elsewhere, terrigenous sediments are mainly represented by continental red sandstones, siltites and conglomerates attributed to the uppermost Triassic (Rutte et al., 2017 and ref. therein).

Useful information about the Upper Triassic succession of the northern Cimmerian mega-terrane comes from the Northern Qiangtang Block (Tibetan plateau) that is considered as a lateral equivalent of the Central Pamir Block. Paleomagnetic data from Norian-Rhaetian volcano-sedimentary rocks occurring in the central part of the terrane indicate a paleolatitude of 31,7 ± 3 N for the Late Triassic (Song et al., 2015). In the central-eastern part (Janghgaida Rinag) an unconformity marks the base of the Carnian succession, followed by conglomerate and arkose beds, grading upward to siltites and pelites alternations, with common coal horizons (Xiaochaka Fm; Liang et al., 2020). This succession has been interpreted as related to a deltaic environment. The Carnian - Norian continues upward with thick platform limestone and thin fine siliciclastic intervals alternations, culminating with a predominant terrigenous unit rich in sandstones and with common coaly layers (Xiaochaka Fm; Liang et al., 2020). The whole stacking patterns recalls what has been reported in the eastern part of the Qiangtang basin by Fu et al. (2020): here, carbonate platform sedimentation (calcarenites and micritic limestones; Boli La Fm) is interrupted in the late early Julian (base of *A. austriacum* ammonoid subzone) by the interposition of pelites, siltites and sandstone layers rich in plant debris, grading upward to an interval mainly consisting of fine siliciclastics (Bagong Fm). The terrigenous interval is marked at the base by a significant negative $\delta^{13}C$ shift (Fu et al., 2020). The overlying Norian succession is mainly characterized by cross-bedded sandstones related to a fluvial to marginal-marine environment (Fu et al., 2020).

The Upper Triassic successions by accretionary complexes with dark sandstones and shales with intercalated basic-to-acid deposited in the southern active margins of the terrane (e.g.,

West Pshart Block; Rutte et al., 2017) are often characterized volcanites, passing upward to arkose.

2.1.10 PANTHALASSA

Relicts of the sedimentary cover of the Panthalassa Ocean have been found in an accretionary complex called Tamba–Mino–Ashio Belt, located in central Japan (Inuyama area). They mainly consist of a bedded chert succession (Nakada et al., 2014; Nozaki et al., 2019; Tomimatsu et al., 2021), spanning in age from the Longobardian and the Tuvalian, on the basis of radiolarian and conodont biostratigraphy (Nakada et al., 2014; Tomimatsu et al., 2021). Cherts are often red or greenish grey, characterized by fine-grained quartz and siliceous muddy layers, and are punctuated by thin white chert layers (Tomimatsu et al., 2021). Nakada et al. (2014) provided mineralogical analyses showing a decrease of chlorite within the Julian and at the Julian-Tuvalian boundary until a short-lived, complete disappearance, and a later reappearance in the late Tuvalian.

In the Sambosan Accretionary Complex (southwestern Japan), remnants of a Mesozoic carbonate platform set on a seamount have been recently discovered (Peybernes et al., 2020). The first colonization by *Tubiphytes*-sponge-coral patch reefs occurred from Ladinian to early Carnian, but in the Carnian a significant turnover of carbonate framework producers has been documented: hypercalcified sponges, encrusting algae and microbial crusts dominate to form a more developed and robust framework reef (Peybernes et al., 2020 and references therein).

2.1.11 WRANGELLIA

Witnesses of a Large Igneous Province (LIP) existing within the Panthalassa Ocean during the Middle-Late Triassic come from the Wrangellia terrane, accreted on the western active margin of the American craton during the Late Jurassic- Early Cretaceous (Greene et al., 2010). Depending on the location, huge volcanic and volcanoclastic deposits are found conformably overlying or intruding Ladinian siliciclastics (e.g., central Vancouver Island, Kluane Ranges, Alaska Range and Wrangell Mountains; Greene et al., 2010) or unconformably covering the Permian succession (e.g., northern Vancouver Island, Wrangell and Talkeetna Mountains; Greene et al., 2010).

The huge stack of volcanics is found disconformably covered by shallow water limestones, with dolostones and cherts to a lesser extent (Chitistone Limestone; MacKevett 1971), or by massive to well-bedded micritic, locally bioclastic, limestones (Quatsino Formation and Sadler Limestone) dated to the early Tuvalian (*dilleri* ammonoid Subzone; Carlisle and Susuki, 1965). The latter are also found interbedded to volcanics in the uppermost part of the Karmutsen Formation (Carlisle and Susuki, 1974). Ages of the sedimentary succession is provided by ammonoids and pelagic bivalves (Greene et al., 2010).

2.2 INTERPRETATION OF SEDIMENTOLOGICAL FEATURES RECORDED DURING THE CARNIAN

2.2.1 SHALLOW MARINE ENVIRONMENTS

The effects of the climatic perturbation on shallow shelf areas are multiple and can be documented differently depending on the region.

In several areas of the Tethys Ocean, a change from microbial-dominated to skeletal grain carbonate factory has been observed in the late Julian (Gattolin et al., 2015; Jin et al., 2020), with the last factory persisting up to the late Tuvalian, when microbial carbonates became relevant frame-builders again (e.g., Caggiati et al., 2018). The change in carbonate factories

is almost coeval with the onset of the CPE recorded by the first NCIE (Dal Corso et al., 2015; 2018a). The consequent demise of high-relief carbonate platforms is well documented as in analyzed areas of the Western Tethys as in those belonging to the Eastern Tethys realm: best examples have been reported from the Dolomites (Breda et al., 2009; Gattolin et al., 2015; Dal Corso et al., 2015, 2018), NCA (Hornung et al., 2007a; Kolar-Jurkovsek et al., 2010; Dal Corso et al., 2015; Mueller et al., 2016b), TR (Rostasi et al., 2011; Dal Corso et al., 2018a), South China Block (Jin et al., 2020, 2021), but evidence of the shift from high-relief to ramp systems can be found also from the Outer Dinarides (Gale et al., 2018) and Central Western Carpathians (Sykora et al., 2011).

Due to the Julian eustatic sea-level fall recorded widely in the Tethys realm, most of the demised carbonate platforms underwent subaerial exposure (Jin et al., 2022). The widespread humid conditions favored the development of karst surfaces and bauxites on top of carbonate platforms. This is the case of the Dolomites (e.g. Preto and Hinnov, 2003), western Julian Alps (e.g., Dogna Valley; Preto et al., 2005; Caggiati et al., 2019), Outer Dinarides (Celarc et al., 2008; Gale et al., 2018) and South China block (Shi et al., 2017; Jiang et al., 2019), where they lie on top of Ladinian-early Julian reefal limestones. Occurrence of bauxites set on Middle Triassic carbonates in the Cimmerian successions can be interpreted in this sense (Mazaheri-Joari et al., 2021).

The enhanced runoff caused by widespread humid conditions also resulted in higher siliciclastic input rates in sedimentary basins, developing marginal systems mainly dominated by coarse sediments. The interruption of carbonate sedimentation by siliciclastic intervals is well documented in the Western Tethys, where the first terrigenous input postdates the demise of platform systems (Dal Corso et al., 2018a; this work Chapter 5). In the Dolomites siliciclastic to mixed siliciclastic-carbonate ramp systems were set (Breda et al., 2009; Gattolin et al., 2013, 2015), as well as in the Transdanubian Range (Dal Corso et al., 2018a) while in other places deltaic systems developed (e.g., Lunz; Dal Corso et al., 2015 and ref, therein). In the Eastern Tethys, evidence of interruption of carbonate sedimentation by siliciclastic input during the late early Carnian is found both in the platform succession of the Qiangtang basin (Fu et al., 2020) and in the ramp succession of the Hanwang area (South China Block; Shi et al., 2017; Jiang et al., 2019), and have been correlated by solid biostratigraphic and/or chemostratigraphic constraints to the onset of the CPE (Shi et al., 2019; Fu et al., 2020). Also in the Balearic Plateaux (Minorca; Lopez-Gomez et al, 2017), the carbonate ramp succession is rapidly covered by a terrigenous unit followed by the development of humid paleosols, and has been interpreted as evidence of the CPE. In Central Pamir, a mainly siliciclastic succession generally ascribed to the Late Triassic and unconformably covering platform carbonates of early Carnian age (Desio, 1975; Dobruskina, 1994) could be interpreted in this sense.

Humid conditions also often favoured dense vegetation and development of coaly horizons in siliciclastic deposits, as for the Outer Dinarides, where clastic intervals with coal layers have been found overlying late Julian carbonate ramp sediments and bauxites (Gale et al., 2018) or for the southern part of Eurasia, where siliciclastic marginal marine deposits with common coaly horizons overlie an early Julian unconformity (Turan Plate; Mazaheri-Joari et al., 2021). Siliciclastic swamp facies with coaly horizons occurring in the South Qiangtang Block (Wang et al., 2022) strictly recall this scenario, even if relationships between sedimentology and paleoclimate have not been discussed yet in this area.

In the Taurus Mountains area, the carbonate platform demise is documented at the transition of the Kartoz and Kasımlar fms, dated to the Julian 2: the platform drowned and it was only later covered by clastic deposits, between Julian 2 and Tuvalian 1 (boundary between the carbonate and the marlstone member of the Kasımlar fm in Lukeneder et al., 2012). Noteworthy, the discrepancy about the CPE onset is just apparent because it is due to a

different definition that Lukeneder et al. (2012) gave to the CPE: they defined the onset of the CPE based on the arrival of terrigenous input into the basin, neglecting the demise of the high-relief carbonate platform of the Kartoz Fm, occurring at the transition from Julian 1 to Julian 2 (Chen and Lukeneder, 2017).

In other areas as Levant margin, Arabian Plate and Tunisia, the sedimentation was characterized by coastal shallow water settings since the Ladinian, with playa-like limestones or dolostones and evaporites, substantially denoting arid conditions. However, one or more discrete, short-lived, fine siliciclastic pulses interrupted those conditions during the Carnian (Bialik et al., 2013, Abu Hamad et al., 2014; Soussi et al., 2017; Lunn et al., 2020). In some cases, features witnessing humidification during the Carnian (humid soils) have been reported (Jordan; Abu Hamad et al., 2014).
The different duration of the siliciclastic-dominated sedimentation through the different areas reflects the possibility that climatic shift is not recorded everywhere with the same intensity (areas more proximal/distal from the source of sediments).

There are also some places where significant changes in sedimentation patterns throughout the whole Carnian succession have not been recorded. However, some effects of the climate change can be found, as in biota associations: in the Tuvalian part of the mixed ramp succession of British Columbia (Baldonnel Fm), three intervals are marked by the appereance of scleractinian- reefs (Schultz et al. 2016), as in the Southern Alps. Similarly, the carbonate factory turnover recorded in the Ladinian-Carnian carbonate succession developed on seamounts of the Panthalassa Ocean (Peybernes et al., 2020) could be linked to the CPE.

2.2.2 DEEP MARINE ENVIRONMENTS

Deep water environments (above the CCD) often display an interruption of previously carbonate sedimentation, replaced by terrigenous materials during the Carnian. Lagonegro, Spiti Basin and Long Chang area (South China) are all characterized by that feature. Their similarities include also a robust stratigraphic resolution based on solid biostratigraphy and isotope stratigraphy, which allow the correlation between the shift in sedimentation and the CPE (Hornung et al., 2007b; Rigo et al., 2007 and 2012; Sun et al., 2016). Rigo et al. (2007) suggest that the lack of carbonate sediments in the Lagonegro basin is due to a rise of CCD, associated with the reduction of carbonate from neritic sources due to the crisis of microbial carbonate platforms.

The Otuk Fm in Alaska shows oxic-dysoxic stable conditions since middle Anisian (Doumoulin et al., 2011). However, the Authors report two interesting negative Carbon isotope shifts during the Carnian below and within a horizon composed of black shales: further investigations about it are needed.

In deep-water settings, below the CCD, conodonts and radiolarian biostratigraphy were helpful to constrain the cherty basinal succession reported from Panthalassa. Here, Nakada et al. (2014) pointed out a possible relationship between a recorded variation in clay minerals association towards more humid conditions and the CPE. No sedimentological variation in basinal successions during the Carnian is reported.

2.2.3 TERRESTRIAL AND MIXED ENVIRONMENTS

Continental/mixed terrestrial-marine settings evolve into different environments, also influenced by the paleolatitude during the Carnian. The developement of lacustrine, fluvio-lacustrine, fluvio-deltaic environments on underlying playa-like is common in the areas located at the lowest latitudes, while higher latitudes experience the expansion of fluvial or deltaic pre-existent systems. The UK and the Germanic Basin are two examples belonging

to the former category, which are important because they are very well-constrained successions and they represent reference areas where the idea of the CPE and the related debate arose. Indeed, Simms and Ruffell (1989) interpreted the shift from arid to humid and then back to arid facies in the Stuttgart (Schilfsanstein) Fm. as the result of the CPE and correlated the succession to the Mercia Mudstone Group in UK, conferring for the first time a global meaning to that. On the other hand, Visscher et al. (1994), studying the palynology of the same Stuttgart Fm, rejected the idea of Simms and Ruffell, *de facto.* Several alternative hypotheses have been proposed to explain the enhanced runoff, which brought the high flux of siliciclastics into the Germanic Basin, triggering the scientific debate that led to today interest around this interval (Simms and Ruffell, 2018): megamonsoonal circulation coupled with a rift shoulder uplift set during the Carnian along the western coast of modern day Scandinavia (Kozur and Bachmann, 2010); marine transgressions (which have also affected the formation of different pedotypes - Franz et al., 2014 and 2019); orbital forcing and particularly long eccentricity (Bahr et al., 2019). The low compositional maturity of the Stuttgart Fm deposits has been interpreted as a signal of an arid to semi-arid climate (Franz et al., 2019). Again, high abundances of the wet Lowland Palynomorph and Macroplant Eco Groups (PEG and MEG) are considered indicative of a taphonomic window controlled by local high-groundwater stages on delta plains and floodplains, while laterally, xerophytic vegetation prevails. Thus, it seems that, according to these Authors, the Stuttgart Fm does not yield sufficient evidence for the CPE (Franz et al., 2019). Conversely, Bahr et al (2019) and Kozur and Bachmann (2010), considered the wide extension of the fluvio-deltaic facies and postulated a warm and wet climate in the Germanic Basin and adjacent Tethyan areas during the deposition of the Stuttgart Formation, but not enough to be considered pluvial, except for the source region.

The development of a delta on a playa environment has been described also in other areas of the CEB, such as Massif Central (Arche and López-Gómez, 2014), Poland (Jewuła et al., 2019) and Moesia (Chatalov, 2017). Poland successions are well palinostratigraphically constrained (Fijałkowska-Mader, 2015; Fijałkowska-Mader et al., 2020); on the other hand, Massif Central and Moesia display scarce stratigraphic markers. Although, the environmental shift has been interpreted as CPE-related for all those areas (Arche and López-Gómez, 2014; Chatalov, 2017; Jewuła et al., 2019; Fijałkowska-Mader et al., 2020). Conversely, in the Danish Basin, playa setting remains unaltered during the Carnian, even if the carbonate-dominated succession becomes more siliciclastic upward (Lindstrom et al., 2017).

At higher latitudes, fluvio-deltaic environments were already well-developed at the beginning of the Carnian, but some Authors have related the setting of even more developed and expanded fluvio-deltaic (Barents Sea) or lacustrine (Greenland) system to the enhanced precipitations triggered by the CPE, by correlations based on palynology, C-isotope stratigraphy, sedimentology and clay minerals analyses (Andrews et al., 2014; Muller et al 2016a; Decou et al., 2017). The case of the Triassic Boreal Ocean (TBO) is particularly significant. The expansion of the largest delta plain in Earth's history has also been related to the enhanced continental runoff and sediment influx linked to the CPE (C3-C4 depositional sequences in Klausen et al., 2019, Gilmullina et al., 2022). The situation is quite different in the North Sea area, where the alternations of sandstones and mudstones reported during the Carnian have been interpreted as climatic fluctuations between arid and humid, even though the succession is lacking stratigraphic biomarkers (McKie, 2014; Burgess et al., 2020).

On the other hand, very well constrained are the Upper Triassic successions of Brazil and Argentina (detrital zircon geochronology and ages from single zircon on tuffs– Marsicano et al., 2016; Langer et al., 2019; Colombi et al., 2021). During the Carnian the sedimentation

in Brazil is characterized by an ephemeral lacustrine-fluvio-deltaic environment with well-developed paleosols, while Argentinian coeval successions are represented by fluvio-lacustrine facies, evolving to lacustrine-deltaic setting, with coal horizons and without evaporites (Mancuso et al., 2020). These features have been interpreted as evidence of humidification and the geochronological constrains suggest a possible correlation with the CPE (Mancuso et al., 2020). Greater India Carnian succession of Maleri and Tiki Fms has been correlated with Argentinian and Brazilian succession based on vertebrate fossil content; the Indian succession represents a river system set on an alluvial plain with no relevant sedimentological variation during the Carnian. Fluvial setting is also reported from Carnian successions from: Antarctica (locally evolving into a lacustrine setting; rich in coal in Victoria Land), Australia (multiple cycles of fluvio-marine environment from Anisian to Norian, with coal and amber deposits of Carnian age), Morocco (cyclical alternation of fluvial and playa setting), Iberia and Algarve (with paleosols), Fundy Basin and Kunlun (Leleu and Hartley, 2010; Liu et al., 2021). Biostratigraphic constrains for all these successions are poor. However, based on sedimentology and palynology, correlation with the CPE have been traced for Iberia and Algarve, Morocco and Australia successions (Arche and Lopez-Gomez, 2014; Mader et al., 2017; Zeng et al., 2019; Stillwell et al., 2020).

In addition to the TBO, during the Carnian we assist to the setting and the expansion of other deltas. For instance, North China Carnian succession evolves from lacustrine to deltaic setting, while fluvio-deltaic environment is set in Turan domain. Lacustrine environments, associated with coal deposits are instead reported from Newark and Taylorsville Basins (precisely constrained by magnetostratigraphy – Kent et al., 2019), Africa, Tian-Shan and Tarim, all lacking of significant biostratigraphic constraints.

Poor biostratigraphic resolution is also common for Caucasus and Caspian area, where no variations in continental siliciclastic-dominated sedimentation with coal intercalations (in southern Armenia) from Carnian to Norian occurred (Brownfield et al., 2000; Palfy and Oszvart, 2005; Adamia et al., 2011; Yutsis et al., 2014).

Also the Chinle Fm has been deposited in a continental setting. The unit is object of another debate related to the CPE. Considering the well-developed fluvial facies and the evidence of gleyded spodosols, interpreted as humid indicators, Lucas and Tanner (2018) have purposed the Shinarump Mb of the Chinle Fm as representing the CPE in western USA. Conversely, according to the geochronological data provided by Rasmussen et al. (2020), the Shinarump Mb nor the entire Chinle Fm could not record the CPE because they are Norian in age. However, is noteworthy to highlight that palynomorph taxa like *Camersoporites secatus, Infernopollenites* spp. and *Lagenella martini*, which are typical Carnian indicators (Cirilli, 2010; Roghi et al., 2010), still occur during the Norian within the Chinle Fm, until the Petrified Forest Mb (Lindström et al., 2016).

Regarding mixed terrestrial-marine environments, siliciclastic sediments dominate the Carnian successions of Siberia and Northern Quiantang Block. The latter in particular is characterized by the setting of a deltaic system rich in coal fragments, and isotope stratigraphy studies highlight a negative C-isotope excursion within the BoliLa Fm. which has been correlated to the CPE in Western Tethys and South China (Sun et al., 2016; Dal Corso et al., 2018a; Fu et al., 2020). Alborz mountains displays a shallow water carbonate succession separated from alluvial facies by a subaerial unconformity. Whakan Basin and Karakoram are affected by really poor stratigraphic resolution, so it is also possible to recognize a mixed or carbonate sequence, respectively, punctuated by siliciclastics intercalations during the Upper Triassic (Kabul Block shows also volcanic tuffs). All these areas are affected by scarce or totally absent stratigraphic resolution and no paleoclimatic studies have been provided yet.

2.3 SUMMARY AND CONCLUSIONS

There has been published multiple evidence for the CPE worldwide, based on several different climatic proxies. Stratigraphic correlations have shown that many changes in both sedimentology and biota were coeval with this event. This demonstrates the global character of the CPE.

What emerges from this work is the fact that in many places around the world almost synchronous changes in sedimentation occurred during the Carnian. Numerous papers have suggested the correlation between such changes and the CPE; in other places, instead, such changes have not been analyzed for paleoclimatic purposes, partly because of the lack or scarcity of stratigraphic markers that make any correlations difficult. We therefore recommend future investigations with stratigraphic and paleoclimatic purposes.

Another feature that emerges from the present review is that the CPE is not characterized everywhere by a climatic change from arid to humid conditions. In fact, in some areas, the climate is humid since the Middle Triassic (e.g., Barents Sea), while in other ones, despite the changes found in sedimentation and biota, they are not also linked to humidification and the climate remains arid (e.g., Lhasa Block). Accordingly, we conclude by suggesting that the name of the event should be changed to Carnian Climatic Episode. Indeed, we consider that the adjective "pluvial" is limiting and not illustrative of all situations referable to the CPE. On the contrary, the more generic term "climatic" would also include cases in which there are environmental changes due to or referable to this event, but not also characterized by climate humidification.

3 SAMPLES AND SAMPLE PREPARATION

85 samples were collected from different well-known sections from the Dolomites, namely Stuores/Wiesen (NST), Pocol (CRP), Milieres (MI20), Lago Scin (LSC), Mietres (MTR), Costalaresc (CLS), Ru Assola (ASS), Rio Falzarego (R5T), Dibona (DIB), Passo Falzarego (TV). Sampling was focused on fine-grained intervals to obtain as homogeneous and comparable data as possible, covering a stratigraphic interval bracketed between the San Cassiano and the Travenanzes Fm. In other words, not only the syn-CPE interval, represented by the Heiligkreuz Fm has been sampled, but also the units below and above, to obtain a more exhaustive weathering trend across the event. The combination of the sampled successions resulted in the composite section reported in figures 1.5 and 5.1. The Lagazuoi mb of the Heilgkreuz Fm has not been sampled because of lack of fine-grained intervals within that unit. Collected samples were crushed using agate mortar for both geochemical and mineralogical analysis.

3.1 GEOCHEMICAL ANALYSES

The geochemical analyses part was carried out at the Wuhan Sample-Solution Analytical Technology Co., Ltd. (China), using a Rigaku ZSX PrimusII XRF spectrometer (Fig. 3.1a) and an Agilent 7700e Inductively Coupled Plasma Mass Spectrometer (ICP-MS) (Fig. 3.1b) respectively for the determination of major, minor and trace elements in the whole rock. The sample pretreatment of whole rock major element analysis was made by melting method. The flux is a mixture of lithium tetraborate, lithium metaborate and lithium fluoride (45:10:5 ratio), Ammonium nitrate and lithium bromide were used as oxidant and release agent respectively. The melting temperature was 1050℃ and the melting time was 15min. The X-ray tube of the XRF-spectrometer is a 4.0Kw. The applied test conditions were voltage: 50kV, current: 60mA. All major element analysis lines are kα. Samples were compared to standard material (rock standard samples: GBW07105-11). The data were corrected by theoretical α coefficient method, The relative standard deviation (RSD) is less than 2%. For ICP-MS analysis, sample preparation involves digestion of 50 mg of powdered sample with 200mg of NH_4HF_2 powder into a vial. This undergoes a heat treatment at 230°C for 3 hours. Then, 2 ml of HNO_3 are added and the vials are re-heated at 160°C. After 1h the vials are opened, helping liquid evaporation. Subsequently, 1 ml of HNO_3, 1ml of Milli-Q water and 1ml of of 1 $\mu g\ g^{-1}$ In internal standard solution are added to the residue, which after is heated at 120°C for 6 hours. Finally, the obtained solution is gravimetrically diluted within a polyethylene bottle with a 2% concentrated solution of HNO_3.

After the analyses, the obtained geochemical data were used to calculate some weathering indices, whose trends have been carefully examined to select the most significant ones. Indeed, each index considers different elements within its equation and has both strengths and weaknesses (Dinis et al., 2020b and references therein). Very recent studies dealing with weathering and paleoclimatic reconstructions use combinations of many indices with clay mineralogy (e.g., Deng et al., 2019; Dinis et al., 2020a and b; Perri, 2020; Xu et al., 2020; Zhang et al., 2021; Mancuso et al., 2022). Considering different indices should allow to better account for possible effects other than the simple climatic factor that could have affected the deposition of clay minerals in the studied area, thus strengthening the interpretation of the mineralogical and geochemical signals.

Geochemical data have also been incorporated into four provenance plots (Figure 5.2). For details about weathering indices and provenance studies, see the paper here reported in the Chapter 5.

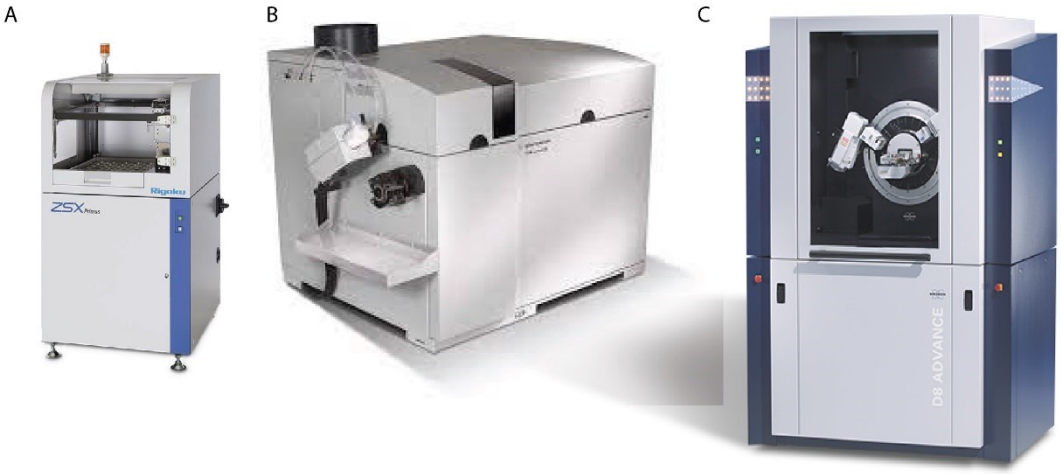

Figure 3.1: Instruments used for this project. A) XRF spectrometer for major and minor elements determination (Rigaku ZSX PrimusII XRF spectrometer). B) ICP-MS for trace elements (Agilent 7700e ICP-MS). C) X-Ray Powder Diffractometer for mineralogical analyses (Bruker D8 Advance DaVinci X-ray powder diffractometer).

3.2 MINERALOGICAL ANALYSES

Mineralogy of the samples was determined by qualitative and quantitative analysis by combination of a Bruker D8 Advance DaVinci X-ray powder diffractometer (Fig. 3.1c - laboratories of the University of Ferrara) equipped with a fast detector (LynxEye – XE) and X-ray Cu tube as radiation source. The Rietveld refinements have been calculated by the software Profex (v. 5.0.2 - Döbelin et al., 2015 – Fig. 3.2). Random powders of the total sample ("bulk") are prepared for qualitative determination of non-clay minerals and for quantitative analysis, while for the correct identification of clay minerals, oriented mounts of the finest fraction are required. Details and data are reported in Chapters 5 and 7. For bulk mineralogical analysis, the powders were further ground until an almost impalpable powder was obtained, which was loaded onto the sample holder base by the side-loading procedure to minimize the preferential orientation phenomenon. This requires that the sample chamber is partially kept covered by a slide; the powder is gradually inserted into the sample holder through the space left by the slide. The slide is slid gently after each addition of powder, until the holder is completely filled. The surface of the sample should be as smooth, homogeneous and uniform as possible; without voids and/or irregularities. The samples thus prepared can then be analyzed by powder X-ray diffractometer. From the intensity and position of the peaks visible on the resulting diffractogram, it is possible to identify at a preliminary level the clay minerals present and already accurately the other phases, as previously stated. The identification of the former is already not as accurate because the reflections of some clay minerals, such as kaolinite [001] and chlorite [002], concur and overlap on the intensities recorded in the low-angle 2θ region.

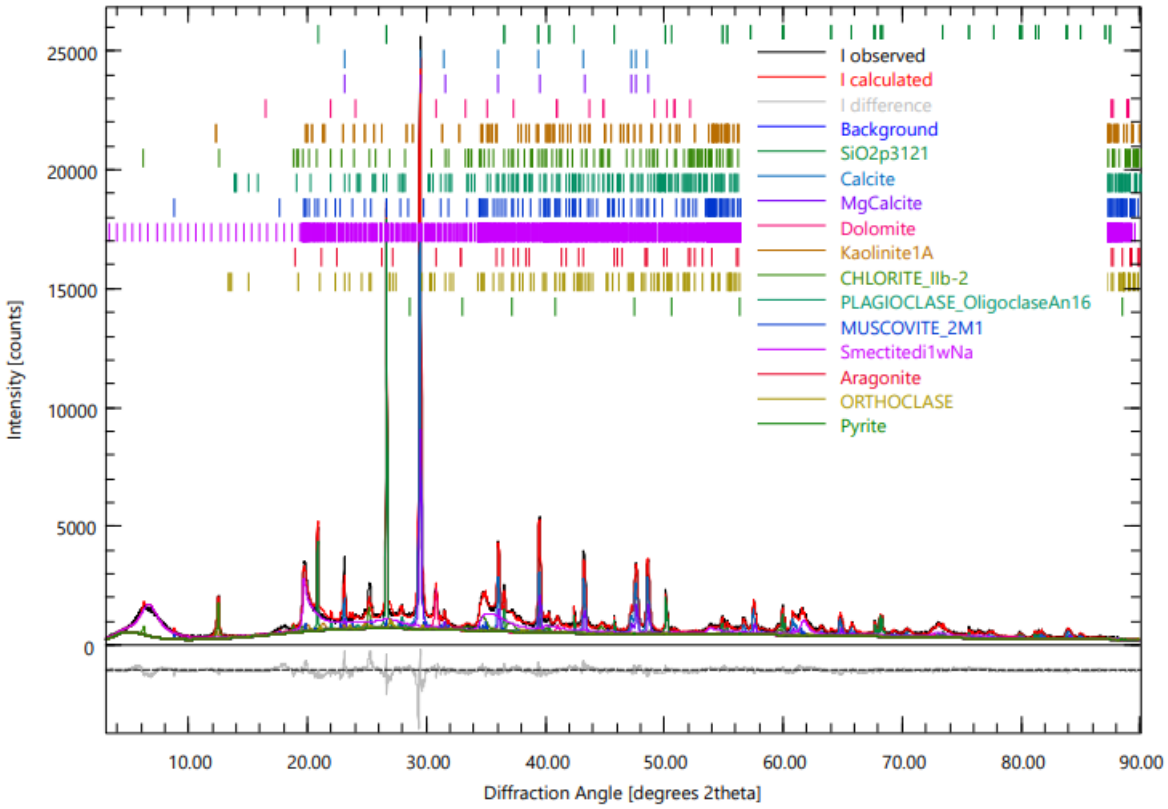

Figure 3.2: Example of Rietveld refinement using Profex v. 5.0.2 on sample MTR21 (Alpe di Specie mb).

To achieve a more accurate identification of clay minerals and especially for discrimination between kaolinite and chlorite, XRD patterns were also collected on oriented mounts of the clay enriched fine fraction <2μm prepared following the procedure for qualitative determination of clay minerals established by USGS (https://pubs.usgs.gov/of/2001/of01-041/htmldocs/methods.htm). It consists of an initial decantation step that allows the separation of clays from silt. A powder aliquot is put into a bottle filled with distilled water and labelled with 0 and 5-cm depths. Since the samples analyzed were found to be very rich in clays, deflocculant was added. The bottle once closed is shaken vigorously and left at a fixed temperature of 22 degrees for 3 hours and 24 minutes. This time is derived from Stokes' law and is the time required to allow the decantation (at that temperature) of granules larger than two Microns and only the finer fraction to remain in suspension within the first 5 cm of the bottle.

Then, 20 ml of supernatant particulate are withdrawn by a syringe and filtered through millipore apparatus connected to a vacuum pump (Fig. 3.3). After filtration, a thin film of isoriented particles remains deposited on the millipore filter (diameter 0.8μm) (Fig. 3.3), which is rapidly transferred to a zero-background slide which is XRD-analyzed. After this first analysis, the isoriented samples are left exposed to ethylene glycol vapors at 60°C overnight (Fig. 3.4) and then again XRD-analyzed. Finally, the protocol involves a final heat treatment of the same samples, at 550°C for one hour, then are analyzed one last time by XRD. The results are three diffractograms for each sample: one of the isoriented sample; one of the glycolated sample; and the third of the post-heat treatment sample. Each diffractogram will show collapses, intensifications or peak shifts consequent to the treatment that they have undergone. The combination of diffractograms allows the recognition and thus the unambiguous qualitative determination of each clay mineral contained within the samples.

Figure 3.3: Millipore filtration apparatus, with detail of the thin film of clays deposited on the filter.

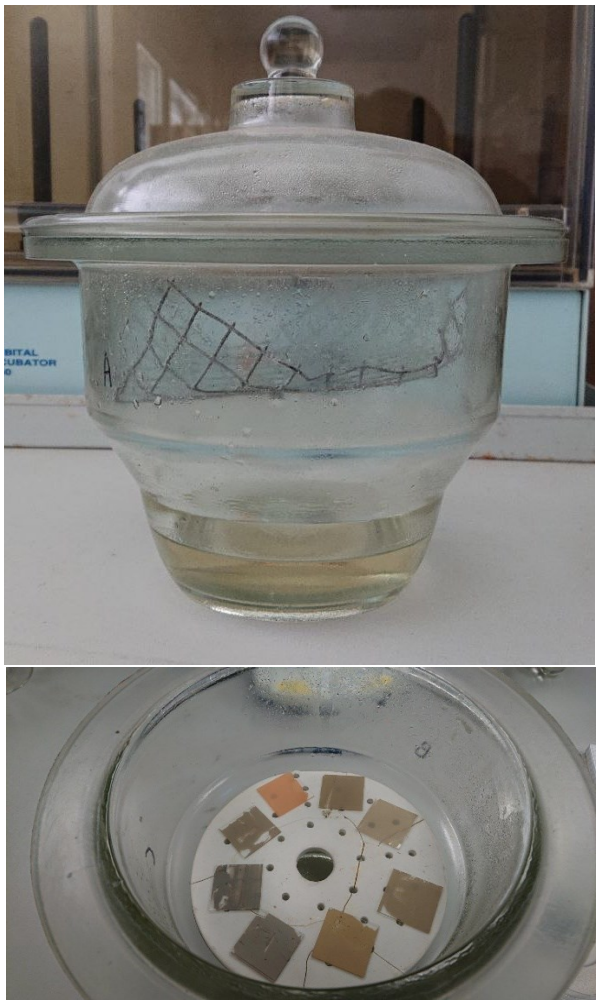

Figure 3.4: Glicolator, with samples in the picture below.

3.2.1 VALIDATION OF QUANTITATIVE MINERALOGICAL DATA

The method that was used to evaluate the quality of the quantitative mineralogical analysis resulting from Rietveld refinement was the calcimetric analysis. This test was conducted only on samples from the Milieres section taken as an example (Heiligkreuz Fm, Alpe di Specie mb - series MI20). Refer to Chapter 8 and Table 8.1 for detailed results.

Calcimetry by Gas-volumetric method is based on the possibility of measuring the volume of CO_2 that is developed by the reaction of carbonate with hydrochloric acid (HCl), from the reaction:

$(X)CO_3 + 2\ HCl = (X)Cl_2 + H_2O + CO_2$

The volume of carbon dioxide, measured in a confined system is thus proportional to the amount of carbonate present in the rock or sediment analyzed. The resulting amount of calcium carbonate was compared with the sum of carbonates calculated by the Rietveld method. Comparable values between carbonates determined by the two methods would be an evidence of robustness of the resulting quantitative mineralogical data and thus that the refining procedure was set up correctly. In other words, it means that it is possible to take the calculated quantities as representative of the real quantities present within the samples.

The sedimentology laboratory of the Department of Physics and Earth Sciences at the University of Ferrara is equipped with a digital calcimeter, which was used for these analyses (Fig. 3.5).

After calibrating the digital calcimeter by performing an analysis with analytical Calcium Carbonate (purity greater than 99.9%), a specific amount of powdered sample (0.500 g) is placed in a bottle with a leakproof cap, then 5 ml of HCl is also placed in a test tube that must be placed inside the same bottle containing the sample, making sure that the acid does not immediately come into contact with the sample.

Once the cap is closed and the command Start Analysis is given, the bottle is tilted to make the acid come into contact with the sample and thus begin the reaction. The bottle must be shaken for at least 30 seconds. At the end of each of the 3 programmed time intervals, the instrument shows the relative percentages of carbonate measured. The first measurement, obtained after the first-time interval of 60 s, corresponds to the $CaCO_3$ content, while subsequent measurements, if greater than the first, show the presence of carbonates other than calcium (e.g., dolomite).

Figure 3.5: Digital calcimeter of the Laboratory of Sedimentology. Department of Physics and Earth Sciences, University of Ferrara

4 WEATHERING INDICES AND CLAY MINERALS AS PALEOCLIMATIC PROXIES

In this project, geochemical and mineralogical data are critically analyzed and interpreted (see Chapter 5). Particular attention is given to evaluate the origin of mineralogical species (climatic or not) and the paleoclimatic significance of each weathering index. Indeed, not all clay minerals have paleoclimatic significance as well as not all weathering indices are suitable for every sample, due to restrictions depending on geochemical composition (Thiry, 2000; Setti et al., 2004; Ehrmann et al., 2005; Buggle et al., 2011; Garzanti et al., 2014; Dinis et al., 2020) This critical evaluation of the data is crucial to avoid paleoclimatic misinterpretations, especially when working on fossil record. Nevertheless, often happens that weathering indices resulting values are taken "at face value" for paleoclimatic interpretation (e.g., Zhang et al., 2021). In the following paragraphs, explanations about the use of weathering indices and clay minerals in paleoclimatic reconstructions are provided, with a particular focus on factors which can bias paleoclimatic interpretations of these proxies. Finally, Paragraph 4.2 summarizes other previous studies dealing with weathering and/or clay minerals applied to the CPE.

4.1 WEATHERING INDICES

Weathering indices are considered paleoclimate proxies because they quantify the chemical weathering undergone by a certain sample. In fact, indices are equations that consider the amount of elements that tend to mobilize when the rock undergoes chemical weathering, normalized for an element considered immobile, usually aluminium. Usually a warmer, wetter climate is characterized by stronger chemical weathering. Increased weathering results in a depletion of mobile elements, thus reflected by an increase or decrease in the value of the weathering index, depending on whether the mobile elements are in the denominator or numerator within the equation, respectively.

Two phenomena which can bias the indices are related to respectively K_2O and CaO. K-metasomatism and illitization are two common transformation phenomena respectively of kaolinite or smectite into illite, which can alter the original content of K_2O within the samples (Buggle et al., 2011; Dinis et al., 2020b). All indices do not consider total CaO as resulting from XRF analysis but CaO*, that is only the CaO incorporated in non-carbonate minerals (McLennan, 1993). However, this is a mathematical correction that does not guarantee that only non-carbonate CaO is really considered, especially in cases of moderate weathering (McLennan et al., 1993; Buggle et al, 2011), as it is the case for samples in the present study. In addition, some authors suggest that samples with large amounts of carbonates (i.e., low in non-carbonate minerals) may give biased or insignificant results for Chemical Index of Alteration (CIA) or similar weathering indices (Goldberg and Humayum, 2010; Buggle et al., 2011).

4.2 CLAY MINERALS

Clay minerals are weathering products par excellence. The persistence of a climatic regime leads the weathering of a parent mineral (for example feldspars), allowing clay minerals formation. Their use as paleoclimatic proxies is based on an assumption deriving from the observation of the modern distribution of clays across different climatic areas (Chamely, 1989). For example, chlorite and illite are generally formed in arid climates, while kaolinite and smectite form under humid conditions and mixed-layer phases (including smectite) witness intervals of high seasonality (Fursich et al., 2005).

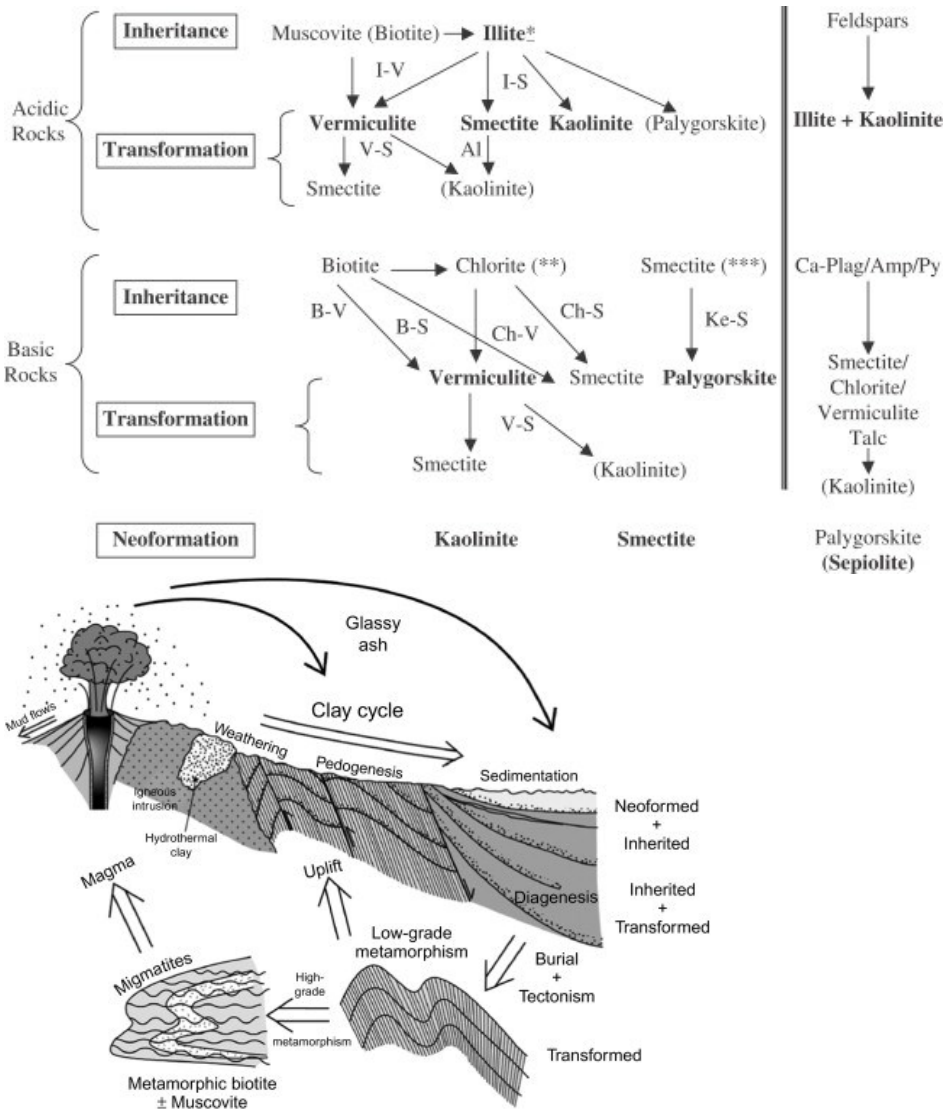

Figure 4.1: Mechanisms of clay minerals formation. From Galán, and Ferrell. (2013).

Changes in temperature, precipitation and in general atmospheric agents are decisive in the genesis of modern clays, but when studying the fossil record, other factors must be taken into consideration: variations in the source area and transport (Thiry, 2000); under the same hydro/aero-dynamic energy, segregation could play an important role; relatively coarser clay components tend to concentrate in areas more proximal to the coastline, while finer species, like illite-smectite mixed layer (I/S), are carried to more distal areas (Dera et al., 2009; Rostasi et al., 2011). In addition, the persistence or change of in situ conditions of the depositional environment; the rate of soil erosion vs. the rate of clay soil formation; intense diagenesis (i.e., illitization of smectite) can favor the transformation of one clay mineral into another. (Lanson and Meunier, 1995; Lanson et al., 2002; Dera et al., 2009; Srodon et al., 2014). Without adequately considering all these factors, the risk is to interpret the data extrapolated from the analysis of the clays in a solely climatic way: the derived paleoclimatic information could be therefore be distorted, as the contribution of the climate to the final

mineralogical association might be overestimated (Thiry, 2000; Setti et al., 2004; Ehrmann et al., 2005).

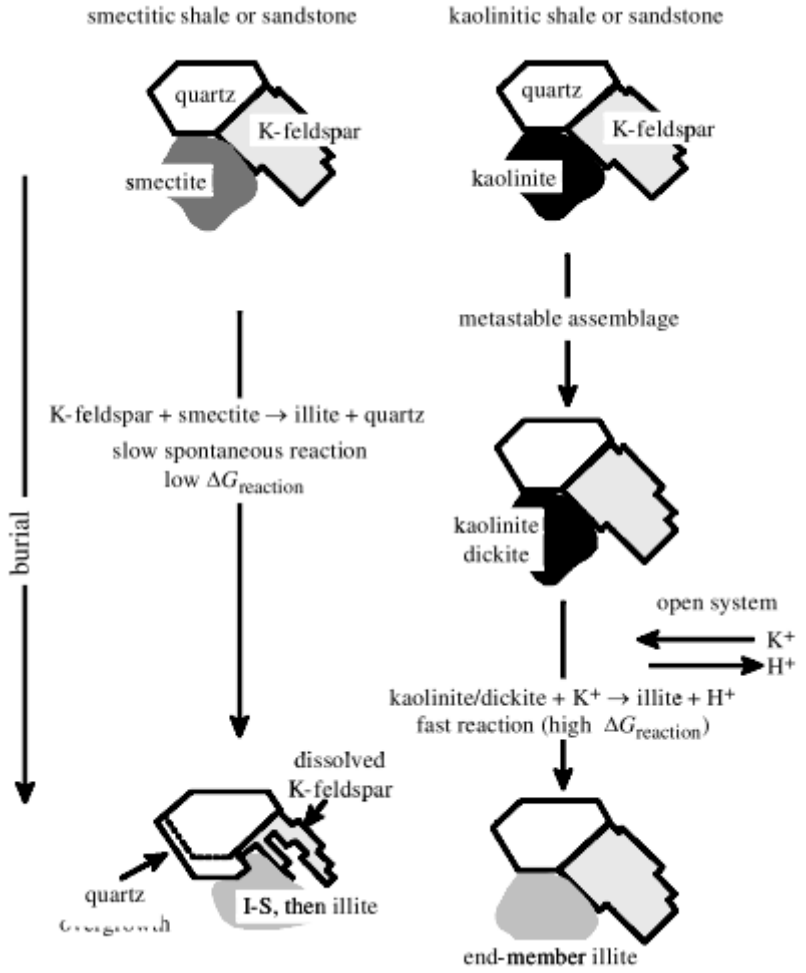

Figure 4.2: Phases of Illitization (from Lanson et al., 2002).

4.3 OTHER PALEOCLIMATIC STUDIES APPLYING WEATHERING INDICES AND CLAY MINERALS ANALYSIS TO THE CPE

Weathering indices and/or clay minerals have already been utilized as paleoclimatic proxies by other studies dealing with the CPE from other regions and from different depositional environments. Noteworthy, the very first idea of a warm humid event in the Carnian rose observing a kaolinite/illite increase in the terrestrial successions of the UK (Simms and Ruffell, 1989 – Figure 4.3).

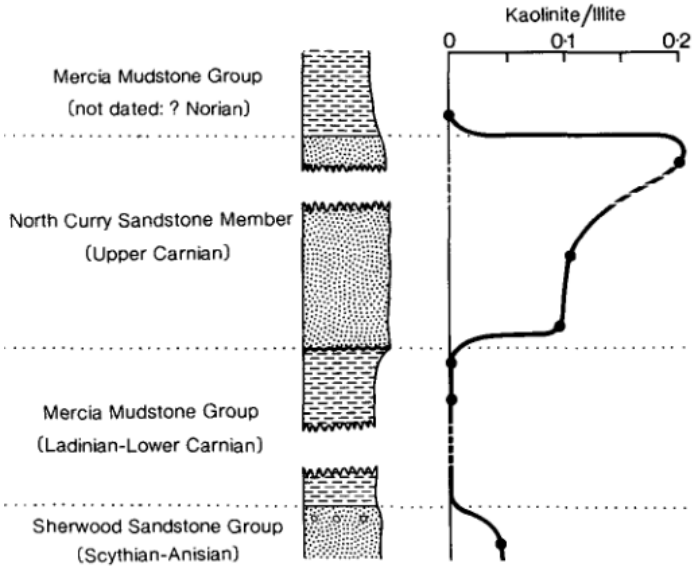

Figure 4.3: The peak in Kaolinite/Illite ratio recognized by Simms and Ruffell (1989) in UK, which was at the base of the idea of the CPE.

However, a succession related to a depositional setting similar to the Dolomites has been investigated only later, by Rostási et al. (2011). They provided quantitative clay minerals analyses form the Transdanubian Range (TDR) succession, while Baranyi et al. (2019b) successively improved those data studying palynological assemblages and using alpha weathering indices (α^{Al}_{i}) formulated by Garzanti et al. (2013). These alpha-indices are ratios between the concentration of mobile elements and the Al concentration (immobile element) obtained from samples, and then compared to those known from the upper continental crust (UCC) (Baranyi et al., 2019b).

Rostási et al. (2011) applied paleoclimatic studies on boreholes and found a first increase in clay content inside the Füred Limestone, where clay fraction is dominated by illite, mixed-layer illite/smectite and chlorite without kaolinite (Figure 4.4); these features are index of arid climate. The clay assemblage upward changes in the succession, within the Veszpém Marls Fm, where the content of kaolinite increases. The first peak of clay content set inside the Füred Limestone suggests a backdating of the onset of the CPE in Transdanubian Range, but the appearance and further enrichment in kaolinite inside the Veszprém Marls (Julian 2) coincides with the proper climate shift towards humid conditions (Rostási et al., 2011).

Palynological analysis indicates a shift towards hygrophytic elements in the Julian 2 (Csicsó Marl Mb). The increase in the hygrophytic forms is also partially coincident with an increase of α-values. This indicates strong continental runoff and more humid climate in the lower part of the Veszprém Formation (Baranyi et al., 2019b). These data agree with the enhanced kaolinite content recorded along the Veszprém Fm by Rostási et al. (2011). The wetter conditions in the Julian 2 are periodically interrupted by shorter periods of drier climate marked by the deposition of carbonates and breccias which interfinger the marly units (Baranyi et al., 2019b). Another humid episode is highlighted in the late Julian 2 by a second peak of hygrophytes species, but a contemporaneous decrease in kaolinite content (Rostási et al., 2011) and the weathering indices might suggest an interval of stronger seasonality. Finally, a return to xerophytic associations is reported during the Tuvalian (Baranyi et al., 2019b).

Rostási et al. (2011) and Baranyi et al. (2019) focused only on the Veszprem Marls, which represents the syn-CPE interval. Their dataset is unfortunately lacking pre- and post-CPE

interval, and it is therefore impossible to highlight variations related to the climatic episode comparing the missed background and subsequent conditions.

In the Inuyama area, central Japan, a deep marine cherty succession named “Section R”, encompassing the CPE- coeval beds, has been investigated by Nakada et al., 2014. A clay minerals association change from the middle of Section R (corresponding in time to the Julian-Tuvalian boundary – age determination by conodont and radiolarian integrated biostratigraphy) has been recorded: moving upward though the Unit 2, chlorite decreases and then slightly increases in the middle portion of the Unit 3, and then gradually decreases again within the upper part of Unit 3, until chlorite disappears. It eventually returns within the upper Unit 6 (Nakada et al., 2014). Conversely, smectite content is detected from the middle Unit 3 to the lower part of Unit 5 (i.e., late Julian-early Tuvalian – Nakada et al., 2014). Mineralogical data from Unit 2 to the middle part of Unit 3 (early to middle Julian) have been interpreted as witnessing the pre-CPE dry climatic conditions. The following sudden disappearance of chlorite and the presence of smectite observed from upper part of Unit 3 to the lower part of Unit 5 (late Julian-early Tuvalian) could be instead related to more humid climate and enhanced rainfall, thus corresponding to the CPE time interval. Finally, the re-appearance of chlorite into the upper portion of Unit 6 (upper Tuvalian) reflects the return to a dry climate similar to pre-CPE conditions.

In the Carnian marginal marine sequence of the Jameson Land Basin (Greenland), Decou et al. (2017) recorded a sharp but short-lived peak in the K/I ratio from the Gråklint Beds (Fig. 4.4), testifying a transient humification period interrupting evaporitic deposition (Andrews et al., 2014). Even though the Authors support the thesis of a connection with the CPE, they also point out that heavy mineral data indicate a simultaneous change in source. This likely might has influenced the observed clay mineralogy.

In continental settings, some paleoclimatic studies have been developed on Manuel Fm, which crops out in Iberia. Some of these works focused on sedimentology, dealing with facies evolution and paleosols (Arche and López-Gómez, 2014; López-Gómez et al., 2017; Barrenechea et al., 2018). Barrenechea et al. (2018) provided also mineralogical analyses from the same succession. All these studies agree by suggesting that the Manuel Fm. was deposited under humid climatic conditions, especially regarding the subunit K2.2. In fact, Barrenechea et al. (2018) noticed that the palaeosols preserved in subunits K2.1 and K2.2 show hydromorphic features, but the younger subunit displays in its lower part a different type of paleosoil: gleysol, which means a higher quantity of water. Even the study provided by López-Gómez et al. (2017) witnessed a more energetic fluvial setting for subunit K 2.2. Moreover, mineralogical analyses by Barrenechea et al. (2018) point out the absence of gypsum and dolomite, an increase in kaolinite and a concomitant fall in orthoclase and albite contents in subunits K2.1 and 2.2. From the upper part of subunit K2.2 the same Authors reported a shift towards more arid conditions (as before the deposition of Manuel Fm.): carbonate pedotypes are present, while orthoclase and albite contents recover, and kaolinite diminishes in the K2.3 subunit. However, Barrenechea et al. 2018 stated that no data suggest rainfalls during the CPE in eastern Iberia. Nevertheless, all the aforementioned publications relate the more humid features of the Manuel Fm. to the CPE.

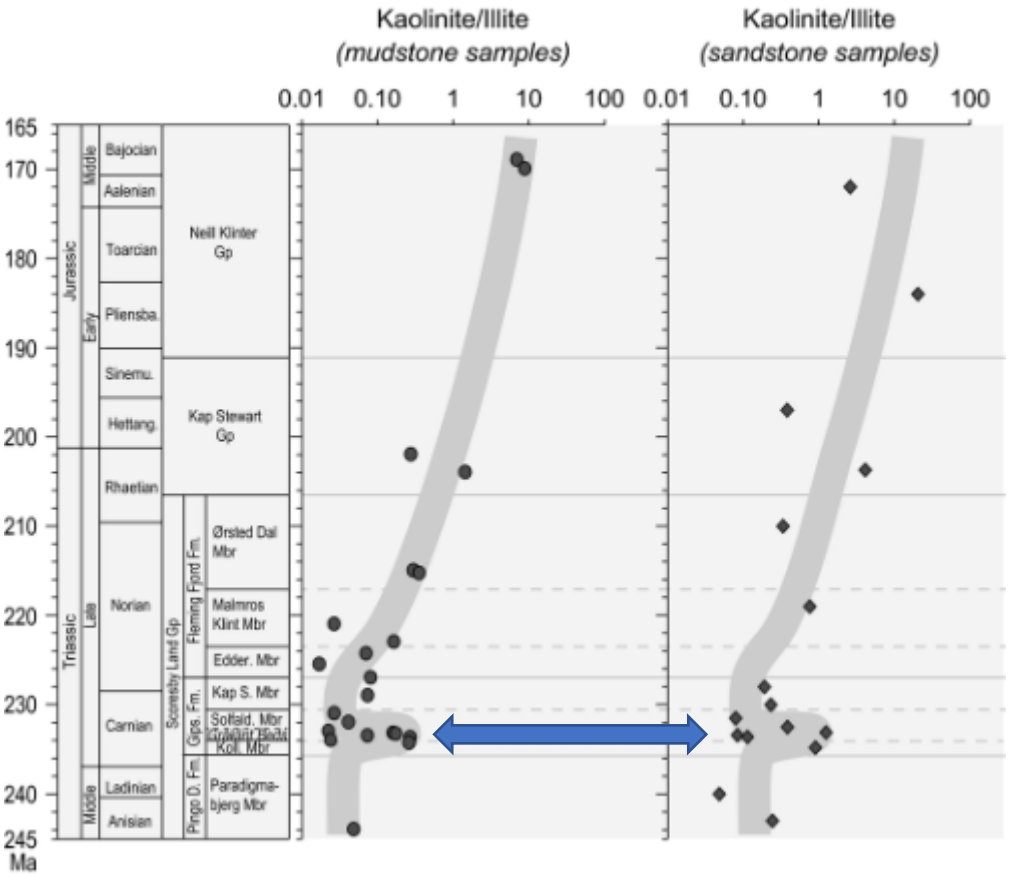

Figure 4.4: The Kaolinite/Illite peak recognized within the Gipsdalen Fm (Jameson Land Basin – Greenland) both in mudstrone and sandstone samples (Greenland), interpreted as CPE-related. Modified from Decou et al. (2017).

Rodrigues et al. (2019) applied XRD, SEM and IR Spectroscopy analyses to the clay fraction of the fluvial Santa Maria Formation in Brazil. The unit results to be sharply dominated by Illite and I/S mixed layers, indicating semi-arid to arid climatic conditions. Also Horn et al. (2018) suggested the same conditions for most of the Santa Maria Fm., considering the CIA values, varying from 2 to 3 along the succession. Nevertheless, at the base of the Candelária Sequence, they observed an interruption of loess deposition, a shift in sedimentary facies from eolian to fluvio-deltaic and a peak in aquatic/semi-aquatic species. Thus, the Authors pointed out that there was a temporary increase in humidity, followed by a return to the pre-existing, definitely, arid conditions, at the top of the Candelária Sequence. Horn et al. (2018) related this rather humid interval to the CPE.

Mancuso et al. (2020) analyzed sedimentology and clay mineralogy of the Ischigualasto-Villa Unión Basin in Argentina. Their study displays evidence of two humid events within Chañares and Los Rastros formations. The former is set prior to 236.1±0.6 Ma, thus it has been linked to the Ladinian humid event, while the latter (within the Los Rastros Fm) is consistent with the CPE (Mancuso et al., 2020). Particularly, a dominance of smectite, I/S mixed-layer with only 15% illite and kaolinite. is recorded, witnessing enhanced seasonality and weathering, and therefore more humid conditions. Moreover, facies representing deltaic and lacustrine environments with coal horizons and without evaporites suggest a wetter climate for the Los Rastros Fm (Mancuso et al., 2020).

A lacustrine environment characterizes also the Carnian of the Ordos Basin (North China). Here Zhang et al. (2021) conducted geochemical and mineralogical analysis focused on clay minerals. Their data show higher chemical weathering (with increases of CIA_{corr} index), increase of I/S but generally low stable kaolinite values in an interval that they correlated to

the CPE (Fig. 4.5). However, the age attribution of the different members of the Yangchang Fm is still debated. The same interval analyzed by Zhang et al. (2021) has been related by other authors (e.g., Jin et al., 2021) to the Ladinian, and it is possible that recorded clay minerals variation reflects local changes in climate circulation and humidity.

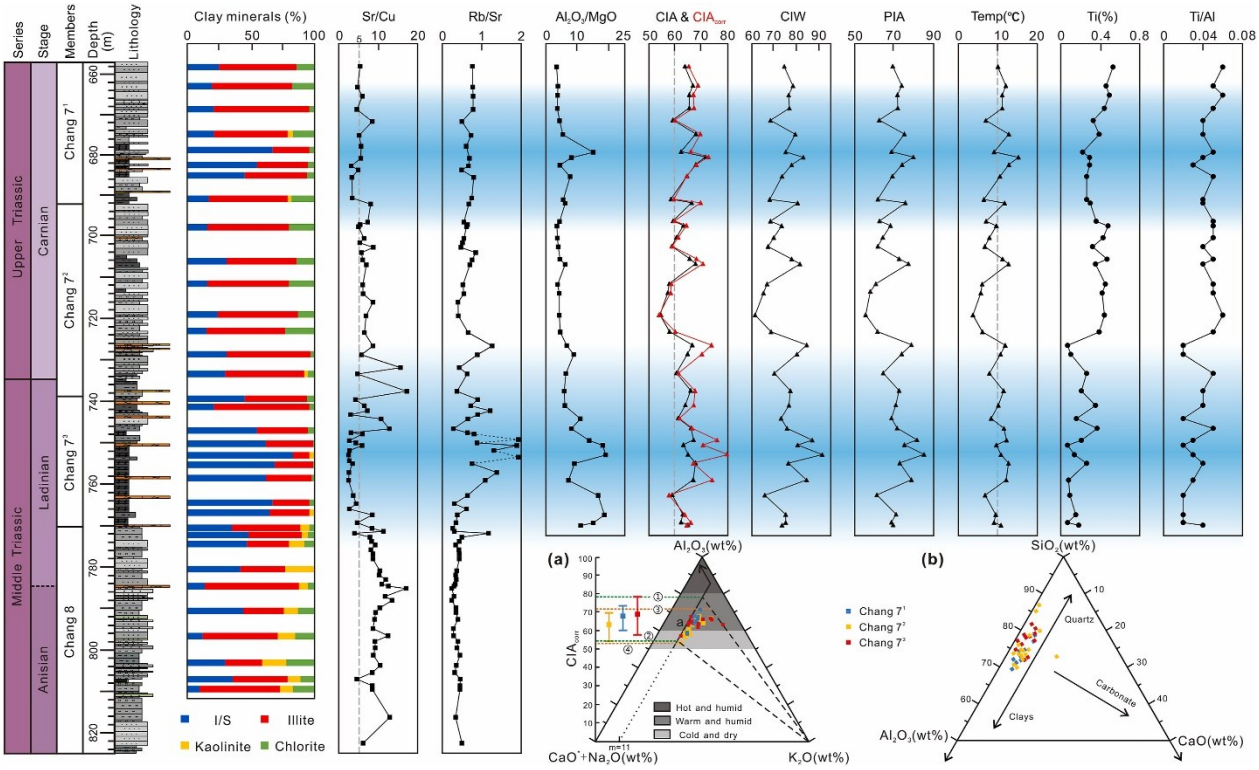

Figure 4.5: Mineralogical and weathering indices analyses provided by Zhang et al. (2021) on lacustrine facies of Ordos Basin (China). Humidification during Ladinian and Carnian are evident by the blue bands highlighting the increase of I/S and the increasing trend of the weathering indices.

5 WEATHERING AND SEA LEVEL CONTROL ON SILICICLASTIC DEPOSITION DURING THE CARNIAN PLUVIAL EPISODE (SOUTHERN ALPS, ITALY)

Research article published on ***Palaeogeography, Palaeoclimatology, Palaeoecology*** *http://dx.doi.org/10.1016/j.palaeo.2023.111495*

Matteo Pecorari[1], Marcello Caggiati[1], Jacopo Dal Corso[2,1], Giuseppe Cruciani[1], Fabio Tateo[3], Daoliang Chu[2], Piero Gianolla[1]

[1] Department of Physics and Earth Science, University of Ferrara, Ferrara, Italy

[2] State Key Laboratory of Biogeology and Environmental Geology, China University of Geosciences, Wuhan, China

[3] Institute of Geosciences and Earth Resources, National Research Council of Italy (CNR), Padova, Italy

*Corresponding author: matteo.pecorari@unife.it

5.1 ABSTRACT

A higher precipitation regime during the early Late Triassic Carnian Pluvial Episode (CPE; 232-234 Ma) in many marine basins is evidenced by thick siliciclastic deposits, which are coeval with C-cycle perturbations and global warming. However, the mechanisms driving higher siliciclastic deposition are still not fully explored and could be linked to different effects of the climate change on depositional environments. Here, we present the first major, minor and trace elements, and mineralogical data from fine-grained sediments across the CPE in the Dolomites (Southern Alps, Western Tethys). Combining weathering indices (CPA and Rb/K_2O), and qualitative and quantitative mineralogical analysis, we recognize two main phases during the CPE. Pre-CPE conditions show no significant weathering variations and some peaks of clay minerals referable to the weathering of Ladinian igneous material. The first C-isotope excursion of the CPE is coincident with an increase of CPA, Rb/K_2O and kaolinite, with no change in the sediment-source and depositional setting, that indicate an enhancement of chemical weathering and confirm a shift to more humid conditions at the onset of the CPE. Such a signal from the Dolomites can be correlated with other similar observations from marine and terrestrial settings worldwide. After this first phase, a major sea level fall, probably linked to aquifer-eustasy and/or limno-eustatism, and following important transgression led to the erosion and recycling of older rocks marked by a decoupling of CPA and Rb/K_2O and a substantial increase of K-feldspar from older volcanic rocks. The eustatic signal overwhelmed the humid climatic signal that is inferred by independent palynological and paleosol data within the same interval. After the CPE, data show high physical weathering under arid climate. Our results are compatible with the general view that the CPE was linked to injections of volcanic CO_2 from Large Igneous Province activity and consequent global warming and enhanced hydrological cycle, which first intensified rock chemical weathering at the onset of the CPE, then promoted higher storage of freshwater on land and a substantial increase of erosion and transport of unweathered material into the basins of the western Tethys that were rapidly infilled.

5.2 INTRODUCTION

The Carnian Pluvial Episode (CPE) is a global environmental and biological change that occurred during the early Late Triassic (Carnian, ca. 232-234 Ma; Simms and Ruffell, 1989; Dal Corso et al., 2020). The CPE was marked by strong enhancements of the hydrological cycle, and by profound changes in global depositional settings (e.g., Simms and Ruffell, 1989; Dal Corso et al., 2012, 2015, 2018, 2020, 2022; Ruffell et al., 2016; Sun et al., 2016; Baranyi et al., 2019; Lu et al., 2021; Jin et al., 2020, 2022; Zhang et al., 2022). The CPE has

been linked to the emplacement of the Wrangellia Large Igneous Province (LIP; e.g., Furin et al., 2006; Dal Corso et al., 2012) and consequent injections of volcanic CO_2 into the atmosphere–ocean system as evidenced by multiple negative C-isotope excursions (NCIEs) that are recorded in different depositional environments by marine and terrestrial organic matter, and marine carbonates (Dal Corso et al., 2012, 2015, 2018, 2020, 2022; Sun et al., 2016, 2019; Mueller et al., 2016; Miller et al., 2017; Jin et al., 2018, 2019; Baranyi et al., 2019; Fu et al., 2020; Lu et al., 2021; Zhang et al., 2022). Being the C-isotope changes isochronous global events, the CPE can be defined as the interval within the first and the last recorded NCIE (Fig. 1).

In tropical marine settings, the onset of the CPE (first NCIE or NCIE-1; Fig. 5.1B) is often characterized by an increase of siliciclastic input into the basins, which is interpreted as the evidence of higher rainfall (and terrestrial runoff) linked to the C-cycle perturbation (e.g., Dal Corso et al., 2015, 2018), as also shown by modeling (Dal Corso et al., 2022). This feature is particularly evident in basins where pre-CPE sedimentation was mainly carbonatic. For example, in the Transdanubian Range (Hungary), the deposition of the hemipelagic Füred Limestone was interrupted by the arrival of the terrigenous Veszprem Marls within the interval containing the NCIE-1 (e.g., Haas et al., 2012; Dal Corso et al., 2015). In the Northern Calcareous Alps (Austria), the mudstones of the Göstling Mb and overlying shales of Reingraben Fm interrupted the deposition of the deep-water nodular carbonates of the Reifling Fm during the NCIE-1 (e.g., Dal Corso et al., 2015; 2018; Mueller et al., 2016). Similarly, the nodular limestone (Zhuganpo Fm) deposited in the deep-water Nanpanjiang Basin (South China) was interrupted by black shales (Wayao Fm) in coincidence with the onset of the CPE (e.g., Sun et al., 2016).

In other tropical marine successions with a prevalent terrigenous sedimentation also before the CPE, such an increase of siliciclastic is less clearly visible. In the Dolomites, which is a reference area for the study of the CPE, the basinal succession across its onset is continuously terrigenous – mixed terrigenous/carbonatic (San Cassiano Fm and Heiligkreuz Fm; Fig. 5.1B). While in this basinal succession the evidence of a crisis of the carbonate factories (Cassian Platforms) at the NCIE-1 is evident in a sharp change in the composition of shallow water carbonates (Stefani et al., 2010; Dal Corso et al., 2015; Gattolin et al., 2015; Jin et al., 2020), a coeval sedimentological evidence of an intensification of the hydrological cycle is less obvious, and it actually appears to have been slightly delayed, being clearly visible only higher up in the sequence with the deposition of coarse siliciclastic material between the first and the second NCIEs, and the formation of "humid" paleosols containing amber (Borca mb; Breda et al., 2009). Moreover, the interplay of different processes (e.g., sea-level changes and changes in the sediment-source) could have controlled siliciclastic sedimentation during different phases of the CPE (cf., Franz et al., 2014; Gattolin et al., 2015; Jin et al., 2022). These observations are possible in the Dolomites because of increasing resolution of the stratigraphy and extensive detailed geological mapping of the entire area in recent years, which have led to the definition of the Alpe di Specie Mb of the Heiligkreuz Fm (Gianolla et al., 2018), and better understanding of the Carnian stratigraphy (e.g., Russo et al., 1991; De Zanche et al., 1993; Keim et al., 2001, 2006; Neri et al., 2007; Stefani et al., 2010; Roghi et al., 2010; Dal Corso et al., 2012, 2015, 2018; Gattolin et al., 2015).

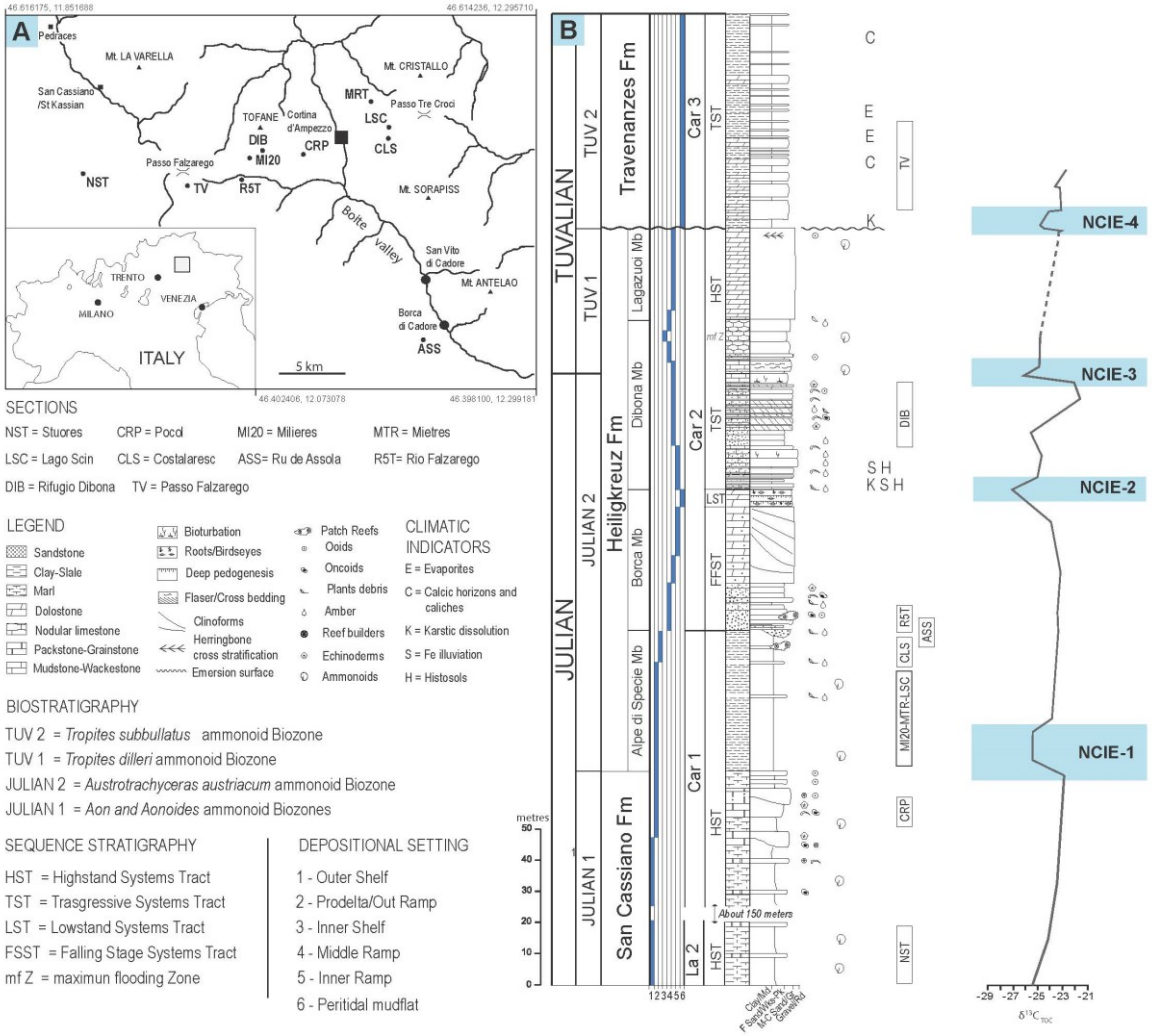

Figure 5.1: A) Geographical setting of the studied area and location of the sampled sections. B) Composite stratigraphic log with climatic indicators, biostratigraphy, sequence stratigraphy and inferred depositional environments, stratigraphic position of the sampled sub-sections, and composite $\delta^{13}C_{TOC}$ curve from Dal Corso et al. (2018). Depositional sequences are after Stefani et al. (2010) and Gianolla et al. (2021).

In order to disentangle the sequence of events that controlled siliciclastic sedimentation in the marginal tropical marine mixed depositional settings of the Dolomites in response to the CPE C-cycle perturbations and intensifications of the hydrological cycle, we here investigated the geochemistry and mineralogy of fine-grained sediments (siltstones and marlstones). Chemical weathering indices and clay mineralogy can reveal paleoclimate changes in the sediment source areas. Clay minerals in sedimentary rocks are thought to reflect the climate of the source area during their genesis, an assumption deriving from the observation of the modern distribution of clays across different climatic areas (Chamley, 1989). For example, chlorite and illite are generally formed in arid climates, while kaolinite and smectite form under humid conditions and mixed-layer phases witness intervals of high seasonality. However, several factors, such as source changes, erosion and transport or/and diagenesis (Lanson and Meunier, 1995; Lanson et al., 2002; Dera et al., 2009; Srodon et al., 2014) affect clay mineral formation in soils and their final deposition in the basin, complicating the use of clay mineral assemblages to reconstruct past climatic conditions (Thiry, 2000). Some studies focused on changes in clay mineralogy and weathering indices during the CPE in terrestrial (fluvio-deltaic-lacustrine settings; Decou et al., 2017; Barrenechea et al., 2018; Mancuso et al., 2020; Zhang et al., 2021), outer shelf (Rostási et al., 2011; Baranyi et al., 2019) and deep marine depositional environments (Nakada et al.,

2014). In general, these studies showed an increase or predominance of kaolinite and/or illite-smectite within clay mineral assemblages and an increase in weathering intensity within the CPE interval. However, these climatic proxies have been applied mainly on terrestrial successions and, in marine sequences, are from within the CPE interval without comparison with background conditions (Rostási et al., 2011, Baranyi et al., 2019), or include only mineralogical data from pelagic sequences, not linked to C-isotope changes (Nakada et al., 2014). By coupling geochemistry and mineralogy, and existing knowledge on basin and climatic evolution across the CPE in the Dolomites, our new dataset shed new light on the main processes that drove sediment-input changes during the CPE.

5.3 GEOLOGICAL SETTING

The study area encompasses the central and eastern Dolomites in northern Italy (Fig. 5.1A). This region is part of the Southern Alps, a south verging thrust-and-fold belt that originated during the Alpine Orogeny by the collision of the Adria and European plates. The typical pop-up structure of the Dolomites (Castellarin and Cantelli, 2000) preserved the region from strong deformation and allowed the original depositional geometries to be maintained.

The analyzed stratigraphic interval (Fig. 5.1B) starts with the San Cassiano Fm (Fürsich and Wendt, 1977; Masetti et al., 1991; Neri et al., 2007), which covers a time span ranging from the *Daxatina canadensis* ammonoid Biozone up to the *Trachyceras aonoides* ammonoid Biozone (Mietto et al., 2012). The San Cassiano Fm consists of an alternation of marls, marly limestones and dark pelites with biocalcarenites, grey oolithic calcarenites and hybrid arenites (Fig. 5.1B), indicating a mixed siliciclastic and carbonate source. The carbonate component derived from sediments of neritic origin and carbonate muds from nearby flat-topped microbial carbonate platforms (Cassian Dolomite; De Zanche et al., 1993; Keim et al., 2006; Stefani et al., 2010; Preto et al., 2017, 2021). The terrigenous component derived from the erosion of the southern shoreline (cf. Viel, 1979; Brusca et al., 1981; Cati et al., 1980; Pisa et al., 1980; De Zanche et al., 1993; Gianolla et al., 1998a) and, especially for the lower part of the unit, of Ladinian volcanics from the Western Dolomites (Ulrichs, 1974; Castellarin and Perri, 1982; De Zanche and Gianolla, 1995; Broglio Loriga et al., 1999). The sediment supply from the western volcanic source progressively decreased due to the growth of a system of attached carbonate platforms, which sealed the previous volcanic area (Keim et al., 2001; Stefani et al., 2010; Mietto et al., 2012).

The progressive input of sediment from the siliciclastic shoreline combined with relative sea-level oscillations and the lateral progradation of carbonate platforms, resulted in the almost complete filling of the basin (Bosellini et al., 2003; Keim et al., 2006; Roghi et al., 2010; Stefani et al., 2010; Gattolin et al., 2015) and basinal deposition persisted only in restricted areas (e.g., Heiligkreuz Hospiz Basin; Cortina-Misurina-Alpe di Specie Basin; Keim et al., 2001, 2006; Neri et al., 2007; Gattolin et al., 2013; Gianolla et al., 2018; Hausmann et al., 2021). The Heiligkreuz Fm deposited during the CPE (Dürrenstein Fm auctorum; *Austrotrachyceras austriacum-Tropites dilleri* ammonoid zones; Dal Corso et al., 2015, 2018) and records the filling and flattening phases of the previous paleogeography that was characterized by highly articulated platform-basin systems. Therefore, the Heiligkreuz Fm displays a great variety of facies depending on the presence of restricted basins, and proximity to emerged land and carbonate platforms (Pisa et al., 1980; De Zanche et al., 1993; Gianolla et al., 1998a; Keim et al., 2001, 2006; Stefani et al., 2010; Gattolin et al., 2013, 2015). The unit also records a widespread carbonate platform crisis, with a change towards a ramp system that is recorded in the whole Tethys (Keim et al., 2001, 2006; Stefani et al.,

2010; Jin et al., 2020). The Heiligkreuz Fm is divided into five members (Neri et al., 2007; Gianolla et al., 2018). The lowermost member is named Alpe di Specie (member A in Russo et al., 1991; Keim et al., 2006; Tosti et al., 2014; Fedares Mb in Brandner et al., 2007; lithozone L-2 in Gattolin et al., 2015) and is constituted by dark, sometimes marly pelites and argillites, with local, rare arenaceous or micritic intercalations and, in the uppermost part, patch reefs (Russo et al., 1991; Gattolin et al., 2015). The succession passes upward to the Borca Mb, which is composed by sandstones, para-conglomerates, hybrid arenites, oolitic calcarenites, limestones intercalated to pelites and marls, with the siliciclastic component decreasing upward while peritidal inner ramp carbonates increase (dolostones with marly or clayey interbeds; Breda et al., 2009; Gattolin et al., 2015). The Borca Mb records a drop in the relative sea-level (Gattolin et al., 2015), as documented by forced regressive deposits in its lower part, while the upper part is characterized by a regressive, shallowing-upward sequence of terrigenous-carbonate deposits (Preto and Hinnov, 2003; Neri et al., 2007). Noteworthy, carbonates of the uppermost part of Borca Mb are capped by paleosols and horizons rich in amber (Gianolla et al., 1998b; Roghi et al., 2006, 2022). The following Dibona Mb is characterized by cross-bedded hybrid arenites alternating to pelites and conglomerates with clasts of metamorphic and carbonate origin. The member shows a transgressive trend, and is marked in the upper part by sandstones, arenaceous dolostones and oolitic-bioclastic limestones followed by hemipelagic carbonates (Preto and Hinnov, 2003; Breda et al., 2009). Coals and plant remains have been found in the lowermost Dibona Mb, together with marine and terrestrial bioclasts, vertebrate remains, and amber droplets (Gianolla et al., 1998b; Breda et al., 2009; Roghi et al., 2006, 2022). The subsequent Lagazuoi Mb consists of doloarenites, hybrid arenites, arenites with carbonate-cement and cross-stratified oolitic-bioclastic calcarenites. The coarse fractions prevail, although fine calcarenites and pelites also locally crop out. The Heiligkreuz Fm is capped by a subaerial unconformity, locally marked by breccias and karstification (Keim and Brandner, 2001; Neri et al., 2007; Breda and Preto, 2011).

The here studied Carnian succession of the Dolomites ends with the lower part of the Travenanzes Fm (*Tropites subbullatus* ammonoid Biozone; Dal Corso et al., 2018). It is constituted by microcrystalline dolostones and light gray or whitish dolomicrites sometimes crystalline, alternating with interbeds of black to greenish dolomicrites and dolomitic pelites, followed by irregular alternations of red and green pelites, thin-laminated dolostones and gypsum levels (Breda and Preto, 2011). The outstanding outcrops of the study region allow very good reading of the geometries and organization of the depositional systems (shoreline trajectories and facies stacking patterns) that, associated with a high-resolution bio-chronostratigraphic framework, make the Dolomites one of the reference areas for the definition and calibration of the Triassic depositional sequences (Gianolla and Jacquin, 1998; Hardenbol et al., 1998; Haq, 2018). Therefore, the considered interval can be framed within a well-established sequence stratigraphy (Brandner, 1984; De Zanche et al., 1993; Rüffer and Zühlke, 1995; Gianolla et al., 1998a; Neri and Stefani, 1998; Stefani et al., 2010; Mietto et al., 2012; Gattolin et al., 2015). In the investigated interval four 3rd order-depositional sequences are present (Fig. 5.1), namely the La 2, Car 1, Car 2 and Car 3 (Gianolla et al., 1998a; Stefani et al., 2010; Gattolin et al., 2013; Gianolla et al., 2021).

5.4 MATERIALS AND METHODS

We built a composite section, enclosing pre-, syn- and post-CPE interval, from previously measured sections, namely Stuores/Wiesen (NST), Pocol (CRP), Milieres (MI20), Lago Scin (LSC), Mietres (MTR), Costalaresc (CLS), Ru Assola (ASS), Rio Falzarego (R5T), Dibona (DIB), Passo Falzarego (TV) (Fig. 5.1). Sampling was focused only on pelitic layers to

ensure lithological uniformity and therefore comparability of the data, the resolution of which is inevitably lower in coarser or carbonatic intervals (Fig. 5.1). We took 85 samples covering the upper part of the San Cassiano Fm, the Alpe di Specie, Borca and Dibona members of the Heiligkreuz Fm, and the Travenanzes Fm. All sections underwent low diagenetic alteration, as testified by the color alteration index of conodonts (between 1 and 1.5) and biomarkers (Dal Corso et al., 2012, 2018).

All geochemical analyses were carried out at the Wuhan Sample-Solution Analytical Technology Co., Ltd. (China). Samples were very finely ground and have been prepared as pearls. The sample pre-treatment of whole rock major element analysis was made by melting method. The flux was a mixture of lithium tetraborate, lithium metaborate and lithium fluoride (45:10:5 ratio). Ammonium nitrate and lithium bromide were used as oxidant and release agent respectively. The melting temperature was 1050°C and the melting time was 15min. The quantitative determination of major and minor elements was performed and analyzed using an X-ray fluorescence (XRF spectrometer) Rigaku ZSX PrimusII XRF spectrometer. Samples were compared to standard material (rock standard samples: GBW07105-11) and resulting data were corrected by theoretical α coefficient method. The relative standard deviation (RSD) was less than 2%.

INDEX	EQUATION	RESPONSE TO WEATHERING INCREASING	REFERENCES
WIP (Weathering Index of Parker)	$(CaO^*/0.7 + 2Na_2O/0.35 + 2K_2O/0.25 + MgO/0.9) \times 100$	Decreases	Parker (1970)
CIA (Chemical Index of Alteration)	$Al_2O_3/(Al_2O_3 + K_2O + CaO^* + Na_2O) \times 100$	Increases	Nesbitt and Young (1982)
CIW (Chemical Index of Weathering)	$Al_2O_3/(Al_2O_3 + CaO + Na_2O) \times 100$	Increases	Harnois (1988)
PIA (Plagioclase Index of Alteration)	$(Al_2O_3-K_2O)/(Al_2O_3 + K_2O + Na_2O) \times 100$	Increases	Fedo et al. (1995)
CPA (Chemical Proxy of Alteration)	$Al_2O_3/(Al_2O_3 + Na_2O) \times 100$	Increases	Cullers (2000); Buggle et al. (2011)
CIX (modified CIA)	$Al_2O_3/(Al_2O_3 + K_2O + Na_2O) \times 100$	Increases	Garzanti et al. (2014)
WI (Weathering Index)	$(Na+K_2O)/Ti$	Decreases	Summa et al. (2018)
Rb/K_2O	Rb/K_2O	Increases	Nesbitt et al. (1980); McLennan et al. (1990); Plank & Langmuir (1998); Dinelli & Lucchini (1999)

Table 5.1: Weathering indices selected for this work, with relative equations and trends with respect to increasing weathering conditions.

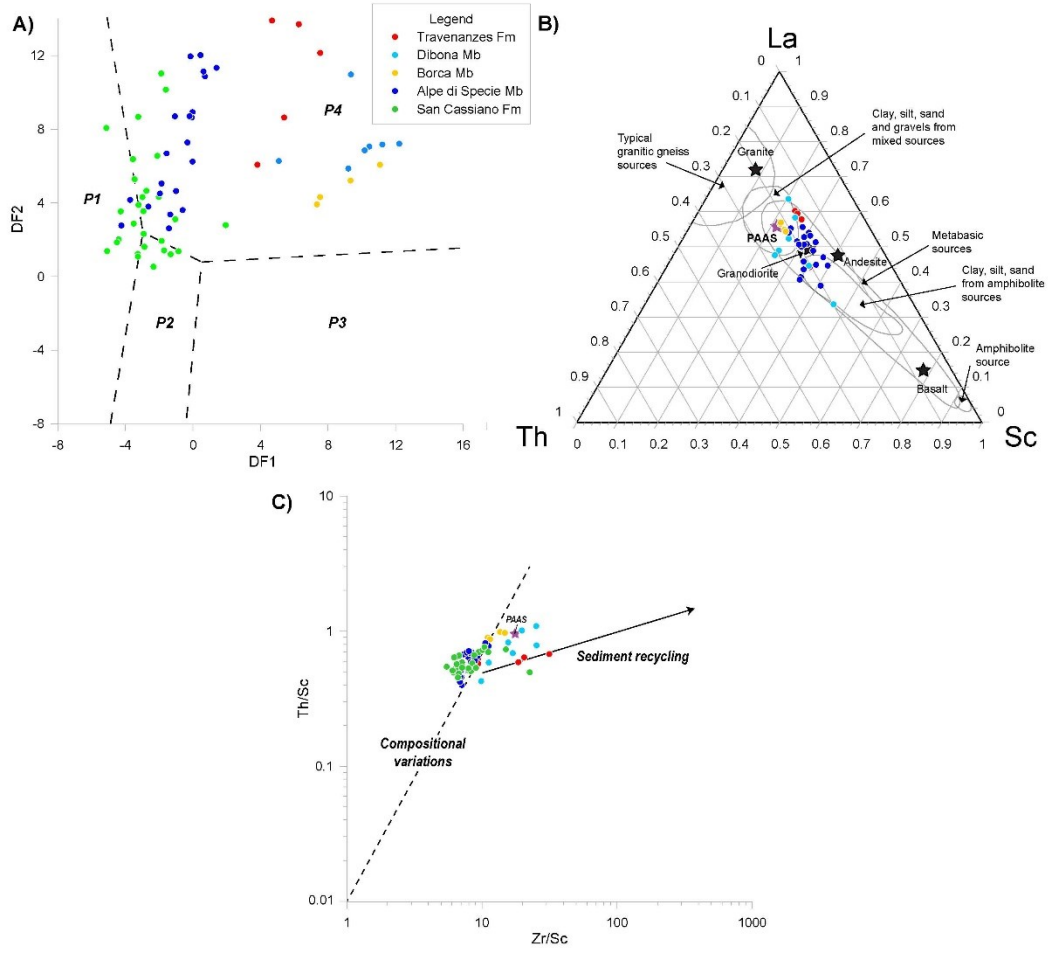

Figure 5.2: A) Discriminant Function (DF2 vs. DF1) plot, corrected for samples rich in CaO, and normalized for Al_2O_3 (after Roser and Korsch, 1988). Discriminant Function 1 = (30.638 TiO_2/Al_2O_3) + (-12.541 Fe_2O_3/Al_2O_3) + (7.329 MgO/Al_2O_3) + 12.031 Na_2O/Al_2O_3) + (35.402 K_2O/Al_2O_3) + (−6.382); Discriminant Function 2 = (56.500 TiO_2/Al_2O_3) + (-10.879 Fe_2O_3/Al_2O_3) + (30.875 MgO/Al_2O_3) + (-5.404 Na_2O/Al_2O_3) + (11.112 K_2O/Al_2O_3) + (-3.890). B) Triangular plot La-Th-Sc which identifies differences in the source of sediments (modified after Bhatia and Crook, 1986; Perri et al., 2012). C) Th/Sc vs. Zr/Sc plot used to evaluate sediment recycling indicated by Zr enrichment (modified after McLennan et al., 1993).

Trace elements have been determined using an Agilent 7700e Inductively Coupled Plasma Mass Spectrometer (ICP-MS). Sample preparation followed the procedure described in Zhang et al. (2012): after the digestion of 50 mg of powdered sample with 200mg of NH_4HF_2 powder into in a 7-mL screw-top PFA vial, the product was heated at 230°C for 3 hours. After cooling, 2 ml of HNO_3 were added and the vials were re-heated at 160°C on a hot plate for 1h. The vials were then opened, helping liquid evaporation. Then, 1 ml of HNO_3, 1ml of Milli-Q water and 1ml of 1 μg g−1 in internal standard solution were added to the residue, which after was heated at 120°C for 6 hours. Finally, the obtained solution was transferred to a polyethylene bottle and diluted with a 2% concentrated solution of HNO_3.

The measured geochemical data have been used to calculate the Chemical Index of Alteration (CIA; Nesbitt and Young, 1982), the Chemical Index of Weathering (CIW; Harnois 1988), the modified CIA (CIX; Garzanti et al., 2014), the Weathering Index of Parker (WIP; Parker, 1970), the Plagioclase Index of Alteration (PIA; Fedo et al., 1995), the Chemical Proxy of Alteration (CPA; Cullers, 2000; Buggle et al., 2011), Rb/K_2O, Weathering Index (WI; (Nesbitt et al., 1980; McLennan et al., 1990; Plank and Langmuir, 1998; Dinelli and Lucchini, 1999; Summa et al., 2018) summarized in Table 5.1. We also used the Discriminant Function (DF2 vs. DF1) plot (Fig. 5.2a), corrected for samples rich in

CaO, and normalized for Al_2O_3 (Roser and Korsch, 1988). Also, the triangular plot La-Th-Sc of Bhatia and Crook (1986) (Fig. 5.2b) is helpful to identify differences in the source of sediments. We used the Th/Sc vs. Zr/Sc diagram (Fig. 5.2c) to evaluate the possible degree of sediment recycling within our samples (McLennan et al., 1993).

For the mineralogical analysis, samples were first dried in air at 60°C overnight. Then, aliquots of each sample were powdered using an agate mortar and pestle. Qualitative and quantitative mineral phase analyses were performed by X-Ray Diffraction (XRD). For the XRD mineralogy, powdered samples were analyzed both as random powders of the total sample ("bulk" – 67 samples) and as oriented aggregate mounts of the finest fraction (29 samples) using a Bruker D8 Advance DaVinci diffractometer at the University of Ferrara (Italy). Diffraction patterns of the "bulks" were processed by the Rietveld method, as implemented into the Profex v. 5.0.2 (Doebelin and Kleeberg, 2015), which encompassed a full-profile fitting procedure in which the refined scale factors, assigned to each modeled crystalline phase occurring in the sample, provided the phase quantitative analyses (QPA) of all phases. The total contents of carbonates obtained from the XRD-QPA-Rietveld method were double checked for a sample sub-set (MI-20) with digital calcimetry. Between the two methods, relative differences in total carbonate contents of less than 10% were found, supporting the reliability of the XRD-QPA-Rietveld results. To achieve a more accurate identification and discrimination between kaolinite and chlorite, XRD patterns were also collected, for selected 29 samples, on oriented aggregate mounts of the clay enriched fine fraction <2 μm prepared by decantation and millipore filtration. Each prepared sample was measured after three treatments (air drying, ethylene glycol solvation for 8 hours, and heating to 550 °C for an hour) and the three powder patterns were compared according to the USGS guidelines (Open-File Report 01-041). Given the 7Å (002) line of chlorite overlapping the (001) line of kaolinite and the broad peak of I/S hiding the 14 Å (001) line of chlorite, the presence of chlorite was assessed from the oriented mount XRD pattern after heating at 550°C which is expected to remove kaolinite but not chlorite. No acid treatments have been applied to the samples before analysis.

5.5 RESULTS

5.5.1 GEOCHEMICAL ANALYSES AND WEATHERING INDICES

XRF analysis shows considerable variations in CaO wt.% along the composite succession, which parallel carbonate content fluctuations shown by quantitative mineralogical analyses (Fig. 5.3). CaO is relatively high (reaching a maximum value of 41%) in the samples from San Cassiano Fm to Alpe di Specie Mb (NST, MTR, LSC, MI20), while it subsequently drops drastically in the samples from Borca (R5T; 1.13%) and Dibona (DIB; 0.11%) Mbs. CaO values, while remaining low, increase slightly, albeit irregularly in the Travenanzes Fm (average value: 4.86%; maximum value: 10.6%). It is important to emphasize that such fluctuations in CaO content are shown by samples of the same rock type. K_2O content, in general, displays an almost symmetrical reverse trend respect to CaO (Fig. 3). K_2O remains low (not exceeding 2.5 wt.%) up to Borca Mb (R5T) and then increase significantly in the units above, reaching its maximum values of 7-8 wt.% in the Dibona Mb, and slightly decreasing in the samples from the Travenanzes Fm (4.5 wt.%). CIA, CIW, WIP, CIX, PIA, WI do not display significant trends along the whole stratigraphic succession (See Supplementary Materials). All the samples show CIA values indicative of intermediate chemical weathering (according to the threshold values of Fedo et al., 1995). CIA, CIX, PIA, and WIP show comparable values from San Cassiano Fm to Borca Mb, showing a sharp

change (decrease for CIA, CIX, PIA and increase for the WIP) in the Dibona Mb and Travenanzes Fm. Despite some fluctuation within each unit, the CIW trend does not show any meaningful variation. The WI is affected by excessive fluctuations within each unit and it biases the recognition of a clear, reliable weathering trend. CPA and Rb/K_2O display similar trends along the succession (Fig. 5.3): both of them increase from the San Cassiano Fm to the Alpe di Specie Mb. From the Borca Mb the CPA remains higher while Rb/K_2O decreases. For each unit and index, the minimum, maximum and average values are reported in Table 5.2 (see supplementary material for complete data).

In the diagram of Roser and Korsch (1988), samples from the San Cassiano Fm and Alpe di Specie Mb both fall near the P1 field, while Borca Mb, Dibona Mb and Travenanzes Fm samples fall within the P4 field (Fig. 5.2A). Borca Mb, Dibona Mb and Travenanzes Fm samples also display La-Th-Sc composition closer to the PAAS or towards a "standard" granite (Fig. 5.2B) and on the sediment recycling line of the Th/Sc vs. Zr/Sc diagram (Fig. 5.2C). On the other hand, the Alpe di Specie samples show a distribution between andesite and granodiorite (Fig. 5.2B) and fall on the line of poor recycling, coupled with most of the San Cassiano samples (Fig. 5.2C).

UNIT	CPA			Rb/K_2O			CIA			CIW			CIX			WIP			PIA			WI		
	MIN	*MAX*	*AVER.*	*MIN*	*MAX*	*AVER.*	*MIN*	*MAX*	*AVER.*	*MIN*	*MAX*	*AVER.*	*MIN*	*MAX*	*AVER.*	*MIN*	*MAX*	*AVER.*	*MIN*	*MAX*	*AVER.*	*MIN*	*MAX*	*AVER.*
Travenanzes Fm	95	97	96	20	25	23	67	70	68	90	95	93	69	71	70	54	70	62	42	45	43	4	9	6
Dibona mb	96	98	96	17	23	20	61	72	65	92	96	94	63	73	66	66	81	75	28	47	35	5	10	7
Borca mb	91	97	95	19	22	21	71	83	81	80	95	91	84	86	85	25	31	27	73	76	74	10	11	11
Alpe di Specie mb	89	96	93	35	43	39	64	81	74	80	93	87	67	84	78	15	74	29	38	72	62	3	8	6
San Cassiano Fm	81	89	87	10	32	27	60	85	78	70	95	88	69	87	82	17	56	29	52	76	70	4	7	5

Table 5.2: Minimum (MIN), maximum (MAX) and average (AVER.) values for all calculated weathering indices. CPA (Chemical Proxy of Alteration), CIA (Chemical Index of Alteration, CIW(Chemical Index of Weathering), CIX (modified CIA), WIP (Weathering Index of Parker), PIA (Plagioclase Index of Alteration), WI (Weathering Index) (Parker, 1970; Nesbitt et al., 1980; Nesbitt and Young, 1982; Harnois 1988; McLennan et al., 1990; Fedo et al., 1995; Plank and Langmuir, 1998; Dinelli and Lucchini, 1999; Buggle et al., 2011; Garzanti et al., 2014; Summa et al., 2018).

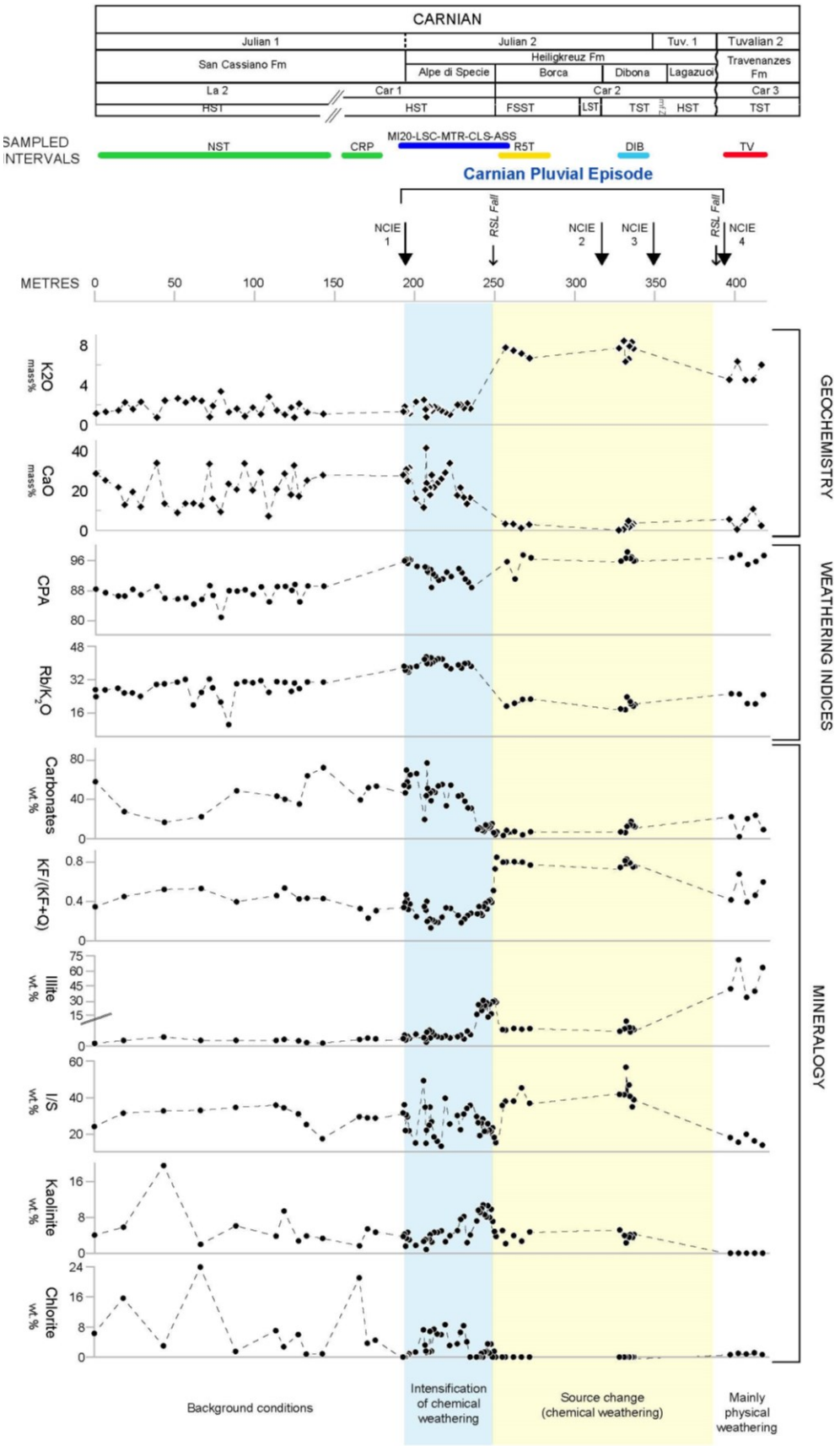

Figure 5.3: Variations of selected weathering indices and minerals along the succession, with interpretation of the recognized phases across the CPE-interval. NCIEs from Dal Corso et al. (2018). Sampled sections and sequence stratigraphy abbreviations as in Fig. 5.1. RSL: Relative Sea Level; CPA: Chemical Proxy of Alteration; KF: K-feldspar; Q: Quartz; I/S: Illite/Smectite mixed-layer.

5.5.2 MINERALOGICAL ANALYSES

The carbonate content is variable through the succession showing fluctuations ranging from a minimum of 1.9% to a maximum of 75.6%. The siliciclastic component, determined by the XRD-QPA-Rietveld method, shows two well defined trends of quartz plus feldspars vs. clay minerals (Fig. 5.4A). The first is a positive correlation which can be related to the enrichment of the siliciclastics compared to the carbonates (Fig. 5.3 and Fig. 5.4A). The second trend displays a negative correlation related to the changing of clay minerals with respect to the tectosilicates within the siliciclastic phases (Fig. 5.4A).

In the San Cassiano Fm, the clay minerals association is composed by Illite/Smectite mixed-layer (I/S), while illite content is low. Kaolinite and chlorite alternate as second and third dominant clay: kaolinite prevails in the samples NST25, NST36, NST43, NST46, NST47; CRP1 and CRP2, while the other samples are richer in chlorite (see supplementary material).

The Alpe di Specie Mb (base of the Heiligkreuz Fm) shows fluctuations in the carbonate content in its lower part (Fig. 5.3; samples MI20, MTR, LSC). The prevailing terrigenous component is mostly represented by clay minerals, whilst quartz averages 10% of the total, and K-feldspar and plagioclase are found in a scarce amount. Among the clay minerals, the dominant species is I/S, and illite is the minor component. Based on the observations of the oriented aggregate mounts, chlorite is not present in all samples, while kaolinite is always present, even if in variable quantities. Noteworthy, when found together, kaolinite and chlorite are in comparable quantities in samples collected from the lower part of the member (Fig. 5.3 and supplementary material).

In the upper part of the Alpe di Specie Mb and in the transitional interval to the Borca Mb data show a sharp decrease in carbonates, the mineralogy of these samples being markedly dominated by siliciclastic phases. We observe a significant increase of K-feldspar, illite (coupled with I/S decrease) and kaolinite within samples CLS and ASS. Samples R5T display the same trend as regards the K-feldspar, but represent an exception for kaolinite and illite whose values return comparable to those of samples collected from the lower member (e.g., MI20). Chlorite is low or completely absent in this part of the succession (Fig. 5.3 and supplementary material). XRD analysis shows the presence of (likely diagenetic) gypsum and jarosite in one sample (ASS9) from the base of the Borca Mb.

Samples from the overlying Dibona Mb are dominated by siliciclastic minerals. If we exclude the small variation of quartz amount among the DIB series samples, all the samples are similarly constituted of clays (50% or more) and K-feldspar (17 to 35 wt.%), while plagioclase is scarce. The dominant clay mineral is I/S, followed by kaolinite and illite, while no chlorite is found (Fig. 5.3 and supplementary material). Noteworthy, the analysis of the oriented aggregate mounts shows that the DIB series samples contain two types of I/S mixed-layer: a smectite-dominated phase similar to that found in the samples from the underlying sequence, and a phase, identified as rectorite, characterized by an ordered distribution of illite and smectite (1:1 ratio) (see supplementary material).

On the whole, samples from the Travenanzes Fm (TV) show an increase in the carbonate content. Samples 2 and 5 represent an exception, recording lower values, while samples 1, 3 and 4 show the highest carbonates content between the TV samples (respectively 22, 20 and 23 wt.%). Dolomite in particular reaches high values within TV1 and TV3 samples respectively 19 and 16.5 wt.%). The TV samples show variable quantities of quartz and K-feldspar (the latter in lower quantities than in the Borca and Dibona Mbs). Plagioclase is still present, but in almost negligible quantities, while clays represent the most abundant constituents. Hematite is present (varying from 0.3 in the TV5 and 1.9 wt.% in TV1), giving

the typical reddish color to the unit. The mineralogical association of the Travenanzes Fm lacks kaolinite, while it is markedly dominated by illite, followed by I/S. Chlorite is present in quantities around 1% (Fig. 5.3 and supplementary material).

5.6 DISCUSSION

The geochemical and mineralogical patterns found in the Carnian succession of the Dolomites allow identifying different phases during the CPE: an increase of chemical weathering at the NCIE-1, and a sediment-source change between the NCIE-1 and 2, which is related to a major sea-level fall and following major transgression (Fig. 5.3). The identification of these phases, which are discussed separately in the following sections, highlight major shifts in the main controls of the sediment geochemical and mineralogical composition that can be linked to global effects of the CPE and consequent profound transformations of the depositional environments.

5.6.1 ONSET OF THE CPE AND INCREASE OF CHEMICAL WEATHERING

Weathering indices CPA and Rb/K_2O from the San Cassiano Fm display values that overall indicate stable chemical weathering and paleoclimatic conditions prior to the onset of the CPE (Fig. 5.3). The content of quartz and feldspars does not change significantly (Fig. 5.4A), whereas an increase in total carbonates (reaching 71%), balanced by corresponding decrease of total clays (down to 22%), is observed between meters 132 and 142 of the composite section (Fig. 5.3 and supplementary materials). The upward increase in carbonates recorded in the San Cassiano Fm can be related to carbonate mud exported by the nearby prograding carbonate platform (HST of La 2 DS, Fig. 5.1B).

A volcanoclastic component in the mudstones of the San Cassiano Fm is evidenced by the presence of chlorite, which here reaches the highest recorded values (NST average 7 wt.% vs. 3 wt.% of MI20; up to 24 wt.% in NST-30). It should be also noted that the occurrence of I/S as the dominant clay mineral in these samples is consistent with the origin from altered volcanic materials. Sediments of volcaniclastic origin, which originated from the erosion of emerged volcanic areas related to volcanism of Ladinian age (Abbas et al., 2018), are indeed found within the San Cassiano Fm as turbiditic beds (Ulrichs 1974; Broglio et al., 1999; Mietto et al., 2012). Erosion and transport of volcanic rocks bring into basins clays that can contaminate and mask the climatic signal (e.g., Meunier, 2005; Velde and Meunier, 2008; Cavalcante, 2021). One data point shows high kaolinite (19,5%) in the lower part of the San Cassiano Fm (Fig. 5.3).

The discriminant function diagram of Roser and Korsch (1988) shows that all the San Cassiano Fm samples fall close to the boundary with igneous products (Fig. 5.4A). This composition is similar to that of the stratigraphically above samples from the Alpe di Specie Mb, suggesting a similar sediment source between the two units. However, an increase of CPA and Rb/K_2O from the San Cassiano Fm (average values, CPA = 87; Rb/K_2O = 27) to the Alpe di Specie Mb (average values, CPA = 92, Rb/K_2O = 40) is observed. This increase suggests intensification of chemical weathering at the onset of the CPE, i.e., in correspondence with the NCIE-1 (Fig. 5.3). Even if the San Cassiano - Alpe di Specie succession is entirely siliciclastic, without substantial evident lithologic changes, CPA and Rb/K_2O show an increase of chemical weathering intensity. Hence, being the source of siliciclastics in San Cassiano Fm and Alpe di Specie Mb constant (Fig. 5.2A and 5.5) and the depositional environment the same, the considered geochemical proxies indicate a

climatic humidification signal, confirming a strong enhancement of the hydrological cycle linked to the initial C-cycle perturbation (e.g., Dal Corso et al., 2022).

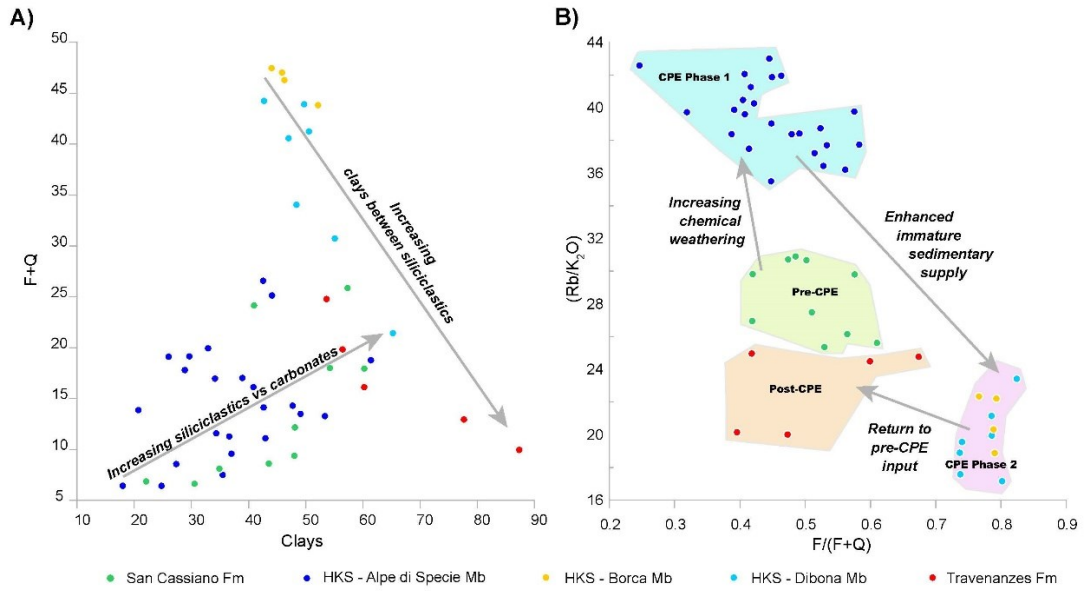

Figure 5.4: A) Comparison graph between feldspars+quartz and clays. The arrows show two clear trends in samples distribution, respectively indicating the proportion between carbonates and siliciclastics and the proportion within the siliciclastics. B) Comparison graph between Rb/K_2O index and non-clays siliciclastic minerals ratio, showing the impact of weathering vs. erosion. Samples distribution sharply highlights the recognized phases across the CPE. Abbreviations: F: Albite+K-feldspar; Q: Quartz. Sampled sections abbreviations as in Fig. 5.1.

The other calculated weathering indices (CIA, CIW, WIP, CIX, PIA, WI) are highly variable throughout this interval and do not show significant trends (see supplementary materials and paragraph 5.5.1). This is likely because CaO and K_2O, which are included in the equations of all these indices (Table 5.1), exhibit large fluctuations in the San Cassiano and Alpe di Specie samples. All those indices do not consider total CaO as resulting from XRF analysis but CaO*, which is only the CaO incorporated in non-carbonate minerals and is calculated using the correction proposed by McLennan (1993). However, this correction does not guarantee that only non-carbonate CaO is considered especially in cases of moderate weathering (McLennan, 1993; Buggle et al, 2011). In addition, some authors suggest that samples with large amounts of carbonates (i.e., low non-carbonate minerals) may give biased values of CIA or similar indices (Cullers, 2000; Goldberg and Humayum, 2010; Buggle et al., 2011; Garzanti and Resentini, 2016). Regarding K_2O fluctuations, it cannot be also excluded the possible effect of K-metasomatism/illitization that could alter the real content of K (Fedo et al., 1995; Goldberg and Humayum, 2010; Buggle et al, 2011; Dai et al., 2022). On the contrary, CPA is more suitable to evaluate chemical weathering of shales rich in carbonates (Cullers 2000), as those analyzed from the Dolomites, because it does not consider CaO and K_2O (Table 5.1) but Al and Na. Moreover, variations of minerals that incorporate Al and Na (clays and feldspars) occurring along our succession, are balanced with each other so they do not affect the whole geochemical content of Al_2O_3 and Na_2O. Rb/K_2O variations are meaningful due to the very strong geochemical affinity between Rb and K.

Mineralogical association does not record changes at the base of the Alpe di Specie Mb (ca. at 192 m in the composite section; Fig. 5.3). This is coherent with similarity in the depositional environment between the basal Alpe di Specie Mb and the upper San Cassiano Fm and indicates a stable sediment source. Mineralogical changes occur higher up within

the Alpe di Specie Mb, at 240 m of our composite record (Fig. 5.3), where we observe a sharp decrease in the amount of carbonates and an increase in non-carbonate minerals (Fig. 5.3). The decrease in carbonates can be explained by the concurrent demise of the nearby high relief carbonate platforms (Cassian Dolomite; Fig. 5.5), and the shift from highly productive microbial to less productive skeletal carbonate factories (Stefani et al., 2010; Dal Corso et al., 2015; Gattolin et al., 2015; Jin et al., 2020). Clays association displays a rise of illite content in the uppermost Alpe di Specie Mb, which could indicate a transient increase of physical weathering (Fursich et al., 2005; Fu et al., 2017). Within the same interval, the kaolinite content increases from < 4% to ca. 12% and the chlorite amount decreases from 7 to 0% (Fig. 5.3). As kaolinite suggest more humid conditions in the terrestrial catchment area, data could appear to indicate a possible relatively short delay between the record of more humid conditions by geochemical indices and mineralogy. However, this delay can be interpreted as due to the time required to weather pristine minerals (e.g., feldspars), transform them into clay minerals, and transport these clays to marine settings. It has been shown that the time gap between the formation of clay minerals and their deposition into marine basins could be from less than 100 kyr up to 1-2 myr (Thiry, 2000.; Dera et al., 2009). Our results seem to confirm such a delay in the order of tens of thousands of years. According to the current stratigraphic framework (e.g., Bernardi et al., 2018; Zhang et al., 2020), the Alpe di Specie Mb (base of the *Austrotrachyceras austriacum* ammonoid Biozone, Julian 1; Fig. 5.1B) likely deposited in less than 100 kyrs.

Our geochemical data agree with those reported from different depositional environments in other localities, confirming a supra-regional increase of chemical weathering at the onset of the CPE. In the deep-marine successions of the Transdanubian Range (Hungary), α weathering indices (i.e., αAl Na, αAl K, αAl Ba as in Garzanti et al., 2013; Baranyi et al., 2019) display a peak in chemical weathering intensity during the NCIE-1, which is synchronous to an increase of hygrophytic sporomorphs indicative of a floristic shift from arid- to more humid-adapted plants (Baranyi et al., 2019). In agreement with palynological and weathering data, mineralogy of the syn-CPE Veszprem Marls of the Transdanubian Range show general high kaolinite contents (on average ca. 16% of the total clay minerals assemblage), with discrete peaks throughout the unit (up to ca. 50% of total clays; Rostási et al., 2011; Baranyi et al., 2019)that are comparable to our increase as recorded in the Alpe di Specie Mb (from a minimum of ca. 4% to a maximum of ca. 20% of the total clay minerals assemblage; Supplementary Material). Unfortunately, in the Transdanubian Range, background (pre-CPE) geochemical and mineralogical values are not available from the carbonatic Füred Limestone Fm (Rostási et al., 2011), and it is therefore not possible to evaluate the actual magnitude of chemical weathering intensification in the Hungarian boreholes. An increase in kaolinite/illite ratio has been observed in the Carnian marginal marine sequence (Gipsdalen Fm) of the Jameson Land Basin (Greenland), which interrupts evaporites' deposition and has been related to the CPE (Andrews et al., 2014; Decou et al., 2017), but the stratigraphic resolution is not higher enough to allow finer correlations with the sections of the Southern Alps. Evidence of higher chemical weathering is recorded in the pelagic sequence of Japan where a smectite spike has been observed (Nakada et al., 2014). On land, kaolinite/illite increases in the successions of the UK, an observation from which the very first idea of a warm humid event in the Carnian arose (Simms and Ruffell, 1989). Barrenechea et al. (2018) reported a decrease in feldspar and plagioclase content coupled with an increase in kaolinite in the Manuel Fm (Stable Meseta, eastern Spain), a sequence of Carnian coarse siliciclastic sediments with paleosols interrupting the deposition of evaporites (Arche and López-Gómez, 2014). Sedimentology and clay mineralogy of the Ischigualasto-Villa Unión Basin (Argentina) display evidence of a more humid interval in

the fluvio-deltaic Los Rastros Fm, with dominance of smectite, I/S with only 15% illite, and kaolinite (Mancuso et al., 2020). Geochemical and mineralogical data from the lacustrine continental setting of the Ordos Basin (North China) show higher chemical weathering (with increases of CIAcorr index), increase of I/S but generally low stable kaolinite values (Zhang et al., 2021). On the other hand, in the fluvial Santa Maria Fm (Parana Basin; Brazil) the mineralogical assemblage is dominated by Illite and I/S mixed layers, indicating semi-arid to arid climatic conditions (Rodrigues et al., 2019), which are confirmed also by low CIA values throughout the whole Middle-Upper Triassic Santa Maria Supersequence (Horn et al., 2018). Nevertheless, Horn and colleagues (2018) also pointed out that, within the same interval, a sharp shift in sedimentary facies from eolian to fluvio-deltaic, and a peak in aquatic and semi-aquatic taxa could indicate a temporary increase in humidity correlatable to the CPE.

Our data, coupled with those from other settings, demonstrate widespread increase in chemical weathering caused by the CPE, although the magnitude of such an increase could have been variable in different localities (e.g., Barrenechea et al., 2018). This is compatible with the currently most accepted general mechanism proposed as the trigger for the CPE. Injection of CO_2 into the atmosphere from Wrangellia LIP activity (e.g., Dal Corso et al., 2020, 2022; Mazaheri-Johari et al., 2021; Lu et al., 2021; Zhao et al., 2022), and subsequent rising temperatures (Trotter et al., 2015; Sun et al., 2016) could lead to a strong enhancement of the hydrological cycle (see, for example, box modeling by Dal Corso et al., 2022) and widespread increase of chemical weathering of rocks on land. Notably, the increase of chemical weathering affects the C-cycle, drawing down CO_2 and resulting in a negative feedback as recorded by the positive C-isotope rebounds following the NCIEs (Fig. 5.1B).

The multiple episodes of hydrological cycle enhancements linked to the NCIEs of the CPE (Dal Corso et al., 2022) would have resulted in discrete chemical weathering intensifications throughout the interval. However, following the NCIE-1, the effects of a huge relative sea level fall and related change of the depositional environment in the Dolomites (Fig. 5.5) were so overwhelming on controlling the sediment supply that, in the study area, they obliterated any other signal, as discussed in the following section.

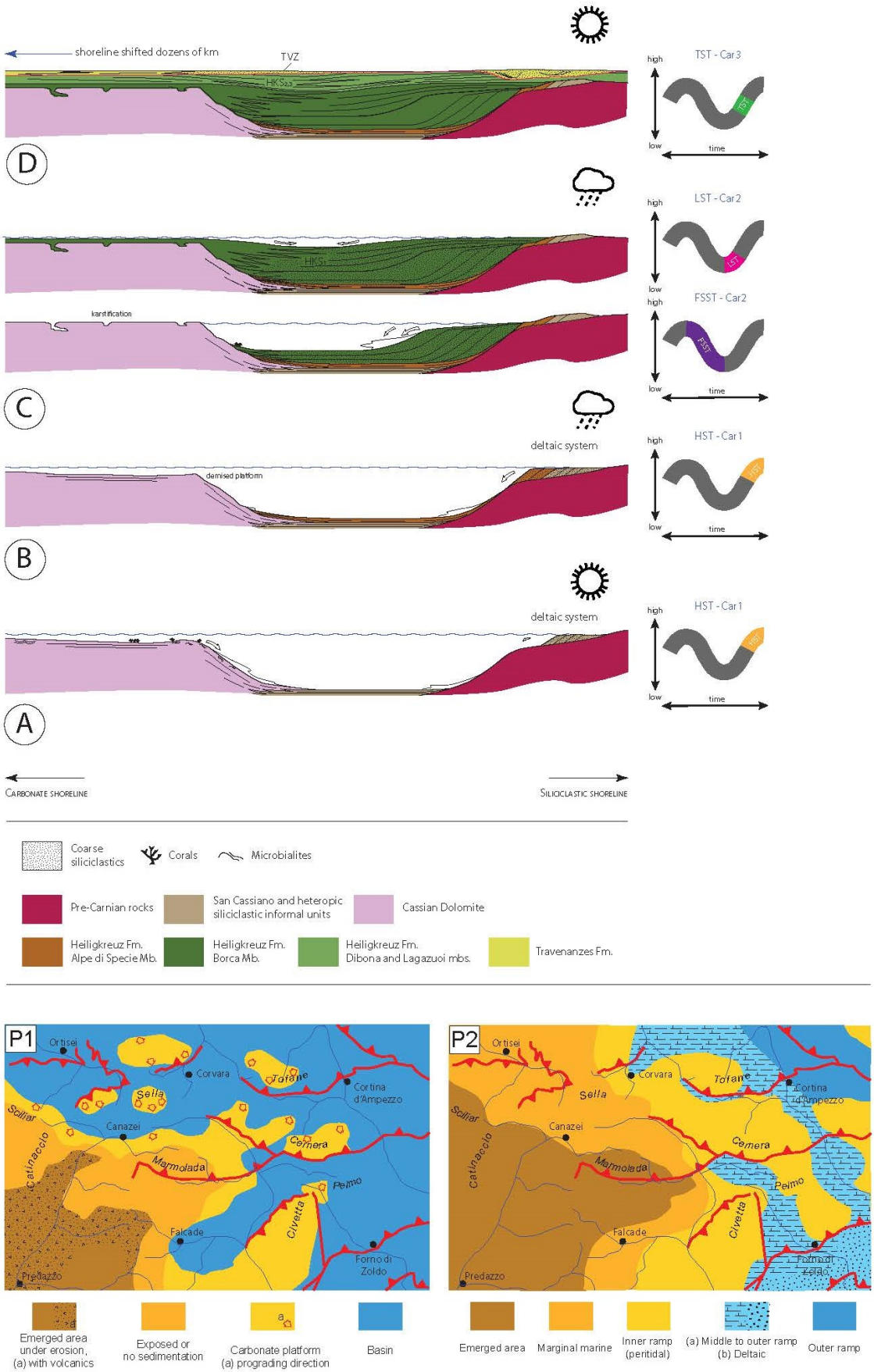

Figure 5.5: Above: schematic geological evolution of the late Carnian succession of the Dolomites, showing the interaction between carbonate and siliciclastic depositional systems, the relative sea-level variations (the corresponding systems tracts are shown on the left) and climate. Below: non palinspastic, paleogeographic scheme of the investigated area during the early Julian (P1) and the late Julian (P2).

5.6.2 SEDIMENT-SOURCE CHANGE AND VARIATIONS IN RELATIVE SEA-LEVEL

At the end of the first phase, i.e., at the boundary between the Alpe di Specie and Borca Mbs, we observe a decoupling in the trends of CPA and Rb/K_2O (Fig. 3): The CPA increases (average value = 95), while Rb/K_2O decreases below pre-CPE values (minimum value = 19; average = 21). This difference persists within the overlying Dibona Mb (average CPA = 96; average Rb/K_2O: 20) and the Travenanzes Fm (average CPA: 96; average Rb/K_2O = 23). The reversal trend exhibited by the Rb/K_2O is coeval to a sharp increase of K-feldspar relative to total terrigenous content (Fig. 5.3). Mineralogy of the Borca and Dibona Mbs is also characterized by an increase in I/S, and a decrease of illite and kaolinite, and very low chlorite (Fig. 5.3). The mineralogical and geochemical changes are stratigraphically synchronous to a relative sea level (RSL) fall in the order of tens of meters, which is clearly recognizable in different basins worldwide and is considered a major eustatic sea-level oscillation (Jin et al., 2022).

In the studied basinal succession, the RSL fall can be identified by the abrupt transition from thin-bedded, fine siliciclastics (mainly pelites) of the Alpe di Specie Mb to the coarse terrigenous (mainly sandstones and conglomerates) sediments of the Borca Mb (Breda et al., 2009; Gattolin et al., 2015), corresponding to the correlative conformity sensu Posamentier and Allen (1999). This major eustatic fall exceeding 75 m in amplitude (Haq, 2018), is much greater than expected under greenhouse conditions, such as those of the Triassic (e.g., Preto et al., 2010). A series of intracontinental rift-basins, which were elongated in a roughly N-S direction and characterized by fluvial sedimentation, developed during the Ladinian – Carnian (Schettino and Turco, 2011; Leleu and Hartley, 2010; Frizon de Lamotte et al., 2015; De Min et al., 2020). In these rift-basins, the depositional environment appears to have changed during the early – late Carnian, with the formation of large deep lakes that is documented globally (Cornet and Olsen, 1990; Mader et al., 2017; Mancuso et al., 2020; Leleu et al., 2016; Lu et al., 2021). These large lacustrine systems could have developed due to the substantial rise in precipitation during the CPE and increased storing of water on land, with some of these basins possibly being endorheic (e.g., McKie et al., 2014; Leleu et al., 2016; Franceschi et al., 2019; Dal Corso et al., 2020). Therefore, the recorded eustatic sea-level fall was likely driven by a variation in freshwater storage, i.e., aquifer-eustasy or limno-eustatism (Wagreich et al., 2014; Wendler et al., 2016; Franceschi et al., 2019; Davies et al., 2020; Sames et al., 2020; Boulila et al., 2021; Jin et al., 2022).

The RSL fall (forced regression) could lead to a rejuvenation of the river systems that were also strengthened by enhanced hydrological cycle. This resulted in the expansion of the catchment area and widespread and strong erosion, increasing the amount of sediment transported to the basins (Fig. 5.4B, 5.5). The following transgression, which is recorded by the Dibona Mb (e.g., Gattolin et al., 2015; Jin et al., 2022), caused wave-ravinement erosion and re-working of the same material (Fig. 5.4B, 5.5). Hence, the studied succession relatively rapidly evolved from an hemipelagic basin – prodelta (San Cassiano Fm and Alpe di Specie Mb), to outer-inner ramp (Borca Mb), then again to tidally-dominated, middle-outer ramp environment (Dibona Mb), and finally to a coastal mudflat with terminal fans (Travenanzes Fm).

These major changes from the San Cassiano Fm and Alpe di Specie Mb to the the Borca Mb, Dibona Mb and Travenanzes Fm are evident in the diagrams presented in Fig.5.2. The La-Th-Sc diagram shows that the samples from Alpe di Specie Mb have values near andesite and granodiorite, while those from Borca Mb, Dibona Mb and Travenanzes Fm fall closer

to the PAAS value representing average upper crustal composition (Perri et al., 2012), and towards a granitic composition (Fig. 5.2B). Moreover, the Th/Sc vs. Zr/Sc (Fig. 5.2C) indicates that the samples from Borca and Dibona Mbs, and Travenanzes Fm are composed of material recycled from older sediments, while the older samples from the San Cassiano Fm and Alpe di Specie Mb show poor recycling (Fig. 5.2B and 5.2C). Hence, the displayed trends suggest that sediments deposited during the RSL fall and transgression (Borca and Dibona Mbs) underwent enhanced recycling (McLennan et al., 1993), which is coherent with our hypothesis of an interplay between eustatic control and higher precipitation on siliciclastic sedimentation in the area.

The high amounts of K-feldspar and the shift of geochemical data towards a granitic composition (Fig. 5.2B) can also be explained by the erosion of Caledonian granites and/or Anisian - Ladinian acid volcanics that were present in the catchment area, and the increase of I/S agrees with immature sediment supply and/or volcanic provenances. Indeed, in the Assunta 1 well from the Adriatic foreland (Gianolla et al., 1998a; Franciosi and Vignolo, 2020), the latest Carnian – Norian Dolomia Principale Fm (Main Dolomite) lies directly on the the Caledonian granites. In the Villaverla well and outcrops from the Vicentinian Prealps (Italy; Gianolla et al., 1998a), the same sequence onlaps the Anisian – Ladinian volcanics. This shows a remarkable erosion on structural highs, linked to the CPE RSL fall and subsequent transgression. Accordingly, while both CPA and Rb/K_2O record variations of weathering intensity in the San Cassiano Fm. – Alpe di Specie Mb, from the Borca Mb the Rb/K_2O records variations in the source of sediments, while the CPA remains high suggesting still a humid climate (Fig. 5.3). A climatic humid signal in the Borca Mb is also independently inferred by the dominance of hygrophytic sporomorphs, the occurrence of amber, and the presence of spodic and histic paleosols at the top of the member (Preto and Hinnov, 2003; Roghi et al., 2006, 2022; Breda et al., 2009; Seyfullah et al., 2018). The same climatic scenario is maintained almost unchanged for the subsequent Dibona Mb, where clay minerals do not exhibit appreciable changes in the already humid climatic signal within this stratigraphic interval, amber droplets are found, and coal levels and hygrophytic plant remains occur (Roghi et al., 2006; Breda et al., 2009; Seyfullah et al., 2018; Roghi et al., 2022). Hence, our data show that, following the RSL fall (basal Borca Mb), any climatic signal in the clay association was obliterated by the increase of immature sediment supply and by enhanced wave-ravinement erosion during the transgression (Dibona Mb; Gattolin et al., 2015), while other proxies (CPA, palynology, paleosols) still indicate humid conditions.

Our observations reconcile apparently different views on the main drivers of CPE sedimentary changes observed in epicontinental and marine environments. Franz et al. (2014) suggested eustatic control on the sedimentation of the immature sandstones of the Stuttgart Fm (Schilfsandstein), which deposited during the CPE interval in the Central European Basin (Middle Keuper; see also Zhang et al., 2020 and references therein). The new data from the Dolomites, coupled with other published observations, confirm that such eustatic control (RSL fall and transgression) played a major role in regulating the sediment supply also in the marine marginal sequences of the northwestern Tethys. However, eustatism alone cannot fully explain the relatively rapid arrival of immature fine and coarse material into marine basins. Globally-recorded synchronous NCIEs testify for major perturbations of the exogenic C-cycle that enhanced the hydrological cycle and total global runoff (Dal Corso et al., 2022). Increased precipitation could have driven a more vigorous erosion and recycling of sediment, as well as higher freshwater storage in lakes and aquifers causing aquifer-eustasy or limno-eustatism. Hence, the interplay of higher runoff and

eustatism—both ultimately linked to the CPE C-cycle perturbation—can explain the siliciclastic sedimentological features that mark the CPE.

5.6.3 POST-CPE PHYSICAL WEATHERING

The decoupling between CPA and Rb/K_2O continues also after the CPE, in the Travenanzes Fm (Fig. 5.3). Interestingly, values of CPA and Rb/K_2O from the Dibona Mb and Travenanzes Fm. are similar (Dibona Mb: average CPA = 96; average Rb/K_2O: 20 - Travenanzes Fm: average CPA: 96; average Rb/K_2O = 23), even if the inferred depositional environments are different. This could be justified considering that in one case (Dibona Mb), enhanced chemical weathering was favored by persisting humid conditions, while in the other case (Travenanzes Fm) clay minerals were transported by rivers and terminal fans from source areas where pristine minerals remained subaerially exposed for hundreds of thousand or possibly even millions of years (Brusca et al., 1981; Franciosi and Vignolo, 2020) and underwent prolonged physical weathering. Moreover, the Rb/K_2O ratio could be affected by the increase in illite content deriving from the metamorphic basement locally exposed in source areas (Cati et al., 1980; Breda and Preto, 2011). This feature is also suggested observing that the highest illite values (up to 71.2%) of the entire succession are reached within the Travenanzes Fm, while K-feldspar returns to lower values. High physical weathering justifies high CPA values although the depositional environment is typically arid (Breda and Preto, 2011). The mineralogical composition of the Travenanzes Fm (illite-dominated I/S, hematite and also large amounts of dolomite and chlorite, and absence of kaolinite; Fig. 5.3) further supports the interpretation that this unit represents a post-CPE phase of mainly physical weathering and aridification, as also witnessed by the presence of calcisols, calcic vertisols, teepee and evaporites (Breda et al., 2009; Stefani et al., 2010; Breda and Preto, 2011). This phase is characterized by a return to quantities of non-clay siliciclastic minerals similar to those of the pre-CPE phase (Fig. 5.4B).

5.7 CONCLUSIONS

Weathering indices (CPA and Rb/K_2O) and mineral data, assessed both qualitatively and quantitatively, show weathering intensity variations along a mainly siliciclastic succession of the Dolomites during the Carnian Pluvial Episode (CPE). The combined use of mineralogy, geochemistry and other published proxies (sedimentology, palynology), along with previous knowledge on basin evolution and sequence stratigraphy, allowed to reconstruct the complex history of the processes that controlled fine sediment supply to the basins of the Dolomites during the CPE.

1. Data suggest stable pre-CPE (background) weathering conditions, as shown by a parallel trend of CPA and Rb/K_2O indices in the early Carnian San Cassiano Fm. During this phase 1, Mineralogy shows irregular fluctuations in carbonates, and clay minerals associations are dominated by I/S and exhibit the highest chlorite contents among all the investigated samples. These features appear influenced by reworking of Ladinian basic volcanic products.

2. Enhanced chemical weathering is found at the onset of the CPE (i.e., first negative C-isotope excursion), shown by an increase of CPA and Rb/K_2O weathering indices at the base of the Alpe di Specie member of the Heiligkreuz Fm. Mineralogy shows some minor differences compared to the underlying San Cassiano Fm (i.e., less clays, in particular kaolinite and much less chlorite), due to similar depositional environments between the two units (hemipelagic basin to prodelta vs. prodelta), but an increase of kaolinite content, which can be interpreted as the evidence of more humid conditions. Overall, geochemical and

mineralogical data agree with previous observations made in other paleo-localities, supporting the interpretation of a widespread climatic humidification at the onset of the CPE.

3. A major source change in the Borca and Dibona members is observed. It is marked by the decoupling of CPA and Rb/K_2O signals (i.e., CPA is still high, while Rb/K_2O decreases), increased amounts of K-feldspar, and changes in clay minerals assemblages. The change at the base of the lower Borca Mb is synchronous with a major eustatic sea level fall. The sea-level fall rejuvenated riverine systems that were strengthened by the more vigorous CPE hydrological cycle, and hence caused widespread and strong erosion of the source area and relatively rapid infilling of the basin. The transgression recorded by the Heiligkreuz Fm is very pronounced and recorded by the return of marine and marine-marginal conditions over areas that were characterized by non-sedimentation and erosion since the late Ladinian. During these phases, the effect of erosion and transport overwhelmed and obliterated the climatic signal inferred by other proxies such palynology and paleosols, which suggest still humid conditions.

4. Mainly physical weathering occurred during the deposition of the Travenanzes Fm, where the decoupling of CPA and Rb/K_2O continues. Mineralogical and sedimentological features (illite, hematite, evaporites, arid paleosols) indicate a return to arid climatic conditions, but the CPA remains at high values. This fact, coupled with the highest recorded amounts of illite, suggests that physical weathering of the crystalline basement occurred during the post-CPE Tuvalian transgression.

6 SYNTHESIS AND CONCLUDING REMARKS

The review work on global sedimentological effects of the CPE has shown on the one hand the extraordinary amount of areas that, despite their location at different paleolatitudes and different environmental setting, shows synchronous humidification features during the Carnian. This allowed to identify and relate some stratigraphic intervals to the CPE in previous studies.

On the other hand, many areas with interesting sedimentological features that would be worth investigating by paleoclimatic studies have emerged from the review and further studies are suggested for them. Thus, this thesis could constitute a database and a basis to facilitate future insights.

Moreover, what also emerged from this work is a disproportion between some regions where the stratigraphic resolution is very high and others where the biostratigraphic constrains are almost or completely absent.

Finally, it is interesting to note that successions from some areas show typical characteristics of a humid climate already before the late early Carnian (e.g., Barents Sea area), and others instead does not display any sedimentological change or humidification feature during the Carnian (e.g., Lhasa Block). On the other hand, the actual global warming causes different exasperation of factors related to climate change, depending on latitudes and overall on geographic setting, leading to local effects on sedimentation. The enhanced/reduced rainfall is one of them, that can be recorded in many areas but not in all. It is in this perspective that it is suggested to put aside the term 'Carnian Pluvial Episode' and possibly use in the future the term 'Carnian Climatic Episode'.

Within this project, the pre/syn/post- CPE weathering has been investigated also through the calculation of weathering indices and determination of qualitative and quantitative mineralogy. This has been carried out for the first time on stratigraphic successions of the Dolomites, a worldwide reference for Triassic stratigraphy and for the comprehension of the CPE. Among the analysed weathering indices, the most meaningful and suitable ones resulted to be the CPA and the Rb/K_2O. Results and trends were coupled with provenance studies, allowing to obtain a more complete reconstruction.

The background conditions were characterized by irregular fluctuations of carbonates and a relative abundance of I/S. At the onset of the CPE (Alpe di Specie Mb; Heiligkreuz Fm), an increase of chemical weathering coupled with a decrease of chlorite and an increase of kaolinite are recorded. These suggest more humid climate, in agreement with previously published literature. From here on out (Borca Mb; Heiligkreuz Fm), mineralogical changes and decoupling between the CPA and Rb/K_2O weathering indices were observed and strictly related to the eustatic sea-level fall occurred during the latemost Julian. Provenance discrimination diagrams demonstrate that a sediment-source change occurred, compared to the underlying succession. Moreover, also the Dibona mb (Heiligkreuz Fm) records supply of reworked Ladinian volcanics associated with the development of wave-ravinement erosion during the transgressive phase. However, previous studies dealing with sedimentological and/or paleobotanical proxies (e.g., humid paleosols and hygrophytic-dominated palynological associations) allow the interpretation of a still humid climate. Upward in the succession, the decoupling of CPA and Rb/K_2O continues, but mineralogical and geochemical data show high physical weathering under arid climate (in agreement with published literature).

It is therefore evident that the rigorous critical analysis of the geochemical and mineralogical data, coupled with proxies (e.g., sedimentological or palaeo-botanical) and provenance and source data from other studies is essential to obtain robust paleoclimatic reconstructions.

By virtue of the tight link existing between Carbon cycle and weathering, results from this project outline that the CO_2 injection into the atmosphere (possibly from Wrangellia LIP volcanism), and the consequent increase of temperature and enhanced hydrological cycle, have determined an intensification of chemical weathering at the onset of the CPE. The increase of rainfall promoted higher storage of freshwater on land, coupled to a substantial increase of erosion and transport of unweathered material into the basins of the Western Tethys, which were rapidly infilled.

7 REFERENCES

Abbas, H., Michail, M., Cifelli, F., Mattei, M., Gianolla, P., Lustrino, M., Carminati, E., 2018. Emplacement modes of the Ladinian plutonic rocks of the Dolomites: Insights from anisotropy of magnetic susceptibility. J. Struct. Geol. 113, 42–61. https://doi.org/10.1016/j.jsg.2018.05.012

Abedini, A., Mongelli, G., Khosravi, M., 2021. Geochemical constraints on the middle Triassic Kani Zarrineh karst bauxite deposit, Irano – Himalayan belt, NW Iran : Implications for elemental fractionation and parental affinity. Ore Geol. Rev. 133, 104099. https://doi.org/10.1016/j.oregeorev.2021.104099

Abu Hamad, A.M.B., Jasper, A., Uhl, D., 2014. Journal of African Earth Sciences Wood remains from the Late Triassic (Carnian) of Jordan and their paleoenvironmental implications. J. African Earth Sci. 95, 168–174. https://doi.org/10.1016/j.jafrearsci.2014.03.011

Adamia, S., Alania, V., Chabukiani, A., Kutelia, Z. and Sadradze, N., 2011, "Great Caucasus (Cavcasioni): A Long-lived North-Tethyan Back-Arc Basin," Turkish Journal of Earth Sciences: Vol. 20: No. 5, Article 3. https://doi.org/10.3906/yer-1005-12

Anderson, J.M., Anderson, H.M., Cruickshank, A.R.I., 1998. Late triassic ecosystems of the molteno/lower elliot biome of Southern Africa. Palaeontology.

Andreozzi, M., Dinelli, E., Tateo, F., 1997. Geochemical and mineralogical criteria for the identification of ash layers in the stratigraphic framework of a foredeep; the Early Miocene Mt. Cervarola Sandstones, northern Italy. Chem. Geol. 137, 23–39. https://doi.org/10.1016/S0009-2541(96)00148-9

Andrews, S.D., Kelly, S.R.A., Braham, W., Kaye, M., 2014. Climatic and eustatic controls on the development of a Late Triassic Climatic and eustatic controls on the development of a Late Triassic source rock in the Jameson Land Basin , East Greenland. J. Geol. Soc. London. https://doi.org/10.1144/jgs2013-075

Angiolini, L., Zanchi, A., Zanchetta, S., Nicora, A., Vezzoli, G., 2013. The Cimmerian geopuzzle: new data from South Pamir. Terra Nov. 25, 352–360. https://doi.org/https://doi.org/10.1111/ter.12042

Arche, A., López-Gómez, J., 2014. The Carnian Pluvial Event in Western Europe : New data from Iberia and correlation with the Western Neotethys and Eastern North America – NW Africa regions. Earth Sci. Rev. 128, 196–231. https://doi.org/10.1016/j.earscirev.2013.10.012

Assereto, R., Desio, A., Di Colbertaldo, D., Passeri, L., 1968. Note Illustrative della Carta Geologica d'Italia alla scala 1:100000 - Foglio 14a, Tarvisio.

Aubrecht, R., Sýkora, M., Uher, P., Li, X.H., Yang, Y.H., Putiš, M., Plašienka, D., 2017. Provenance of the Lunz Formation (Carnian) in the Western Carpathians, Slovakia: Heavy mineral study and in situ LA–ICP–MS U–Pb detrital zircon dating. Palaeogeogr. Palaeoclimatol. Palaeoecol. 471, 233–253. https://doi.org/10.1016/j.palaeo.2017.02.004

Bacon, C.A., 1991. The Coal Resources of Tasmania. Geolgical Surv. Bull. 64, 170.

Badrikolalo, N., Hamidi, B., Vaziri, S.H., Aghanabati, S.A., 2015. Biostratigraphic Correlation of Elikah Formation in Zal Section (Northwestern Iran) with Ruteh and Type Sections in Alborz Mountains Based on Conodonts Biostratigraphic Correlation of Elikah

Formation in Zal Section (Northwestern Iran) with Ruteh and type sections in Alborz Mountains based on conodonts. Iranian Journal of Earth Sciences, 7(1), 78-88.

Bahr, A., Kolber, G., Kaboth-Bahr, S., Reinhardt, L., Friedrich, O., Pross, J., 2019. Mega-monsoon variability during the late Triassic: Re-assessing the role of orbital forcing in the deposition of playa sediments in the Germanic Basin. Sedimentology 67, 951–970. https://doi.org/10.1111/sed.12668

Bandyopadhyay, S., Ray, S., 2020. Gondwana vertebrate faunas of india: Their diversity and intercontinental relationships. Episodes 43, 438–460. https://doi.org/10.18814/EPIIUGS/2020/020028

Baranyi, V., Miller, C.S., Ruffell, A., Hounslow, M.W., Kürschner, W.M., 2019a. A continental record of the carnian pluvial episode (CPE) from the mercia mudstone group (UK): Palynology and climatic implications. J. Geol. Soc. London. 176, 149–166. https://doi.org/10.1144/jgs2017-150

Baranyi, V., Rostási, Á., Raucsik, B., Michael, W., 2019b. Palynology and weathering proxies reveal climatic fluctuations during the Carnian Pluvial Episode (CPE) (Late Triassic) from marine successions in the Transdanubian Range (western Hungary). Glob. Planet. Change 177, 157–172. https://doi.org/10.1016/j.gloplacha.2019.01.018

Baron, M.G., Norman, D.B., Barrett, P.M., 2017. A new hypothesis of dinosaur relationships and early dinosaur evolution. Nature 543, 501–506. https://doi.org/10.1038/nature21700

Barrenechea, J.F., López-Gómez, J., De La Horra, R., 2018. Sedimentology, clay mineralogy and palaeosols of the mid-carnian pluvial episode in eastern Spain: Insights into humidity and sea-level variations. J. Geol. Soc. London. 175, 993–1003. https://doi.org/10.1144/jgs2018-024

Barrett, P.J., Elliot, D.H., Lindsay, J.F., 1986, The Beacon Supergroup (Devonian–Triassic) and Ferrar Group (Jurassic) in the Beardmore Glacier area, Antarctica, in Turner, M.D., and Splettstoesser, J.D., eds., Geology of the Central Transantarctic Mountains: American Geophysical Union, Antarctic Research Series, v. 36, no. 14, p. 339–428.

Bechstädt, T., Schweizer, T., 1991. The carbonate-clastic cycles of the East-Alpine Raibl group: Result of third-order sea-level fluctuations in the Carnian. Sediment. Geol. 70, 241–270. https://doi.org/10.1016/0037-0738(91)90143-2

Benton, M.J., Forth, J., Langer, M.C., 2014. Models for the rise of the dinosaurs. Curr. Biol. 24, R87–R95. https://doi.org/10.1016/j.cub.2013.11.063

Bernardi, M., Gianolla, P., Petti, F.M., Mietto, P., Benton, M.J., 2018. Dinosaur diversification linked with the Carnian Pluvial Episode. Nat. Commun. 9. https://doi.org/10.1038/s41467-018-03996-1

Bhargava, O.N., Krystyn, L., Balini, M., Lein, R., Nicora, A., 2004. Revised Litho- and Sequence Stratigraphy of the Spiti Triassic. Albertiana.

Bhatia, M.R., Crook, K.A.W., 1986. Trace element characteristics of graywackes and tectonic setting discrimination of sedimentary basins. Contrib. to Mineral. Petrol. 92, 181–193. https://doi.org/10.1007/BF00375292

Bialik, O.M., Korngreen, D., Benjamini, C., 2012. Lithofacies and cyclicity of Mohilla evaporite basins on the rifted margin of the Levant in the Late Triassic, Makhtesh Ramon ,

southern Israel. Sedimentology 59, 2097–2124. https://doi.org/10.1111/j.1365-3091.2012.01336.x

Bialik, O.M., Korngreen, D., Benjamini, C., 2013. Carnian (Triassic) aridization on the Levant margin: Evidence from the M1 member, Mohilla Formation, Makhtesh Ramon, south Israel. Facies 59, 559–581. https://doi.org/10.1007/s10347-012-0321-5

Bordy, E.M., Abrahams, M., Sharman, G.R., Viglietti, P.A., Benson, R.B.J., McPhee, B.W., Barrett, P.M., Sciscio, L., Condon, D., Mundil, R., Rademan, Z., Jinnah, Z., Clark, J.M., Suarez, C.A., Chapelle, K.E.J., Choiniere, J.N., 2020. A chronostratigraphic framework for the upper Stormberg Group: Implications for the Triassic-Jurassic boundary in southern Africa. Earth-Science Rev. 203, 103120. https://doi.org/10.1016/j.earscirev.2020.103120

Bosellini, A., Gianolla, P., Stefani, M., 2003. Geology of the Dolomites. Episodes 26, 181–185. https://doi.org/10.18814/epiiugs/2003/v26i3/005

Boulila, S., Haq, B.U., Hara, N., Müller, R.D., Galbrun, B., Charbonnier, G., 2021. Potential encoding of coupling between Milankovitch forcing and Earth's interior processes in the Phanerozoic eustatic sea-level record. Earth-Science Rev. 220, 103727. https://doi.org/10.1016/j.earscirev.2021.103727

Bourquin, S., Durand, M., 2007. International Field Workshop on "The Triassic of eastern France." Pan-European Correl. Epic. Triassic 80.

Bragin, N.Y., Konstantinov, A.G., Sobolev, E.S., 2012. Upper Triassic stratigraphy and paleobiogeography of Kotel'nyi Island (New Siberian Islands). Stratigr. Geol. Correl. 20, 541–566. https://doi.org/10.1134/S0869593812050036

Brandner, R., Gruber, A., Keim, L., 2007. Sediment 2007 Exkursionsführer. Geoalp 4, 95–121.

Breda, A., Preto, N., 2011. Anatomy of an Upper Triassic continental to marginal-marine system: The mixed siliciclastic-carbonate Travenanzes Formation (Dolomites, Northern Italy). Sedimentology 58, 1613–1647. https://doi.org/10.1111/j.1365-3091.2011.01227.x

Breda, A., Preto, N., Roghi, G., Furin, S., Meneguolo, R., Ragazzi, E., Fedele, P., Gianolla, P., 2009. The Carnian Pluvial Event in the Tofane Area (Cortina d'Ampezzo, Dolomites, Italy). Geoalp 6, 80–115.

Broglio Loriga, C., Cirilli, S., De Zanche, V., Bari, D.D.I., Gianolla, P., Laghi, G.F., Lowrie, W., Manfrin, S., Mastandrea, A., Mietto, P., Muttoni, G., Neri, C., Posenato, R., Rechichi, M., Rettori, R., Roghi, G., 1999. The Prati di Stuores/Stuores Wiesen section (Dolomites, Italy): A candidate Global Stratotype Section and Point for the base of the Carnian Stage. Riv. Ital. di Paleontol. e Stratigr. 105, 37–78.

Brookfield, M.E., Hashmat, A., 2001. The geology and petroleum potential of the North Afghan platform and adjacent areas (northern Afghanistan, with parts of southern Turkmenistan, Uzbekistan and Tajikistan). Earth-Science Rev. 55, 41–71. https://doi.org/https://doi.org/10.1016/S0012-8252(01)00036-8

Brownfield, M.E., Martirosyan, A., Pierce, B.S., Johnson, E.A., 2000. Geologic map of the Jermanis Coal Field, Central Armenia, Miscellaneous Field Studies Map. https://doi.org/10.3133/mf2350

Brusatte, S.L., Nesbitt, S.J., Irmis, R.B., Butler, R.J., Benton, M.J., Norell, M.A., 2010. The origin and early radiation of dinosaurs. Earth-Science Rev. 101, 68–100. https://doi.org/10.1016/j.earscirev.2010.04.001

Brusca, C., Gaetani, M., Jadoul, F., Viel, G., 1981. Paleogeografia Ladinico-Carnica e Metallogenesi del Sudalpino. Mem. della Soc. Geol. Ital. 22, 65–82.

Bubnic, J., Fors, G., Office, B., 2010. Depositional sequences and palynology of Triassic carbonate-evaporite platform deposits in the Palmyrides , Syria. Spec. Pubblication Geol. Soc. London 43–63.

Budai, T., and Haas, J., 1997, Triassic sequence stratigraphy of the Balaton Highland, Hungary: Acta Geologica Hungarica, v. 40, no. 3, p. 307–335.

Buffa, V., Jalil, N., Steyer, J.-S., 2019. Redescription of Arganasaurus (Metoposaurus) azerouali (Dutuit) comb. nov. from the Upper Triassic of the Argana Basin (Morocco), and the first phylogenetic analysis of the Metoposauridae (Amphibia, Temnospondyli). Pap. Palaeontol. 1–19. https://doi.org/10.1002/spp2.1259

Buggle, B., Glaser, B., Hambach, U., Gerasimenko, N., Marković, S., 2011. An evaluation of geochemical weathering indices in loess-paleosol studies. Quat. Int. 240, 12–21. https://doi.org/10.1016/j.quaint.2010.07.019

Burgess, R., Jolley, D., Hartley, A., 2020. Stratigraphical palynology of the Middle to Late Triassic successions of the Central North Sea. Pet. Geosci. https://doi.org/10.5860/choice.41-4685

Caggiati, M., Breda, A., Gianolla, P., Rigo, M., Roghi, G., 2012. Depositional systems of the Eastern Southern Alps (NE Italy, WSlovenia) during the late Carnian. Rend. della Soc. Geol. Ital. 20, 24–27. https://doi.org/10.1017/CBO9781107415324.004

Caggiati, M., Gianolla, P., Breda, A., Celarc, B., Preto, N., 2018. The start-up of the Dolomia Principale/Hauptdolomit carbonate platform (Upper Triassic) in the eastern Southern Alps. Sedimentology 65, 1097–1131. https://doi.org/10.1111/sed.12416

Cairncross, B., Anderson, J.M., Anderson, H.M., 1995. Palaeoecology of the Triassic Molteno Formation, Karoo Basin, South Africa - sedimentological and palaeontological evidence. South African J. Geol. 98, 452–478.

Carlisle, D. and T. Susuki 1965 Structure, stratigraphy and paleontology of an Upper Triassic section on the west coast of British Columbia. Canadian Journal of Earth Sciences, V.2, I.5

Carlisle, D., Susuki, T., 1974. Emergent Basalt and Submergent Carbonate–Clastic Sequences Including the Upper Triassic Dilleri and Welleri Zones on Vancouver Island. Can. J. Earth Sci. 11, 254–279.

Castellarin, A., Cantelli, L., 2000. Neo-Alpine evolution of the Southern Eastern Alps. J. Geodyn. 30, 1–2. https://doi.org/10.1016/S0264-3707(99)00036-8

Cati, A., Sartorio, D., Venturini, S., 1980. Carbonate platforms in the subsurface of the northern Adriatic Sea. Mem. della Soc. Geol. Ital. 40, 295–308.

Catuneanu, O., Wopfner, H., Eriksson, P.G., Cairncross, B., Rubidge, B.S., Smith, R.M.H., Hancox, P.J., 2005. The Karoo basins of south-central Africa. J. African Earth Sci. 43, 211–253. https://doi.org/10.1016/j.jafrearsci.2005.07.007

Cavalcante, F., 2021. Editorial for special issue “clays, clay minerals, and geology.” Minerals 11. https://doi.org/10.3390/min11101057

Celarc, B., 2008. Carnian bauxite horizon on the Kopitov grič near Borovnica (Slovenia) – is there a »forgotten« stratigraphic gap in its footwall? Geologija 51, 147–152. https://doi.org/10.5474/geologija.2008.015

Césari, S.N., Colombi, C.E., 2013. A new Late Triasssic phytogeographical scenario in westernmost Gondwana. Nat. Commun. 1–6. https://doi.org/10.1038/ncomms2917

Césari, S.N., Colombi, C., 2016. Palynology of the Late Triassic Ischigualasto Formation, Argentina: Paleoecological and paleogeographic implications. Palaeogeogr. Palaeoclimatol. Palaeoecol. 449, 365–384. https://doi.org/10.1016/j.palaeo.2016.02.023

Chamley, H., 1989. Clay Sedimentology. Springer-Verlag, Berlin.

Chatalov, A., 2017. Quartz arenites and laterites in the Moesian Group (Upper Triassic), northwestern Bulgaria: possible evidence for the effect of the Carnian Humid Episode. Geol. Balc. 46, 3–25.

Chen, H., Zhu, M., Chen, S., Xiao, A., Jia, D., Yang, G., 2020. Basin-orogen patterns and the late Triassic foreland basin conversion process in the western Yangtze Block, China. J. Asian Earth Sci. 194, 104311. https://doi.org/https://doi.org/10.1016/j.jseaes.2020.104311

Chen, Y., Lukeneder, A., 2017. Late Triassic (Julian) conodont biostratigraphy of a transition from reefal limestones to deep-water environments on the Cimmerian terranes (Taurus Mountains, southern Turkey). Pap. Palaeontol. 3, 441–460. https://doi.org/10.1002/spp2.1082

Cirilli, S., 2010. Upper Triassic-lowermost Jurassic palynology and palynostratigraphy: a review. Geol. Soc. Spec. Publ. 334, 285–314. https://doi.org/10.1144/SP334.12

Colombi, C.E., Parrish, J.T., 2008. Late Triassic Environmental Evolution in Southwestern Pangea: Plant Taphonomy of the Ischigualasto Formation. Palaios 23, 778–795. https://doi.org/10.2110/palo.2007.p07-101r

Colombi, C.E., Limarino, C.O., Alcober, O.A., 2017. Allogenic controls on the fluvial architecture and fossil preservation of the Upper Triassic Ischigualasto Formation, NW Argentina. Sediment. Geol. 362, 1–16. https://doi.org/10.1016/j.sedgeo.2017.10.003

Colombi, C., Martínez, R.N., Silvia, N.C., Limarino, C.O., Monta, I., 2021. Journal of South American Earth Sciences A high-precision U – Pb zircon age constraints the timing of the faunistic and palynofloristic events of the Carnian Ischigualasto Formation , San. J. South Am. Earth Sci. 111.

Cornet, B., Olsen, P.E., 1990. Early to Middle Carnian (Triassic) flora and fauna of the Richmond and Taylorsville basins, Virginia and Maryland, USA. Virginia Museum Nat. Hist.

Csillag, G., Földvári, M., 2007. Upper Triassic amber fragments from the Balaton Highland, Hungary. Annu. Rep. Geol. Inst. Hungary 37–46.

Cullers, R.L., 2000. The geochemistry of shales, siltstones and sandstones of Pennsylvanian-Permian age, Colorado, USA: Implications for provenance and metamorphic studies. Lithos 51, 181–203. https://doi.org/10.1016/S0024-4937(99)00063-8

Dai, X., Du, Y., Ziegler, M., Wang, C., Ma, Q., Chai, R., Guo, H., 2022. Middle Triassic to Late Jurassic climate change on the northern margin of the South China Plate: Insights from chemical weathering indices and clay mineralogy. Palaeogeogr. Palaeoclimatol. Palaeoecol. 585, 110744. https://doi.org/10.1016/j.palaeo.2021.110744

Dal Corso, J., Preto, N., Kustatscher, E., Mietto, P., Roghi, G., Jenkyns, H.C., 2011. Carbon-isotope variability of Triassic amber, as compared with wood and leaves (Southern Alps, Italy). Palaeogeogr. Palaeoclimatol. Palaeoecol. 302, 187–193. https://doi.org/10.1016/j.palaeo.2011.01.007

Dal Corso, J., Mietto, P., Newton, R.J., Pancost, R.D., Preto, N., Roghi, G., Wignall, P.B., 2012. Discovery of a major negative δ13C spike in the Carnian (Late Triassic) linked to the eruption of Wrangellia flood basalts. Geology 40, 79–82. https://doi.org/10.1130/G32473.1

Dal Corso, J., Gianolla, P., Newton, R.J., Franceschi, M., Roghi, G., Caggiati, M., Raucsik, B., Budai, T., Haas, J., Preto, N., 2015. Carbon isotope records reveal synchronicity between carbon cycle perturbation and the "Carnian Pluvial Event" in the Tethys realm (Late Triassic). Glob. Planet. Change 127, 79–90. https://doi.org/10.1016/j.gloplacha.2015.01.013

Dal Corso, J., Benton, M.J., Bernardi, M., Franz, M., Gianolla, P., Hohn, S., Kustatscher, E., Merico, A., Roghi, G., Ruffell, A., Ogg, J.G., Preto, N., Schmidt, A.R., Seyfullah, L.J., Simms, M.J., Shi, Z., Zhang, Y., 2018a. First workshop on the Carnian Pluvial Episode (Late Triassic): A report. Albertiana 44, 49–57.

Dal Corso, J., Gianolla, P., Rigo, M., Franceschi, M., Roghi, G., Mietto, P., Manfrin, S., Raucsik, B., Budai, T., Jenkyns, H.C., Reymond, C.E., Caggiati, M., Gattolin, G., Breda, A., Merico, A., Preto, N., 2018b. Multiple negative carbon-isotope excursions during the Carnian Pluvial Episode (Late Triassic). Earth-Science Rev. 185, 732–750. https://doi.org/10.1016/j.earscirev.2018.07.004

Dal Corso, J., Ruffell, A., Preto, N., 2018c. The carnian pluvial episode (Late triassic): New insights into this important time of global environmental and biological change. J. Geol. Soc. London. 175, 986–988. https://doi.org/10.1144/jgs2018-185

Dal Corso, J., Ruffell, A., Preto, N., 2019. Carnian (Late triassic) C-isotope excursions, environmental changes, and biotic turnover: A global perturbation of the earth's surface system. J. Geol. Soc. London. 176, 129–131. https://doi.org/10.1144/jgs2018-217

Dal Corso, J., Bernardi, M., Sun, Y., Song, H., Seyfullah, L.J., Preto, N., Gianolla, P., Ruffell, A., Kustatscher, E., Roghi, G., Merico, A., Hohn, S., Schmidt, A.R., Marzoli, A., Newton, R.J., Wignall, P.B., Benton, M.J., 2020. Extinction and dawn of the modern world in the Carnian (Late Triassic). Sci. Adv. 6, 1–13. https://doi.org/10.1126/sciadv.aba0099

Dal Corso, J., Mills, B.J.W., Chu, D., Newton, R.J., Song, H., 2022. Background Earth system state amplified Carnian (Late Triassic) environmental changes. Earth Planet. Sci. Lett. 578, 117321. https://doi.org/10.1016/j.epsl.2021.117321

Dalla Vecchia, M.F., 2020. Raibliania calligarisi Gen. N., Sp. N., A New Tanystropheid (Diapsida, Tanystropheidae) From The Upper Triassic (Carnian) Of Northeastern Italy. Riv. Ital. di Paleontol. e Stratigr. 126, 197–222.

Dasgupta, S., Ghosh, P., 2017. A Discontinuous Ephemeral Stream Transporting Mud Aggregates In A Continental Rift Basin : The Late Triassic Maleri Formation , India Pranhita

– Godavari continental rift basin , India , indicate that it is a fluvial deposit , the formation is characteriz. J. Sediment. Res. 838–865.

Datta, D., Ray, S., Bandyopadhyay, S., 2019. Cranial morphology of a new phytosaur (Diapsida, Archosauria) from the Upper Triassic of India: implications for phytosaur phylogeny and biostratigraphy. Pap. Palaeontol. 1–34. https://doi.org/10.1002/spp2.1292

Davies, A., Gréselle, B., Hunter, S.J., Baines, G., Robson, C., Haywood, A.M., Ray, D.C., Simmons, M.D., van Buchem, F.S.P., 2020. Assessing the impact of aquifer-eustasy on short-term Cretaceous sea-level. Cretac. Res. 112. https://doi.org/10.1016/j.cretres.2020.104445

Davies, R.B., Simmons, M.D., 2020. Dating and correlation of the Baluti Formation, Kurdistan, IRAQ: Implications for the regional recognition of a Carnian "marker dolomite", and a review of the Triassic to Early Jurassic sequence stratigraphy of the Arabian Plate. J. Pet. Geol. 43, 95–108. https://doi.org/https://doi.org/10.1111/jpg.12751

De Min, A., Velicogna, M., Ziberna, L., Chiaradia, M., Alberti, A., Marzoli, A., 2020. Triassic magmatism in the European Southern Alps as an early phase of Pangea break-up. Geol. Mag. 157, 1800–1822. https://doi.org/10.1017/S0016756820000084

De Zanche, V., Gianolla, P., 1995. Litostratigrafia al limite Ladinico-Carnico (Sudalpino orientale). Ann. dell'Università di Ferrara, Sci. Terra 5, 41–48.

De Zanche, V., Gianolla, P., Mietto, P., Siorpaes, C., Vail, P.R., 1993. Triassic sequence stratigraphy in the Dolomites (Italy). Mem. di Sci. Geol. 45, 1–27.

De Zanche, V., Gianolla, P., Roghi, G., 2000. Carnian stratigraphy in the Raibl/Cave del Predil area (Julian Alps, Italy). Eclogae Geol. Helv. 93, 331–347.

Decou, A., Andrews, S.D., Alderton, D.H.M., Morton, A., 2017a. Triassic to Early Jurassic climatic trends recorded in the Jameson Land Basin , East Greenland : clay mineralogy , petrography and heavy mineralogy. Basin Res. 29, 658–673. https://doi.org/10.1111/bre.12194

Deng, T., Li, Y., Wang, Z., Yu, Q., Dong, S., Yan, L., Hu, W., Chen, B., 2019. Geochemical characteristics and organic matter enrichment mechanism of black shale in the Upper Triassic Xujiahe Formation in the Sichuan basin: Implications for paleoweathering, provenance and tectonic setting. Mar. Pet. Geol. 109, 698–716. https://doi.org/10.1016/j.marpetgeo.2019.06.057

Dera, G., Pellenard, P., Neige, P., Deconinck, J.F., Pucéat, E., Dommergues, J.L., 2009. Distribution of clay minerals in Early Jurassic Peritethyan seas: Palaeoclimatic significance inferred from multiproxy comparisons. Palaeogeogr. Palaeoclimatol. Palaeoecol. 271, 39–51. https://doi.org/10.1016/j.palaeo.2008.09.010

Desio, A., 1975 - Geology of Central Badakhshan (North-East Afghanistan) and surrounding countries. 628 p.

Desojo, J.B., Fiorelli, L.E., Ezcurra, M.D., Martinelli, A.G., 2020. The Late Triassic Ischigualasto Formation at Cerro Las Lajas (La Rioja , Argentina): fossil tetrapods , high - resolution chronostratigraphy , and faunal correlations, Scientific Reports. Nature Publishing Group UK. https://doi.org/10.1038/s41598-020-67854-1

Dill, H.G., Bechtel, A., Berner, Z., Botz, R., Kus, J., Heunisch, C., Hamad, A.M.B.A., 2012. The evaporite – coal transition: Chemical , mineralogical and organic composition of the Late Triassic Abu Ruweis Formation , NW Jordan — Reference type of the " Arabian Keuper ." Chem. Geol. 298–299, 20–40. https://doi.org/10.1016/j.chemgeo.2011.12.028

Dinelli, E., Lucchini, F., 1999. Sediment supply to the Adriatic sea basin from the Italian rivers: Geochemical features and environmental constraints. G. di Geol. 121–132.

Ding, L., Yang, D., Cai, F.L., Pullen, A., Kapp, P., Gehrels, G.E., Zhang, L.Y., Zhang, Q.H., Lai, Q.Z., Yue, Y.H., Shi, R.D., 2013. Provenance analysis of the Mesozoic Hoh-Xil-Songpan-Ganzi turbidites in northern Tibet: Implications for the tectonic evolution of the eastern Paleo-Tethys Ocean. Tectonics 32, 34–48. https://doi.org/https://doi.org/10.1002/tect.20013

Dinis, P.A., Carvalho, J., Callapez, P.M., Mendes, M.M., Santos, V.F., Fernandes, P., 2020a. Composition of Lower Cretaceous mudstones of the Algarve Basin and implications for Iberian palaeoclimates. Cretac. Res. 110. https://doi.org/10.1016/j.cretres.2020.104404

Dinis, P.A., Garzanti, E., Hahn, A., Vermeesch, P., Cabral-Pinto, M., 2020b. Weathering indices as climate proxies. A step forward based on Congo and SW African river muds. Earth-Science Rev. 201, 103039. https://doi.org/10.1016/j.earscirev.2019.103039

Dobruskina IA. 1994. Triassic Floras of Eurasia. Heidelberg, Springer, 422 p.

Dobruskina, I.A., 1995. Keuper (Triassic) Flora from Middle Asia (Madygen, Souhern Fergana), New Mexico Museum of Natural History and Science.

Doebelin, N., Kleeberg, R., 2015. Profex: a graphical user interface for the Rietveld refinement program BGMN. J. Appl. Crystallogr. 48, 1573–1580. https://doi.org/doi:10.1107/S1600576715014685

Dozet, S., 2009. Mohorje Formation, Southern Slovenia. Geologija 52, 11–20. https://doi.org/10.5474/geologija.2009.002

Dozet, S., Godec, M., 2009. Carnian bauxites at Muljava in central Slovenia. Mater. Tehnol. 43, 97–102.

Dumoulin, J.A., Burruss, R.C., Blome, C.D., 2011. Lithofacies, age, depositional setting, and geochemistry of the Otuk Formation in the Red Dog District, northwestern Alaska. USGS Prof. Pap. 1795 – B, 1–32. https://doi.org/10.3133/pp1795b

Dunkl, I., Farics, É., Józsa, S., Lukács, R., Haas, J., Budai, T., 2019. Traces of Carnian volcanic activity in the Transdanubian Range,. Int. J. Earth Sci. 108, 1451–1466. https://doi.org/10.1007/s00531-019-01714-w

Ehrmann, W., Setti, M., Marinoni, L., 2005. Clay minerals in Cenozoic sediments off Cape Roberts (McMurdo Sound, Antarctica) reveal palaeoclimatic history. Palaeogeogr. Palaeoclimatol. Palaeoecol. 229, 187–211. https://doi.org/10.1016/j.palaeo.2005.06.022

Elliot, D.H., 1996. The Hanson Formation: A new stratigraphical unit in the Transantarctic Mountains, Antarctica. Antarct. Sci. 8, 389–394.

Escapa, I.H., Taylor, E., Bomfleur, B., Serbet, R., 2011. Triassic floras of Antarctica: Plant diversity and distribution in high paleolatitude communities. Palaios 26, 522–544. https://doi.org/10.2110/palo.2010.p10-122r

Ezcurra, M.D., Fiorelli, L.E., Martinelli, A.G., Rocher, S., Baczko, M.B. Von, Ezpeleta, M., Taborda, J.R.A., Hechenleitner, E.M., Trotteyn, M.J., Desojo, J.B., 2017. Deep faunistic turnovers preceded the rise of dinosaurs in southwestern Pangaea. Nat. Ecol. Evol. 590. https://doi.org/10.1038/s41559-017-0305-5

Fedo, C.M., Nesbitt, H.W., Young, G.M., 1995. Unravelling the effects of potassium metasomatism in sedimentary rocks and paleosols, with implications for paleoweathering conditions and provenance. Geology 23, 921–924. https://doi.org/10.1130/0091-7613(1995)023<0921:UTEOPM>2.3.CO

Fijałkowska-Mader, A., 2015. A record of climatic changes in the triassic palynological spectra from Poland. Geol. Q. 59, 615–653. https://doi.org/10.7306/gq.1239

Fijałkowska-Mader, A., Heunisch, C., Szulc, J., 2015. Palynostratigraphy and palynofacies of the upper silesian keuper (Southern poland). Ann. Soc. Geol. Pol. 85, 637–661. https://doi.org/10.14241/asgp.2015.025

Fijałkowska-Mader, A., Jewuła, K., Bodor, E., 2020. Record of the Carnian Pluvial Episode in the Polish microflora. Palaeoworld. https://doi.org/10.1016/j.palwor.2020.03.006

Fischer, J., 1971. Zur Geologie des Kohe Safi bei Kabul(Afghanistan). Neues Jahrb. für Geol. und Paläontologie-Monatschefte 267–315, 267–315.

Floyd, P.A., Leveridge, B.E., 1987. Tectonic environment of the Devonian Gramscatho basin, south Cornwall: framework mode and geochemical evidence from turbiditic sandstones (England). J. - Geol. Soc. 144, 531–542. https://doi.org/10.1144/gsjgs.144.4.0531

Franceschi, M., Dal Corso, J., Cobianchi, M., Roghi, G., Penasa, L., Picotti, V., Preto, N., 2019. Tethyan carbonate platform transformations during the Early Jurassic (Sinemurian-Pliensbachian, Southern Alps): Comparison with the Late Triassic Carnian Pluvial Episode. Bull. Geol. Soc. Am. 131, 1255–1275. https://doi.org/10.1130/B31765.1

Franciosi, R., Vignolo, A., 2020. Northern Adriatic Foreland - a Promising Setting for the Southalpine Midtriassic Petroleum System. EAGE 64th Conf. Exhib. https://doi.org/10.3997/2214-4609-pdb.5.h025

Franz, M., Nowak, K., Berner, U., Heunisch, C., Bandel, K., Röhling, H.G., Wolfgramm, M., 2014. Eustatic control on epicontinental basins: The example of the stuttgart formation in the central european basin (Middle Keuper, Late Triassic). Glob. Planet. Change 122, 305–329. https://doi.org/10.1016/j.gloplacha.2014.07.010

Franz, M., Kustatscher, E., Heunisch, C., Niegel, S., Röhling, H.G., 2019. The schilfsandstein and its flora; arguments for a humid mid-carnian episode? J. Geol. Soc. London. 176, 133–148. https://doi.org/10.1144/jgs2018-053

Frizon De Lamotte, D., Fourdan, B., Leleu, S., Leparmentier, F., De Clarens, P., 2015. Style of rifting and the stages of Pangea breakup. Tectonics 34, 1009–1029. https://doi.org/10.1002/2014TC003760

Fu, X., Wang, J., Zeng, S., Feng, X., Wang, D., Song, C., 2017. Continental weathering and palaeoclimatic changes through the onset of the Early Toarcian oceanic anoxic event in the Qiangtang Basin, eastern Tethys. Palaeogeogr. Palaeoclimatol. Palaeoecol. 487, 241–250. https://doi.org/10.1016/j.palaeo.2017.09.005

Fu, X., Wang, J., Wen, H., Wang, Z., Zeng, S., Song, C., Chen, W., Wan, Y., 2020. A possible link between the Carnian Pluvial Event, global carbon-cycle perturbation, and volcanism: New data from the Qinghai-Tibet Plateau. Glob. Planet. Change 194, 103300. https://doi.org/10.1016/j.gloplacha.2020.103300

Furin, S., Preto, N., Rigo, M., Roghi, G., Gianolla, P., Crowley, J.L., Bowring, S.A., 2006. High-precision U-Pb zircon age from the Triassic of Italy : Implications for the Triassic time scale and the Carnian origin of calcareous nannoplankton and dinosaurs. Geology 34, 1009–1012. https://doi.org/10.1130/G22967A.1

Fürsich, F.T., Wendt, J., 1977. Biostratinomy and palaeoecology of the cassian formation (Triassic) of the Southern Alps. Palaeogeogr. Palaeoclimatol. Palaeoecol. 22, 257–323. https://doi.org/10.1016/0031-0182(77)90005-0.

Fürsich, F.T., Singh, I.B., Joachimski, M., Krumm, S., Schlirf, M., Schlirf, S., 2005. Palaeoclimate reconstructions of the Middle Jurassic of Kachchh (western India): An integrated approach based on palaeoecological, oxygen isotopic, and clay mineralogical data. Palaeogeogr. Palaeoclimatol. Palaeoecol. 217, 289–309. https://doi.org/10.1016/j.palaeo.2004.11.026

Fürsich, F.T., Wilmsen, M., Seyed-emami, K., Reza, M., Wilmsen, M., Seyed-emami, K., Fu, F.T., Majidifard, M.R., 2009. Lithostratigraphy of the Upper TriassicMiddle Jurassic Shemshak Group of Northern Iran. Spec. Pubblication Geol. Soc. London. https://doi.org/10.1144/SP312.6

Gaetani, M., Nicora, A., Henderson, C. et al. Refinements in the Upper Permian to Lower Jurassic stratigraphy of Karakorum, Pakistan. Facies 59, 915–948 (2013). https://doi.org/10.1007/s10347-012-0346-9

Galán, E., and Ferrell, R. E. (2013). Genesis of clay minerals. In *Developments in clay science* (Vol. 5, pp. 83-126). Elsevier

Gale, L., Skaberne, D., 2014. Composition and importance of Upper Triassic (Upper Ladinian – Lower Carnian) breccia in stratigraphy of External Dinarides. RMZ - Mater. geoenvironment 61, 107–123.

Gale, L., Celarc, B., Caggiati, M., Kolar-Jurkovšek, T., Jurkovšek, B., Gianolla, P., 2015. Paleogeographic significance of Upper Triassic basinal succession of the Tamar Valley, northern Julian Alps (Slovenia). Geol. Carpathica 66, 269–283. https://doi.org/10.1515/geoca-2015-0025

Gale, L., Peybernes, C., Celarc, B., Hočevar, M., Šelih, V.S., Martini, R., 2018. Biotic composition and microfacies distribution of Upper Triassic build-ups: new insights from the Lower Carnian limestone of Lesno Brdo, central Slovenia. Facies 64. https://doi.org/10.1007/s10347-018-0531-6

Gallois, R., 2019. The stratigraphy of the Permo-Triassic rocks of the Dorset and East Devon Coast World Heritage Site, U.K. Proc. Geol. Assoc. 130, 274–293. https://doi.org/10.1016/j.pgeola.2018.01.006

Garcia, M.S., Müller, R.T., Da-rosa, Á.A.S., Dias-da-silva, S., 2019. The oldest known co-occurrence of dinosaurs and their closest relatives : A new lagerpetid from a Carnian (Upper Triassic) bed of Brazil with implications for dinosauromorph biostratigraphy , early diversi fi cat. J. South Am. Earth Sci. 91, 302–319. https://doi.org/10.1016/j.jsames.2019.02.005

Garzanti, E., Resentini, A., 2016. Provenance control on chemical indices of weathering (Taiwan river sands). Sediment. Geol. 336, 81–95. https://doi.org/10.1016/j.sedgeo.2015.06.013

Garzanti, E., Padoan, M., Peruta, L., Setti, M., Villa, I.M., 2013. Weathering geochemistry and Sr-Nd fi ngerprints of equatorial upper Nile and Congo muds. Geochemistry, Geophys. Geosystems 14, 292–316. https://doi.org/10.1002/ggge.20060

Garzanti, E., Padoan, M., Setti, M., López-Galindo, A., Villa, I.M., 2014. Provenance versus weathering control on the composition of tropical river mud (southern Africa). Chem. Geol. 366, 61–74. https://doi.org/10.1016/j.chemgeo.2013.12.016

Gattolin, G., Breda, A., Preto, N., 2013. Demise of late triassic carbonate platforms triggered the onset of a tide-dominated depositional system in the dolomites, northern italy. Sediment. Geol. 297, 38–49. https://doi.org/10.1016/j.sedgeo.2013.09.005

Gattolin, G., Preto, N., Breda, A., Franceschi, M., Isotton, M., Gianolla, P., 2015. Sequence stratigraphy after the demise of a high-relief carbonate platform (Carnian of the Dolomites): Sea-level and climate disentangled. Palaeogeogr. Palaeoclimatol. Palaeoecol. 423, 1–17. https://doi.org/10.1016/j.palaeo.2015.01.017

Gianolla, P., De Zanche, V., Mietto, P., 1998a. Triassic Sequence Stratigraphy in the Southern Alps (Northern Italy): Definition of Sequences and Basin Evolution. Mesozoic Cenozoic Seq. Stratigr. Eur. Basins 719–747. https://doi.org/10.2110/pec.98.02.0719

Gianolla, P., Ragazzi, E., Roghi, G., 1998b. Upper Triassic amber from the Dolomites (Northern Italy). A paleoclimatic indicator?.pdf. Riv. Ital. di Paleontol. e Stratigr. 104, 381–390.

Gianolla, P., Zanche, V.D.E., Mietto, P., 1998c. Triassic Sequence Stratigraphy in the Southern Alps (Northern Italy): Definition of Sequences and Basin Evolution. SEPM Spec. Publ. 719–747.

Gianolla, P., De Zanche, V., Roghi, G., 2003. An Upper Tuvalian (Triassic) Platform-Basin System in the Julian Alps: the Start-up of the Dolomia Principale (Southern Alps, Italy). Facies 49, 135–150.

Gianolla, P., Morelli, C., Cucato, M., Siorpaes, C., 2018. Note Illustrative della Carta Geologica d'Italia alla scala 1:50.000. Foglio 016 Dobbiaco.

Glørstad-clark, E., Inge, J., Anders, B., Petter, J., 2010. Triassic seismic sequence stratigraphy and paleogeography of the western Barents Sea area. Mar. Pet. Geol. 27, 1448–1475. https://doi.org/10.1016/j.marpetgeo.2010.02.008

Goldberg, K., Humayun, M., 2010. The applicability of the Chemical Index of Alteration as a paleoclimatic indicator: An example from the Permian of the Paraná Basin, Brazil. Palaeogeogr. Palaeoclimatol. Palaeoecol. 293, 175–183. https://doi.org/10.1016/j.palaeo.2010.05.015

Golonka, J., Embry, A., Krobicki, M., 2018. Late Triassic Global Plate Tectonics. https://doi.org/10.1007/978-3-319-68009-5_2

Goričan, Š., Horvat, A., Kukoč, D., Verbič, T., 2022. Stratigraphy And Structure Of The Julian Alps In Nw Slovenia. Folia Biol. Geol. 63, 61–83.

Greene, A.R., Scoates, J.S., Weis, D., Katvala, E.C., Israel, S., Nixon, G.T., 2010. The architecture of oceanic plateaus revealed by the volcanic stratigraphy of the accreted Wrangellia oceanic plateau. Geosphere 6, 47–73. https://doi.org/10.1130/GES00212.1

Guiraud, R., 1998. Mesozoic rifting and basin inversion along the northern African Tethyan margin: an overview. Geol. Soc. London, Spec. Publ. 132, 217–229.

Haas, J., Budai, T., Raucsik, B., 2012. Climatic controls on sedimentary environments in the Triassic of the Transdanubian. Palaeogeogr. Palaeoclimatol. Palaeoecol. 353–355, 31–44. https://doi.org/10.1016/j.palaeo.2012.06.031

Haas, J., Lukoczki, G., Budai, T., Demény, A., 2015. Genesis of Upper Triassic peritidal dolomites in the Transdanubian Range, Hungary. Facies 61, 1–28. https://doi.org/10.1007/s10347-015-0435-7

Hadouth, S., Bouaziz, S., Lathuili, B., 2016. Journal of African Earth Sciences Basin geodynamics and sequence stratigraphy of Upper Triassic to Lower Jurassic deposits of Southern Tunisia 117. https://doi.org/10.1016/j.jafrearsci.2016.01.029

Handy, M.R., Schmid, S.M., Bousquet, R., Kissling, E., Bernoulli, D., 2010. Earth-Science Reviews Reconciling plate-tectonic reconstructions of Alpine Tethys with the geological – geophysical record of spreading and subduction in the Alps. Earth Sci. Rev. 102, 121–158. https://doi.org/10.1016/j.earscirev.2010.06.002

Haq, B.U., 2018. Triassic Eustatic Variations Reexamined. GSA Today 28, 4–9.

Hardenbol, J., Thierry, J., Farley, M.B., Jacquin, T., Graciansky, P.-C. de, Vail, P.R., 1998. Mesozoic and Cenozoic Sequence Chronostratigraphic Framework of European Basins. Mesozoic Cenozoic Seq. Stratigr. Eur. Basins. https://doi.org/10.2110/pec.98.02.0003

Harnois, L., 1988. The CIW index: A new chemical index of weathering. Sediment. Geol. 55, 319–322. https://doi.org/10.1016/0037-0738(88)90137-6

Hausmann, I.M., Nützel, A., Roden, V.J., Reich, M., 2021. Palaeoecology of tropical marine invertebrate assemblages from the Late Triassic of Misurina, Dolomites, Italy. Acta Palaeontol. Pol. 66, 1–50. https://doi.org/10.4202/APP.00659.2019

Hochuli, P.A., Vigran, J.O., 2010. Climate variations in the Boreal Triassic — Inferred from palynological records from the Barents Sea. Palaeogeogr. Palaeoclimatol. Palaeoecol. 290, 20–42. https://doi.org/10.1016/j.palaeo.2009.08.013

Horn, B.L.D., Goldberg, K., Schultz, C.L., 2018. A loess deposit in the Late Triassic of southern Gondwana, and its significance to global paleoclimate. J. South Am. Earth Sci. 81, 189–203. https://doi.org/10.1016/j.jsames.2017.11.017

Hornung, T., Brandner, R., Krystyn, L., Joachimski, M.M., Keim, L., 2007a. Multistratigraphic constraints on the NW Tethyan “Carnian Crisis,” in: The Global Triassic. pp. 59–67.

Hornung, T., Krystyn, L., Brandner, R., 2007b. A Tethys-wide mid-Carnian (Upper Triassic) carbonate productivity crisis: Evidence for the Alpine Reingraben Event from Spiti (Indian Himalaya)? J. Asian Earth Sci. 30, 285–302. https://doi.org/10.1016/j.jseaes.2006.10.001

Huang, B., Yan, Y., Piper, J.D.A., Zhang, D., Yi, Z., Yu, S., Zhou, T., 2018. Paleomagnetic constraints on the paleogeography of the East Asian blocks during Late Paleozoic and Early

Mesozoic times. Earth-Science Rev. 186, 8–36. https://doi.org/https://doi.org/10.1016/j.earscirev.2018.02.004

Ikeda, M., Ozaki, K., Legrand, J., 2020. Impact of 10-Myr scale monsoon dynamics on Mesozoic climate and ecosystems. Sci. Rep. 10, 1–10. https://doi.org/10.1038/s41598-020-68542-w

Ilyina, N. V, Egorov, A.Y., Ilyina, N. V, Egorov, A.Y., 2016. The Upper Triassic of northern Middle Siberia : stratigraphy and palynology The Upper Triassic of northern Middle Siberia : stratigraphy and palynology 8369. https://doi.org/10.1111/j.1751-8369.2008.00083.x

Imrecke, D.B., Robinson, A.C., Owen, L.A., Chen, J., Schoenbohm, L.M., Hedrick, K.A., Lapen, T.J., Li, W., Yuan, Z., 2019. Mesozoic evolution of the eastern Pamir. Lithosphere 11, 560–580.

Jelen, B., Kusej, J., 1982. Quantitative palynologîcal analysis of Julian clastic rocks from the lead-zinc deposit of Mežica Kvantitativna palinolo š ka analiza julijskih klasti č nih kamenin v me ž i š kem rudi šč u Quantitative palynologîcal analysis of Julian clastic rocks from t. Geologija.

Jewuła, K., Matysik, M., Paszkowski, M., Szulc, J., 2019. The late Triassic development of playa, gilgai floodplain, and fluvial environments from Upper Silesia, southern Poland. Sediment. Geol. 379, 25–45. https://doi.org/10.1016/j.sedgeo.2018.11.005

Jian, X., Weislogel, A., Pullen, A., 2019. Triassic Sedimentary Filling and Closure of the Eastern Paleo-Tethys Ocean: New Insights From Detrital Zircon Geochronology of Songpan-Ganzi, Yidun, and West Qinling Flysch in Eastern Tibet. Tectonics 38, 767–787. https://doi.org/https://doi.org/10.1029/2018TC005300

Jiang, D., Wang, Y., Robbins, E., Wei, J., and Tian, N. (2008). Mesozoic non-marine petroleum source rocks determined by palynomorphs in the Tarim Basin, Xinjiang, northwestern China. Geological Magazine, 145(6), 868-885. doi:10.1017/S0016756808005384

Jiang, H., Yuan, J., Chen, Y., Ogg, J.G., Yan, J., 2019. Synchronous onset of the Mid-Carnian Pluvial Episode in the East and West Tethys: Conodont evidence from Hanwang, Sichuan, South China. Palaeogeogr. Palaeoclimatol. Palaeoecol. 520, 173–180. https://doi.org/10.1016/j.palaeo.2019.02.004

Jin, X., Shi, Z., Rigo, M., Franceschi, M., Preto, N., 2018. Carbonate platform crisis in the Carnian (Late Triassic) of Hanwang (Sichuan Basin, South China): Insights from conodonts and stable isotope data. J. Asian Earth Sci. 164, 104–124. https://doi.org/10.1016/j.jseaes.2018.06.021

Jin, X., McRoberts, C.A., Shi, Z., Mietto, P., Rigo, M., Roghi, G., Manfrin, S., Franceschi, M., Preto, N., 2019. The aftermath of the CPE and the Carnian–Norian transition in northwestern Sichuan basin, South China. J. Geol. Soc. London. 176, 179–196. https://doi.org/10.1144/jgs2018-104

Jin, X., Gianolla, P., Shi, Z., Franceschi, M., Caggiati, M., Du, Y., Preto, N., 2020. Synchronized changes in shallow water carbonate production during the Carnian Pluvial Episode (Late Triassic) throughout Tethys. Glob. Planet. Change 184, 103035. https://doi.org/10.1016/j.gloplacha.2019.103035

Jin, X., Caggiati, M., Franceschi, M., Wall, C.J., Liu, G., Schmitz, M.D., Gianolla, P., Ogg, J.G., Lu, G., Shi, Z., 2021. Middle Triassic lake deepening in the Ordos Basin of North China linked with global sea-level rise 207. https://doi.org/10.1016/j.gloplacha.2021.103670

Jin, X., Franceschi, M., Martini, R., Shi, Z., Gianolla, P., Rigo, M., Wall, C.J., Schmitz, M.D., Lu, G., Du, Y., Huang, X., Preto, N., 2022. Eustatic sea-level fall and global fluctuations in carbonate production during the Carnian Pluvial Episode. Earth Planet. Sci. Lett. 594, 117698. https://doi.org/10.1016/j.epsl.2022.117698

Jolivet, M., Heilbronn, G., Robin, C., Barrier, L., Bourquin, S., Guo, Z., Jia, Y., Guerit, L., Yang, W., Fu, B., 2013. Advances in Geosciences Reconstructing the Late Palaeozoic – Mesozoic topographic evolution of the Chinese Tian Shan: available data and remaining uncertainties. Adv. Geosci. 37, 7–18. https://doi.org/10.5194/adgeo-37-7-2013

Keim, L., Brandner, R., 2001. Facies interfingering and synsedimentary tectonics on late Ladinian–early Carnian carbonate platforms (Dolomites, Italy). Int. J. Earth Sci. 90, 813–830.

Keim, L., Brandner, R., Krystyn, L., Mette, W., 2001. Termination of carbonate slope progradation: An example from the Carnian of the Dolomites, Northern Italy. Sediment. Geol. 143, 303–323. https://doi.org/10.1016/S0037-0738(01)00106-3

Keim, L., Schlager, W., 1999. Automicrite facies on steep slopes (Triassic, Dolomites, Italy). Facies 41, 15–25. https://doi.org/10.1007/bf02537457

Keim, L., Spötl, C., Brandner, R.R., 2006. The aftermath of the Carnian carbonate platform demise: A basinal perspective (Dolomites, Southern Alps). Sedimentology 53, 361–386. https://doi.org/10.1111/j.1365-3091.2006.00768.x

Kent, D. V., Malnis, P.S., Colombi, C.E., Alcober, O.A., Martínez, R.N., 2014. Age constraints on the dispersal of dinosaurs in the Late Triassic from magnetochronology of the Los. Proc. Natl. Acad. Sci. U. S. A. 111. https://doi.org/10.1073/pnas.1402369111

Kent, D. V., Olsen, P.E., Muttoni, G., 2017. Astrochronostratigraphic polarity time scale (APTS) for the Late Triassic and Early Jurassic from continental sediments and correlation with standard marine stages. Earth-Science Rev. 166, 153–180. https://doi.org/10.1016/j.earscirev.2016.12.014

Kent, D. V., Olsen, P.E., Lepre, C., Rasmussen, C., Mundil, R., Gehrels, G.E., Giesler, D., Irmis, R.B., Geissman, J.W., Parker, W.G., 2019. Magnetochronology of the Entire Chinle Formation (Norian Age) in a Scientific Drill Core From Petrified Forest National Park (Arizona, USA) and Implications for Regional and Global Correlations in the Late Triassic. Geochemistry, Geophys. Geosystems 20, 4654–4664. https://doi.org/10.1029/2019GC008474

Klausen, T.G., Nyberg, B., Helland-hansen, W., 2019. The largest delta plain in Earth's history. Geology 47, 1–5. https://doi.org/10.1130/G45507.1/4665819/g45507.pdf

Kohút, M., Hofmann, M., Havrila, M., Linnemann, U., Havrila, J., 2017. Tracking an upper limit of the "Carnian Crisis" and/or Carnian stage in the Western Carpathians (Slovakia). Int. J. Earth Sci. 107, 321–335. https://doi.org/10.1007/s00531-017-1491-8

Kolar-Jurkovšek, T., Jurkovšek, B., 2009. Holothurian sclerites of Carnian strata in the Mežica area, Slovenia. Geologija 52, 5–10. https://doi.org/10.5474/geologija.2009.001

Kolar-Jurkovšek, T., Jurkovšek, B., 2010. New paleontological evidence of the Carnian strata in the Mežica area (Karavanke Mts, Slovenia): Conodont data for the Carnian Pluvial Event. Palaeogeogr. Palaeoclimatol. Palaeoecol. 290, 81–88. https://doi.org/10.1016/j.palaeo.2009.06.015

Korngreen, D., Benjamini, C., 2011. Platform to shelf edge transect, Triassic of northern Israel, North Arabian Plate. Sediment. Geol. 236, 164–184. https://doi.org/10.1016/j.sedgeo.2011.01.004

Korngreen, D., Benjamini, C., 2013. Tectonophysics Stratigraphic evidence for shear in structural development of the Triassic Levant margin : New borehole data on the epicontinental to deep marine transition in Israel. Tectonophysics 591, 3–15. https://doi.org/10.1016/j.tecto.2011.11.017

Kos'ko, M., Korago, E., 2009. Review of geology of the New Siberian Islands between the Laptev and the East Siberian Seas , North East Russia. Stephan Mueller Spec. Publ. Ser. 4, 45–64.

Kováč, M., Márton, E.M.Ő., Klučiar, T., Vojtko, R., 2018. Miocene basin opening in relation to the north-eastward tectonic extrusion of the ALCAPA Mega-Unit. Geol. Carpathica 69, 254–263. https://doi.org/10.1515/geoca-2018-0015

Kozur, H. W. 2003. Integrated ammonoid, conodont and radiolarian zonation of the Triassic and some remarks to stage/substage subdivision and the numeric age of the Triassic stages. Albertiana, 28, 57–83.

Kozur, H.W., Bachmann, G.H., 2010. The Middle Carnian Wet Intermezzo of the Stuttgart Formation (Schilfsandstein), Germanic Basin. Palaeogeogr. Palaeoclimatol. Palaeoecol. 290, 107–119. https://doi.org/10.1016/j.palaeo.2009.11.004

Krystyn, L., Bouquerel, H., Kuerschner, W., Richoz, S., Gallet, Y., 2007. Proposal for a Candidate Gssp for the Base of the Rhaetian Stage. Nat. Hist. 41, 164–173.

Krystyn, L., Balini, M., Aghababalou, B.S., Hairapetian, V., 2019. Norian Ammonoids From The Nayband Formation (Iran) And Their Bearing On Late Triassic Sedimentary And Geodynamic History Of The Iran Plate n 125, 231–248.

Kustatscher, E., van Konijnenburg-van Cittert, J.H.A., Roghi, G., 2010. Macrofloras and palynomorphs as possible proxies for palaeoclimatic and palaeoecological studies: A case study from the Pelsonian (Middle Triassic) of Kühwiesenkopf/Monte Prà della Vacca (Olang Dolomites, N-Italy). Palaeogeogr. Palaeoclimatol. Palaeoecol. 290, 71–80. https://doi.org/10.1016/j.palaeo.2009.07.001

Labandeira, C.C., Anderson, J.M., Anderson, H.M., 2018. Expansion of arthropod herbivory in late Triassic South Africa: the Molteno Biota, Aasvoëlberg 411 site and developmental biology of a gall, in: Tanner, L.H. (Ed.), The Late Triassic World. Springer, pp. 623–719.

Langer, M.C., Ramezani, J., Da, Á.A.S., 2018. U-Pb age constraints on dinosaur rise from south Brazil. Gondwana Res. 57, 133–140. https://doi.org/10.1016/j.gr.2018.01.005

Lanson B., Meunier A., 1995. La transformation des interstratifiés ordonnés (S>1) illite-smectite en illite dans les séries diagénétiques. Etat des connaissances et perspectives. Bull. Cent. Rech. Explor. Elf Aquitaine, 19, p. 149-165.

Lanson, B., Beaufort, D., Berger, G., Bauer, A., Cassagnabère, A., Meunier, A., 2002. Authigenic kaolin and illitic minerals during burial diagenesis of sandstones: a review. Clay Miner. 37, 1–22. https://doi.org/10.1180/0009855023710014

Lara, M.B., Bustos-Escalona, E.L., Mancuso, A.C., Arcucci, A., 2021. Upper Triassic hemipterans from the south-western Gondwana: Taxonomical, paleobiological, and paleogeographical implications. J. South Am. Earth Sci. 107, 103119. https://doi.org/10.1016/j.jsames.2020.103119

Lein, R., Krystyn, L., Richoz, S., Lieberman, H., 2012. Middle Triassic platform / basin transition along the Alpine passive continental margin facing the Tethys Ocean - The Gamsstein : The rise and fall of a Middle Triassic platform / basin transition along the Alpine passive continental margin facing the Tet. F. Trip Guid. 29th IAS Meet. Sedimentol. Schladming, Austria.

Leleu, S., Hartley, A.J., 2010. Controls on the stratigraphic development of the Triassic Fundy Basin, Nova Scotia: Implications for the tectonostratigraphic evolution of Triassic Atlantic rift basins. J. Geol. Soc. London. 167, 437–454. https://doi.org/10.1144/0016-76492009-092

Leleu, S., Van Lanen, X.M.T., Hartley, A.J., 2010. Controls on the Architecture of a Triassic Sandy Fluvial System, Wolfville Formation, Fundy Basin, Nova Scotia, Canada: Implications for the Interpretation and Correlation of Ancient Fluvial Successions. J. Sediment. Res. 80, 867–883. https://doi.org/10.2110/jsr.2010.080

Leleu, S., Hartley, A.J., van Oosterhout, C., Kennan, L., Ruckwied, K., Gerdes, K., 2016. Structural, stratigraphic and sedimentological characterisation of a wide rift system: The Triassic rift system of the Central Atlantic Domain. Earth-Science Rev. 158, 89–124. https://doi.org/10.1016/j.earscirev.2016.03.008

Li, Z., Chen, Z.Q., Zhang, F., Ogg, J.G., Zhao, L., 2020. Global carbon cycle perturbations triggered by volatile volcanism and ecosystem responses during the Carnian Pluvial Episode (late Triassic). Earth-Science Rev. 211, 103404. https://doi.org/10.1016/j.earscirev.2020.103404

Li, L., Kürschner, W.M., Lu, N., Chen, H., An, P., Wang, Y., 2022. Review of Palaeobotany and Palynology Palynological record of the Carnian Pluvial Episode from the northwestern Sichuan Basin, SW China. Rev. Palaeobot. Palynol. 304. https://doi.org/10.1016/j.revpalbo.2022.104704

Liang, X., Sun, X., Wang, G., Gao, J., and An, X. (2020). Sedimentary evolution and provenance of the late Permian–middle Triassic Raggyorcaka deposits in North Qiangtang (Tibet, Western China): Evidence for a forearc basin of the Longmu Co-Shuanghu Tethys Ocean. Tectonics, 39, e2019TC005589. https://doi.org/10.1029/2019TC005589

Lindström, S., Irmis, R.B., Whiteside, J.H., Smith, N.D., Nesbitt, S.J., Turner, A.H., 2016. Palynology of the upper Chinle Formation in northern New Mexico, U.S.A.: Implications for biostratigraphy and terrestrial ecosystem change during the Late Triassic (Norian-Rhaetian). Rev. Palaeobot. Palynol. 225, 106–131. https://doi.org/10.1016/j.revpalbo.2015.11.006

Lindström, S., Erlström, M., Piasecki, S., Henrik, L., Mathiesen, A., 2017. Palynology and terrestrial ecosystem change of the Middle Triassic to lowermost Jurassic succession of the

eastern Danish Basin. Rev. Palaeobot. Palynol. 244, 65–95. https://doi.org/10.1016/j.revpalbo.2017.04.007

Linol, B., de Wit, M.J., Barton, E., Guillocheau, F., de Wit, M.C.J., Colin, J.-P., 2015. Paleogeography and Tectono-Stratigraphy of Carboniferous-Permian and Triassic 'Karoo-Like' Sequences of the Congo Basin BT - Geology and Resource Potential of the Congo Basin, in: de Wit, M.J., Guillocheau, François, de Wit, M.C.J. (Eds.), . Springer Berlin Heidelberg, Berlin, Heidelberg, pp. 111–134. https://doi.org/10.1007/978-3-642-29482-2_7

Liu, D., Li, H., Ge, C., Bai, M., Wang, Y., Pan, J., Zheng, Y., Wang, P., Liu, F., Wang, S., 2021. Northward Growth of the West Kunlun Mountains: Insight From the Age–Elevation Relationship of New Apatite Fission Track Data. Front. Earth Sci. 9, 1–13. https://doi.org/10.3389/feart.2021.784812

López-Gómez, J., Escudero-Mozo, M.J., Martín-Chivelet, J., Arche, A., Lago, M., Galé, C., 2017. Western Tethys continental-marine responses to the Carnian Humid Episode: Palaeoclimatic and palaeogeographic implications. Glob. Planet. Change 148, 79–95. https://doi.org/10.1016/j.gloplacha.2016.11.016

Lord, G.S., Solvi, K.H., Ask, M., Mørk, A., Hounslow, M.W., Paterson, N.W., 2014. The Hopen Member: A new member of the Triassic De Geerdalen Formation, Svalbard. Nor. Pet. Dir. Bull. 11, 81–96.

Lu, J., Zhang, P., Dal Corso, J., Yang, M., Wignall, P.B., Greene, S.E., Shao, L., Lyu, D., Hilton, J., 2021. Volcanically driven lacustrine ecosystem changes during the Carnian Pluvial Episode (Late Triassic). Proc. Natl. Acad. Sci. U. S. A. 118, 1–8. https://doi.org/10.1073/pnas.2109895118

Lucas, S.G., Tanner, L.H., 2018. Record of the carnian wet episode in strata of the chinle group, western USA. J. Geol. Soc. London. 175, 1004–1011. https://doi.org/10.1144/jgs2017-134

Lukeneder, S., Lukeneder, A., 2014. A new ammonoid fauna from the Carnian (Upper Triassic) Kasimlar Formation of the Taurus Mountains (Anatolia, Turkey). Palaeontology 57, 357–396. https://doi.org/10.1111/pala.12070

Lukeneder, S., Lukeneder, A., Harzhauser, M., İslamoğlu, Y., Krystyn, L., Lein, R., 2012. A delayed carbonate factory breakdown during the Tethyan-wide Carnian Pluvial Episode along the Cimmerian terranes (Taurus, Turkey). Facies 58, 279–296. https://doi.org/10.1007/s10347-011-0279-8

Lunn, G.A., 2020. Reply to 'Dating and correlation of the Baluti Formation, Kurdistan, IRAQ: Implications for the regional recognition of a Carnian "marker dolomite", and a review of the Triassic to Early Jurassic sequence stratigraphy of the Arabian Plate'. J. Pet. Geol. 43, 109–125. https://doi.org/https://doi.org/10.1111/jpg.12752

Lutz, A., Gnaedinger, S., Mancuso, A., Crisafulli, A., 2011. Paleoflora de la Formación los Rastros (Triásico Medio), Provincia de San Juan, Argentina. Consideraciones Taxonómicas y Tafonómicas. Ameghiniana 48, 568–588.

MacKevett, E.M., 1971 - Stratigraphy and general geology of the McCarthy C-5 quadrangle, Alaska.Geological Survey Bulletin, 1323, 1-35

Mader, N.K., Redfern, J., El Ouataoui, M., 2017. Sedimentology of the Essaouira Basin (Meskala Field) in context of regional sediment distribution patterns during upper Triassic

pluvial events. J. African Earth Sci. 130, 293–318. https://doi.org/10.1016/j.jafrearsci.2017.02.012

Mancuso, A.C., Marsicano, C.A., 2008. Paleoenvironments and taphonomy of a Triassic lacustrine system (Los Rastros Formation, central-western Argentina). Palaios 23, 535–547. https://doi.org/10.2110/palo.2007.p07-064r

Mancuso, A.C., Caselli, A.T., 2012. Paleolimnology evolution in rift basins: the Ischigualasto–Villa Unión Basin (Central-Western Argentina) during the Triassic. Sediment. Geol. 275–276, 38–54. https://doi.org/10.1016/j.sedgeo.2012.07.012

Mancuso, A.C., Benavente, C.A., Irmis, R.B., Mundil, R., 2020. Evidence for the Carnian Pluvial Episode in Gondwana: New multiproxy climate records and their bearing on early dinosaur diversification. Gondwana Res. https://doi.org/https://doi.org/10.1016/j.gr.2020.05.009

Mancuso, A.C., Irmis, R.B., Pedernera, T.E., Gaetano, L.C., Benavente, C.A., Breeden, B.T., 2022. Paleoenvironmental and Biotic Changes in the Late Triassic of Argentina: Testing Hypotheses of Abiotic Forcing at the Basin Scale. Front. Earth Sci. 10, 1–27. https://doi.org/10.3389/feart.2022.883788

Mandl, G.W., 2000. The Alpine sector of the Tethyan shelf - Examples of Triassic to Jurassic sedimentation and deformation from the. Mitt. Osterr. Geol. Ges.

Mantle, D.J., Riding, J.B., Hannaford, C., 2020. Late Triassic dinoflagellate cysts from the Northern Carnarvon Basin, Western Australia. Rev. Palaeobot. Palynol. 104254. https://doi.org/10.1016/j.revpalbo.2020.104254

Maron, M., Rigo, M., Bertinelli, A., Katz, M.E., Godfrey, L., Zaffani, M., Muttoni, G., 2015. chemostratigraphy of the Pignola-Abriola section : New constraints for the Norian-Rhaetian boundary 1–13. https://doi.org/10.1130/B31106.1

Maron, M., Muttoni, G., Dekkers, M.J., Mazza, M., Roghi, G., Breda, A., Krijgsman, W., Rigo, M., 2017. Contribution to the magnetostratigraphy of the Carnian : new magneto-biostratigraphic constraints from Pignola-2 and Dibona marine sections , Italy. Newsletters Stratigr. 50, 187–203. https://doi.org/10.1127/nos/2017/0291

Maron, M., Muttoni, G., Rigo, M., Gianolla, P., Kent, D. V, 2019. New magnetobiostratigraphic results from the Ladinian of the Dolomites and implications for the Triassic geomagnetic polarity timescale. Palaeogeogr. Palaeoclimatol. Palaeoecol. 517, 52–73. https://doi.org/10.1016/j.palaeo.2018.11.024

Marsicano, C.A., Irmis, R.B., Mancuso, A.C., Mundil, R., Chemale, F., 2016. The precise temporal calibration of dinosaur origins. Proc. Natl. Acad. Sci. U. S. A. 113. https://doi.org/10.1073/pnas.1512541112

Martindale, R.C., Zonneveld, J.P., Bottjer, D.J., 2010. Microbial framework in Upper Triassic (Carnian) patch reefs from Williston Lake, British Columbia, Canada. Palaeogeogr. Palaeoclimatol. Palaeoecol. 297, 609–620. https://doi.org/10.1016/j.palaeo.2010.09.009

Martínez, R.N., Apaldetti, C., Alcober, O.A., Colombi, C.E., Sereno, P.C., Fernandez, E., Malnis, P.S., Correa, G.A., Abelin, D., 2013. Vertebrate succession in the Ischigualasto Formation. J. Vertebr. Paleontol. 32, 10–30. https://doi.org/10.1080/02724634.2013.818546

Martinez, R.N., Sereno, P.C., Alcober, O.A., Colombi, C.E., Renne, P.R., Montañez, I.P., Currie, B.S., 2011. A basal dinosaur from the dawn of the dinosaur era in southwestern pangaea. Science (80). 331, 206–210. https://doi.org/10.1126/science.1198467

Masetti, D., Neri, C., Bosellini, A., 1991. Deep-water asymmetric cycles and progradation of carbonate platforms governed by high-frequency eustatic oscillations (Triassic of the Dolomites, Italy). Geology 19, 336–339. https://doi.org/10.1130/0091-7613(1991)019<0336:DWACAP>2.3.CO;2

Mazaheri-Johari, M., 2021. Carnian Pluvial Episode in Iran (Turan Plate and Iran Plate) and western Tethys domain. PhD Thesis. University of Ferrara.

Mazaheri-Johari, M., Gianolla, P., Mather, T.A., Frieling, J., Chu, D., Dal Corso, J., 2021. Mercury deposition in Western Tethys during the Carnian Pluvial Episode (Late Triassic). Sci. Rep. 11, 1–10. https://doi.org/10.1038/s41598-021-96890-8

Mazaheri-johari, M., Roghi, G., Caggiati, M., Kustatscher, E., Ghasemi-nejad, E., Zanchi, A., Gianolla, P., 2022. Disentangling climate signal from tectonic forcing : The Triassic Aghdarband Basin (Turan Domain , Iran). Palaeogeogr. Palaeoclimatol. Palaeoecol. 586, 110777. https://doi.org/10.1016/j.palaeo.2021.110777

McKie, T., 2014. Climatic and tectonic controls on Triassic dryland terminal fluvial system architecture , central North Sea, in: Depositional Systems to Sedimentary Successions on the Norwegian Continental Margin. pp. 19–58.

McLennan, S.M., 1993. Weathering and Global Denudation. J. Geol. 101, 295–303.

McLennan, S.M., Taylor, S.R., McCulloch, M.T., Maynard, J.B., 1990. Geochemical and NdSr isotopic composition of deep-sea turbidites: Crustal evolution and plate tectonic associations. Geochim. Cosmochim. Acta 54, 2015–2050. https://doi.org/10.1016/0016-7037(90)90269-Q

McLennan, S.M., Hemming, S., McDaniel, D.K., Hanson, G.N., 1993. Geochemical approaches to sedimentation, provenance and tectonics. Spec. Pap. Soc. Am. 284, 21–40.

Meilijson, A., Bialik, O.M., Benjamini, C., 2015. Stromatolitic biotic systems in the mid-Triassic of Israel – a product of stress on an epicontinental margin. Palaeogeogr. Palaeoclimatol. Palaeoecol. 440, 696–711. https://doi.org/10.1016/j.palaeo.2015.09.030

Meunier, A., 2005. Clays. https://doi.org/10.1007/b138672

Mietto, P., Manfrin, S., 1995. A high resolution Middle Triassic ammonoid standard scale in the Tethys Realm. A preliminary report. Bull. - Soc. Geol. Fr. 166, 539–563. https://doi.org/10.2113/gssgfbull.166.5.539

Mietto, P., Manfrin, S., Preto, N., Rigo, M., Roghi, G., Gianolla, P., Posenato, R., Muttoni, G., Nicora, A., Buratti, N., Cirilli, S., Spötl, C., Ramezani, J., Bowring, S.A., 2012. The Global Boundary Stratotype Section and Point (GSSP) of the Carnian Stage (Late Triassic) at Prati Di Stuores / Stuores Wiesen Section (Southern Alps , NE Italy). Episodes 35, 414–430.

Mietto, P., Jin, X., Manfrin, S., Lu, G., Shi, Z., Gianolla, P., Huang, X., Preto, N., 2021. Onset of sedimentation near the Carnian / Norian boundary in the northwestern Sichuan Basin : New evidence from ammonoid biostratigraphy and zircon U – Pb geochronology.

Palaeogeogr. Palaeoclimatol. Palaeoecol. 567, 110246. https://doi.org/10.1016/j.palaeo.2021.110246

Miller, C.S., Baranyi, V., 2019. Triassic Climates. Ref. Modul. Earth Syst. Environ. Sci. 0–11. https://doi.org/10.1016/b978-0-12-409548-9.12070-6

Miller, C.S., Peterse, F., Da Silva, A.C., Baranyi, V., Reichart, G.J., Kürschner, W.M., 2017. Astronomical age constraints and extinction mechanisms of the Late Triassic Carnian crisis. Sci. Rep. 7, 1–7. https://doi.org/10.1038/s41598-017-02817-7

Milroy, P., Wright, V.P., Simms, M.J., 2019. Dryland continental mudstones: Deciphering environmental changes in problematic mudstones from the Upper Triassic (Carnian to Norian) Mercia Mudstone Group, south-west Britain. Sedimentology 66, 2557–2589. https://doi.org/10.1111/sed.12626

Moisan, P., Voigt, S., Pott, C., Buchwitz, M., Schneider, J.W., Kerp, H., 2011. Cycadalean and bennettitalean foliage from the Triassic Madygen Lagerstätte (SW Kyrgyzstan, Central Asia). Rev. Palaeobot. Palynol. 164, 93–108. https://doi.org/10.1016/j.revpalbo.2010.11.008

Moix, P., Beccaletto, L., Kozur, H.W., Hochard, C., Rosselet, F., Stampfli, G.M., 2008. A new classification of the Turkish terranes and sutures and its implication for the paleotectonic history of the region 451, 7–39. https://doi.org/10.1016/j.tecto.2007.11.044

Montenat, C., 2009. The Mesozoic of Afghanistan. Geoarabia 14, 145–208. https://doi.org/10.2113/geoarabia1401147

Moore, D.M., Reynolds Jr, R.C., 1989. X-Ray Diffraction and the Identification and Analysis of Clay Minerals.

Mueller, S., Veld, H., Nagy, J., Kürschner, W.M., 2014. Depositional history of the Upper Triassic Kapp Toscana Group on Svalbard , Norway , inferred from palynofacies analysis and organic geochemistry. Sediment. Geol. 310, 16–29. https://doi.org/10.1016/j.sedgeo.2014.06.003

Mueller, S., Hounslow, M.W., Kürschner, W.M., 2016a. Integrated stratigraphy and palaeoclimate history of the Carnian Pluvial Event in the Boreal realm; new data from the Upper Triassic Kapp Toscana Group in central Spitsbergen (Norway). J. Geol. Soc. London. 173, 186–202. https://doi.org/10.1144/jgs2015-028

Mueller, S., Krystyn, L., Kürschner, W.M., 2016b. Climate variability during the Carnian Pluvial Phase — A quantitative palynological study of the Carnian sedimentary succession at Lunz am. Palaeogeogr. Palaeoclimatol. Palaeoecol. 441, 198–211. https://doi.org/10.1016/j.palaeo.2015.06.008

Mukherjee, D., Ray, S., 2012. Taphonomy of an Upper Triassic vertebrate bonebed: A new rhynchosaur (Reptilia; Archosauromorpha) accumulation from India. Palaeogeogr. Palaeoclimatol. Palaeoecol. 333–334, 75–91. https://doi.org/10.1016/j.palaeo.2012.03.010

Nakada, R., Ogawa, K., Suzuki, N., Takahashi, S., Takahashi, Y., 2014. Late Triassic compositional changes of aeolian dusts in the pelagic Panthalassa : Response to the continental climatic change. Palaeogeogr. Palaeoclimatol. Palaeoecol. 393, 61–75. https://doi.org/10.1016/j.palaeo.2013.10.014

Neri, C., Stefani, M., 1988. Sintesi cronostratigrafica e sequenziale dell'evoluzione permiana superiore e triassica delle Dolomiti. Mem. della Soc. Geol. Ital. 53, 417–463.

Neri, C., Gianolla, P., Furlanis, S., Caputo, R., Bosellini, A., 2007. Note Illustrative della Carta Geologica d'Italia alla scala 1:50.000. Foglio 029 Cortina d'Ampezzo.

Nesbitt, H.W., Markovics, G., price, R.C., 1980. Chemical processes affecting alkalis and alkaline earths during continental weathering. Geochim. Cosmochim. Acta 44, 1659–1666. https://doi.org/10.1016/0016-7037(80)90218-5

Nesbitt, H.W., Young, G.M., 1982. Early Proterozoic climates and plate motions inferred from major element chemistry of lutites. Nature 299, 715–717.

Nozaki, T., Nikaido, T., Onoue, T., Takaya, Y., Sato, K., Kimura, J.I., Chang, Q., Yamashita, D., Sato, H., Suzuki, K., Kato, Y., Matsuoka, A., 2019. Triassic marine Os isotope record from a pelagic chert succession, Sakahogi section, Mino Belt, southwest Japan. J. Asian Earth Sci. X 1, 100004. https://doi.org/10.1016/j.jaesx.2018.100004

Ogg, J.G., 2015. The mysterious Mid-Carnian "Wet Intermezzo" global event. J. Earth Sci. 26, 181–191. https://doi.org/10.1007/s12583-015-0527-x

Ogg, J. G., Chen, Z. Q., Orchard, M. J., Jiang, H. S. (2020). The Triassic Period. In *Geologic Time Scale 2020* (pp. 903-953). ElsevierOrchard, M.J., 2010. Triassic conodonts and their role in stage boundary definition. Geol. Soc. Spec. Publ. 334, 139–161. https://doi.org/10.1144/SP334.7

Orchard, M.J., 2019. The Carnian-Norian boundary GSSP candidate at Black Bear Ridge, British Columbia, Canada: update, correlation, and conodont taxonomy. Albertiana 45, 50–68.

Ordoñez, M. de los A., Marsicano, C.A., Mancuso, A.C., 2020. New specimen of Dinodontosaurus (Therapsida, Anomodontia) from west-central Argentina (Chañares Formation) and a reassessment of the Triassic Dinodontosaurus Assemblage Zone of southern South America. J. South Am. Earth Sci. 100, 102597. https://doi.org/10.1016/j.jsames.2020.102597

Ortí, F., Pérez-López, A., Salvany, J.M., 2017. Triassic evaporites of Iberia: Sedimentological and palaeogeographical implications for the western Neotethys evolution during the Middle Triassic–Earliest Jurassic. Palaeogeogr. Palaeoclimatol. Palaeoecol. 471, 157–180. https://doi.org/10.1016/j.palaeo.2017.01.025

Parker, A., 1970. An Index of Weathering for Silicate Rocks. Geol. Mag. 107, 501–504. https://doi.org/10.1017/S0016756800058581

Paterson, N.W., Mangerud, G., 2015. Late Triassic (Carnian- Rhaetian) palynology of Hopen, Svalbard. Rev. Palaeobot. Palynol. 220, 98–119. https://doi.org/10.1016/j.revpalbo.2015.05.001

Paterson, N.W., Mangerud, G., 2017. Palynology and depositional environments of the Middle – Late Triassic (Anisian – Rhaetian) Kobbe, Snadd and Fruholmen formations, southern Barents Sea, Arctic Norway. Mar. Pet. Geol. 86, 304–324. https://doi.org/10.1016/j.marpetgeo.2017.05.033

Paterson, N.W., Mangerud, G., 2019. A revised palynozonation for the Middle–Upper Triassic (Anisian–Rhaetian) Series of the Norwegian Arctic. Geol. Mag. 1–25. https://doi.org/10.1017/s0016756819000906

Paterson, N.W., Mangerud, G., Cetean, C.G., Mørk, A., Lord, G.S., Klausen, T.G., Mørkved, P.T., 2016a. A multidisciplinary biofacies characterisation of the Late Triassic (late Carnian-Rhaetian) Kapp Toscana Group on Hopen, Arctic Norway. Palaeogeogr. Palaeoclimatol. Palaeoecol. 464, 16–42. https://doi.org/10.1016/j.palaeo.2015.10.035

Paterson, N.W., Mangerud, G., Mørk, A., 2016b. Late Triassic (early Carnian) palynology of shallow stratigraphical core 7830 / 5-U-1 , offshore Kong Karls Land , Norwegian Arctic offshore Kong Karls Land , Norwegian Arctic. Palynology 6122, 1–25. https://doi.org/10.1080/01916122.2016.1163295

Paterson, N.W., Mangerud, G., Holen, L.H., Landa, J., Lundschien, B.A., Eide, F., 2019. Late Triassic (early Carnian–Norian) palynology of the Sentralbanken High, Norwegian Barents Sea. Palynology 43, 53–75. https://doi.org/10.1080/01916122.2017.1413018

Pattemore G.A. and Rigby J.F. 2005. Fructifications and foliage from the Mesozoic of southeast Queensland. Mem. Qd Mus., 50(2): 329–345.

Pedernera, T.E., Mancuso, A.C., Ottone, E.G., Benavente, C.A., 2020. Paleobotany of the Upper Triassic Los Rastros Formation, Ischigualasto–Villa Unión Basin, La Rioja, Argentina. J. South Am. Earth Sci. 102, 102660. https://doi.org/10.1016/j.jsames.2020.102660

Peng, J., Li, J., Li, W. Slater, S.M., Zhu, H., Vajda, V., 2018. The Triassic to Early Jurassic palynological record of the Tarim Basin, China. Palaeobio Palaeoenv 98, 7–28 https://doi.org/10.1007/s12549-017-0279-y

Peng, J., Slater, S.M., Vajda, V., 2021. A Late Triassic vegetation record from the Huangshanjie Formation, Junggar Basin, China: possible evidence for the Carnian Pluvial Episode. Spec. Publ. https://doi.org/10.1144/SP521-2021-151

Perez Loinaze, V.S., Vera, E.I., Fiorelli, L.E., Desojo, J.B., 2018. Palaeobotany and palynology of coprolites from the Late Triassic Chañares Formation of Argentina: implications for vegetation provinces and the diet of dicynodonts. Palaeogeogr. Palaeoclimatol. Palaeoecol. 502, 31–51. https://doi.org/10.1016/j.palaeo.2018.04.003

Perri, F., 2020. Chemical weathering of crystalline rocks in contrasting climatic conditions using geochemical proxies: An overview. Palaeogeogr. Palaeoclimatol. Palaeoecol. 556, 109873. https://doi.org/10.1016/j.palaeo.2020.109873

Perri, F., Critelli, S., Cavalcante, F., Mongelli, G., Dominici, R., Sonnino, M., De Rosa, R., 2012. Provenance signatures for the Miocene volcaniclastic succession of the Tufiti di Tusa Formation, southern Apennines, Italy. Geol. Mag. 149, 423–442. https://doi.org/10.1017/S001675681100094X

Peybernes, C., Peyrotty, G., Chablais, J., Onoue, T., Yamashita, D., Martini, R., 2020. Birth and death of seamounts in the Panthalassa Ocean: Late Triassic to Early Jurassic sedimentary record at Mount Sambosan, Shikoku, Southwest Japan. Glob. Planet. Change 192, 103250. https://doi.org/10.1016/j.gloplacha.2020.103250

Philipp, R.P., Schultz, C.L., Kloss, H.P., Horn, B.L.D., Soares, M.B., Basei, M.A.S., 2018. Middle Triassic SW Gondwana paleogeography and sedimentary dispersal revealed by

integration of stratigraphy and U-Pb zircon analysis: The Santa Cruz Sequence, Paraná Basin, Brazil. J. South Am. Earth Sci. 88, 216–237. https://doi.org/10.1016/j.jsames.2018.08.018

Pisa, G., Marinelli, M., Viel, G., 1980. Infraraibl Group: a proposal (Southern Calcareous Alps, Italy). Riv. Ital. Paleont. 85, 983–1002.

Placer, L., 2008. Principles of the tectonic subdivision of Slovenia. Geologija 51, 205–217. https://doi.org/10.5474/geologija.2008.021

Plank, T., Langmuir, C.H., 1998. The chemical composition of subducting sediment and its consequences for the crust and mantle. Chem. Geol. 145, 325–394. https://doi.org/10.1016/S0009-2541(97)00150-2

Plašienka, D., 2019. Linkage of the Manín and Klape units with the Pieniny Klippen Belt and Central Western Carpathians: Balancing the ambiguity. Geol. Carpathica 70, 35–61. https://doi.org/10.2478/geoca-2019-0003

Posamentier, H.W., Allen, G.P., 1999. Siliciclastic sequence stratigraphy: concepts and applications., SEPM Conce. ed.

Preto, N., Hinnov, L.A., 2003. Unraveling the origin of carbonate platform cyclothems in the Upper Triassic Dürresntein Formation (Dolomites, Italy). J. Sediment. Res. 73, 774–789. https://doi.org/10.1306/030503730774

Preto, N., Roghi, G., Gianolla, P., 2005. Carnian stratigraphy of the Dogna area (Julian Alps, northern Italy): Tessera of a complex palaeogeography. Boll. della Soc. Geol. Ital. 124, 269–279.

Preto, N., Kustatscher, E., Wignall, P.B., 2010. Triassic climates - State of the art and perspectives. Palaeogeogr. Palaeoclimatol. Palaeoecol. 290, 1–10. https://doi.org/10.1016/j.palaeo.2010.03.015

Preto, N., Willems, H., Guaiumi, C., Westphal, H., 2013. Onset of significant pelagic carbonate accumulation after the Carnian Pluvial Event (CPE) in the western Tethys. Facies 59, 891–914. https://doi.org/10.1007/s10347-012-0338-9

Preto, N., Gianolla, P., Franceschi, M., Gattolin, G., Riva, A., 2017. Geometry and evolution of Triassic high-relief, isolated microbial platforms in the Dolomites, Italy: The Anisian Latemar and Carnian Sella platforms compared. Am. Assoc. Pet. Geol. Bull. 101, 475–483. https://doi.org/10.1306/011817DIG17026

Preto, N., Bernardi, M., Dal Corso, J., Gianolla, P., Kustatscher, E., Roghi, G., Rigo, M., 2019. The carnian pluvial episode in Italy: History of the research and perspectives. Boll. della Soc. Paleontol. Ital. 58, 35–49. https://doi.org/10.4435/BSPI.2019.07

Preto, N., Gianolla, P., Franceschi, M., Gattolin, G., Riva, A., 2021. The depositional architecture of Latemar and Sella, isolated Triassic microbial platforms of the Dolomites, NE Italy, in: Wright, V.P., Della Porta, G. (Eds.), Field Guides to Exceptionally Exposed Carbonate Outcrops. IAS, pp. 209–264.

Ragazzi, E., Roghi, G., Giaretta, A., Gianolla, P., 2003. Classification of amber based on thermal analysis. Thermochim. Acta 404, 43–54. https://doi.org/https://doi.org/10.1016/S0040-6031(03)00062-5

Rakshit, N., Bhat, M.S., Mukherjee, D., Ray, S., 2018. First record of Mesozoic scroll coprolites: classification, characteristics, elemental composition and probable producers. Palaeontology 62, 451–471. https://doi.org/10.1111/pala.12409

Ramirez-Montoya, E., Madhavaraju, J., Monreal, R., 2021. Geochemistry of the sedimentary rocks from the Antimonio and Río Asunción formations, Sonora, Mexico: Implications for weathering, provenance and chemostratigraphy. J. South Am. Earth Sci. 106, 103035. https://doi.org/10.1016/j.jsames.2020.103035

Rasmussen, C., Mundil, R., Irmis, R.B., Geisler, D., Gehrels, G.E., Olsen, P.E., Kent, D. V, Lepre, C., Kinney, S.T., Geissman, J.W., Parker, W.G., 2020. U-Pb zircon geochronology and depositional age models for the Upper Triassic U-Pb zircon geochronology and depositional age models for the Upper Triassic Chinle Formation (Petrified Forest National Park , Arizona , USA): Implications for Late Triassic p. Geol. Soc. Am. Bull. https://doi.org/10.1130/B35485.1

Ray, S., 2015. A new Late Triassic traversodontid cynodont (Therapsida, Eucynodontia) from India. J. Vertebr. Paleontol. 35. https://doi.org/10.1080/02724634.2014.930472

Reolid, M., Márquez-Aliaga, A., Belinchón, M., García-Forner, A., Villena, J., Martínez-Pérez, C., 2018. Ichnological evidence of semi-aquatic locomotion in early turtles from eastern Iberia during the Carnian Humid Episode (Late Triassic). Palaeogeogr. Palaeoclimatol. Palaeoecol. 490, 450–461. https://doi.org/10.1016/j.palaeo.2017.11.025

Retallack, G.J., Veevers, J.J., Morante, R., 1996. Global coal gap between Permian-Triassic extinction and Middle Triassic recovery of peat-forming plants. Bull. Geol. Soc. Am. 108, 195–207. https://doi.org/10.1130/0016-7606(1996)108<0195:GCGBPT>2.3.CO;2

Rigo, M., Preto, N., Roghi, G., Tateo, F., Mietto, P., 2007. A rise in the Carbonate Compensation Depth of western Tethys in the Carnian (Late Triassic): Deep-water evidence for the Carnian Pluvial Event. Palaeogeogr. Palaeoclimatol. Palaeoecol. 246, 188–205. https://doi.org/10.1016/j.palaeo.2006.09.013

Rigo, M., Preto, N., Franceschi, M., Guaiumi, C., 2012a. Proceedings of the Palermo Workshop ` New Developments on Triassic Integrated Stratigraphy ' ' The Upper Triassic in the Lagonegro Basin is re- presented by two formations : the Calcari con Selce (i . e . Cherty Limestone) and the Scisti Silicei (Silice 118, 143–154.

Rigo, M., Trotter, J.A., Preto, N., Williams, I.S., 2012b. Oxygen isotopic evidence for late Triassic monsoonal upwelling in the northwestern Tethys. Geology 40, 515–518. https://doi.org/10.1130/G32792.1

Rigo, M., Mazza, M., Karádi, V., Nicora, A., 2018. New Upper Triassic Conodont Biozonation of the Tethyan Realm, in: The Late Triassic World. pp. 189–235. https://doi.org/10.1007/978-3-319-68009-5_6

Rodrigues, I.C., Mizusaki, A.M.P., Lima, L.G., Maraschin, A.J., 2019. Comparative evolution of clay minerals in southern Paraná Basin (Brazil): Implications for triassic paleoclimate. J. South Am. Earth Sci. 90, 181–190. https://doi.org/10.1016/j.jsames.2018.12.012

Roghi, G., 2004. Palynological investigations in the Carnian of the Cave del Predil area (Julian Alps, NE Italy). Rev. Palaeobot. Palynol. 132, 1–35. https://doi.org/10.1016/j.revpalbo.2004.03.001

Roghi, G., Ragazzi, E., Gianolla, P., 2006. Triassic Amber of the Southern Alps (Italy). Palaios 21, 143–154. https://doi.org/10.2110/palo.2005.p05-68

Roghi, G., Gianolla, P., Minarelli, L., Pilati, C., Preto, N., 2010. Palynological correlation of Carnian humid pulses throughout western Tethys. Palaeogeogr. Palaeoclimatol. Palaeoecol. 290, 89–106. https://doi.org/10.1016/j.palaeo.2009.11.006

Roghi, G., Gianolla, P., Kustatscher, E., Schmidt, A.R., Seyfullah, L.J., 2022. An Exceptionally Preserved Terrestrial Record of LIP Effects on Plants in the Carnian (Upper Triassic) Amber-Bearing Section of the Dolomites, Italy. Front. Earth Sci. 10, 1–18. https://doi.org/10.3389/feart.2022.900586

Roser, B.P., Korsch, R.J., 1988. Provenance signatures of sandstone-mudstone suites determined using discriminant function analysis of major-element data. Chem. Geol. 67, 119–139. https://doi.org/10.1016/0009-2541(88)90010-1

Rossignol, C., Bourquin, S., Hallot, E., Poujol, M., Dabard, M.-P., Martini, R., Villeneuve, M., Cornée, J.-J., Brayard, A., Roger, F., 2018. The Indosinian orogeny: A perspective from sedimentary archives of north Vietnam. J. Asian Earth Sci. 158, 352–380. https://doi.org/https://doi.org/10.1016/j.jseaes.2018.03.009

Rostási, Á., Raucsik, B., Varga, A., 2011. Palaeoenvironmental controls on the clay mineralogy of Carnian sections from the Transdanubian Range (Hungary). Palaeogeogr. Palaeoclimatol. Palaeoecol. 300, 101–112. https://doi.org/10.1016/j.palaeo.2010.12.013

Ruffell, A., Simms, M.J., Wignall, P.B., 2016. The Carnian Humid Episode of the late Triassic: A review. Geol. Mag. 153, 271–284. https://doi.org/10.1017/S0016756815000424

Ruffer, T., Zuhlke, R., 1995. Sequence stratigraphy and sea-level changes in the early to middle Triassic of the Alps: a global comparison, in: Haq, B.U. (Ed.), Sequence Stratigraphy and Depositional Response to Eustatic, Tectonic and Climatic Forcing. Springer Netherlands, Dordrecht, pp. 161–207. https://doi.org/10.1007/978-94-015-8583-5_7

Russo, F., Neri, C., Mastandrea, A., Laghi, G., 1991. Depositional and diagenetic history of the Alpe di Specie (Seelandalpe) fauna (Carnian, Northeastern Dolomites). Facies 25, 187–210. https://doi.org/10.1007/BF02536759

Rutte, D., Ratschbacher, L., Schneider, S., Stübner, K., Stearns, M.A., Gulzar, M.A., Hacker, B.R., 2017. Building the Pamir-Tibetan Plateau — Crustal stacking, extensional collapse, and lateral extrusion in the Central Pamir: 1. Geometry and kinematics. Tectonics 36, 342–384. https://doi.org/10.1002/2016TC004293

Sames, B., Wagreich, M., Conrad, C.P., Iqbal, S., 2020. Aquifer-eustasy as the main driver of short-term sea-level fluctuations during cretaceous hothouse climate phases. Geol. Soc. Spec. Publ. 498, 9–38. https://doi.org/10.1144/SP498-2019-105

Sarkar, S., 1988. Petrology of caliche-derived peloidal calcirudite/ calcarenite in the late triassic maleri formation of the pranhita-Godavari valley, South India. Sediment. Geol. 55, 263–282. https://doi.org/https://doi.org/10.1016/0037-0738(88)90134-0

Schettino, A., Turco, E., 2011. Tectonic history of the Western Tethys since the Late Triassic. Bull. Geol. Soc. Am. 123, 89–105. https://doi.org/10.1130/B30064.1

Schlager, W., 2003. Benthic carbonate factories of the Phanerozoic. Int. J. Earth Sci. 92, 445–464. https://doi.org/10.1007/s00531-003-0327-x

Schmid, Stefan Martin, Schmid, Stefan M, Fügenschuh, B., Kounov, A., Mat, L., Pleuger, J., Schefer, S., Schuster, R., Tomljenovi, B., Ustaszewski, K., Hinsbergen, D.J.J. Van, 2020. Tectonic units of the Alpine collision zone between Eastern Alps and western Gondwana Research Tectonic units of the Alpine collision zone between Eastern Alps and western Turkey. Gondwana Res. 78. https://doi.org/10.1016/j.gr.2019.07.005

Schmidt, A.R., Jancke, S., Lindquist, E.E., Ragazzi, E., Roghi, G., Nascimbene, P.C., Schmidt, K., Wappler, T., Grimaldif, D.A., 2012. Arthropods in amber from the Triassic Period. Proc. Natl. Acad. Sci. U. S. A. 109, 14796–14801. https://doi.org/10.1073/pnas.1208464109

Schoch, R.R., Werneburg, R., Voigt, S., 2020. A Triassic stem-salamander from Kyrgyzstan and the origin of salamanders. Proc. Natl. Acad. Sci. U. S. A. 117. https://doi.org/10.1073/pnas.2001424117

Schöner, R. , Bomfleur, B. , Schneider, J. and Viereck-Götte, L. (2011): A systematic description of the Triassic to Lower Jurassic Section Peak Formation in North Victoria Land (Antarctica). Polarforschung, Alfred Wegener Institute for Polar and Marine Research and German Society of Polar Research, 80 (2), pp. 71-87 .

Schubert, R.J., 1906. Über das angebliche Vorkommen der Carbonformation von Strmica (Rastel Grab) nördlich Knin (Dalmatien). Verhandlungen der k.k. Geol. Reichsanstalt 9, 263–265.

Schubert, R.J., 1909. Das Trias- und Juragebiet im Nordwesten von Knin (Dalmatien). Verhandlungen der k.k. Geol. Reichsanstalt 3, 67–79.

Schultz, S.K., Furlong, C.M., Zonneveld, J.-P., 2016. The Co-Occurence of Trypanites and Glossifungites Substrate-Controlled Trace-Fossil Assemblages In A Triassic Mixed Siliciclastic–Carbonate Depositional System: Baldonnel Formation, Williston Lake, B.C., Canada . J. Sediment. Res. 86, 879–893. https://doi.org/10.2110/jsr.2016.61

Schultz, C.L., Martinelli, A.G., Soares, M.B., Pinheiro, F.L., Kerber, L., Horn, B.L.D., Pretto, F.A., Müller, R.T., Melo, T.P., 2020. Triassic faunal successions of the Paraná Basin, southern Brazil. J. South Am. Earth Sci. 104. https://doi.org/10.1016/j.jsames.2020.102846

Setti, M., Marinoni, L., López-Galindo, A., 2004. Mineralogical and geochemical characteristics (major , minor , trace elements and REE) of detrital and authigenic clay minerals in a Cenozoic sequence from Ross Sea , Antarctica. Clay Miner. 39, 405–421. https://doi.org/10.1180/000985503540143

Seyed-Emami, K., Fuersich, F. T., Wilmsen, M., Majidifard, M. R., Shekarifard, A.,2009. Upper Triassic (Norian) cephalopods from the Ekrasar Formation (Shemshak Group) of Northern Alborz, Iran. Riv. Ital. di Paleontol. e Stratigr., 115, 189-98

Seyfullah, L.J., Beimforde, C., Dal Corso, J., Perrichot, V., Rikkinen, J., Schmidt, A.R., 2018a. Production and preservation of resins – past and present. Biol. Rev. 93, 1684–1714. https://doi.org/10.1111/brv.12414

Seyfullah, L.J., Roghi, G., Dal Corso, J., Schmidt, A.R., 2018b. The carnian pluvial episode and the first global appearance of amber. J. Geol. Soc. London. 175, 1012–1018. https://doi.org/10.1144/jgs2017-143

Shi, Z., Preto, N., Jiang, H., Krystyn, L., Zhang, Y., Ogg, J.G., Jin, X., Yuan, J., Yang, X., Du, Y., 2017. Demise of Late Triassic sponge mounds along the northwestern margin of the

Yangtze Block, South China: Related to the Carnian Pluvial Phase? Palaeogeogr. Palaeoclimatol. Palaeoecol. 474, 247–263. https://doi.org/10.1016/j.palaeo.2016.10.031

Shi, Z., Jin, X., Preto, N., Rigo, M., Du, Y., Han, L., 2019. The carnian pluvial episode at ma'antang, jiangyou in upper yangtze block, southwestern China. J. Geol. Soc. London. 176, 197–207. https://doi.org/10.1144/jgs2018-038

Simms, M.J., Ruffell, A.H., 1989. Synchroneity of climatic change and extinctions in the Late Triassic. Geology 17, 265–268. https://doi.org/10.1130/0091-7613(1989)017<0265:SOCCAE>2.3.CO;2

Simms, M.J., Ruffell, A.H., 2018. The carnian pluvial episode: From discovery, through obscurity, to acceptance. J. Geol. Soc. London. 175, 989–992. https://doi.org/10.1144/jgs2018-020

Song, P., Ding, L., Li, Z., Lippert, P.C., Yang, T., Zhao, X., Fu, J., Yue, Y., 2015. Late Triassic paleolatitude of the Qiangtang block: Implications for the closure of the Paleo-Tethys Ocean. Earth Planet. Sci. Lett. 424, 69–83. https://doi.org/https://doi.org/10.1016/j.epsl.2015.05.020

Soua, M., 2014. Early Carnian anoxic event as recorded in the southern Tethyan margin, Tunisia: an overview. Int. Geol. Rev. 56, 1884–1905. https://doi.org/10.1080/00206814.2014.967315

Soussi, M., Nied, G., Sulej, T., Boukhalfa, K., Mermer, J., 2017. Middle Triassic (Anisian-Ladinian) Tejra red beds and Late Triassic (Carnian) carbonate sedimentary records of southern Tunisia , Saharan Platform : Biostratigraphy , sedimentology and implication on regional stratigraphic correlations. Mar. Pet. Geol. 79, 222–256. https://doi.org/10.1016/j.marpetgeo.2016.10.019

Środoń, J., Szulc, J., Anczkiewicz, A., Jewuła, K., Banaś, M., Marynowski, L., 2014. Weathering, sedimentary and diagenetic controls of mineral and geochemical characteristics of the vertebrate-bearing Silesian Keuper. Clay Miner. 49, 569–594. https://doi.org/10.1180/claymin.2014.049.4.07

Stefani, M., Furin, S., Gianolla, P., 2010. The changing climate framework and depositional dynamics of Triassic carbonate platforms from the Dolomites. Palaeogeogr. Palaeoclimatol. Palaeoecol. 290, 43–57. https://doi.org/10.1016/j.palaeo.2010.02.018

Stilwell, J.D., Langendam, A., Mays, C., Sutherland, L.J.M., Arillo, A., Bickel, D.J., De Silva, W.T., Pentland, A.H., Roghi, G., Price, G.D., Cantrill, D.J., Quinney, A., Peñalver, E., 2020. Amber from the Triassic to Paleogene of Australia and New Zealand as exceptional preservation of poorly known terrestrial ecosystems. Sci. Rep. 10. https://doi.org/10.1038/s41598-020-62252-z

Sugiyama, K. 1997. Triassic and Lower Jurassic radiolarian biostratigraphy in the siliceous claystone and bedded chert units of the southeastern Mino Terrane, Central Japan. Bulletin of the Mizunami Fossil Museum, 24, 79–193.

Summa, V., Margiotta, S., Medici, L., Tateo, F., 2018. Compositional characterization of fine sediments and circulating waters of landslides in the southern Apennines – Italy. Catena 171, 199–211. https://doi.org/10.1016/j.catena.2018.07.009

Sun, Y.D., Wignall, P.B., Joachimski, M.M., Bond, D.P.G., Grasby, S.E., Lai, X.L., Wang, L.N., Zhang, Z.T., Sun, S., 2016. Climate warming, euxinia and carbon isotope perturbations

during the Carnian (Triassic) Crisis in South China. Earth Planet. Sci. Lett. 444, 88–100. https://doi.org/10.1016/j.epsl.2016.03.037

Sun, Y.D., Richoz, S., Krystyn, L., Zhang, Z.T., Joachimski, M.M., 2019. Perturbations in the carbon cycle during the carnian humid episode: Carbonate carbon isotope records from southwestern China and Northern Oman. J. Geol. Soc. London. 176, 167–177. https://doi.org/10.1144/jgs2017-170

Sun, Y.D., Orchard, M.J., Kocsis, T., Joachimski, M.M., 2020. Carnian–Norian (Late Triassic) climate change: Evidence from conodont oxygen isotope thermometry with implications for reef development and Wrangellian tectonics. Earth Planet. Sci. Lett. 534, 116082. https://doi.org/10.1016/j.epsl.2020.116082

Sýkora, M., Siblík, M., Soták, J., 2011. Siliciclastics in the Upper Triassic dolomite formations of the Krížna Unit (Malá Fatra Mountains, Western Carpathians): Constraints for the Carnian Pluvial Event in the Fatric Basin. Geol. Carpathica 62, 121–138. https://doi.org/10.2478/v10096-011-0011-1

Szaniawski, R., Ludwiniak, M., Mazzoli, S., Szczygieł, J., Jankowski, L., 2020. Paleomagnetic and magnetic fabric data from lower triassic redbeds of the central western carpathians: New constraints on the paleogeographic and tectonic evolution of the carpathian region. J. Geol. Soc. London. 177, 509–522. https://doi.org/10.1144/jgs2018-232

Tang, X and Zhang, K (2012), 40Ar-39Ar Geochronology and Tectonic Implications of the Blueschist from Northwestern Qiangtang, Northern Tibet, Western China. Acta Geologica Sinica - English Edition, 86: 1471-1478. https://doi.org/10.1111/1755-6724.12015

Thiry, M., 2000. Palaeoclimatic interpretation of clay minerals in marine deposits: an outlook from the continental origin. Earth-Science Rev. 49, 200–221.

Tomimatsu, Y., Nozaki, T., Sato, H., Takaya, Y., Kimura, J.I., Chang, Q., Naraoka, H., Rigo, M., Onoue, T., 2021. Marine osmium isotope record during the Carnian "pluvial episode" (Late Triassic) in the pelagic Panthalassa Ocean. Glob. Planet. Change 197, 103387. https://doi.org/10.1016/j.gloplacha.2020.103387

Tosti, F., Mastandrea, A., Guido, A., Demasi, F., Russo, F., Riding, R., 2014. Biogeochemical and redox record of mid-late Triassic reef evolution in the Italian Dolomites. Palaeogeogr. Palaeoclimatol. Palaeoecol. 399, 52–66. https://doi.org/10.1016/j.palaeo.2014.01.029

Trotter, J.A., Williams, I.S., Nicora, A., Mazza, M., Rigo, M., 2015. Long-term cycles of Triassic climate change: A new δ18O record from conodont apatite. Earth Planet. Sci. Lett. 415, 165–174. https://doi.org/10.1016/j.epsl.2015.01.038

Ulrichs, M., 1974. Zur Stratigraphie und Ammonitenfauna der Cassianer Schichten von Cassian (Dolomiten/Italien). Schrift. Erdwiss. Komm. Öst. Akad. Wiss. 2, 207–222.

Velde, B., Meunier, A., 2008. The origin of clay minerals in soils and weathered rocks, The Origin of Clay Minerals in Soils and Weathered Rocks. https://doi.org/10.1007/978-3-540-75634-7

Viel, G., 1979. Litostratigrafia ladinica: una revisione. Ricostruzione paleogeografica e paleostrutturale dell'area Dolomitico-Cadorina (Alpi Meridionali). Riv. Ital. di Paleontol. e Stratigr. 85, 85–125.

Vigran, J.O., Mangerud, G., Mørk, A., Worsley, D., Hochuli, P.A., 2014. Paynology and geology of the Triassic succession of Svalbard and the Barents Sea, Geological Survey of Norway Special Publication. https://doi.org/10.1111/j.1751-8369.1990.tb00382.x

Visscher, H., Van Houte, M., Brugman, W.A., Poort, R.J., 1994. Rejection of a Carnian (Late triassic) "pluvial event" in Europe. Rev. Palaeobot. Palynol. 83, 217–226. https://doi.org/10.1016/0034-6667(94)90070-1

Wagreich, M., Lein, R., Sames, B., 2014. Eustasy, its controlling factors, and the limno-eustatic hypothesis - Concepts inspired by Eduard Suess. Austrian J. Earth Sci. 107, 115–131.

Wang, Z., Shen, L., Wang, J., Fu, X., Xiao, Y., Song, C., Zhan, W., 2022. Organic matter enrichment of the Late Triassic Bagong Formation (Qiangtang Basin, Tibet) driven by paleoenvironment: Insights from elemental geochemistry and mineralogy. J. Asian Earth Sci. 236, 105329. https://doi.org/https://doi.org/10.1016/j.jseaes.2022.105329

Weems, R.E., Tanner, L.H., Lucas, S.G., 2016. Synthesis and revision of the lithostratigraphic groups and formations in the Upper Permian? - Lower Jurassic Newark Supergroup of eastern North America. Stratigraphy 13, 111–153.

Wendler, J.E., Wendler, I., Vogt, C., Kuss, J., 2016. Link between cyclic eustatic sea-level change and continental weathering: Evidence for aquifer-eustasy in the Cretaceous. Palaeogeogr. Palaeoclimatol. Palaeoecol. 441, 430–437. https://doi.org/10.1016/j.palaeo.2015.08.014

Wu, G., Ji, Z., Liao, W., Yao, J.; 2019. New biostratigraphic evidence of Late Permian to Late Triassic deposits from Central Tibet and their paleogeographic implications. Lithosphere; 11 (5): 683–696. doi: https://doi.org/10.1130/L1046.1

Wu, G., Ji, Z., Lash, G.G., Yao, J., 2021. The Upper Triassic deposits of the west Bangong-Nujiang suture zone and their paleogeographic implications. Sci Rep 11, 19509. https://doi.org/10.1038/s41598-021-98257-5

Wu, G., Ji, Z., Lash, G.G., Yao, J., Zhang, S., Li, Y., 2021. Newly discovered Wuchiapingian to Olenekian conodonts from the Longgar area, southern Lhasa Terrane and their palaeobiogeographical implications. Lethaia 54, 723–735. https://doi.org/https://doi.org/10.1111/let.12435

Xu, G., Hannah, J.L., Stein, H.J., Mørk, A., Os, J., Bingen, B., Schutt, D.L., Lundschien, B.A., 2014. Cause of Upper Triassic climate crisis revealed by Re – Os geochemistry of Boreal black shales. Palaeogeogr. Palaeoclimatol. Palaeoecol. 395, 222–232. https://doi.org/10.1016/j.palaeo.2013.12.027

Xu, X.T., Shao, L.Y., Lan, B., Wang, S., Hilton, J., Qin, J.Y., Hou, H.H., Zhao, J., 2020. Continental chemical weathering during the Early Cretaceous Oceanic Anoxic Event (OAE1b): a case study from the Fuxin fluvio-lacustrine basin, Liaoning Province, NE China. J. Palaeogeogr. 9. https://doi.org/10.1186/s42501-020-00056-y

Yogibekov, D., Windley, B.F., 2020. Late Palaeozoic to Late Triassic northward accretion and incorporation of seamounts along the northern South Pamir : Insights from the anatomy of the Pshart accretionary complex. Geol. J. 7837–7857. https://doi.org/10.1002/gj.3906

Yutsis, V.V., Stafeev, A.N. and Sukhanova, T.V. 2014. Paleozoic Exotic Blocks of the Crimean

Zagorchev, I., Budurov, K., 2007. Stratigraphic problems of the Moesian Group (Upper Triassic, peri-Tethyan type), Bulgaria. Geol. Balc. 36, 31–53.

Zanchi, A. and Gaetani, M. 2011. The geology of the Karakoram range, Pakistan: the new 1:100,000 geological map of Central-Western Karakoram. Italian journal of geosciences, 130 (2). pp. 161-262. ISSN 2038-1727

Zeng, Z., Zhu, H., Yang, X., Zeng, H., Hu, X., Xia, C., 2019. The Pangaea Megamonsoon records: Evidence from the Triassic Mungaroo Formation , Northwest Shelf of Australia. Gondwana Res. 69, 1–24. https://doi.org/10.1016/j.gr.2018.11.015

Zhang, K., Liu, R., Liu, Z., Li, L., 2021. Geochemical characteristics and geological significance of humid climate events in the Middle-Late Triassic (Ladinian-Carnian) of the Ordos Basin, central China. Mar. Pet. Geol. 131. https://doi.org/10.1016/j.marpetgeo.2021.105179

Zhang, W., Hu, Z., Liu, Y., Chen, H., Gao, S., Gaschnig, R.M., 2012. Total rock dissolution using ammonium bifluoride (NH4HF 2) in screw-top Teflon vials: A new development in open-vessel digestion. Anal. Chem. 84, 10686–10693. https://doi.org/10.1021/ac302327g

Zhang, Y., Li, M., Ogg, J.G., Montgomery, P., Huang, C., Chen, Z.Q., Shi, Z., Enos, P., Lehrmann, D.J., 2015. Cycle-calibrated magnetostratigraphy of middle Carnian from South China: Implications for Late Triassic time scale and termination of the Yangtze Platform. Palaeogeogr. Palaeoclimatol. Palaeoecol. 436, 135–166. https://doi.org/10.1016/j.palaeo.2015.05.033

Zhang, Y., Ogg, J.G., Franz, M., Bachmann, G.H., Szurlies, M., Röhling, H.G., Li, M., Rolf, C., Obst, K., 2020. Carnian (Late Triassic) magnetostratigraphy from the Germanic Basin allowing global correlation of the Mid-Carnian Episode. Earth Planet. Sci. Lett. 541, 116275. https://doi.org/10.1016/j.epsl.2020.116275

Zhang, Z., Yang, X., Zhang, L., Wu, C., Luo, T., Zhu, W., Xu, J., Hu, P., Li, X., Jin, Z., 2021. Sedimentation and mineralization of the Late Paleozoic extensional basin in the western Kunlun Mountains, China. Solid Earth Sci. 6, 142–177. https://doi.org/10.1016/j.sesci.2021.02.001

Zhang, Z.T., Joachimski, M.M., Grasby, S.E., Sun, Y.D., 2022. Intensive ocean anoxia and large δ13Ccarb perturbations during the Carnian Humid Episode (Late Triassic) in Southwest China. Glob. Planet. Change 217, 103942. https://doi.org/10.1016/j.gloplacha.2022.103942

Zhao, H., Grasby, S.E., Wang, X., Zhang, L., Liu, Y., Chen, Z.-Q., Hu, Z., Huang, Y., 2022. Mercury enrichments during the Carnian Pluvial Event (Late Triassic) in South China. GSA Bull. 134, 2709–2720. https://doi.org/10.1130/b36205.1

Zhu, D.-C., Zhao, Z.-D., Niu, Y., Dilek, Y., Mo, X.-X., 2011. Lhasa terrane in southern Tibet came from Australia. Geology 39, 727–730. https://doi.org/10.1130/G31895.1

Zonneveld, J.P., Henderson, C.M., Stanley, G.D., Orchard, M.J., Gingras, M.K., 2007. Oldest scleractinian coral reefs on the North American craton: Upper Triassic (Carnian), northeastern British Columbia, Canada. Palaeogeogr. Palaeoclimatol. Palaeoecol. 243, 421–450. https://doi.org/10.1016/j.palaeo.2006.08.012

Zouheir, T., Hminna, A., Klein, H., Lagnaoui, A., Saber, H., Schneider, J.W., 2018. Unusual archosaur trackway and associated tetrapod ichnofauna from Irohalene member

(Timezgadiouine formation, late Triassic, Carnian) of the Argana Basin, Western High Atlas, Morocco. Hist. Biol. 00, 1–13. https://doi.org/10.1080/08912963.2018.1513506.

8 SUPPLEMENTARY DATA

In this section are firstly reported the graph and interpretation of the discrimination diagram of Andreozzi et al. (1997), which has been excluded from the submitted article reported in Chapter 5 because it did not display very significant results. Moreover, some examples of oriented mounts diffractograms are here presented and interpreted (one for each unit) and the results of validation test on MI20 samples for Rietveld refinement (comparison with carbonate amounts from calcimetry) are reported. In addition, tables containing: geographic coordinates of the sampled sections; analytical results of major, minor and trace elements concentrations; calculated weathering indices (with relative graphs) and quantitative mineralogical data and significant ratios have been showed at the end of this section.

8.1 DISCRIMINATION DIAGRAM OF ANDREOZZI ET AL. (1997)

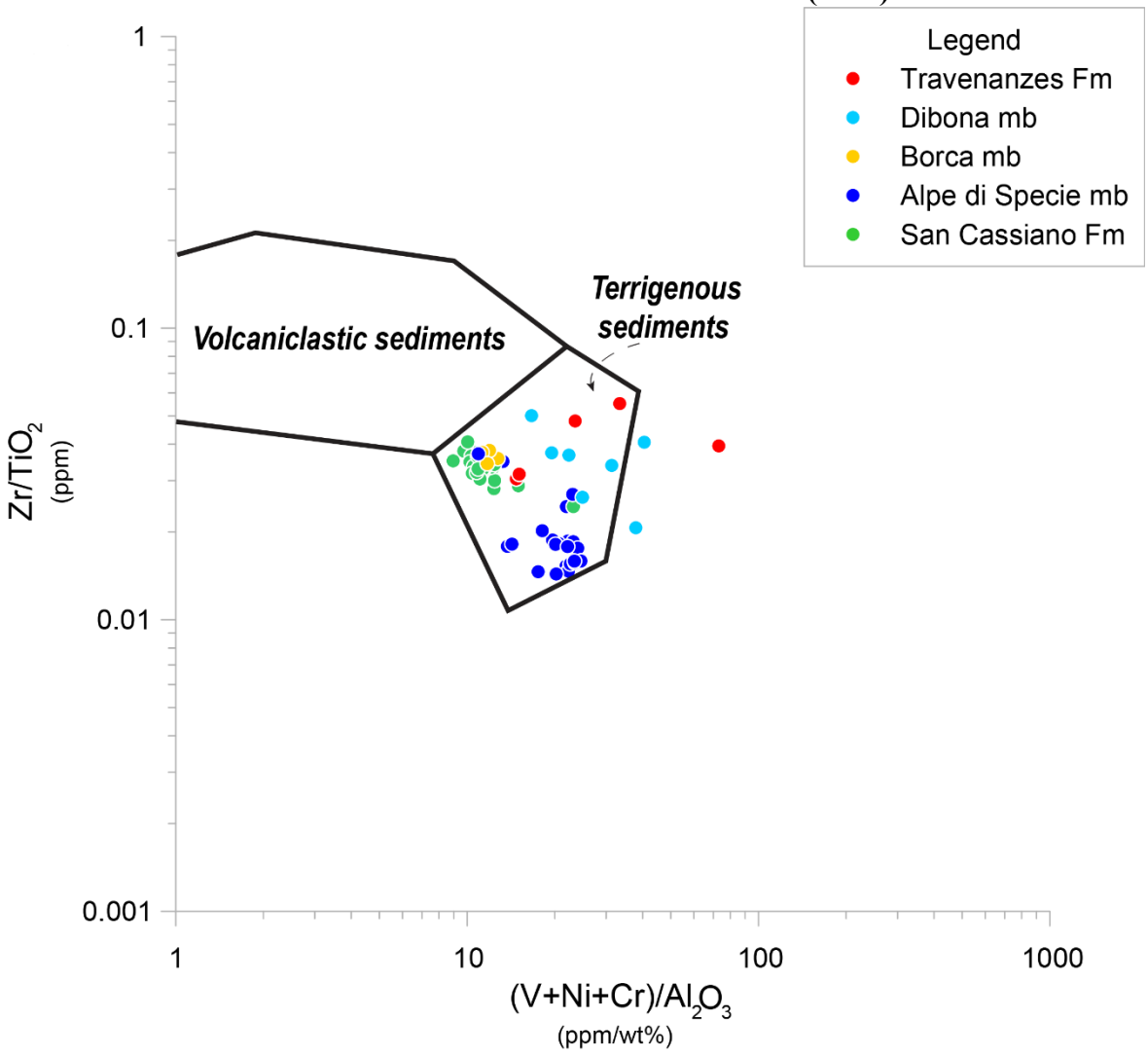

Figure 8.1: Diagram of Andreozzi et al. (1997) discriminating sediments of terrigenous origin from sediments of basic volcaniclastic origin.

This graph was proposed by Andreozzi et al. (1997) to discriminate whether sediments have a pristine sedimentary origin or derive from volcanic products (of intermediate-acid origin), based on the area of the graph in which they fall. In fact, this diagram plotted ratios considers elements such as V, Ni Cr, which tend to be enriched in clay sediments with respect to intermediate-acidic magmatic products, mobilized during diagenetic transformations in comparison to and Zr, Ti and Al, which are considered immobile (Andreozzi et al., 1997). In the discrimination diagram, almost all the samples fall within the area indicative of a

terrigenous origin of the sediments (Fig. 8.1). Particularly, the samples from the San Cassiano Fm fall very close to the area, suggesting that they are richer than other samples in sediments of volcaniclastic origin (Fig. 8.1).

8.2 BULK AND ORIENTED MOUNTS XRD PATTERNS OF SELECTED SAMPLES

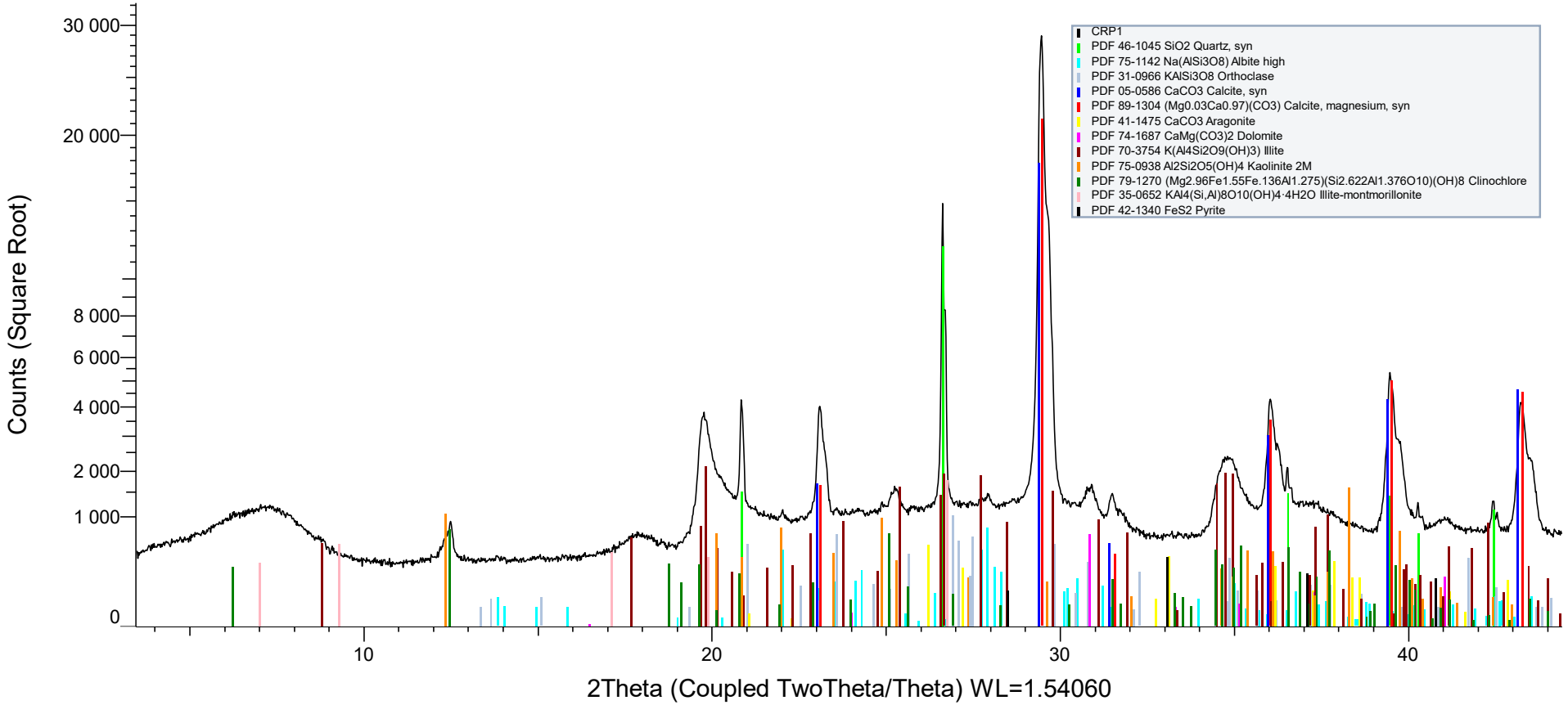

Figure 8.2: XRD pattern of sample CRP1 (San Cassiano Fm) showing the identified mineral phases based on matching with the Powder Diffraction File cards. Intensity scale is plotted as the square root of counts. Plot is made by the Bruker EVA software.

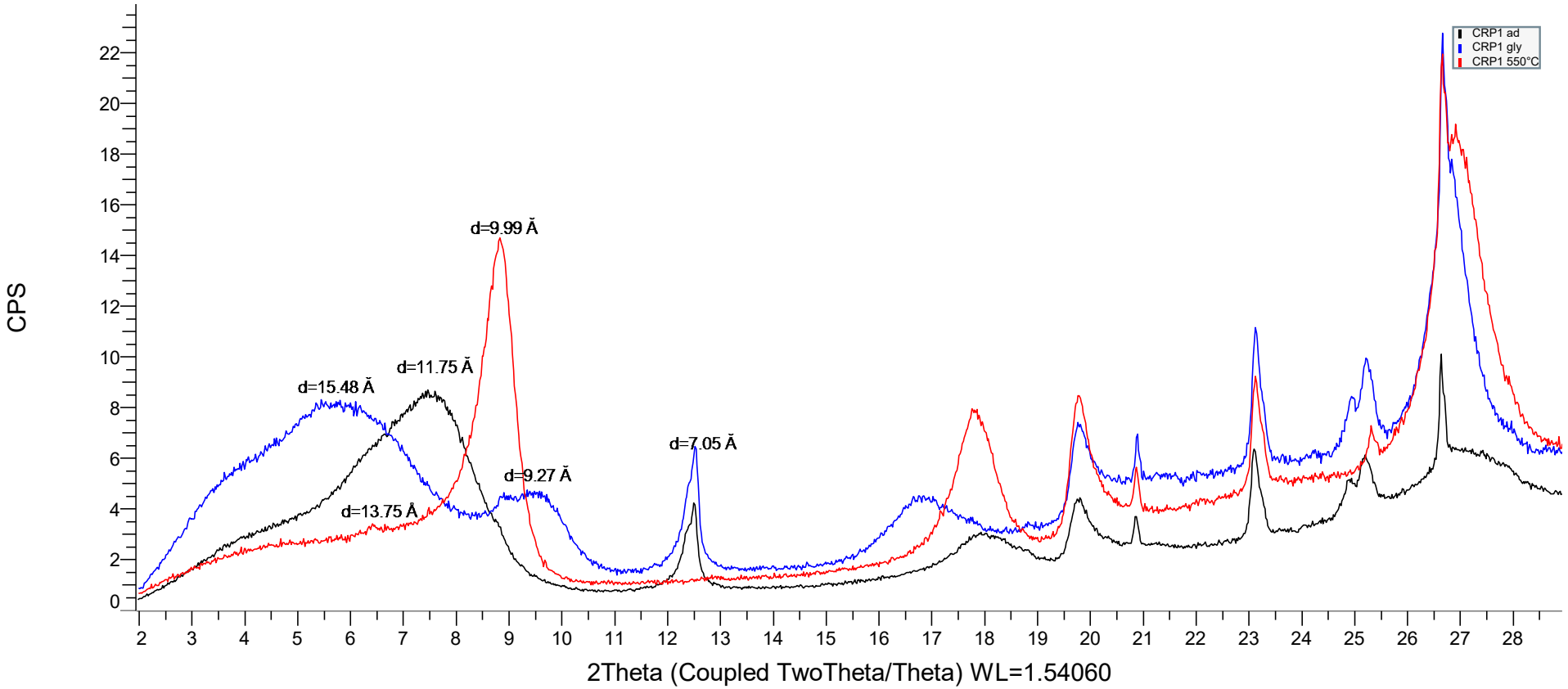

Figure 8.3: XRD patterns of oriented mount from San Cassiano Fm (sample CRP1). Black trace: as dried sample (ad); blue trace: sample exposed to ethyl glycol (gly); red trace: sample heated at 550°C (550°C). Attribution of peaks to clay minerals: d=11.75 Å (ad) and 15.48 Å+9.27 Å: I/S (Illite/Smectite mixed-layer); d=13.75 Å: chlorite; d=9.99 Å: illite (ad) + collapsed I/S (550°C); d=7.05 Å kaolinite and chlorite. Plot is made by the Bruker EVA software.

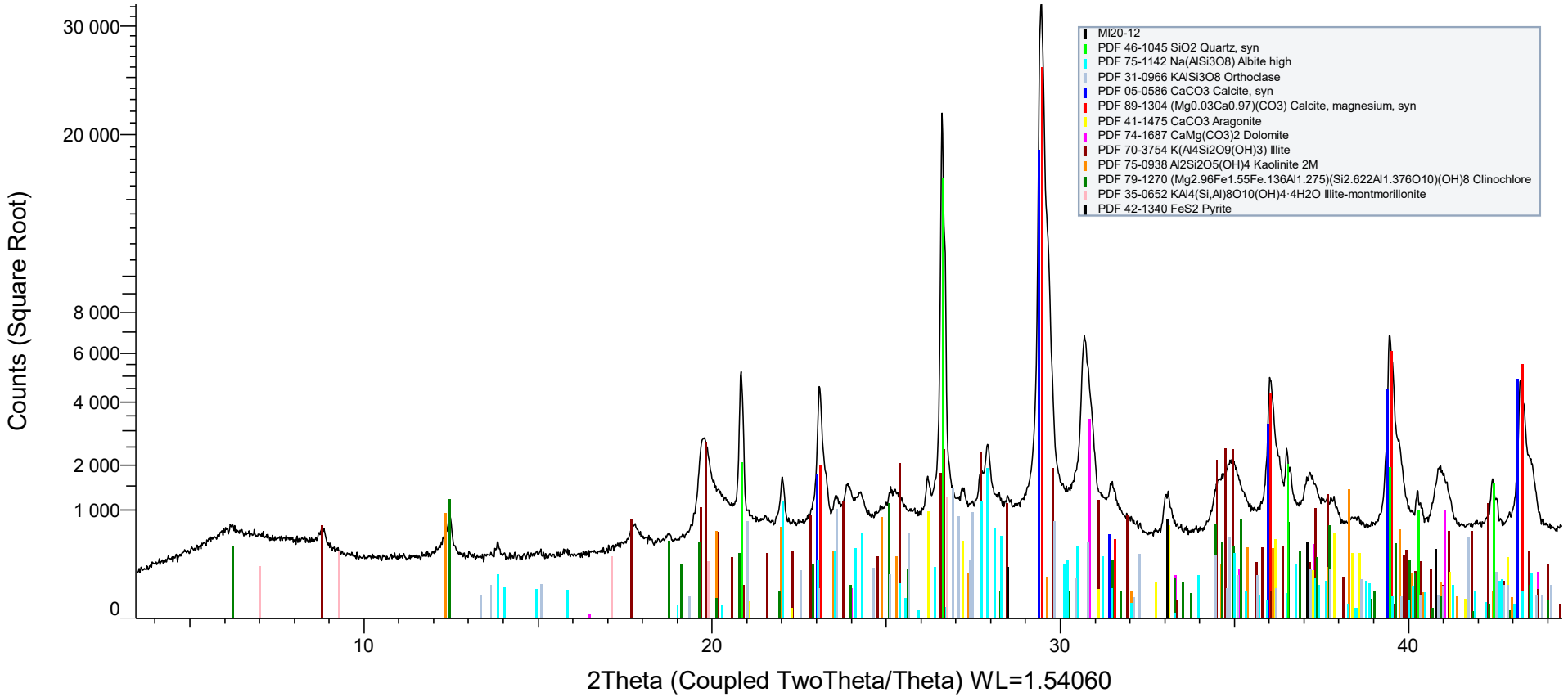

Figure 8.4: XRD pattern of sample MI20-12 (Heiligkreuz Fm- Alpe di Specie Mb) showing the identified mineral phases based on matching with the Powder Diffraction File cards. Intensity scale is plotted as the square root of counts. Plot is made by the Bruker EVA software.

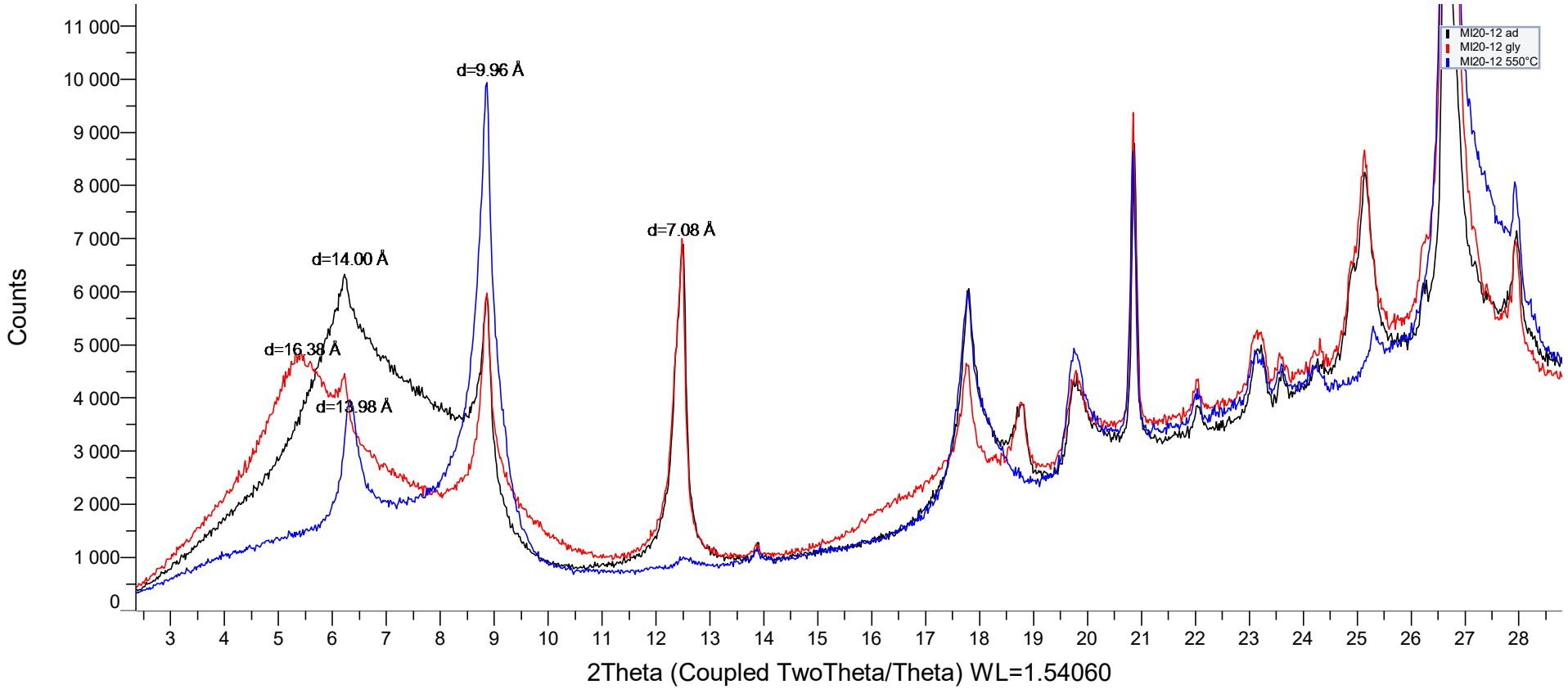

Figure 8.5: XRD patterns of oriented mount from Heiligkreuz Fm – Alpe di Specie Mb (sample MI20-12). Black trace: as dried sample (ad); red trace: sample exposed to ethyl glycol (gly); blue trace: sample heated at 550°C (550°C). Attribution of peaks to clay minerals: d=14 Å (ad) and 16.38 Å+9.96 Å: I/S (Illite/Smectite mixed-layer); d=13.98 Å: chlorite; d=9.96 Å: illite (ad) + collapsed I/S (550°C); d=7.08Å kaolinite and chlorite. Plot is made by the Bruker EVA software.

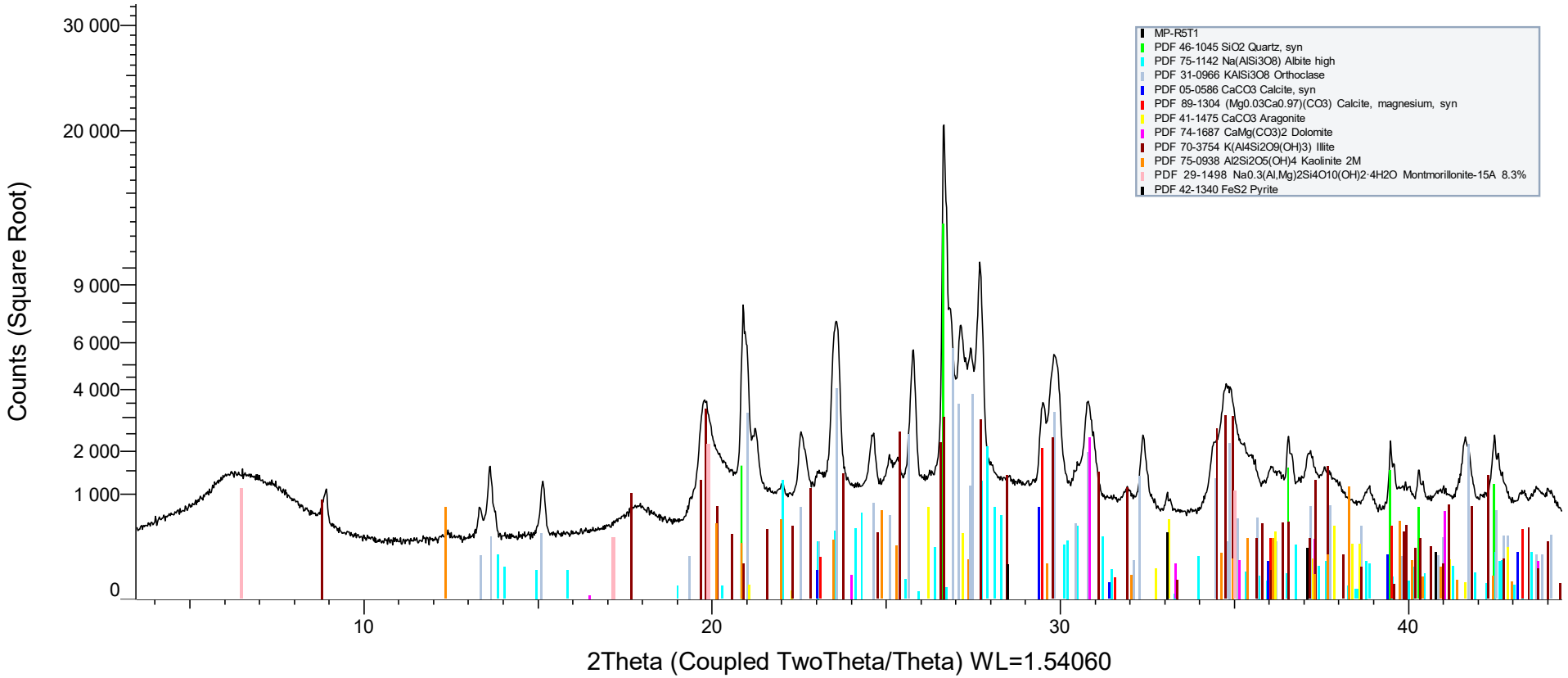

Figure 8.6: XRD pattern of sample R5T1 (Heiligkreuz Fm- Borca Mb) showing the identified mineral phases based on matching with the Powder Diffraction File cards. Intensity scale is plotted as the square root of counts. Plot is made by the Bruker EVA software.

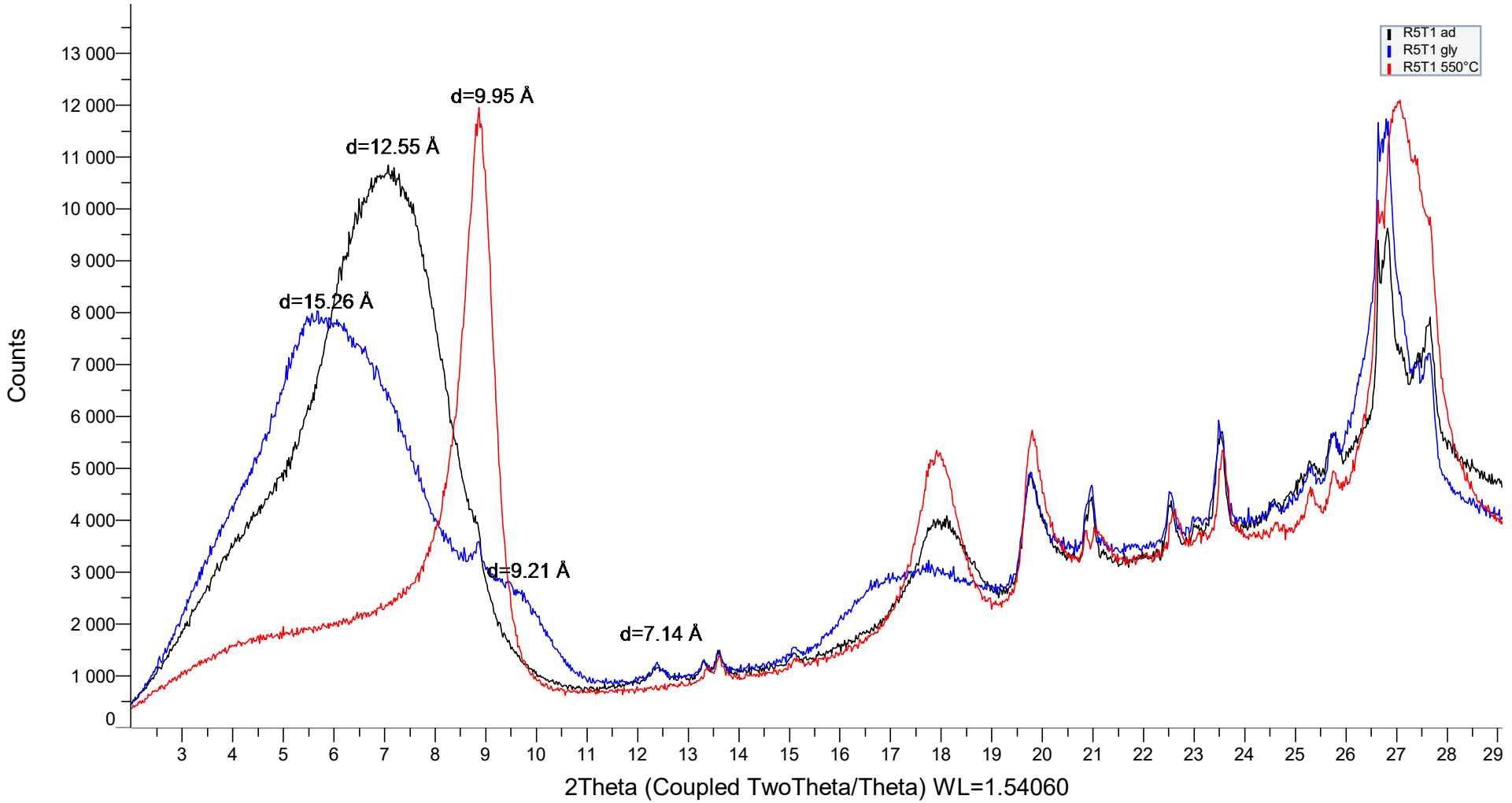

Figure 8.7: XRD patterns of oriented mount from Heiligkreuz Fm – Borca Mb (sample R5T1). Black trace: as dried sample (ad); blue trace: sample exposed to ethyl glycol (gly); red trace: sample heated at 550°C (550°C). Attribution of peaks to clay minerals: d=12.55 Å (ad) and 15.26 Å+9.21 Å: I/S (Illite/Smectite mixed-layer); d=9.95 Å: illite (ad) + collapsed I/S (550°C); d=7.14Å kaolinite. Plot is made by the Bruker EVA software.

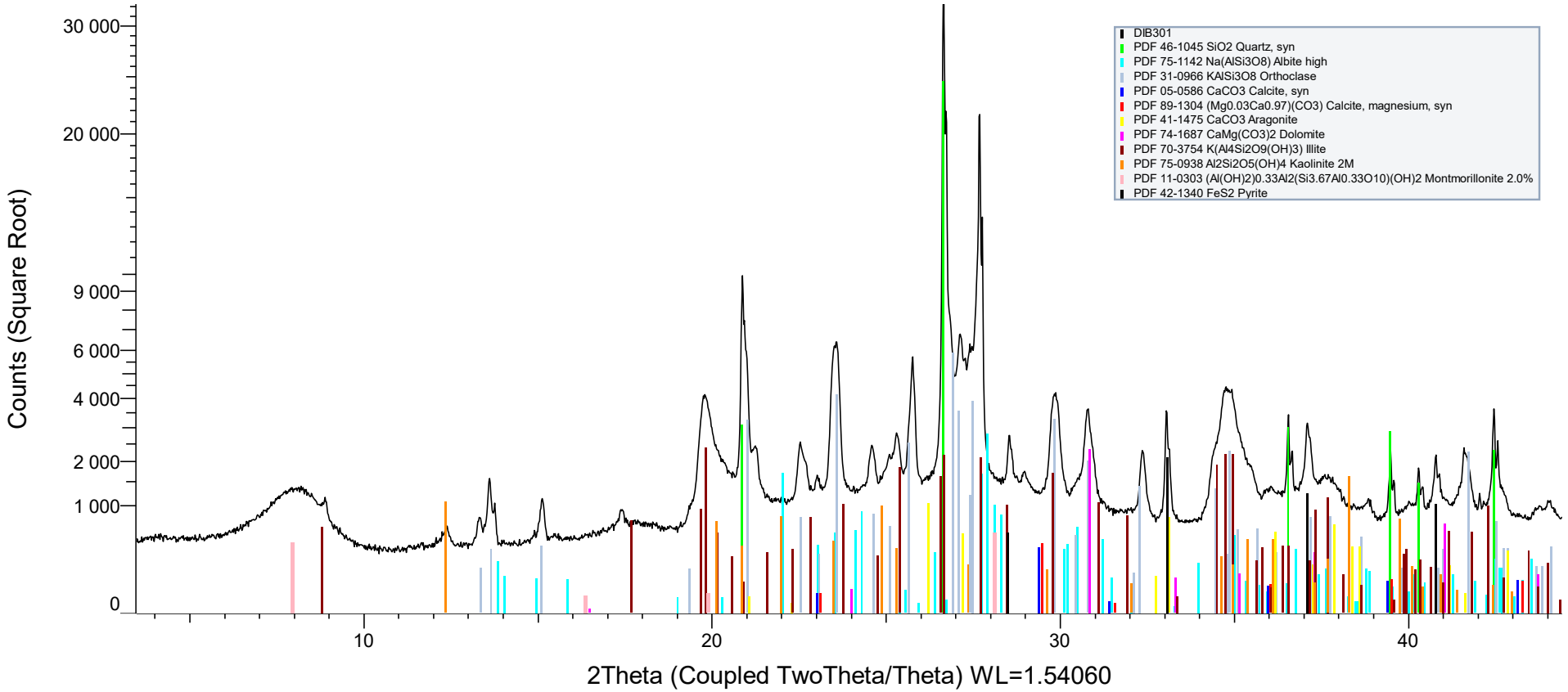

Figure 8.8: XRD pattern of sample DIB301 (Heiligkreuz Fm- Dibona Mb) showing the identified mineral phases based on matching with the Powder Diffraction File cards. Intensity scale is plotted as the square root of counts. Plot is made by the Bruker EVA software.

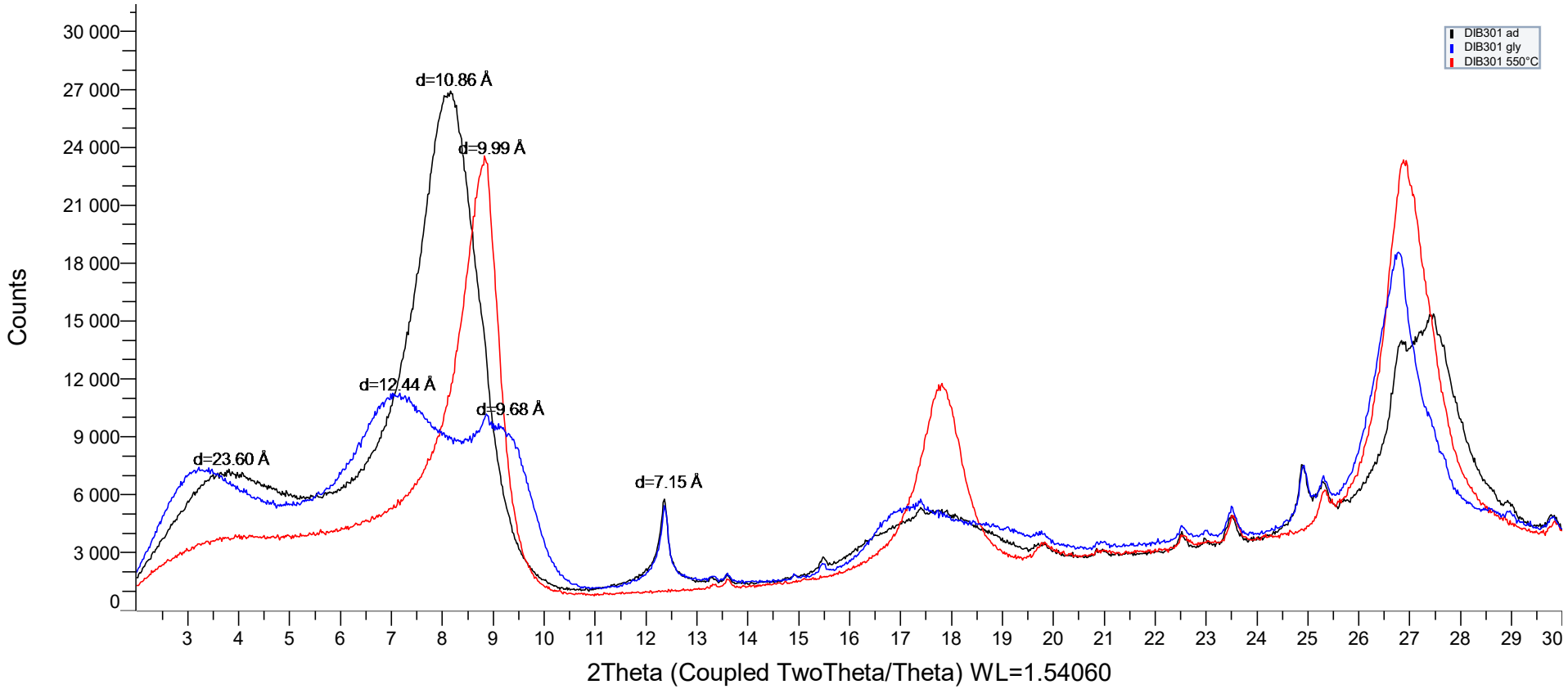

Figure 8.9: XRD patterns of oriented mount from Heiligkreuz Fm – Dibona Mb (sample DIB301). Black trace: as dried sample (ad); blue trace: sample exposed to ethyl glycol (gly); red trace: sample heated at 550°C (550°C). Attribution of peaks to clay minerals: d=10.86 Å (ad) and 12.44 Å+9.68 Å: I/S (Illite/Smectite mixed-layer); d=23.60 Å: rectorite; d=9.99 Å: illite + collapsed I/S (550°C); d=7.15 Å kaolinite. Plot is made by the Bruker EVA software.

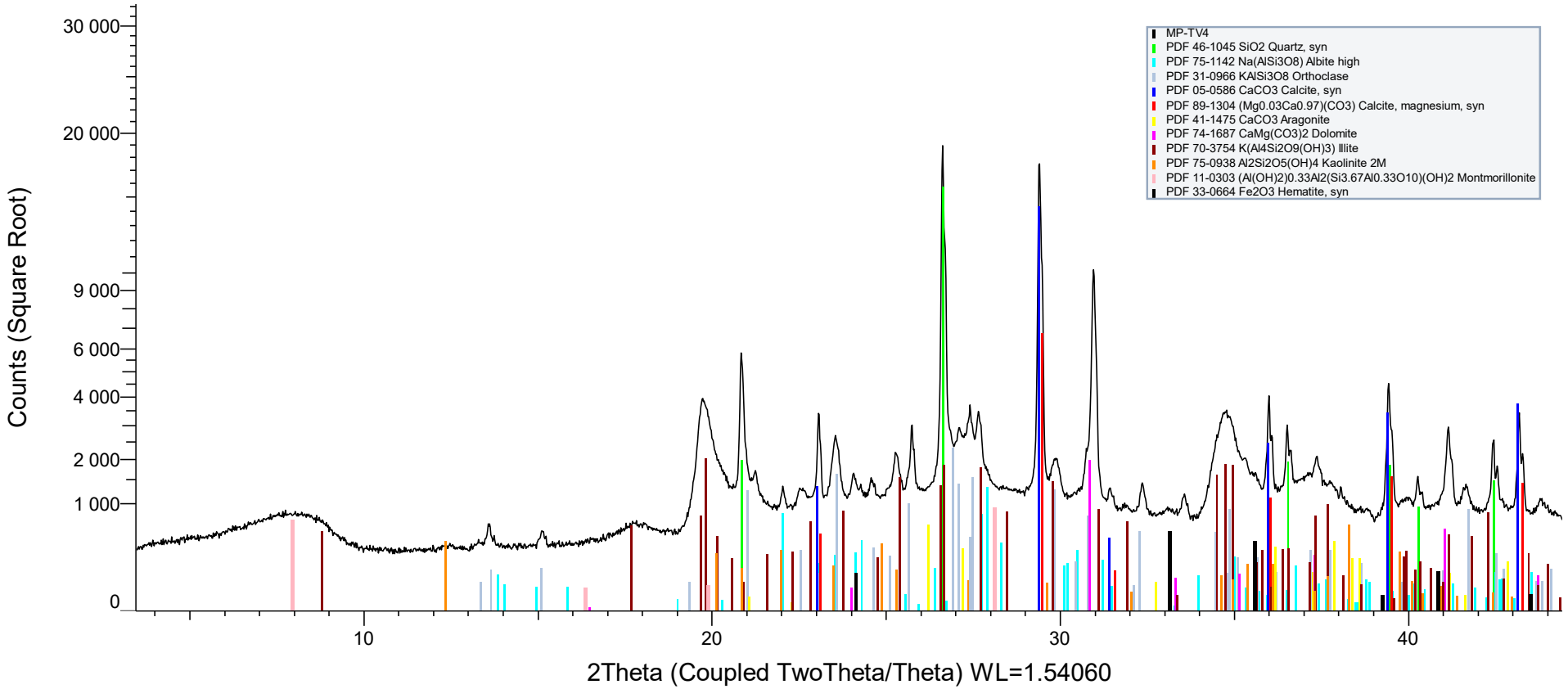

Figure 8.10: XRD pattern of sample TV4 (Travenanzes Fm) showing the identified mineral phases based on matching with the Powder Diffraction File cards. Intensity scale is plotted as the square root of counts. Plot is made by the Bruker EVA software.

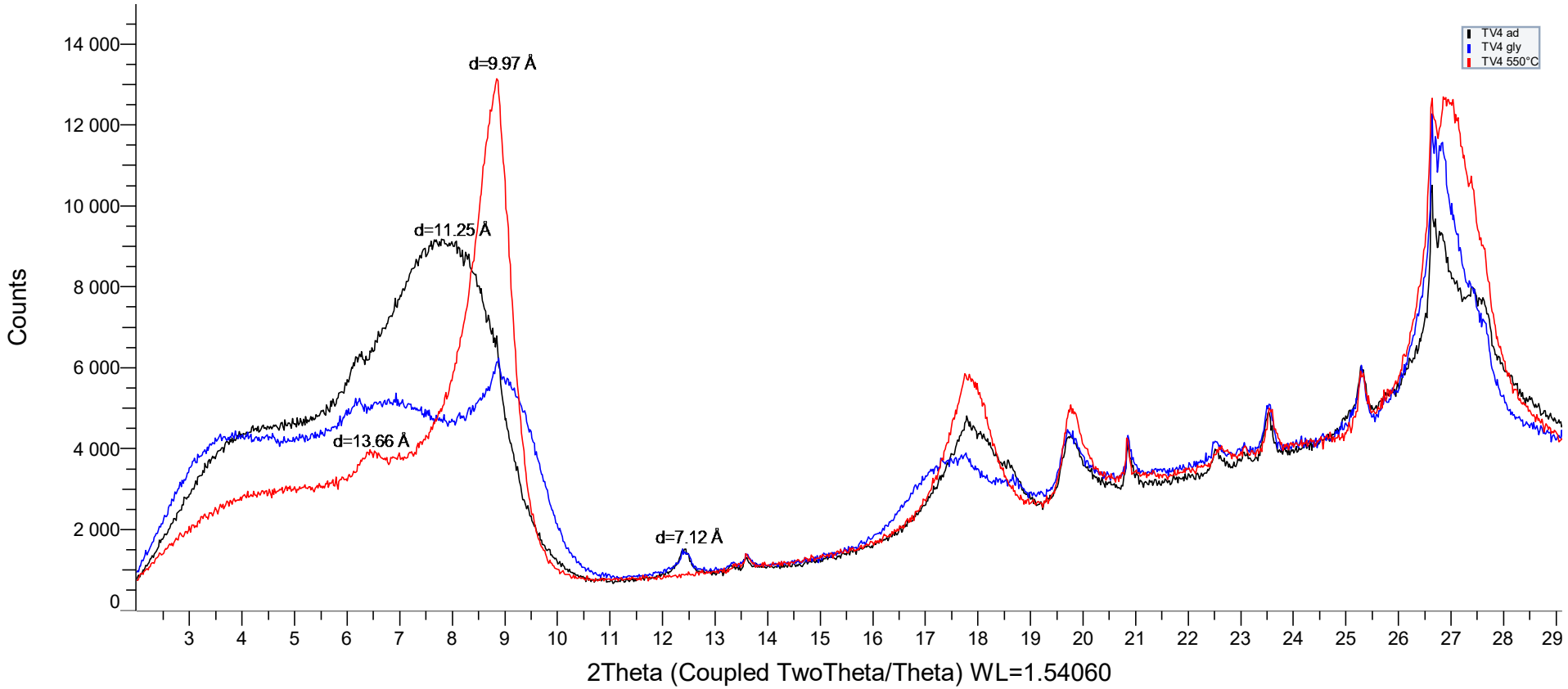

Figure 8.11: XRD patterns of oriented mount from Travenanzes Fm (sample TV4). Black trace: as dried sample (ad); blue trace: sample exposed to ethyl glycol (gly); red trace: sample heated at 550°C (550°C). Attribution of peaks to clay minerals: d=11.25 Å (ad) and 9.97 Å (gly): I/S (Illite/Smectite mixed-layer); d=13.66 Å: chlorite; d=9.97 Å: illite + collapsed I/S (550°C); d=7.12Å chlorite. Plot is made by the Bruker EVA software.

8.3 COMPARISON BETWEEN CARBONATES FROM CALCIMETRY VS RIETVELD REFINEMENT

SAMPLES	Carbonates		Difference (Profex-Calcimetry)
	Calcimetry	Profex	
MI20-18	24	30	6
MI20-17	25	31	6
MI20-17B	40	43	3
MI20-16	36	43	7
MI20-15	53	53	0
MI20-14	28	33	5
MI20-13	51	54	3
MI20-12	48	53	5
MI20-11	46	46	0
MI20-10	40	47	7
MI20-9	37	46	9
MI20-8	44	50	6
MI20-7	77	76	-1
MI20-6	55	65	10
MI20-5	60	64	4
MI20-4B	44	52	8
MI20-4	54	57	3
MI20-3	65	69	4
MI20-2	43	46	3
MI20-1	54	53	-1

Table 8.2: Results of validation test for Rietveld refinement on MI20 samples. Carbonates determinations after calcimetry and differences between quantities of carbonates determined by Rietveld Refinement (using Profex v5.0.2) and by digital calcimeter.

8.4 GEOGRAPHIC COORDINATES OF THE SAMPLED SECTIONS

Section	*Location*	*Latitude*	*Longitude*	*Selected previous literature*
NST	Prati di Stuores/Stuores Wiesen	46.5283	11.9301	Ulrichs, 1974; Bizzarrini & Braga, 1987; Bizzarrini & Gnoli, 1991; Broglio Loriga et al.., 1999; Mietto et al., 2012
CRP	Pocol	46.5256	12.1198	---
MI20	Milieres	46.5282	12.0633	Bizzarrini & Braga, 1987; Bizzarrini & Gnoli, 1991; Dal Corso et al., 2012, 2015, 2018; Gattolin et al., 2015;
MTR	Mietres	46.5533	12.1645	---
LSC	Lago Scin	46.5444	12.1661	---
CLS	Costalaresc	46.5376	12.1651	Bizzarrini & Gnoli, 1991
ASS	Ru de Assola	46.4268	12.2115	---
R5T	Rio Falzarego	46.5182	12.0307	---
DIB	Rifugio Dibona	46.5329	12.0760	Preto & Hinnow, 2003; Neri et al., 2007; Breda et al., 2009; Dal Corso et al., 2012, 2015, 2018; Gattolin et al., 2013, 2015; Maron et al., 2017
TV	Passo Falzarego	46.5179	12.0106	Breda et al., 2009; Breda & Preto, 2011

Table 8.3: Geographic coordinates of the sampled sections and selected references.

8.5 MAJOR, MINOR AND TRACE ELEMENTS CONCENTRATIONS

		SiO_2	TiO_2	Al_2O_3	TFe_2O_3	MnO	MgO	CaO	Na_2O	K_2O	P_2O_5	LOI	SUM	Li	Be	Na	Mg	Al	P	K	Ca	Sc	Ti	V	Cr	Mn	Fe	Co	Ni	Cu	Zn	Ga	Rb	Sr	Y	Zr	Nb	Sn	Cs	Ba	La	Ce	Pr	Nd	Sm	Eu	Gd	Tb	Dy	Ho	Er	Tm	Yb	Lu	Hf	Ta	Tl	Pb	Th	U
SAMPLES	m	mass%	mass%	mass%	mass%	mass%	mass%	mass%	mass%	mass%	mass%	mass%	mass%	ppm	ppm	ppm	ppm	ppm	ppm	ppm	ppm	ppm	ppm	ppm	ppm	ppm	ppm	ppm	ppm	ppm	ppm	ppm	ppm	ppm	ppm	ppm	ppm	ppm	ppm	ppm	ppm	ppm	ppm	ppm	ppm	ppm	ppm	ppm	ppm	ppm	ppm	ppm	ppm	ppm	ppm	ppm	ppm	ppm	ppm
TV5	416	53,07	1,01	16,36	7,43	0,09	5,30	2,39	0,29	6,01	0,06	8,03	100,03	48,4	2,42	2151	32500	88898	333	49878	17344	20,3	6043	104	100,0	685	52225	26,5	42,9	186	33,2	20,4	147	90,1	29,9	191	17,8	2,67	7,44	306	49,3	91,7	11,2	43,1	8,37	1,92	7,11	0,97	5,71	1,07	3,19	0,42	2,92	0,42	5,12	1,19	0,31	18,9	12,8	2,46
TV4	411	47,24	1,33	12,79	4,67	0,09	4,28	10,64	0,36	4,52	0,10	13,51	99,53	30,6	1,74	2656	24974	66580	490	37508	75017	16,9	7997	713	180	658	31874	23,4	42,0	65,3	33,3	16,5	90,4	252	29,3	316	20,1	2,03	4,60	345	36,9	60,4	8,42	32,8	6,19	1,59	5,53	0,87	5,30	1,07	2,98	0,44	2,81	0,46	7,64	1,20	0,28	19,6	9,99	3,51
TV3	406	52,24	1,50	12,35	7,43	0,14	5,37	5,21	0,41	4,50	0,11	10,68	99,92	25,7	1,28	3056	31133	64950	507	37326	36439	15,7	8987	184	187	1027	50739	22,8	42,3	35,7	34,2	14,2	90,6	82,6	29,6	495	22,2	1,85	4,22	428	39,9	75,2	8,73	34,7	6,75	1,73	5,80	0,85	5,32	1,04	3,05	0,47	3,13	0,49	11,6	1,29	0,30	18,9	10,6	1,89
TV2	401	54,34	1,07	17,18	9,58	0,04	4,73	0,49	0,29	6,34	0,06	5,83	99,93	41,8	2,24	2114	27680	89903	314	52635	3595	20,8	6397	99,5	110	326	64858	26,2	44,2	68,0	31,1	21,0	157	54,0	21,5	195	17,8	2,53	7,51	216	26,0	47,1	5,77	22,2	4,27	1,07	4,09	0,65	3,91	0,78	2,32	0,34	2,50	0,35	5,00	1,16	0,34	15,1	11,9	1,74
TV1	396	47,43	1,24	13,37	8,28	0,14	6,77	5,57	0,29	4,54	0,07	12,21	99,90	30,2	1,84	2129	39874	70695	353	37691	39246	17,3	7410	128	151	1054	56364	21,0	35,5	17,2	28,0	16,6	113	71,1	33,3	356	19,2	2,13	5,39	233	41,7	74,2	9,05	35,5	7,00	1,67	6,34	0,95	5,69	1,13	3,24	0,46	2,92	0,45	8,50	1,22	0,26	16,7	11,1	1,71
DIB 308	336	55,85	1,48	16,35	4,97	0,02	2,17	3,42	0,43	7,65	0,16	6,13	98,61	29,6	2,56	3212	12883	86633	726	63544	25509	16,4	8849	124	212	168	34348	19,8	29,8	25,6	30,8	20,3	150	123	21,7	325	26,3	3,03	10,9	260	31,7	63,5	7,33	28,2	5,24	1,15	4,47	0,68	4,28	0,82	2,46	0,38	2,62	0,39	8,08	1,84	0,47	20,4	16,6	2,88
DIB 307	335	59,04	1,26	16,22	4,06	0,02	2,05	2,27	0,44	8,29	0,12	5,26	99,04	27,6	2,44	3279	12040	85989	602	68832	16720	15,0	7560	108	141	169	27724	16,2	20,7	13,6	35,9	23,1	157	91,2	21,0	379	22,1	3,27	11,1	280	28,5	57,2	6,61	25,3	4,94	1,17	4,16	0,63	4,08	0,78	2,37	0,36	2,49	0,38	9,40	1,45	0,48	22,7	16,4	5,10
DIB 306	333,5	57,10	1,40	17,69	5,26	0,02	2,10	1,62	0,36	7,88	0,11	5,36	98,88	28,9	2,67	2656	12583	94654	551	65387	11189	20,0	8405	141	175	132	35970	21,1	28,4	25,4	35,1	22,6	157	92,4	25,2	314	25,1	3,19	12,4	221	40,2	83,2	9,35	36,7	6,91	1,60	5,57	0,87	5,43	0,99	2,90	0,44	2,93	0,43	7,70	1,84	0,42	17,1	16,5	2,40
DIB 305	333	49,79	1,94	16,29	5,53	0,04	3,94	4,74	0,37	6,57	0,17	9,48	98,86	27,9	1,91	2775	23884	86965	799	54569	34486	21,4	11618	166	389	284	38804	25,7	63,1	37,6	34,5	19,5	139	167	19,9	240	35,1	2,59	9,38	198	27,2	54,1	6,50	25,7	4,65	1,36	4,22	0,67	4,03	0,82	2,32	0,35	2,35	0,33	5,93	1,89	0,25	12,1	12,5	2,10
DIB 304	331	51,93	1,56	19,53	6,11	0,02	3,48	1,89	0,22	6,34	0,12	7,64	98,83	38,9	2,42	1662	20688	103917	563	52618	13612	24,9	9364	148	257	144	41993	29,1	81,0	40,9	34,0	22,1	148	121	12,4	246	28,9	2,74	11,3	112	18,0	33,2	4,09	15,5	2,80	0,70	2,54	0,41	2,43	0,48	1,42	0,21	1,47	0,22	6,14	1,86	0,24	12,8	10,6	1,84
DIB 302	330	59,20	1,68	17,60	4,64	0,02	1,91	0,61	0,39	8,41	0,15	4,93	99,53	30,2	2,34	2915	11021	91152	688	69812	4636	20,1	10054	179	333	120	30948	21,4	40,0	30,3	31,5	22,3	144	215	25,2	340	28,5	2,94	10,0	245	47,5	96,3	11,2	43,1	8,12	1,90	6,41	0,92	5,00	0,93	2,66	0,38	2,44	0,36	8,22	1,85	0,43	14,6	13,8	4,23
DIB 301	327	57,35	2,10	16,38	6,48	0,01	1,45	0,11	0,45	7,68	0,11	6,62	98,73	31,0	1,86	3323	8321	85406	522	63751	918	20,2	12613	184	440	63,6	43188	17,0	40,5	30,1	32,8	20,7	135	69,6	25,4	512	35,2	3,00	8,63	233	63,0	137	15,4	59,1	10,7	2,64	7,44	1,05	5,87	1,07	3,02	0,44	3,17	0,48	12,0	2,01	0,41	23,4	15,8	4,72
R5T4	271	57,27	0,95	16,78	4,32	0,02	1,95	2,95	0,63	6,68	0,16	7,68	99,40	17,2	2,88	4703	11588	89318	733	55474	21112	17,7	5701	114	64,6	176	29524	14,1	18,2	20,5	63,4	21,2	149	112	32,1	196	18,2	3,42	11,5	279	40,8	80,7	9,66	37,1	7,39	1,57	6,44	0,99	6,08	1,16	3,37	0,46	3,29	0,47	5,23	1,32	0,61	24,7	15,9	3,30
R5T3	266	59,61	0,99	18,07	4,64	0,02	1,94	1,13	0,70	7,15	0,16	5,40	99,80	13,7	3,34	5193	11487	96117	714	59343	8210	19,4	5941	123	67,5	144	31401	10,4	13,0	20,5	92,5	22,3	159	114	33,7	223	19,0	3,57	13,1	308	43,2	85,0	9,93	38,7	7,77	1,53	6,84	1,04	6,63	1,26	3,46	0,52	3,47	0,54	6,05	1,41	0,58	18,3	16,9	3,74
R5T2	261	57,53	1,00	16,66	4,21	0,02	1,98	3,20	0,52	7,43	0,15	6,33	99,03	15,2	2,45	3835	11571	88191	699	61709	22903	16,7	5995	121	62,1	158	29092	13,3	16,1	18,9	59,0	20,9	151	139	28,2	228	18,7	3,39	11,0	289	43,2	83,9	9,79	37,2	7,04	1,41	5,93	0,85	5,18	0,98	2,78	0,39	2,53	0,39	6,16	1,36	0,60	20,1	16,5	3,62
R5T1	256	58,77	1,10	15,95	3,96	0,03	1,85	3,29	0,57	7,74	0,15	5,85	99,25	13,9	2,13	4251	10589	84419	714	64224	23599	15,9	6589	118	70,1	209	27144	12,8	15,6	17,2	64,6	19,5	146	130	31,4	235	19,6	3,31	10,1	303	41,4	79,2	9,22	36,4	6,72	1,54	6,14	0,96	5,87	1,14	3,28	0,46	3,11	0,46	6,15	1,42	0,54	22,9	15,4	3,32
MI20-18	234	39,79	0,67	11,21	5,59	0,08	3,09	16,37	0,87	1,64	0,11	19,05	98,49	23,4	1,70	6484				13648		12,5	4035	79,0	61,3			11,7	23,1	13,1	50,7	13,1	63,1	698	19,9	140	12,3	2,11	4,93	160	27,4	53,5	6,37	23,8	4,98	1,04	4,24	0,67	3,70	0,76	2,07	0,31	1,97	0,31	3,67	0,90	0,31	12,5	9,70	2,37
MI20-17	232	44,67	0,79	13,85	5,07	0,06	3,00	13,26	0,93	2,15	0,13	15,78	99,89	29,1	1,85	6899				17841		15,7	4706	100	79,7			11,1	25,7	19,1	48,6	16,7	85,7	611	23,4	167	14,5	2,58	7,19	173	33,6	64,6	7,62	27,7	5,60	1,25	4,80	0,74	4,52	0,92	2,44	0,37	2,36	0,35	4,31	1,10	0,33	12,2	12,8	2,42
MTR24	230	37,01	0,87	13,02	6,42	0,07	3,52	16,57	0,28	1,68	0,08	19,49	99,00	33,1	1,44	2085	20853	70618	423	13922	119973	17,6	5216	100	133	524	46117	20,3	58,3	28,0	41,2	15,4	66,6	951	15,1	125	14,3	1,89	4,85	38,4	19,8	39,9	4,76	18,5	3,74	0,86	3,11	0,50	2,96	0,58	1,68	0,24	1,54	0,23	3,22	0,90	0,23	10,9	7,00	1,53
MI20-17B	228	35,91	0,60	11,00	3,98	0,05	2,34	21,41	0,53	2,02	0,10	20,87	98,79	27,5	1,51	3910				16745		12,2	3603	77,3	78,8			9,04	31,3	18,1	39,0	13,5	75,6	295	13,9	113	10,2	1,62	5,03	108	15,5	32,7	3,88	14,3	3,07	0,63	2,53	0,43	2,57	0,56	1,45	0,22	1,41	0,20	2,95	0,71	0,29	7,25	7,94	1,90
MI20-16	226	38,08	0,72	12,73	4,27	0,05	3,07	17,51	0,52	2,01	0,11	19,42	98,48	32,4	1,55	3872				16687		15,2	4316	91,1	88,7			20,9	47,7	20,6	45,5	15,0	78,5	517	16,2	132	12,3	2,16	5,92	118	21,1	43,9	5,26	19,4	3,87	0,84	3,19	0,52	3,14	0,63	1,73	0,27	1,68	0,26	3,52	0,88	0,31	9,75	9,74	1,91
MI20-15	221,3	19,74	0,39	6,34	2,98	0,05	3,29	33,64	0,36	1,04	0,08	30,97	98,87	17,4	0,89	2641				8593		8,32	2320	48,1	56,4			8,82	25,9	12,4	25,1	7,48	38,5	937	12,7	69,2	6,52	0,97	2,63	60,1	13,5	29,6	3,45	13,1	2,79	0,61	2,39	0,38	2,30	0,51	1,29	0,19	1,20	0,18	1,74	0,44	0,17	8,66	4,73	1,40
MI20-14	218,5	25,63	0,50	7,82	3,68	0,06	3,18	28,88	0,37	1,26	0,09	27,56	99,02	18,8	1,13	2760				10436		10,8	3015	59,4	72,1			12,0	32,6	15,2	31,5	9,56	48,7	878	17,3	87,3	8,39	1,22	3,15	74,1	19,2	41,5	4,75	18,3	3,82	0,91	3,18	0,54	3,11	0,65	1,75	0,27	1,85	0,24	2,19	0,55	0,16	10,9	5,58	1,53
MI20-13	216	27,15	0,37	8,24	3,55	0,06	4,40	25,79	0,52	1,44	0,11	26,65	98,28	26,6	1,23	3872				11947		8,59	2200	60,2	49,8			8,83	30,8	13,9	41,2	10,4	60,4	666	15,0	72,2	6,53	1,32	4,47	108	15,5	30,5	3,68	13,7	2,82	0,60	2,63	0,42	2,46	0,51	1,41	0,22	1,37	0,20	1,95	0,48	0,29	10,1	5,98	1,84
MI20-12	213,5	30,94	0,40	9,42	3,90	0,07	4,05	23,50	0,57	1,70	0,13	24,39	99,06	30,9	1,43	4236				14088		9,61	2374	66,3	53,1			9,42	33,7	16,7	44,6	12,0	71,4	626	15,4	78,5	7,01	1,46	5,44	124	16,5	32,9	3,92	14,7	3,03	0,68	2,60	0,45	2,62	0,56	1,52	0,23	1,45	0,21	2,10	0,50	0,37	10,3	6,65	2,02
MI20-11	211,5	32,20	0,43	9,56	3,91	0,06	4,62	21,66	0,53	1,80	0,13	23,75	98,62	28,0	1,26	3910				14902		10,3	2548	70,1	59,9			9,96	32,4	17,4	48,4	12,2	74,1	560	15,8	81,7	7,51	1,50	5,29	142	17,0	34,4	4,16	15,8	3,14	0,71	2,73	0,45	2,72	0,55	1,55	0,23	1,49	0,21	2,16	0,55	0,32	10,2	6,67	2,74
MI20-10	210	26,83	0,42	7,86	3,31	0,05	3,77	27,76	0,40	1,45	0,26	26,88	98,99	20,0	1,16	2967				12013		9,52	2500	63,0	65,3			9,46	30,6	13,5	28,4	9,78	58,3	663	17,3	79,0	7,21	1,24	3,85	88,3	19,0	40,0	4,81	19,0	3,66	0,92	3,41	0,56	3,06	0,62	1,65	0,24	1,54	0,22	2,05	0,47	0,33	8,27	5,62	2,26
MTR21	209	36,73	0,84	12,74	6,85	0,09	2,98	17,77	0,21	1,71	0,12	19,47	99,32	32,6	1,62	1598	17472	68714	570	14188	127704	17,8	5036	103	123	708	47396	22,1	58,7	31,5	43,2	15,2	72,8	340	16,8	123	13,4	1,81	7,17	75,3	22,5	45,7	5,34	21,6	4,28	1,03	3,76	0,55	3,50	0,62	1,84	0,25	1,73	0,25	3,11	0,87	0,23	11,0	7,50	1,85
MI20-9	208,5	34,10	0,54	10,02	4,05	0,05	3,94	21,40	0,43	1,80	0,18	22,46	98,96	24,9	1,37	3175				14902		11,8	3231	76,9	77,2			12,1	34,8	17,2	37,5	12,1	71,1	452	18,7	104	9,01	1,48	4,84	105	21,0	44,2	5,28	20,2	4,14	0,95	3,54	0,56	3,47	0,68	1,92	0,27	1,78	0,26	2,64	0,63	0,37	10,5	6,96	2,61
MI20-8	206,8	31,99	0,49	9,50	3,74	0,04	3,34	23,61	0,46	1,68	0,13	23,91	98,89	25,2	1,26	3398				13939		10,8	2914	70,0	72,3			9,76	31,9	17,3	38,8	11,8	67,9	722	16,0	95,5	8,32	1,53	4,87	111	17,7	35,9	4,26	16,4	3,28	0,71	2,90	0,49	2,92	0,59	1,63	0,23	1,51	0,22	2,42	0,58	0,30	10,2	6,52	2,19
MI20-7	206,5	12,39	0,19	3,74	1,84	0,04	2,83	41,27	0,18	0,77	0,09	36,01	99,35	10,6	0,74	1335				6401		4,47	1121	31,0	30,5			4,42	17,9	5,79	14,6	4,68	30,7	695	7,69	34,4	3,12	0,59	2,07	43,6	7,67	15,4	1,87	7,33	1,37	0,35	1,32	0,20	1,22	0,25	0,68	0,100	0,65	0,098	0,83	0,23	0,12	2,82	2,28	1,25
LSC3	206	34,30	0,50	10,88	4,45	0,06	3,20	20,36	0,85	1,55	0,09	22,24	98,47	29,5	1,57	6283	18991	58513	442	12860	146525	13,2	3009	70,3	48,7	470	33009	16,0	21,8	17,0	36,5	13,5	66,6	889	18,0	107	9,76	2,27	7,45	119	22,8	45,4	5,21	20,5	4,05	0,84	3,62	0,55	3,39	0,65	1,94	0,26	1,95	0,28	2,88	0,72	0,30	13,4	9,07	1,93
LSC1	205	45,11	0,58	15,00	5,34	0,04	3,25	11,47	0,92	2,51	0,07	14,63	98,90	34,3	1,97	6788	19451	80641	378	20838	82340	17,8	3459	88,2	58,8	314	37830	14,3	21,7	18,3	47,3	19,2	105	636	25,2	130	11,7	3,27	9,99	137	30,6	61,7	7,26	28,7	5,71	1,08	5,08	0,80	4,75	0,93	2,60	0,36	2,57	0,35	3,84	0,85	0,42	17,3	12,0	2,55
MI20-6	200	38,58	0,62	11,37	4,51	0,05	5,29	15,85	0,42	2,32	0,11	19,48	98,59	34,6	1,33	3108				19227		13,9	3741	76,2	86,3			10,9	41,5	20,5	41,9	13,7	88,9	293	12,4	98,3	10,0	1,68	5,41	101	13,3	26,7	3,26	12,5	2,63	0,60	2,23	0,39	2,32	0,47	1,31	0,20	1,31	0,19	2,58	0,66	0,38	10,0	6,95	2,22
MI20-5	196	23,62	0,33	7,89	2,80	0,03	2,70	31,35	0,20	1,15	0,03	28,97	99,07	18,7	0,77	1461				9556		8,60	1984	49,8	29,0			5,22	18,6	11,7	21,2	9,26	43,4	401	10,7	66,4	6,41	1,44	3,88	36,4	10,3	20,4	2,55	9,29	2,02	0,41	1,77	0,30	1,82	0,36	1,05	0,16	0,97	0,13	1,85	0,51	0,15	5,18	5,98	1,53
MI20-4B	195	31,27	0,45	10,25	3,29	0,02	2,84	24,74	0,25	1,41	0,03	24,58	99,12	17,7	0,98	1818				11731		10,6	2692	65,1	37,2			4,94	14,9	12,8	24,2	12,4	50,2	748	11,7	85,2	8,60	1,94	4,15	87,9	12,5	24,6	3,24	11,9	2,54	0,45	2,17	0,36	2,12	0,41	1,17	0,18	1,12	0,17	2,45	0,67	0,14	5,39	7,57	1,68
MI20-4	194,2	23,24	0,43	7,79	3,27	0,05	3,08	30,53	0,25	1,43	0,06	28,83	98,94	17,9	0,96	1818				11839		9,53	2548	52,7	54,8			10,4	29,2	13,0	22,6	8,99	51,6	643	11,3	67,6	7,18	1,33	3,41	53,6	11,7	24,0	2,83	11,0	2,39	0,51	2,05	0,32	1,96	0,41	1,05	0,15	1,05	0,14	1,80	0,48	0,14	7,36	4,83	1,60
MI20-3	193,7	20,41	0,38	6,69	4,44	0,08	6,89	28,10	0,16	1,36	0,10	31,09	99,69	16,0	1,12	1202				11249		8,70	2266	49,5	51,5			9,76	28,5	14,0	23,1	7,82	51,1	479	12,9	61,6	6,12	1,14	2,91	186	13,5	27,1	3,35	13,2	2,67	0,60	2,39	0,38	2,14	0,43	1,21	0,17	1,10	0,15	1,56	0,42	0,14	5,40	4,00	1,37
MI20-2	193	27,76	0,50	9,05	3,65	0,05	2,71	27,30	0,23	1,85	0,07	25,88	99,05	20,4	1,26	1677				15317		11,8	3009	65,4	64,5			11,9	37,4	18,6	32,9	10,5	67,2	360	15,4	82,8	8,40	1,53	4,38	52,6	17,1	35,4	4,21	15,9	3,22	0,76	3,02	0,47	2,81	0,54	1,48	0,22	1,39	0,20	2,22	0,61	0,21	8,26	6,03	1,95
MI20-1	192,22	20,02	0,37	6,55	4,35	0,08	6,78	27,78	0,18	1,33	0,10	31,18	98,70	15,8	1,04	1306				11000		8,85	2200	49,5	51,7			9,61	29,6	13,8	22,7	7,71	50,9	481	13,2	61,2	6,02	0,97	2,86	189	13,7	27,6	3,32	13,0	2,60	0,61	2,49	0,39	2,28	0,44	1,27	0,18	1,11	0,16	1,58	0,43	0,13	5,58	4,11	1,38
NST-47	142	24,87	0,42	9,55	3,96	0,07	2,10	27,69	0,16	1,09	0,07	29,62	99,60	20,1	0,97	1158				9063		11,8	2493	57,4	29,4			11,2	17,5	19,7	31,9	10,3	33,5	498		82,1	6,02	1,63	4,86	82,3																					2,5	0,54	0,12	9,14	6,30	1,17
NST-46	132	28,30	0,46	11,03	4,61	0,08	2,41	25,03	0,18	1,25	0,07	26,20	99,63	23,2	1,08	1359				10407		13,7	2786	66,3	33,7			12,5	18,9	22,7	37,1	12,2	38,5	583		89,3	6,75	2,06	5,54	98,8																					2,6	0,58	0,14	10,1	6,97	1,24
NST-45	127	40,88	0,62	12,75	4,26	0,07	2,62	17,10	0,71	2,11	0,10	18,19	99,41	36,2	1,47	5239				17499		14,3	3720	73,6	43,9			14,1	21,1	16,5	53,9	13,8	57,9	644		135,4	9,68	2,77	7,38	199																					4,3	0,89	0,28	14,1	10,0	2,01
NST-44	124	21,66	0,27	6,76	2,56	0,04	3,46	32,53	0,24	0,74	0,06	31,21	99,52	18,1	0,68	1795				6110		7,68	1599	36,0	20,3			5,72	11,7	12,9	21,5	7,33	22,2	1052		65,1	4,21	1,05	3,14	49,1																					2,4	0,37	0,12	6,15	4,45	1,12
NST-43	122	35,59	0,66	13,68	5,54	0,05	3,16	17,80	0,30	1,74	0,11	20,87	99,51	35,3	1,38	2246				14443		15,2	3976	91,6	42,7			14,8	17,0	30,6	49,1	13,2	45,5	878		120,9	7,86	2,25	5,34	128																					3,3	0,73	0,18	11,6	7,83	1,40
NST-42	118	24,33	0,40	8,98	4,06	0,06	3,34	28,38	0,23	1,03	0,07	28,65	99,56	26,4	1,04	1700				8577		11,9	2426	55,1	28,1			9,15	18,3	20,9	28,5	10,7	31,6	936		79,7	5,97	1,68	4,17	69,4																					2,4	0,53	0,11	8,12	6,48	1,23
NST-41	113	33,64	0,56	12,55	4,50	0,04	3,26	20,64	0,30	1,45	0,07	22,51	99,52	37,5	1,35	2189				12068		16,6	3342	73,5	37,6			12,3	19,7	28,7	40,8	15,2	44,9	829		106,2	8,39	2,47	6,39	87,2																					3,5

8.6 CALCULATED WEATHERING INDICES

SAMPLES	m	CIA	CIW	CIX	WIP	PIA	CPA	WI	Rb/K_2O
TV5	416	69	94	70	69	42	97	9	24
TV4	411	68	92	70	54	43	96	5	20
TV3	406	67	90	69	58	42	95	4	20
TV2	401	69	95	70	70	42	97	9	25
TV1	396	70	93	71	61	45	97	5	25
DIB 308	336	63	92	64	76	32	96	8	20
DIB 307	335	61	92	63	81	28	96	10	19
DIB 306	333,5	65	94	66	77	34	97	8	20
DIB 305	333	66	93	68	71	38	96	5	21
DIB 304	331	72	96	73	66	47	98	6	23
DIB 302	330	63	93	64	81	31	96	7	17
DIB 301	327	65	96	64	73	32	96	5	18
R5T4	271	83	93	85	27	73	97	11	22
R5T3	266	83	95	85	25	73	97	11	22
R5T2	261	77	83	84	26	76	91	11	20
R5T1	256	82	91	86	31	75	96	10	19
MI20-18	234	71	80	78	27	65	89	5	38
MI20-17	232	72	82	78	29	65	90	5	40
MTR24	230	72	83	78	41	64	91	3	40
MI20-17B	228	74	86	78	25	63	93	6	37
MI20-16	226	77	88	81	26	67	94	5	39
MI20-15	221,3	73	84	79	20	65	92	5	37
MI20-14	218,5	75	86	80	21	66	93	4	39
MI20-13	216	72	83	77	27	62	91	7	42
MI20-12	213,5	72	83	77	26	63	91	8	42
MI20-11	211,5	72	85	77	29	62	92	7	41
MI20-10	210	73	86	78	23	62	92	6	40
MTR21	209	71	80	78	32	66	89	3	43
MI20-9	208,5	75	88	79	26	64	93	6	40
MI20-8	206,8	74	86	79	24	64	93	6	40
MI20-7	206,5	73	87	77	15	60	93	7	40
LSC3	206	64	89	67	74	38	94	6	43
LSC1	205	64	89	67	69	38	94	8	42
MI20-6	200	75	89	78	32	61	94	6	38
MI20-5	196	81	92	83	17	70	96	6	38
MI20-4B	195	81	93	84	19	72	96	5	35
MI20-4	194,2	77	91	80	21	64	95	5	36
MI20-3	193,7	77	93	79	29	62	96	5	38
MI20-2	193	77	92	79	22	62	96	6	36
MI20-1	192,22	76	92	79	29	62	96	6	38
NST-47	142	85	95	87	17	76	89	4	31
NST-46	132	85	95	87	19	76	89	4	31
NST-45	127	73	85	79	33	65	85	6	27
NST-44	124	81	89	85	19	75	89	5	30
NST-43	122	83	93	85	27	73	88	4	26
NST-42	118	83	92	86	21	75	89	4	31
NST-41	113	83	93	86	25	75	89	4	31
NST-40	108	70	81	77	45	63	85	6	26
NST-39	103	74	82	81	25	71	89	6	31
NST-38	98	80	91	83	28	71	87	6	30
NST-37	93	79	89	84	20	72	88	6	31
NST-36	88	83	94	85	25	73	88	6	30
NST-35	83	76	84	81	26	70	88	6	10
NST-34	78	60	70	69	56	52	81	4	21
NST-33	73	73	83	79	34	67	87	5	28
NST-31	71	82	91	85	18	75	89	5	32
NST-30	66	74	85	80	37	66	85	5	26
NST-29	61	69	80	76	42	62	84	7	19
NST-28	56	81	94	83	30	70	86	7	32
NST-27	51	77	89	81	36	68	86	7	31
NST-25	43	79	91	82	33	69	86	7	30
NST-23	38	82	91	85	17	75	89	5	30
NST-21	28	77	88	82	35	69	87	4	24
NST-20	23	77	85	82	29	71	88	4	25
NST-19	18	79	90	83	32	70	86	5	25
NST-18	14	78	89	82	25	69	86	5	28
NST-16	6	72	81	79	27	68	87	6	27
NST-14	0	82	92	85	21	74	88	4	27

8.7 OTHER GRAPHS

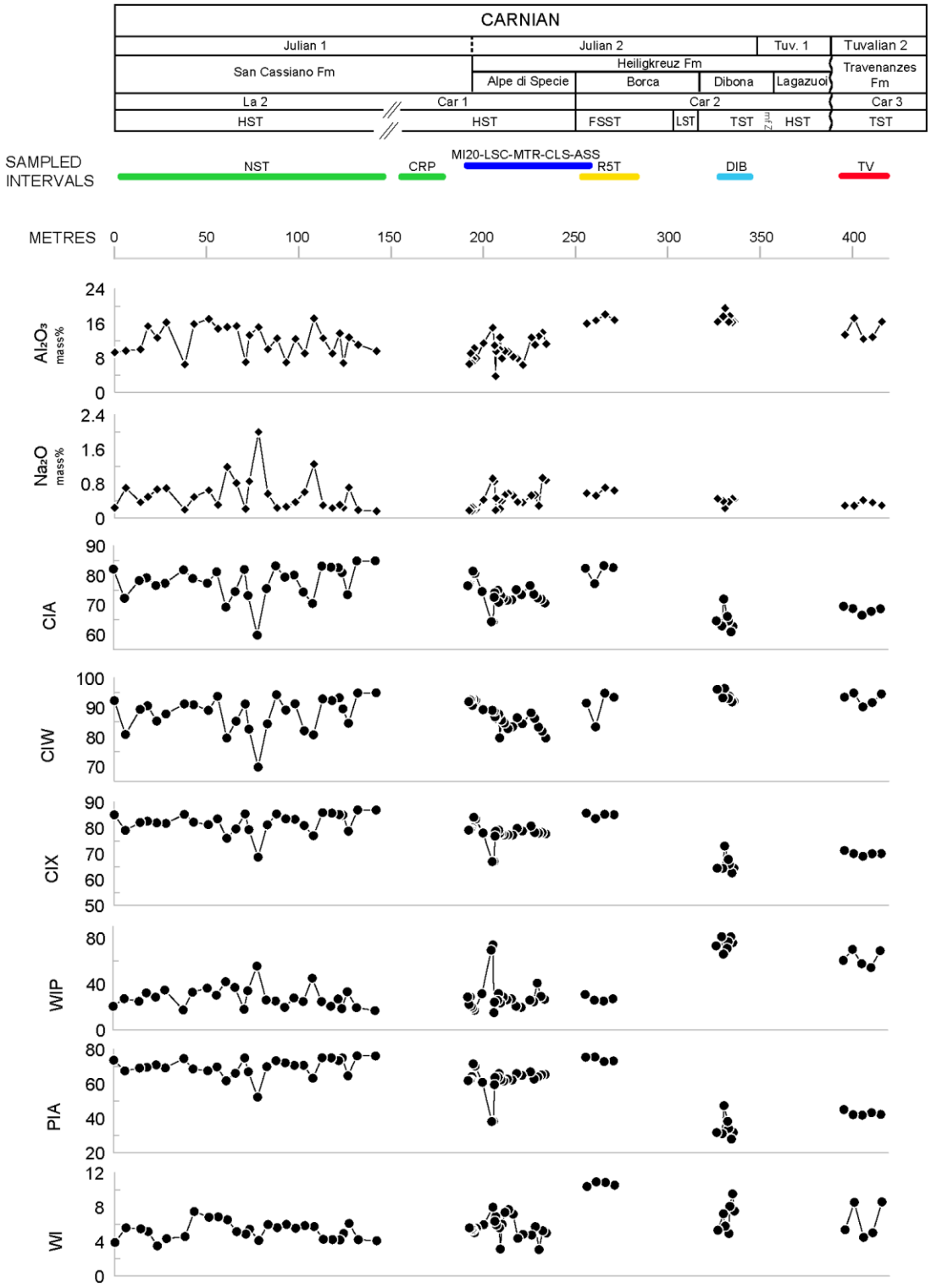

Figure 8.12: Variations of selected major elements and weathering indices excluded for final interpretation along the succession. Abbreviations and acronyms as in Fig. 5.3 and Table 5.1.

8.8 QUANTITATIVE MINERALOGICAL DATA AND SIGNIFICANT RATIOS

SAMPLES	m	Albite		Anorthite		K-Feldspar		Aragonite		Calcite		Mg-Calcite		Dolomite		Chlorite		Kaolinite		Illite		I/S		Quartz		Gypsum		Hematite		Jarosite		Pyrite		Carbonates	Clays	KF/(KF+Q)	F/(F+Q)	Clays normalized to 100%			
		wt%	ESD	wt%	ESD	wt%	ESD	wt%	ESD	wt%	ESD	wt%	ESD	wt%	ESD	wt%	ESD	wt%	ESD	wt%	ESD	wt%	ESD	wt%	ESD	wt%	ESD	wt%	ESD	wt%	ESD	wt%	ESD	%	%			I/S	Kao	Chl	Illite
TV5	416	0,4	0,1	0,0	0,0	7,4	0,2	1,1	0,1	2,1	0,3	0,5	0,1	5,4	0,2	0,6	0,2	0,0	0,0	63,4	0,9	13,7	0,9	5,2	0,2	0,0	0,0	0,3	0,0	0,0	0,0	0,0	0,0	9,0	77,7	0,6	0,60	17,6	0,0	0,8	81,6
TV4	411	0,7	0,1	0,0	0,0	8,7	0,2	1,4	0,1	12,4	0,2	0,3	0,1	9,1	0,2	1,1	0,1	0,0	0,0	39,4	0,8	16,0	0,8	10,5	0,2	0,0	0,0	0,5	0,0	0,0	0,0	0,0	0,0	23,3	56,4	0,5	0,47	28,3	0,0	2,0	69,7
TV3	406	0,4	0,1	0,0	0,0	9,4	0,2	1,1	0,1	1,9	0,7	0,5	0,1	16,5	0,2	0,8	0,1	0,0	0,0	33,2	0,7	19,7	0,6	15,0	0,3	0,0	0,0	1,6	0,0	0,0	0,0	0,0	0,0	19,9	53,7	0,4	0,40	36,7	0,0	1,5	61,8
TV2	401	0,2	0,2	0,0	0,0	6,5	0,2	0,9	0,2	0,9	0,2	0,0	0,0	0,0	0,0	1,0	0,2	0,0	0,0	71,2	0,7	15,2	10,0	3,2	0,1	0,0	0,0	0,7	0,1	0,0	0,0	0,0	0,0	1,9	87,4	0,7	0,67	17,4	0,0	1,1	81,5
TV1	396	0,3	0,1	0,0	0,0	6,5	0,2	1,2	0,1	1,2	0,6	0,1	0,0	19,3	0,3	0,6	0,2	0,0	0,0	41,8	0,9	17,8	0,8	9,4	0,2	0,0	0,0	1,9	0,1	0,0	0,0	0,0	0,0	21,8	60,2	0,4	0,42	29,6	0,0	1,0	69,4
DIB308	336	0,1	0,2	0,0	0,0	29,9	0,4	0,9	0,2	3,9	0,3	4,1	0,1	2,9	0,2	0,0	0,0	4,1	0,3	4,0	0,2	38,9	0,6	10,5	0,2	0,0	0,0	0,0	0,0	0,0	0,0	0,6	0,1	11,9	47,0	0,7	0,74	82,7	8,8	0,0	8,5
DIB307	335	0,0	0,0	0,0	0,0	32,6	1,3	1,5	0,2	7,1	3,7	0,1	0,0	4,2	0,2	0,0	0,0	3,5	0,3	4,3	0,2	34,9	1,5	11,6	0,5	0,0	0,0	0,0	0,0	0,0	0,0	0,2	0,0	12,8	42,7	0,7	0,74	81,7	8,2	0,0	10,1
DIB306	333,5	1,4	0,2	0,0	0,0	25,4	0,6	1,1	0,2	14,7	1,9	0,9	0,1	0,5	0,1	0,0	0,0	4,1	0,3	3,5	0,2	40,8	1,1	7,3	0,3	0,0	0,0	0,0	0,0	0,0	0,0	0,3	0,0	17,2	48,4	0,8	0,79	84,3	8,5	0,0	7,2
DIB305	333	1,1	0,2	0,0	0,0	23,1	0,4	1,8	0,2	2,6	0,7	0,2	0,1	9,2	0,3	0,0	0,0	3,5	0,4	4,5	0,2	47,1	0,8	6,6	0,3	0,0	0,0	0,0	0,0	0,0	0,0	0,5	0,1	13,7	55,1	0,8	0,79	85,4	6,4	0,0	8,2
DIB304	331	1,0	0,3	0,0	0,0	16,6	0,4	2,3	0,3	4,9	0,4	0,0	0,0	5,0	0,3	0,0	0,0	2,3	0,4	6,1	0,3	56,9	0,8	3,8	0,2	0,0	0,0	0,0	0,0	0,0	0,0	1,2	0,1	12,2	65,3	0,8	0,82	87,2	3,5	0,0	9,3
DIB302	330	0,5	0,2	0,0	0,0	34,7	0,4	1,6	0,2	3,8	0,2	0,3	0,1	0,4	0,1	0,0	0,0	3,9	0,3	4,2	0,2	41,6	0,6	8,7	0,2	0,0	0,0	0,0	0,0	0,0	0,0	0,3	0,0	6,1	49,7	0,8	0,80	83,7	7,8	0,0	8,4
DIB301	327	0,8	0,2	0,0	0,0	29,6	0,4	1,3	0,2	3,4	0,3	0,3	0,1	1,7	0,2	0,0	0,0	5,2	0,3	3,6	0,2	41,8	0,6	10,8	0,3	0,0	0,0	0,0	0,0	0,0	0,0	1,5	0,1	6,7	50,6	0,7	0,74	82,7	10,2	0,0	7,1
R5T4	271	2,0	0,2	0,0	0,0	34,0	0,4	0,4	0,1	3,3	0,2	1,2	0,2	1,9	0,2	0,0	0,0	4,7	0,4	4,2	0,2	36,9	0,6	11,0	0,2	0,0	0,0	0,0	0,0	0,0	0,0	0,3	0,0	6,8	45,9	0,8	0,77	80,5	10,3	0,0	9,2
R5T3	266	1,7	0,2	0,0	0,0	33,0	0,4	1,3	0,2	0,9	0,2	0,4	0,1	1,2	0,2	0,0	0,0	2,7	0,4	4,1	0,2	45,4	0,6	9,1	0,2	0,0	0,0	0,0	0,0	0,0	0,0	0,3	0,1	3,8	52,2	0,8	0,79	87,1	5,1	0,0	7,8
R5T2	261	0,0	0,0	0,0	0,0	36,5	0,4	0,6	0,1	2,6	0,2	2,0	0,3	1,9	0,2	0,0	0,0	3,9	0,3	4,3	0,2	38,1	0,5	9,8	0,2	0,0	0,0	0,0	0,0	0,0	0,0	0,3	0,0	7,1	46,3	0,8	0,79	82,3	8,4	0,0	9,3
R5T1	256	0,9	0,2	0,0	0,0	36,7	0,4	1,2	0,2	2,6	0,3	2,4	0,3	2,1	0,2	0,0	0,0	2,1	0,3	3,9	0,2	38,0	0,5	10,0	0,2	0,0	0,0	0,0	0,0	0,0	0,0	0,2	0,1	8,3	44,0	0,8	0,79	86,4	4,8	0,0	8,8
ASS10A	254	0,0	0,0	7,7	0,6	34,2	0,4	0,8	0,2	0,0	0,0	1,4	0,1	0,9	0,1	0,0	0,0	5,0	0,3	4,0	0,1	35,7	0,5	9,4	0,2	0,0	0,0	0,0	0,0	0,0	0,0	0,9	0,0	3,1	44,7	0,8	0,82	79,8	11,3	0,0	8,9
ASS9	250	1,3	0,2	0,0	0,0	33,8	0,3	1,7	0,1	2,7	0,2	1,4	0,1	0,8	0,1	0,0	0,0	3,7	0,3	28,3	0,6	15,0	0,5	6,7	0,2	1,6	0,1	0,0	0,0	2,6	0,1	0,3	0,0	6,7	47,0	0,8	0,84	31,9	7,9	0,0	60,2
ASS8	249	1,9	0,2	0,0	0,0	28,7	0,3	1,1	0,1	1,1	0,1	0,8	0,1	1,0	0,1	1,5	0,2	4,8	0,3	29,7	0,6	17,9	0,7	11,3	0,2	0,0	0,0	0,0	0,0	0,0	0,0	0,3	0,0	4,0	54,0	0,7	0,73	33,2	8,9	2,8	55,1
ASS7	248	5,5	0,1	0,0	0,0	14,7	0,2	1,0	0,1	3,2	0,2	0,6	0,1	1,3	0,1	0,0	0,0	7,1	0,4	28,7	0,5	23,2	0,4	14,6	0,2	0,0	0,0	0,0	0,0	0,0	0,0	0,2	0,0	6,0	59,0	0,5	0,58	39,4	11,9	0,0	48,7
ASS6	247	7,5	0,2	0,0	0,0	10,2	0,2	0,2	0,1	10,0	0,3	3,3	0,2	1,3	0,1	3,5	0,7	9,8	0,3	16,3	0,6	21,2	0,8	16,3	0,2	0,0	0,0	0,0	0,0	0,0	0,0	0,3	0,0	14,9	50,8	0,4	0,52	41,8	19,2	6,8	32,1
ASS5	246	4,2	0,2	0,0	0,0	10,7	0,2	1,1	0,2	5,9	0,2	3,6	0,1	1,1	0,1	1,1	0,2	7,9	0,3	26,3	0,5	22,0	0,5	15,6	0,2	0,0	0,0	0,0	0,0	0,0	0,0	0,6	0,0	11,7	57,3	0,4	0,49	38,4	13,9	1,9	45,9
ASS4	245	8,4	0,2	0,0	0,0	10,0	0,2	0,7	0,1	3,2	0,5	8,8	0,6	0,4	0,1	3,5	0,3	10,5	0,4	13,2	0,3	25,6	0,6	15,3	0,2	0,0	0,0	0,0	0,0	0,0	0,0	0,5	0,0	13,1	52,8	0,4	0,55	48,4	20,0	6,6	25,0
ASS3	244	6,3	0,1	0,0	0,0	7,1	0,2	1,1	0,1	9,1	0,2	1,1	0,2	0,7	0,1	1,5	0,1	8,1	0,3	27,8	0,5	21,2	0,5	15,4	0,2	0,0	0,0	0,0	0,0	0,0	0,0	0,5	0,0	12,1	58,6	0,3	0,47	36,2	13,7	2,6	47,5
ASS2	243	5,0	0,1	0,0	0,0	9,2	0,2	1,2	0,2	7,6	0,2	3,1	0,2	1,7	0,1	1,4	0,1	8,6	0,3	24,9	0,5	21,3	0,5	15,5	0,2	0,0	0,0	0,0	0,0	0,0	0,0	0,6	0,0	13,6	56,2	0,4	0,48	37,9	15,2	2,4	44,4
CLS1	242	1,9	0,1	0,0	0,0	7,5	0,2	2,3	0,1	2,1	0,1	2,0	0,1	0,9	0,1	0,0	0,0	10,7	0,3	30,0	0,5	28,2	0,5	14,5	0,2	0,0	0,0	0,0	0,0	0,0	0,0	0,0	0,0	7,2	68,9	0,3	0,39	40,9	15,6	0,0	43,6
CLS2	241	1,8	0,1	0,0	0,0	8,4	0,2	2,3	0,2	3,6	0,2	1,9	0,2	0,4	0,1	1,0	0,1	9,9	0,3	19,9	0,5	25,8	0,6	25,0	0,3	0,0	0,0	0,0	0,0	0,0	0,0	0,0	0,0	8,2	56,6	0,3	0,29	45,6	17,5	1,7	35,2
CLS3	240	1,5	0,1	0,0	0,0	9,4	0,2	1,9	0,1	3,6	0,1	3,5	0,1	1,3	0,1	0,0	0,0	9,0	0,3	24,5	0,5	18,9	0,5	25,3	0,2	0,0	0,0	0,0	0,0	0,0	0,0	1,0	0,0	10,3	52,5	0,3	0,30	36,1	17,2	0,0	46,7
CLS4	239	1,0	0,1	0,0	0,0	9,0	0,2	2,2	0,2	3,1	0,1	4,0	0,2	1,4	0,1	0,0	0,0	9,5	0,2	25,7	0,6	26,1	0,5	17,4	0,2	0,0	0,0	0,0	0,0	0,0	0,0	0,7	0,0	10,6	61,4	0,3	0,36	42,6	15,5	0,0	41,9
CLS5	238	2,1	0,1	0,0	0,0	9,7	0,2	2,0	0,2	3,7	0,2	3,3	0,3	0,3	0,1	0,0	0,0	7,2	0,5	15,9	0,5	29,5	0,5	26,4	0,3	0,0	0,0	0,0	0,0	0,0	0,0	0,0	0,0	9,3	52,6	0,3	0,31	56,1	13,6	0,0	30,3
MI20-18	234	7,5	0,2	0,0	0,0	5,2	0,2	0,3	0,1	10,3	0,3	19,2	0,3	0,6	0,1	0,0	0,0	4,0	0,2	2,8	0,1	35,7	0,4	13,8	0,2	0,0	0,0	0,0	0,0	0,0	0,0	0,6	0,0	30,3	42,5	0,3	0,48	84,0	9,5	0,0	6,5
MI20-17	232	4,7	0,2	0,0	0,0	5,2	0,2	1,4	0,2	11,2	0,3	17,0	0,3	1,0	0,1	4,0	0,4	2,3	0,3	3,6	0,1	34,1	0,6	15,3	0,3	0,0	0,0	0,0	0,0	0,0	0,0	0,1	0,0	30,7	44,1	0,3	0,39	77,3	5,3	9,2	8,2
MTR24	230	1,8	0,1	0,0	0,0	2,5	0,2	0,0	0,0	12,6	0,3	21,7	0,3	3,2	0,6	8,4	0,3	8,2	0,4	1,7	0,1	30,9	0,5	9,2	0,2	0,0	0,0	0,0	0,0	0,0	0,0	0,0	0,0	37,4	49,1	0,2	0,32	62,9	16,6	17,0	3,5
MI20-17B	228	4,9	0,1	0,0	0,0	2,2	0,2	0,2	0,1	33,7	0,4	8,8	0,4	0,8	0,1	6,6	0,3	7,5	0,3	2,6	0,1	22,2	0,5	10,0	0,2	0,0	0,0	0,0	0,0	0,0	0,0	0,6	0,0	43,5	38,9	0,2	0,41	57,1	19,3	16,9	6,7
MI20-16	226	4,2	0,1	0,0	0,0	3,0	0,2	0,8	0,1	11,7	0,3	29,7	0,3	0,4	0,1	3,5	0,2	5,0	0,3	2,3	0,1	30,1	0,4	8,9	0,2	0,0	0,0	0,0	0,0	0,0	0,0	0,5	0,0	42,5	40,9	0,3	0,45	73,6	12,3	8,6	5,6
MI20-15	221,3	3,3	0,1	0,0	0,0	2,7	0,1	0,7	0,1	14,5	0,4	37,4	0,4	0,9	0,1	3,1	0,2	3,9	0,3	2,0	0,1	25,4	0,4	5,6	0,1	0,0	0,0	0,0	0,0	0,0	0,0	0,7	0,0	53,4	34,3	0,3	0,51	73,9	11,3	9,0	5,8
MI20-14	218,5	3,9	0,1	0,0	0,0	3,1	0,2	1,4	0,2	9,5	0,3	21,4	0,3	0,5	0,1	8,6	0,5	2,6	0,3	2,5	0,1	39,7	0,5	6,3	0,2	0,0	0,0	0,0	0,0	0,0	0,0	0,5	0,0	32,8	53,4	0,3	0,52	74,4	4,8	16,2	4,6
MI20-13	216	5,7	0,1	0,0	0,0	3,1	0,2	0,8	0,1	18,4	0,3	24,9	0,3	10,1	0,2	6,0	0,3	5,0	0,3	2,0	0,1	13,0	0,5	10,3	0,2	0,0	0,0	0,0	0,0	0,0	0,0	0,7	0,0	54,1	26,0	0,2	0,46	50,0	19,1	23,1	7,9
MI20-12	213,5	4,9	0,1	0,0	0,0	2,3	0,2	1,4	0,1	28,6	0,3	14,4	0,4	8,2	0,2	6,2	0,3	4,6	0,3	2,3	0,1	15,8	0,4	10,6	0,2	0,0	0,0	0,0	0,0	0,0	0,0	0,8	0,0	52,6	28,8	0,2	0,41	54,7	16,0	21,4	8,0
MI20-11	211,5	5,6	0,1	0,0	0,0	2,7	0,2	0,7	0,1	23,0	0,4	12,6	0,5	10,1	0,2	7,4	0,3	4,6	0,3	2,7	0,1	18,2	0,5	11,6	0,2	0,0	0,0	0,0	0,0	0,0	0,0	0,9	0,1	46,2	32,9	0,2	0,42	55,2	14,1	22,5	8,2
MI20-10	210	4,6	0,1	0,0	0,0	2,6	0,2	0,2	0,1	26,0	0,5	12,7	0,6	8,6	0,2	1,6	0,2	2,5	0,4	3,5	0,1	26,6	0,4	9,8	0,2	0,0	0,0	0,0	0,0	0,0	0,0	1,5	0,1	47,5	34,1	0,2	0,42	78,0	7,2	4,6	10,1
MTR21	209	2,0	0,1	0,0	0,0	1,6	0,2	0,0	0,0	22,0	1,0	12,8	1,1	3,1	0,5	6,8	0,3	4,1	0,3	2,0	0,1	34,8	0,5	10,8	0,2	0,0	0,0	0,0	0,0	0,0	0,0	0,1	0,0	37,9	47,7	0,1	0,25	72,9	8,6	14,3	4,2
MI20-9	208,5	4,9	0,1	0,0	0,0	3,3	0,2	0,0	0,0	23,8	10,0	12,6	1,2	9,3	0,2	1,3	0,2	3,1	0,3	3,8	0,1	24,7	0,2	11,8	0,2	0,0	0,0	0,0	0,0	0,0	0,0	1,5	0,1	45,7	32,9	0,2	0,41	75,0	9,4	4,0	11,6
MI20-8	206,8	5,0	0,1	0,0	0,0	2,7	0,2	0,7	0,1	30,2	0,5	12,9	0,6	6,6	0,2	1,3	0,2	3,1	0,3	3,4	0,1	21,9	0,4	11,4	0,2	0,0	0,0	0,0	0,0	0,0	0,0	0,9	0,0	50,3	29,6	0,2	0,40	74,0	10,4	4,3	11,3
MI20-7	206,5	1,9	0,1	0,0	0,0	1,8	0,1	0,4	0,1	52,3	1,0	16,3	1,0	6,6	0,1	1,6	0,1	0,8	0,1	0,9	0,1	14,6	0,3	2,7	0,1	0,0	0,0	0,0	0,0	0,0	0,0	0,0	0,0	75,6	18,0	0,4	0,58	81,4	4,5	8,8	5,3
LSC3	206	2,9	0,1	0,0	0,0	3,4	0,1	1,8	0,1	11,5	0,2	28,2	0,3	1,5	0,1	3,2	0,2	3,0	0,3	1,7	0,1	34,7	0,4	7,8	0,1	0,0	0,0	0,0	0,0	0,0	0,0	0,3	0,0	43,0	42,6	0,3	0,45	81,5	7,0	7,5	4,0
LSC1	205	3,1	0,1	0,0	0,0	5,4	0,2	0,6	0,1	12,2	0,2	3,6	0,2	2,7	0,1	7,3	0,4	2,6	0,3	2,1	0,1	49,5	0,5	10,3	0,2	0,0	0,0	0,0	0,0	0,0	0,0	0,6	0,0	19,2	61,4	0,3	0,45	80,6	4,3	11,8	3,3
MI20-6	200	2,7	0,1	0,0	0,0	2,7	0,2	0,0	0,0	30,9	1,2	18,3	1,3	15,9	0,2	1,3	0,2	1,7	0,2	2,9	0,1	14,8	0,3	8,5	0,2	0,0	0,0	0,0	0,0	0,0	0,0	0,4	0,0	65,1	20,7	0,2	0,39	71,5	8,3	6,3	13,9
MI20-5	196	2,3	0,1	0,0	0,0	2,3	0,1	0,0	0,0	37,5	10,0	22,9	1,1	3,4	0,1	0,9	0,1	2,9	0,2	1,9	0,1	21,6	0,2	4,0	0,1	0,0	0,0	0,0	0,0	0,0	0,0	0,3	0,0	63,8	27,3	0,4	0,53	79,2	10,8	3,3	6,8
MI20-4B	195	2,2	0,1	0,0	0,0	2,8	0,2	0,0	0,0	40,8	0,8	10,6	0,9	0,5	0,1	0,3	0,1	4,6	0,2	2,4	0,1	29,3	0,3	6,2	0,2	0,0	0,0	0,0	0,0	0,0	0,0	0,2	0,0	51,9	36,6	0,3	0,45	80,0	12,6	0,9	6,4
MI20-4	194,2	1,9	0,1	0,0	0,0	2,3	0,1	0,7	0,1	35,3	0,4	18,6	0,4	2,4	0,1	0,0	0,0	3,3	0,2	1,7	0,1	30,4	0,4	3,3	0,1	0,0	0,0	0,0	0,0	0,0	0,0	0,1	0,0	56,9	35,5	0,4	0,56	85,8	9,3	0,0	4,9
MI20-3	193,7	1,5	0,1	0,0	0,0	2,3	0,1	0,4	0,1	36,7	0,6	8,2	0,7	23,4	0,2	0,0	0,0	1,6	0,2	1,5	0,1	21,7	0,4	2,7	0,2	0,0	0,0	0,0	0,0	0,0	0,0	0,3	0,0	68,6	24,8	0,5	0,58	87,7	6,3	0,0	6,0
MI20-2	193	2,6	0,1	0,0	0,0	3,2	0,2	0,2	0,1	25,5	1,5	17,0	1,6	3,1	0,2	0,0	0,0	4,2	0,3	2,7	0,1	36,1	0,5	5,2	0,2	0,0	0,0	0,0	0,0	0,0	0,0	0,3	0,0	45,7	43,0	0,4	0,53	84,0	9,8	0,0	6,2
MI20-1	192,22	2,3	0,1	0,0	0,0	2,4	0,1	0,7	0,1	33,2	0,4	19,2	0,4	0,2	0,1	0,0	0,0	3,7	0,2	1,8	0,1	31,5	0,4	4,9	0,2	0,0	0,0	0,0	0,0	0,0	0,0	0,2	0,0	53,3	37,0	0,3	0,49	85,1	10,0	0,0	4,9
CRP2	175	1,2	0,1	0,0	0,0	2,0	0,1	0,5	0,1	35,2	1,0	16,7	10,0	0,0	0,0	4,5	0,2	4,7	0,3	1,8	0,1	28,7	0,5	4,7	0,1	0,0	0,0	0,0	0,0	0,0	0,0	0,1	0,0	52,4	39,6	0,3	0,40	72,4	11,8	11,3	4,4
CRP1	170	1,4	0,1	0,0	0,0	1,7	0,2	0,1	0,0	32,1	0,4	17,0	0,4	1,8	0,1	3,7	0,2	5,4	0,3	1,9	0,1	28,8	0,5	6,0	0,2	0,0	0,0	0,0	0,0	0,0	0,0	0,1	0,0	51,0	39,8	0,2	0,34	72,4	13,5	9,2	4,9
CRP0	165	1,3	0,1	0,0	0,0	1,9	0,1	0,3	0,1	24,1	0,4	14,1	0,3	0,3	0,0	21,1	0,9	1,6	0,2	1,6	0,1	29,4	0,5	4,1	0,1	0,0	0,0	0,0	0,0	0,0	0,0	0,2	0,0	38,8	53,7	0,3	0,44	54,7	3,0	39,3	3,0
NST-47	142	1,0	0,1	0,0	0,0	2,5	0,1	1,8	0,1	54,6	0,5	14,5	0,5	0,0	0,0	0,8	0,0	3,3	0,1	0,7	0,1	17,2	0,3	3,4	0,1	0,0	0,0	0,0	0,0	0,0	0,0	0,1	0,0	71,0	22,1	0,4	0,50	78,1	14,9	3,8	3,3
NST-46	132	0,6	0,1	0,0	0,0	2,6	0,1	0,8	0,1	27,7	0,3	34,3	0,3	0,0	0,0	0,8	0,1	3,8	0,2	0,8	0,1	25,1	0,3	3,5	0,1	0,0	0,0	0,0	0,0	0,0	0,0	0,0	0,0	62,8	30,5	0,4	0,47	82,2	12,5	2,6	2,8
NST-45	127	3,9	0,2	0,0	0,0	8,5	0,3	0,5	0,1	11,7	0,5	22,3	0,8	0,2	0,1	6,0	2,8	2,7	0,3	1,3	0,1	31,0	0,9	11,8	0,4	0,0	0,0	0,0	0,0	0,0	0,0	0,3	0,0	34,6	41,0	0,4	0,51	75,7	6,6	14,7	3,1
NST-43	122	1,0	0,1	0,0	0,0	5,9	0,1	0,5	0,1	12,0	0,5	26,9	0,4	0,0	0,0	2,7	0,2	9,4	0,3	1,6	0,1	34,4	0,5	5,3	0,2	0,0	0,0	0,0	0,0	0,0	0,0	0,3	0,0	39,4	48,1	0,5	0,56	71,5	19,5	5,7	3,4
NST-41	113	0,6	0,1	0,0	0,0	4,0	0,1	0,6	0,1	12,3	0,4	29,6	0,5	0,0	0,0	7,0	0,4	3,8	0,3	1,4	0,1	35,8	0,4	4,8

8.9 OTHER DATA NOT CONSIDERED FOR PUBLICATION

	SAMPLES	CT1	CT2	TMR1	TAM4	TAM3	TAM2	TAM1
SiO_2	mass%	52,54	47,63	39,59	38,81	33,67	42,44	39,16
TiO_2	mass%	1,59	1,34	1,09	0,78	0,63	0,78	0,77
Al_2O_3	mass%	18,81	12,57	13,97	12,68	11,04	13,09	12,32
TFe_2O_3	mass%	6,94	9,15	8,56	5,60	4,65	4,53	5,03
MnO	mass%	0,040	0,113	0,078	0,065	0,084	0,072	0,079
MgO	mass%	2,55	2,77	3,98	1,93	1,85	1,93	2,11
CaO	mass%	4,43	10,36	12,13	18,49	23,29	16,63	18,31
Na_2O	mass%	0,54	0,76	0,70	0,37	0,65	1,63	1,16
K_2O	mass%	2,08	1,12	2,04	1,68	1,39	1,30	1,33
P_2O_5	mass%	0,14	0,13	0,13	0,08	0,10	0,10	0,09
LOI	mass%	9,56	12,64	16,37	18,89	22,24	17,17	19,14
SUM	mass%	99,22	98,58	98,63	99,37	99,60	99,67	99,51
Li	ppm	31,9	44,3	35,4	22,0	20,9	23,3	24,6
Be	ppm	2,37	1,39	1,68	1,49	1,62	1,65	1,83
Na	ppm	3854	5624	5010	2573	4693	11929	8776
Mg	ppm	15045	16331	23515	11288	10775	11182	12410
Al	ppm	98718	67727	73278	67391	58488	68977	66215
P	ppm	669	602	594	420	485	504	438
K	ppm	17004	9546	16619	13854	11652	10654	11102
Ca	ppm	31634	71588	86033	131790	167015	115955	130641
Sc	ppm	26,0	17,5	20,1	17,5	13,7	14,6	14,3
Ti	ppm	9204	7764	6234	4575	3693	4467	4583
V	ppm	164	130	115	103	89,3	95,4	98,5
Cr	ppm	288	255	166	112	87,4	94,6	108
Mn	ppm	310	842	602	496	657	539	616
Fe	ppm	47620	63246	59844	39929	33853	31966	36113
Co	ppm	23,2	31,1	29,8	16,0	9,65	11,0	12,7
Ni	ppm	70,9	73,0	97,0	45,6	28,8	27,7	33,4
Cu	ppm	45,4	28,0	48,9	23,8	16,6	17,3	16,2
Zn	ppm	48,0	55,6	53,3	30,4	34,5	36,9	38,5
Ga	ppm	22,0	14,7	15,7	15,2	16,2	17,5	16,6
Rb	ppm	80,2	44,1	76,8	71,7	61,9	57,4	60,7
Sr	ppm	167	209	1100	262	395	339	400
Y	ppm	25,5	28,3	18,5	18,3	18,0	20,2	19,8
Zr	ppm	302	202	140	121	107	208	140
Nb	ppm	24,7	21,1	16,3	13,1	11,1	13,6	13,9
Sn	ppm	2,72	2,17	1,74	1,79	1,90	2,07	2,14
Cs	ppm	5,36	2,88	4,87	6,17	4,87	4,99	5,35
Ba	ppm	74,2	72,6	71,8	76,7	128	71,1	86,2
La	ppm	34,9	35,6	25,7	24,4	22,6	28,5	27,7
Ce	ppm	65,1	61,2	56,9	53,1	44,7	54,2	54,2
Pr	ppm	7,46	7,29	6,41	6,31	5,19	6,23	6,13
Nd	ppm	28,5	29,5	25,7	24,6	20,5	23,9	24,2
Sm	ppm	5,69	5,53	5,20	5,04	3,93	4,61	4,54
Eu	ppm	1,28	1,46	1,28	1,12	0,93	1,11	1,06
Gd	ppm	4,89	5,12	4,41	4,05	3,73	4,15	4,06
Tb	ppm	0,78	0,81	0,64	0,63	0,55	0,64	0,63
Dy	ppm	5,04	5,14	4,00	3,67	3,35	3,60	3,72
Ho	ppm	0,98	0,97	0,74	0,69	0,62	0,73	0,70
Er	ppm	2,77	2,79	2,15	1,93	1,83	2,15	2,11
Tm	ppm	0,42	0,41	0,30	0,29	0,25	0,29	0,29
Yb	ppm	2,82	2,71	1,97	1,87	1,59	1,93	1,99
Lu	ppm	0,41	0,40	0,29	0,28	0,25	0,31	0,28
Hf	ppm	7,27	4,71	3,49	3,13	2,82	5,30	3,61
Ta	ppm	1,50	1,27	0,99	0,84	0,73	0,92	0,94
Tl	ppm	0,33	0,20	0,30	0,25	0,23	0,25	0,28
Pb	ppm	14,0	16,0	11,8	8,58	5,78	9,02	9,44
Th	ppm	12,0	9,61	7,74	7,69	7,57	9,52	9,51
U	ppm	2,33	2,23	1,45	1,92	2,04	2,26	2,32
CIA		82	77	76	81	75	66	70
CIW		91	83	86	91	84	71	76
CIX		86	84	81	84	81	76	79
WIP		31	26	36	24	24	35	30
PIA		75	76	68	72	70	68	69
CPA		96	91	92	95	91	83	87
WI		2	2	3	4	4	5	4
Rb/K_2O		39	39	38	43	44	44	46

Sample	Aragonite	Calcite	Mg-Calcite	Dolomite	Chlorite	Kaolinite	Illite	I/S	K-Feldspar	Albite	Anorthite	Quartz	Gypsum	Jarosite	Hematite	Pyrite
CT1	0,9	6,0	0,0	2,4	6,0	6,3	2,9	53,7	3,1	4,5	0,0	13,6	0,0	0,0	0,0	0,8
CT2	0,4	4,2	9,3	2,1	6,7	1,2	1,5	45,1	1,9	6,7	0,0	20,6	0,0	0,0	0,0	0,3
TMR1	0,8	15,1	3,9	5,0	10,5	2,8	1,8	43,2	3,5	5,0	0,0	8,2	0,0	0,0	0,0	0,2
TAM4	0,0	21,2	13,9	0,1	5,1	5,1	2,2	35,1	1,8	3,1	0,0	12,4	0,0	0,0	0,0	0,1
TAM3	0,1	25,6	18,3	0,0	5,3	3,8	1,9	27,9	2,2	5,3	0,0	9,6	0,0	0,0	0,0	0,0
TAM2	0,0	19,9	10,7	0,0	2,6	5,1	1,9	32,1	2,2	13,4	0,0	12,0	0,0	0,0	0,0	0,0
TAM1	0,0	21,1	13,7	0,1	4,8	4,1	2,2	31,0	1,2	10,2	0,0	11,8	0,0	0,0	0,0	0,0
SPD0	1,8	22,8	21,6	8,2	4,0	4,6	11,9	10,0	2,1	3,0	0,0	9,7	0,0	0,0	0,0	0,5
SPD1	0,6	16,6	32,2	2,2	1,0	2,0	23,9	12,0	1,4	1,5	0,0	6,2	0,0	0,0	0,0	0,3
SPD2	0,0	3,6	9,5	0,2	0,0	5,4	17,8	43,5	5,8	2,2	0,0	11,9	0,0	0,0	0,0	0,3